Lamb waves based active sparse tomography for damage size quantification in composite structures : data-driven and parameter inversion methods

William Briand

HESAM UNIVERSITÉ

Arts et Métiers Sciences et Technologies

ÉCOLE DOCTORALE SCIENCES ET MÉTIERS DE L'INGÉNIEUR

Laboratoire PIMM - Campus de Paris

THÈSE

présentée par : **William BRIAND**

soutenue le : **23 Mars 2022**

pour obtenir le grade de : **Docteur d'HESAM Université**

préparée à : **École Nationale Supérieure d'Arts et Métiers**

Spécialité : **Acoustique**

Lamb waves based active sparse tomography for damage size quantification in composite structures: data-driven and parameter inversion methods

THÈSE dirigée par :

M. MECHBAL Nazih

et co-encadrée par :

M. GUSKOV Mikhail

M. RÉBILLAT Marc

Jury

M. Wiesław OSTACHOWICZ	Professeur, Institute of Fluid-Flow Machinery, PAN	Président
M. Patrice MASSON	Professeur, GAUS, Université de Sherbrooke	Rapporteur
M. Emmanuel MOULIN	Professeur, IEMN, UPHF	Rapporteur
M. Nazih MECHBAL	Professeur, PIMM, ENSAM	Examinateur
M. Mikhail GUSKOV	Maître de conférence, PIMM, ENSAM	Examinateur
M. Marc REBILLAT	Maître de conférence, PIMM, ENSAM	Examinateur
M. Bruno SANTOS	Maître de conférence, ATO, TU Delft	Invité

THÈSE

Acknowledgements

Mes premiers remerciements vont à mon équipe encadrante, Nazih, Marc et Mikhail. Merci de m'avoir fait confiance au début de cette thèse et m'avoir permis de faire partie de ce projet. Merci également pour votre disponibilité et votre encadrement pendant ces trois ans. J'ai beaucoup appris à vos côtés, d'un point de vue scientifique, technique et humain.

I deeply thank the members of the jury for having accepted to examine this manuscript and to have attended my defense. Thank you for your very pertinent remarks and questions.

I also thank all the members of the ReMAP project, in particular the partners involved in package 3 and 4. It was a great project and an extremely enriching experience for me where I learned a lot on a technical level. Special thanks to Agnes, Nan and George for their work during the test campaigns.

Je remercie tous les membres du laboratoire que j'ai pu croiser durant ma thèse, en particulier Laurent Berthe pour son aide lors de mes manips. Je tiens également à remercier Eric pour le temps qu'il a passé à m'aider sur mes simulations. Merci aux doctorants et post-doc que j'ai pu rencontrer dans l'équipe durant ces trois années et avec lesquels j'ai passé de très bons moments: Hadrien Postorino, Nassim, Quentin, Hadrien Pinault, Juan, Mattias, Rafael, Florian, Vincent, Christophe, Marc, Arthur, Julie, Erika, Sebastian et Thibault.

J'ai également une pensée pour une communauté (qui se reconnaitra), en particulier Valentin, Fabien, Hedi, Etienne, François, Julien, Jonathan, Victor, Lukas, Alexis, Alexandre, Mathieu et Yanis.

Merci à ma famille pour votre soutien (depuis un autre continent) pendant cette thèse et pendant tout ma scolarité. Merci également à ma belle-famille pour vos encouragements.

Merci à Oka pour sa fonction "anti-stress" qui m'a bien aidé dans les moments difficiles.

Enfin je remercie profondément Kenza pour ta patience et ton soutien sans faille. C'est une nouvelle vie qui commence pour nous deux et j'espère que nous pourrons réaliser tous nos projets.

Table of contents

List of figures

List of tables

Chapter 1

Résumé étendu

1.1 Introduction

1.1.1 Structural Health Monitoring

Le SHM (Structural Health Monitoring) est une approche multidisciplinaire dont l'objectif est d'évaluer l'intégrité et la durabilité des structures de façon à maintenir et étendre leur durée de vie en détectant les dommages et en prédisant leur ruine. Cette approche est basée sur un large panel de techniques qui peuvent être appliquées séparément ou de façon conjointe. On peut mentionner les méthodes passive telles que les mesures de déformation par fibre optique ou encore les mesures d'émission acoustique. Il existe également des méthodes actives telles que l'émission-réception d'ondes guidées par excitation de patch piézoélectriques. Depuis plus de vingt ans, la communauté scientifique étudie ce sujet avec un intérêt grandissant comme le montre l'évolution du nombre de publication contenant les termes "structural health monitoring" (Fig. 1.1). L'approche SHM est classiquement découpée en quatre niveaux de complexité croissante :

- La détection: la méthode peut identifier la présence d'un dommage dans la structure
- La localisation: la méthode donne la position du dommage
- Quantification de la taille : la méthode donne la taille du dommage
- Pronostic : la méthode donne la durée de vie restant de la structure, c'est-à-dire le temps restant avant que celle-ci ne soit plus opérationnelle

Il est important de noter que chaque niveau repose sur les niveaux précédents. Par exemple, pour localiser un dommage sa présence doit être confirmer par une méthode de détection. Le secteur aéronautique est un secteur très intéressé par cette technologie. En effet, les matériaux composites constituent une part grandissante des avions modernes (plus de 50% pour l'A350 XWB d'Airbus), en particulier grâce à leurs propriétés mécaniques et leur faible poids. Cependant cela pose de nouveaux problèmes : comme ces matériaux sont sujets à des dommages qui ne peuvent être détectés par des inspections visuelles, cela complique grandement la tâche des opérateurs de maintenance. Pour gagner du temps lors d'une inspection, un appareil muni d'un système SHM pourrait signaler

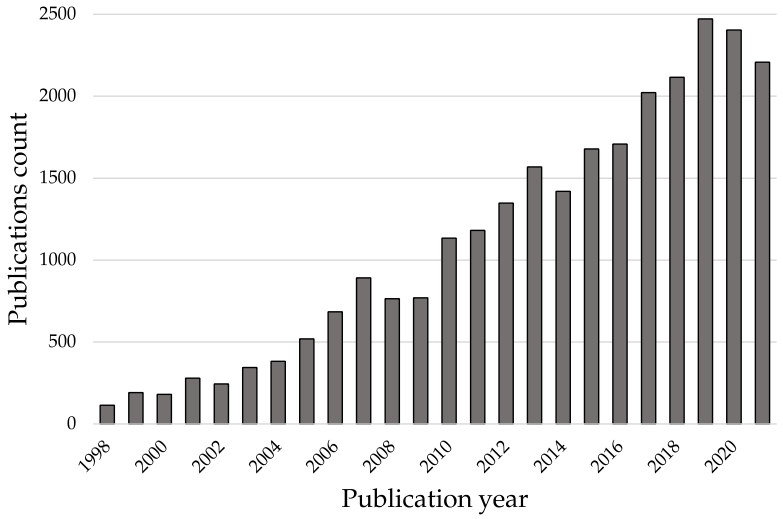

Fig. 1.1 Nombre d'articles de recherche contenant les termes "structural health monitoring" publiés chaque année. Données provenant du site Web of Science.

aux techniciens les zones à contrôler en priorité. De plus, un tel système peut être utilisé pour surveiller des endroits habituellement peu ou pas accessibles par un opérateur.

Un autre intérêt du SHM pour le secteur aéronautique est l'intégration de ces résultats dans une approche globale de la maintenance d'une flotte d'avions. On se baserait alors sur l'état de santé réel de l'avion, à l'opposé du système actuel qui repose sur l'utilisation d'un calendrier de maintenance fixe fourni par le constructeur. Cette approche est appelée "Condition-based maintenance" ou CBM. En réalisant la maintenance seulement quand elle est nécessaire, les compagnies aériennes pourraient réaliser d'importantes économies par rapport à une maintenance trop tardive (qui provoque des retards) ou une maintenance prématurée, comme la Fig. 1.2 l'illustre.

Pour ces raisons, l'Advisory Council for Aeronautical Research in Europe prévoit qu'en 2050 tous les nouveaux avions seront conçus pour la CBM entrainant une baisse de 40% des frais de maintenance et une hausse de la disponibilité des appareils.

1.1.2 Problématique

Dans cette thèse, nous nous intéressons à la surveillance de structures aéronautiques en matériaux composites carbone/époxy. Pour cela nous utilisons la technologie d'émission-réception d'ondes guidées qui consiste à équiper la structure de patchs piézoélectriques sur sa surface. Ces transducteurs sont capables d'émettre et de recevoir des ondes de Lamb. Ainsi quand une onde est émise par un patch, celle-ci interagit avec l'éventuel dommage situé dans la structure et est convertie en signal électrique par les autres éléments piézoélectriques. L'idée du SHM basé sur les ondes de Lamb est de développer des algorithmes qui permettent d'extraire des informations sur le dommage à partir de ces signaux : sa présence, sa position, son type, etc.

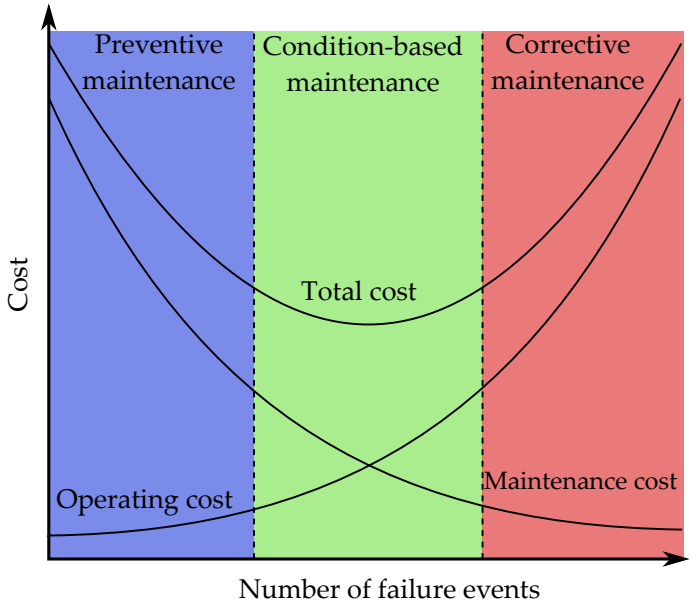

Fig. 1.2 Graphique des coûts de maintenance optimaux.

Dans le cadre de cette thèse, nous nous attaquons au problème de la quantification de taille de dommage mentionné plus haut. C'est une étape cruciale d'un procédé de SHM puisque la taille d'un dommage est une information primordiale pour nourrir un algorithme de pronostic, c'est-à-dire pour prédire la durée de vie restante d'une structure. Cette donnée peut être utilisée par exemple pour établir une date de maintenance optimale.

Dans la littérature, on trouve peu de méthodes dédiées exclusivement à la quantification et encore moins sont appliquées à des données expérimentales provenant de structures composites réalistes. De plus, les dommages artificiels considérés sont souvent peu réalistes (aimant, ruban adhésif collé en surface). Le premier objectif de cette thèse est d'abord de proposer une base de données de signaux provenant d'essais de fatigue réalisés sur des échantillons composites représentatif de composants aéronautiques. Ces tests ont été réalisé avec différents types de chargements et sur des structures comportant un dommage artificiel (impact, délaminage artificiel) pour initier la propagation d'un dommage. Ces tests ont été réalisé dans le cadre du projet européen H2020 ReMAP qui finance cette thèse. Les mesures effectuées ont été publiés en libre accès [1] pour permettre leur réutilisation par la communauté scientifique [1].

Le second objectif de cette thèse est de fournir des méthodes de quantification de taille de dommage c'est-à-dire des stratégies pour estimer l'étendu d'un dommage de la façon la plus fiable possible à partir de signaux mesurés. Les méthodes existantes dans la littérature sont principalement des approches basées sur un apprentissage à partir de données connues. Cependant ces approches requièrent des jeux de données conséquents pour cette phase d'entraînement, or ces données sont souvent difficiles à obtenir.

[1] Lien

1.1.3 Le projet ReMAP

ReMAP est un projet H2020 de l'Union Européenne qui implique de nombreuses universités, centres de recherche et industriels comme le montre la Fig. 1.3. Le but de ce programme de quatre ans est de développer un démonstrateur de gestion de la maintenance pour une flotte d'avions. L'objectif est de permettre la réduction des coûts de maintenance en passant d'une approche classique qui suit un calendrier préétabli par le constructeur à des interventions basées sur l'état de santé réel de l'appareil. Les avions modernes possèdent déjà des centaines de capteurs pour surveiller tous les sous-systèmes à bord (roues, freins, système de contrôle de la température, climatisation, etc.). Il y a déjà eu des tentatives d'utiliser les données de ces capteurs pour surveiller chacun de ces sous-systèmes de façon isolée, en revanche aucun travail n'a été réalisé pour incorporer ces résultats de diagnostic ou pronostic dans un système de CBM. Le but ultime de ReMAP est donc de développer chaque brique de la CBM d'un point de vue technologique, méthodologique et législatif. Un tel système doit être capable d'acquérir et traiter rapidement les données d'un capteur pour pouvoir adapter le calendrier de maintenance en continu. Le projet a pour but de démontrer et quantifier les bénéfices d'un système SHM dans ce contexte : réduction des coûts de maintenance, gain potentiel en poids et réduction des pannes matérielles. Enfin, il est prévu d'écrire une feuille de route pour le déploiement du CBM en Europe en proposant des lignes directrices et des standards pour la certification.

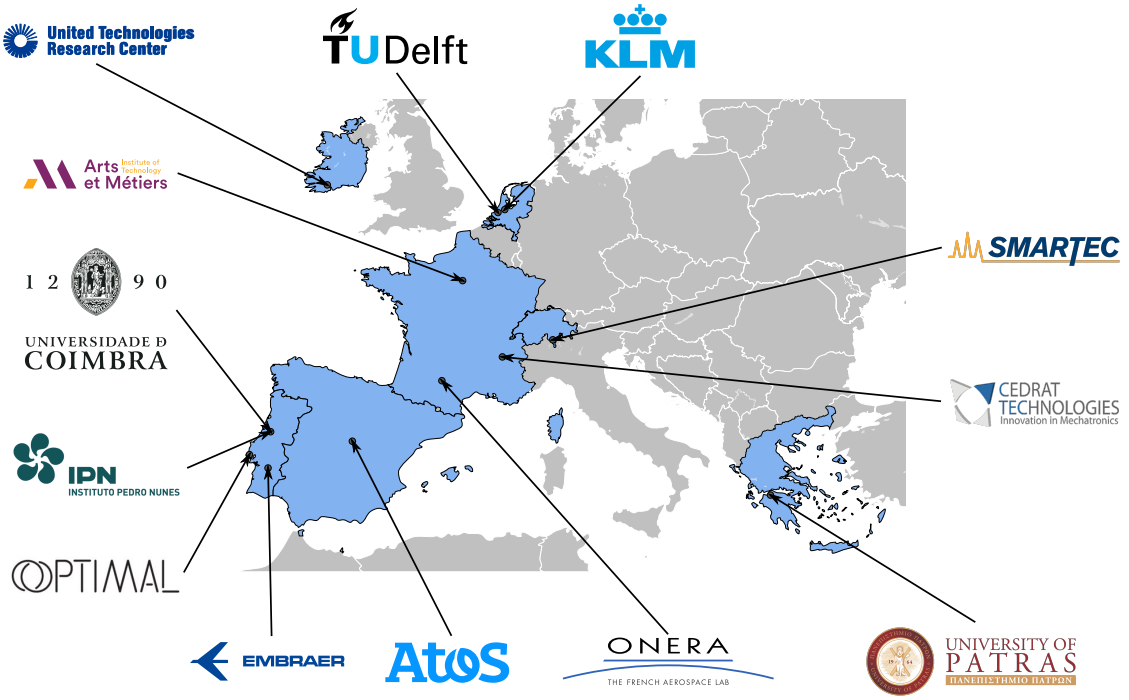

Fig. 1.3 Carte des partenaires impliqués dans ReMAP.

1.1.4 Organisation du manuscrit

Ce manuscrit s'articule de la façon suivante. Après cette partie introductive, on présente les campagnes d'essais réalisées pendant le projet ReMAP. On détaille ensuite une première méthode développée pendant cette thèse, reposant sur une approche d'apprentissage à partir de données. La théorie de la méthode est sommairement présentée avant de donner quelques résultats obtenus sur des données expérimentales. Une deuxième méthode est ensuite introduite, cette fois basée sur une approche d'inversion de modèle. Pour cela on décrit d'abord le développement d'un modèle analytique permettant de prédire le signal reçu par un PZT après diffraction d'une onde par un dommage. Le modèle est validé en le comparant à des données provenant de simulation éléments finis. A partir de ce modèle analytique, on établit une méthode d'identification des caractéristiques du dommage (taille et sévérité). Cette approche est validée sur des données numériques et des données expérimentales.

1.1.5 Contributions

Articles publiés dans des journaux à comité de lecture

- **W. Briand, M. Rébillat, M. Guskov, and N. Mechbal**. "Upcoming damage size quantification in aeronautic composite structures based on imaging results post-processing." *Journal of Intelligent Material Systems and Structures*, 2021.
- (Submitted) **W. Briand, M. Rébillat, M. Guskov, and N. Mechbal**. "Damage size and severity quantification in quasi-isotropic composites by parameters identification approach." *Mechanical Systems and Signal Processing*, 2022.

Présentations dans des congrès internationaux

- **W. Briand, M. Rébillat, M. Guskov, and N. Mechbal**, "Damage Size Quanftification In Aeronautic Composite Structures Based On Imaging Results Post-Processing", in *IX ECCOMAS Thematic Conference on Smart Structures and Materials* (pp. 1-12). A. Benjeddou, N. Mechbal and JF Deu.
- **W. Briand, M. Rébillat, M. Guskov, and N. Mechbal**, "Damage imaging post processing for delamination size assessment of CFRP aeronautic structures." In *European Workshop on Structural Health Monitoring*, pp. 140-148. Springer, Cham, 2020.
- **W. Briand, M. Rébillat, M. Guskov, and N. Mechbal**, "Damage size quantification using Lamb waves by analytical model identification." In *European Workshop on Structural Health Monitoring*, 2022.
- **W. Briand, M. Rébillat, M. Guskov, and N. Mechbal**, "Lamb waves scattering model for identification of damage parameters." In *International Conference for CBM in Aerospace*, 2022.

Base de données en libre accès

– **D. Zarouchas, A. Broer, G. Galanopoulos, W. Briand, R. Benedictus, T. Loutas**, "Compression Compression fatigue tests on single stiffener aerospace structures", DataverseNL,https://doi.org/10.34894/QNURER, 2021.

1.2 Campagnes d'essais

Un des objectifs majeurs du projet européen ReMAP dans lequel s'inscrit cette thèse est de valider les approches SHM sur des données proches de la réalité. Ces données sont obtenues lors d'essais de fatigue sur des échantillons représentatifs de composants utilisés dans l'industrie aéronautique. Les spécimens étudiés sont de complexité croissante, nous avons donc d'abord utilisés des éprouvettes de traction pour valider la tenue des PZTs. Des campagnes de fatigue en compression-compression ont ensuite été réalisées sur des plaques comportant un raidisseur central. Afin de réduire la durée de vie de la structure, des dommages locaux sont introduits artificiellement à la fabrication (morceau de Téflon entre deux plis du composite) ou par impact. Ces essais de fatigue sont suivis en utilisant plusieurs types de technologies SHM : ondes de Lamb, émission acoustiques et mesures de déformation par fibre optique. Enfin, des essais similaires ont été réalisés sur des panneaux de plus grandes dimensions comportant plusieurs raidisseurs.

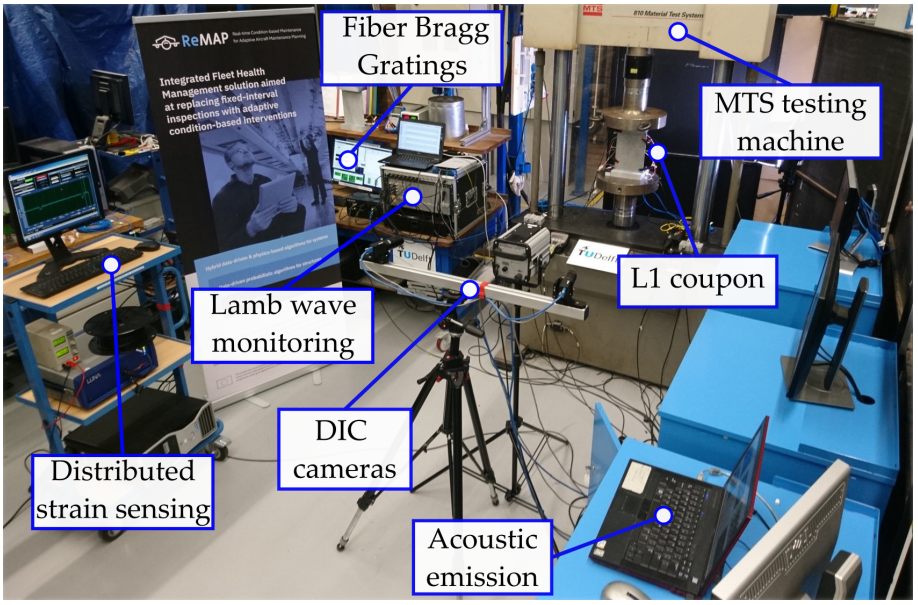

Fig. 1.4 Banc de test expériemental pour la campagne d'essais L1 à l'Université de Delft.

Tous ces essais ont généré des données de taille considérable. En effet, pour les mesures d'émission-réception par ondes de Lamb, on dispose d'un signal temporel pour chaque chemin actionneur-capteur à chaque fréquence d'excitation et chaque point de mesure durant l'essai. Afin de pouvoir analyser plus facilement ces résultats, nous avons réduit la dimension des données en calculant pour chaque signal temporel un grand nombre de de-

scripteurs provenant de la littérature (énergie du signal, corrélation croisée, non-linéarité, etc.). Nous avons ensuite cherché à identifier lesquels de ces descripteurs pouvaient être utilisés pour faire de la surveillance de structure. Pour cela nous avons quantifié leurs performances à l'aide d'un score pris comme la moyenne des attributs de monotocité, trendabilité et prognosabilité. Ces deux derniers critères permettent de mesurer respectivement pour une population d'échantillons, l'auto-corrélation d'un indicateur et si les valeurs finales sont proches les unes des autres. Nous avons alors pu isoler une partie des descripteurs qui remplissaient bien ces critères.

1.3 Méthode par par traitement d'images de localisayion

Dans cette thèse, nous proposons une méthode de quantification de taille de dommage par post-traitement de résultats de localisation. En effet, il existe de nombreuses méthodes de localisation dans la littérature et certains auteurs se sont penchés sur l'utilisation de ces résultats pour obtenir la taille des dommages détectés. Cela consiste essentiellement à utiliser ces méthodes de localisation pour estimer la position des bords du dommage et ainsi remonter à son étendue. Cependant, ces méthodes sont valides pour une méthode de localisation bien particulière et ne sont pas vérifiées sur des données expérimentales provenant de structures composites complexes comportant des dommages réalistes. Ici, nous proposons une méthode pouvant être appliquée avec n'importe quelle méthode de localisation. On prend en données d'entrée les images provenant d'un algorithme de localisation quelconque qui attribue à chaque point de la structure un indice de probabilité de présence du dommage (Damage Localization Index ou DLI). Pour cela on définit un nouvel indice d'endommagement dénommé HDLI (High Damage Localization Index) qui correspond à l'aire de la zone où le DLI dépasse un seuil préfinit. L'indice HDLI est défini comme l'aire de cette zone divisée par l'aire totale de la structure.

La méthode de quantification s'articule en deux temps. D'abord une phase d'apprentissage puis une étape de prédiction. La phase d'apprentissage consiste à calculer le HDLI de plusieurs cas d'endommagement à partir d'images de localisation dont on connait la taille du dommage associé. Cela permet de créer une base de données où l'on dispose de couples de valeurs HDLI-taille. A partir de cette base de données, on réalise une régression polynomiale en écartant les valeurs de HDLI proches de zéro pour ne pas perturber le modèle. On peut alors passer à la seconde étape, qui consiste à estimer la taille d'un dommage dont la taille est inconnue, à partir d'une image de localisation. Pour cela on calcule le HDLI et on utilise le modèle de quantification établi pendant la phase d'apprentissage pour estimer la taille de dommage correspondante. Dans la suite, on procède à la phase d'apprentissage sur les prémices du dommage et on applique le modèle pour prédire les tailles du dommage pour suivre son évolution dans le temps. Dans cette méthode, le choix du seuil utilisé dans le calcul du HDLI est établi de façon automatique en testant plusieurs valeurs possibles et en regardant les résultats obtenus par le modèle de régression sur les données d'apprentissage. De même, le degré du polynôme utilisé dans la régression est

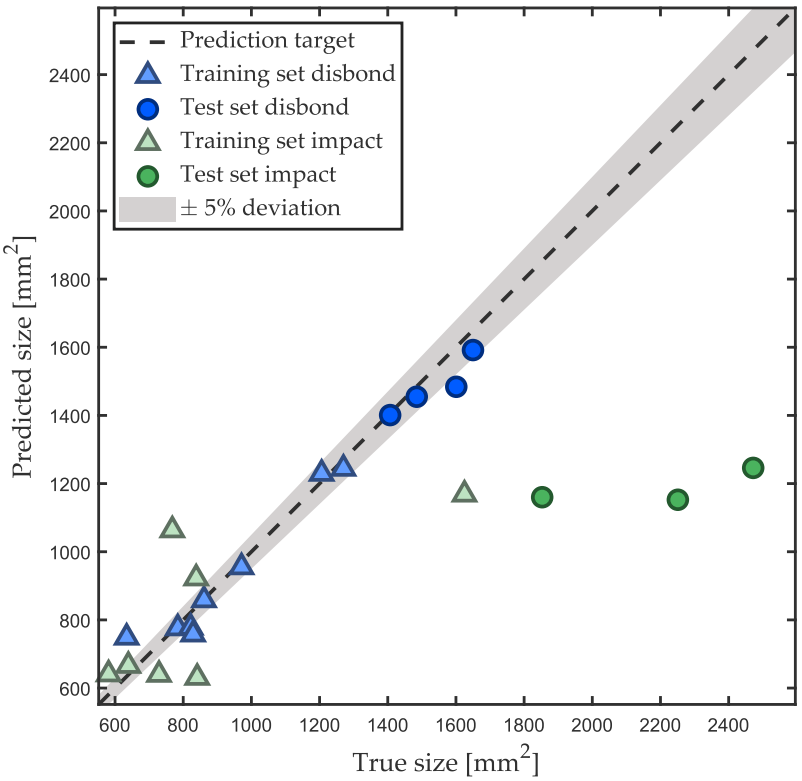

Fig. 1.5 Résultats obtenus sur les échantillons L1 du projet ReMAP.

choisi arbitrairement et un terme de régularisation permet de contraindre le modèle à choisir le polynôme le plus simple possible. En outre, chacune des méthodes de localisation considérée dépend d'un paramètre propre. Ce paramètre ayant peu d'influence sur le résultat de localisation, on décide de fixer ces valeurs arbitrairement.

Pour tester cette méthode, on l'applique sur des données de simulations numériques en utilisant des images provenant de méthodes de localisation classiques : ToA, DToA, DAS et RAPID. On trouve alors que les résultats sont très supérieurs dans le cas de la méthode RAPID. En effet, avec cette méthode on obtient de bons résultats à la fois sur les données d'entrainement et pour la prédiction. Pour l'application aux données expérimentales, on ne conserve donc que cette méthode. Pour valider la méthode de quantification, on utilise des données expérimentales provenant du projet ReMAP. On teste alors deux types de dommages : délaminage artificiel et impact. Les résultats sont présentés Fig. 1.5. On remarque ici que les résultats sont globalement bons pour le délaminage artificiel, tant en apprentissage qu'en prédiction. En revanche la prédiction dans le cas de l'impact est assez décevante. Cela provient sans doute du fait que dans le cas de l'impact, on ne créé pas uniquement un délaminage mais aussi d'autres types de dommage qui ne sont pas pris en compte dans la méthode développée ici. Comme on ne s'intéresse qu'au délaminage ici, on peut donc conclure que la méthode fonctionne bien pour ce type de dommage.

1.4 Méthode par identification de paramètres d'un modèle physique analytique

Dans cette thèse, nous proposons une deuxième méthode de quantification de la taille des dommages qui se base sur l'inversion d'un modèle analytique. Pour cela on considère une plaque en composite stratifié sur laquelle sont collés deux éléments piézoélectriques, l'un fonctionnant comme actionneur tandis que l'autre sert de récepteur. La plaque comporte un dommage que l'on modélise par une inhomogénéité cylindrique où les propriétés matériaux sont différentes du reste de la structure. L'objectif est ici de prédire le signal de sortie mesuré par le récepteur lorsque l'on émet une onde avec l'actionneur et que cette onde intéragit avec le dommage. Pour simplifier le modèle, on fait plusieurs hypothèses : on homogénéise le matériau comme une plaque d'une seule couche transverse isotrope, les PZTs sont considérés parfaitement collés à la plaque et on assimile les ondes de Lamb à des ondes de plaque. Par ailleurs, on s'intéresse uniquement au premier mode en compression puisque c'est le mode de propagation le plus rapide et donc le plus simple à manipuler expérimentalement.

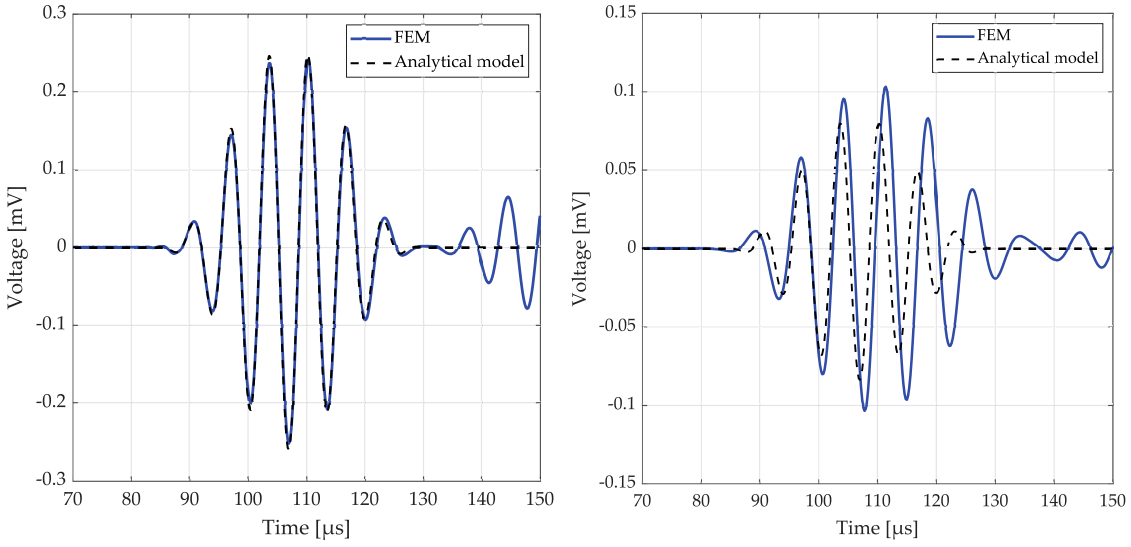

(a) (b)

Fig. 1.6 Comparaison des signaux temporels obtenus avec le modèle analytique et avec la méthode des éléments finis dans le cas sans atténuation et avec des PZTs d'épaisseur 0.1mm (a) et dans le cas avec atténuation et avec des PZTs d'épaisseur 0.5mm (b).

Après développement, on obtient un modèle analytique pouvant se calculer très rapidement. Ce modèle est validé en comparant ses résultats à ceux obtenus avec une simulation éléments finis avec la même configuration. On remarque alors que pour des PZTs de faibles épaisseur et en négligeant l'atténuation, on obtient un résultat excellent lorsque l'on compare le signal reçu avec celui obtenu en simulation par la méthode des éléments finis avec un temps de calcul 1000 fois inférieur (cf. Fig. 1.6). En revanche lorsqu'on considère des PZTs de même épaisseur que ceux utilisés dans ReMAP et en prenant en

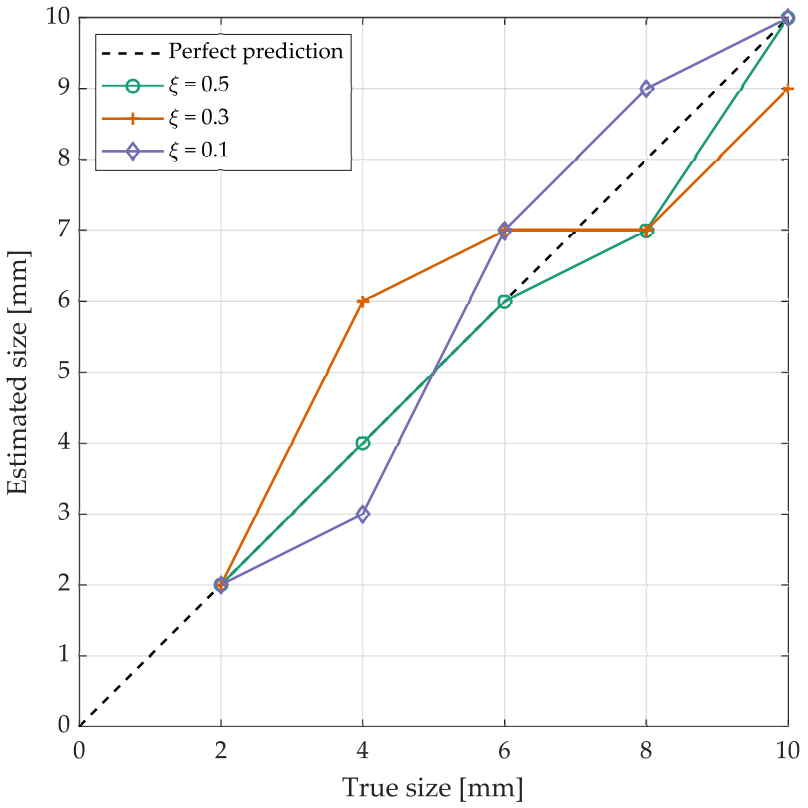

Fig. 1.7 Résultats obtenus avec la méthode par identification de paramètres.

compte l'atténuation, on obtient un signal qui diffère de la simulation. On remarque en particulier un décalage en temps, qui ne nous dérangera pas dans l'exploitation du modèle car la taille du dommage est surtout corrélée avec l'amplitude du signal reçu. Or on observe une différence d'amplitude entre le modèle et la simulation. Ces résultats sont cependant à tempérer : on obtient des amplitudes du même ordre de grandeur qui seront recalées pour permettre l'exploitation pour la quantification.

A partir de ce modèle, on développe une méthode de quantification sans apprentissage pour caractériser un dommage en estimant sa taille et sa sévérité (le ratio entre le module Young dans la plaque et dans le dommage). Pour cela on cherche à minimiser l'écart entre l'amplitude du signal expérimental et l'amplitude du signal obtenu avec le modèle en faisant varier les caractéristiques du modèle. Pour ce faire on commence par réaliser une étape de pré-calcul où l'on calcule les valeurs d'amplitudes avec le modèle analytique pour tout un jeu de paramètres et pour chacun des chemins actionneur-récepteur du problème considéré. On réalise également ces calculs pour toutes les fréquences d'excitation considérées. On peut alors passer à la partie prédiction de la méthode qui consiste à comparer l'amplitude d'un signal expérimental pour un chemin et une fréquence donnés, aux valeurs pré-calculées avec le modèle. On cherche alors le couple de caractéristiques du dommage sévérité et taille qui minimise l'écart entre ces deux valeurs. On teste cette approche sur des données éléments finis en faisant varier à la fois la taille de dommage

et la sévérité. On peut voir qu'on obtient des résultats très satisfaisants tant en prédiction de la taille qu'en prédiction de la sévérité.

1.5 Conclusion

Dans cette thèse, le but était de proposer des méthodes de quantification de taille de délaminage dans les matériaux composites. Ce travail multidisciplinaire apporte des réponses à ce problème dans le cas où on utilise des éléments piézoélectriques pour générer des ondes de Lamb.

Pour valider proprement les méthodes développées, il est nécessaire d'avoir des données expérimentales obtenues dans des conditions proches du contexte industriel. Pour cela, nous avons réalisé des campagnes de fatigue sur des échantillons proches de structures aéronautique utilisées dans l'industrie pour créer une base de données qui nous a permis de tester nos algorithmes. La première étape de ces campagnes de test était de vérifier la résistance des éléments piézoélectriques au chargement en fatigue ce qui nous a permis de conclure que ces transducteurs remplissaient le cahier des charges. Puis nous avons réalisé des tests de fatigue sur des échantillons comportant des raidisseurs en imposant différents chargements et en initiant différents types de dommage. En suivant ce principe, nous avons réalisé des tests en fatigue sur de grands panneaux. Les données générées permettent une validation rigoureuse des méthodes proposées. De plus, comme ces données sont disponibles en libre accès, les membres du projet espèrent que la communauté utilisera ces résultats pour valider leurs propres méthodes ce qui donnera un point de comparaison pour juger leurs performances des différentes approches. Nous avons analysé les données des échantillons L1 pour identifier, parmi les indices d'endommagement classiques, ceux qui étaient les plus à même d'être utilisé pour faire de la quantification ou du prognostic. Pour faire une sélection avec des critères quantitatifs, nous avons utilisé une approche qui classe les DI selon leur monotonicité, leur trendabilité et leur prognosabilité. Nous avons identifié plusieurs descripteurs qui pourraient servir à faire de la surveillance de structure. Enfin, nous avons caractérisé le bruit de mesure des données expérimentales pour s'assurer de la bonne qualité des mesures d'une part, et d'autre part pour pouvoir reproduire un bruit similaire lors des simulations numériques.

La problématique de cette thèse était de proposer des méthodes d'évaluation de la taille de dommage par ondes guidées. Nous avons proposé deux méthodes avec des approches très distinctes. La première repose sur l'apprentissage d'un modèle mathématique à partir d'un jeu de données labélisées. La deuxième approche consiste quant à elle à utiliser un modèle analytique préalablement développer pour utiliser une méthode d'inversion et obtenir une estimation des caractéristiques du dommage. Dans les deux cas les méthodes ont été validées avec succès sur des données issues de simulation numériques et sur des données expérimentales.

Chapter 2

Introduction

2.1 Context

In recent years, we have seen several disasters caused by the collapse of civil engineering structures. In April 2020, a bridge in the city of Aulla in northern Italy, usually very frequented, collapsed with no fatalities thanks to the lockdown in place. This disaster comes two years after the collapse of the Morandi bridge in Genoa, which killed 43 people and injured 16. In June 2021, part of a 12-story building in Miami failed in the middle of the night killing 98 people and injuring 11. In December 2021 in the suburbs of Paris, a building with 200 inhabitants was evacuated because it threatened to collapse. This list is unfortunately not exhaustive, and if investigations are in progress to better understand the causes of these tragedies, they have for origin the presence of a localized damage which spread very quickly without being noticed. With the aging of reinforced concrete infrastructures, other disasters may occur. In order to prevent this, and to react in time while keeping a reasonable cost, a solution may be to rely on the use of structural heath monitoring.

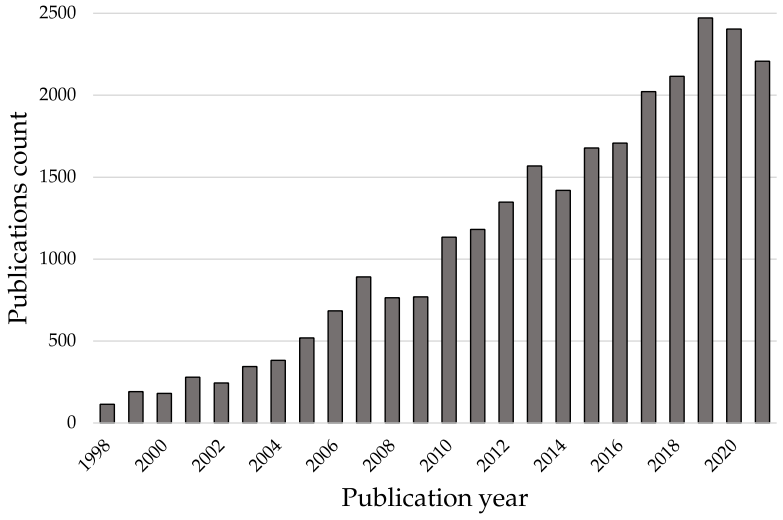

Fig. 2.1 Number of publications containing the words "structural health monitoring" versus the publication year. Data provided by Web of Science.

Structural Health Monitoring or SHM, is a multidisciplinary approach whose objective is to evaluate the integrity and durability of structures, in order to maintain and extend their service life, and to detect and predict their failures. This approach is based on a wide range of techniques that can be used separately or in a combined manner. We can mention passive methods such as the measurement of deformation by optical fibers or FBG, the measurement of acoustic emission or noise correlation computation [2]. Active methods also exist such as guided wave propagation by excitation of piezoelectric patches. For more than twenty years, the scientific community has been studying the subject with a growing interest as shown by the evolution of the number of publications containing the terms "structural health monitoring" Fig. 2.1. Classically, the SHM approach is declined in four levels of increasing complexity [3]:

- **Detection**: the method can identify the presence of damage in the structure.
- **Localization**: the method gives the location of damage.
- **Size quantification**: the method gives the size of damage.
- **Prognosis**: the method gives the remaining useful life of the structure, i.e. the time left before it is no longer operational.

It has to be noticed that each level rely on the results from the lower levels. For example, to localize a damage its presence needs to be confirmed by a detection method.

The aerospace sector is very interested in this technology. While composites constitute a growing part of recent aircraft (more than 50% for the A350 XWB from Airbus), particularly thanks to their mechanical properties and their low weight, their use poses new problems related with airplane inspections. Indeed, these materials are subject to damage that cannot be spotted by visual inspection such as Barely Visible Impact Damage (BVID), which greatly complicates the task of maintenance operators. To gain speed in an inspection, a device with an SHM system can notify maintenance technicians of the areas to be inspected. In addition, an SHM system can be used to monitor locations that are usually inaccessible to an operator.

Another interest of SHM in aeronautics is the integration of these SHM results in a global approach to fleet maintenance based on the overall health of the aircraft, as opposed to the current system based on a maintenance schedule set by the manufacturer. This approach is called condition-based maintenance or CBM. By performing maintenance only when it is needed, we save the costs of a belated maintenance that leads to a increased downtime for repair or limits the inspection costs of a premature inspection as shown in Fig. 2.2.

For that reason the Advisory Council for Aeronautical Research in Europe envisions that by 2050 all new aircraft will be designed for CBM, resulting in a significant decrease of 40% maintenance time and cost, an increase in aircraft availability and a maximization of asset utilization [4]. Maintenance is a major issue for the airline industry since it is estimated that a large proportion of flight delays are caused by maintenance issues. For

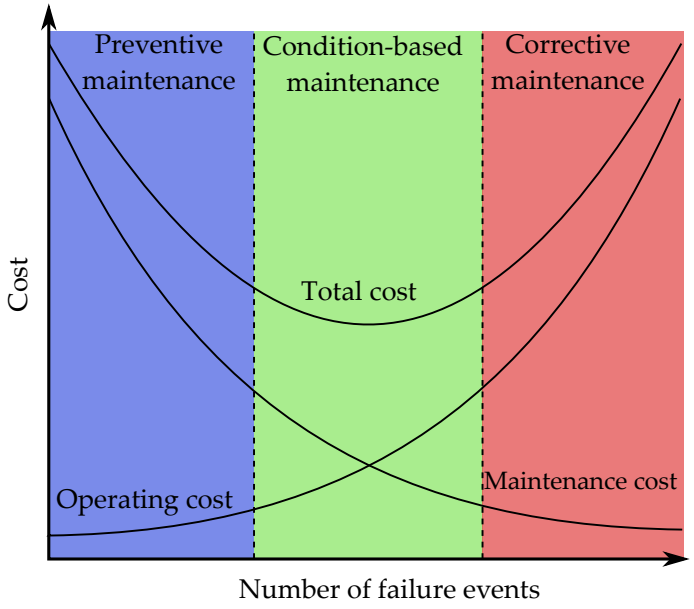

Fig. 2.2 Optimal maintenance cost diagram.

example, Zámková et al. have shown that for an European airline about 4% of the delays are due to hardware defects but that these represent 13% of the delays of more than two hours [5].

2.2 Scientific challenges and scope of this thesis

In this thesis, we are interested in the health monitoring of aeronautical parts made of carbon/epoxy composite material. For this purpose, we use the guided wave technology, which consists in equipping a structure with piezoelectric patches on its surface that are able to send and receive Lamb waves within it. Thus, when a wave is emitted by a patch, it will be altered by the possible damage on its propagation path and converted into an electrical signal by the other patches. The idea of guided wave-based SHM is to develop algorithms to extract information about the damage from these signals —its presence, its position, its type, etc [6].

The scope of this thesis is to address the problem of damage size quantification mentioned earlier. This issue is crucial since it is necessary to know the size of the damage to feed a prognostic algorithm, i.e. a process to predict the remaining useful life of the structure. This information can be used for example to schedule maintenance at the optimal time.

In the literature, there are few methods dedicated exclusively to quantification, and even fewer applied to experimental data from realistic composite structures. Moreover, artificial damages are often unrealistic, such as adding a magnet on both sides of the structure or adding a thick adhesive to the surface of the part. The first objective of this thesis is therefore to propose a database of signals from fatigue tests on composite samples representative of aeronautical components. These tests will be conducted with different types

of loading and on structures with impact damage or artificial disbond made to initiate the propagation of the defect. These tests will be carried out within the framework of the European project H2020 ReMAP (Real-time Condition-based Maintenance for Adaptive Aircraft Maintenance Planning) which funded this thesis. The measurements performed will then be published in a public repository and will be freely available to the scientific community.

The main objective of this thesis is to provide damage size quantification methods, i.e. strategies to estimate the damage extent in the more reliable manner from measured signals. From the few methods available in literature, data-driven approaches seem suitable for this task. However, this kind of method require a significative ammount of data to train mathematical model. This is a major challenge that will be addressed in this thesis.

2.3 Thesis overview and contributions

This thesis is structured in five chapters. The first part is a presentation of the different tools for the modeling of the physical phenomena involved: piezoelectric elements, damage of composite materials and Lamb waves. We also formulate the damage size quantification problem that we address in the rest of the thesis.

The second chapter deals with the ReMAP project. It presents the objectives of the project, the samples and the sensors used as well as the testing campaigns. Preliminary analyses of the results obtained are also provided.

The third part concerns a data-driven damage size quantification method based on supervised learning by post-processing of images from localization algorithms. This method consists in training a quantification model on data coming from the beginning of a damage's life and then predicting its size from unknown signals. We study the localization method that allows us to obtain the best results using data from finite element simulations. This method is then successfully applied to experimental data.

Chapter four describes an analytical model to predict the voltage measured by a piezoelectric sensor at the passage of a wave generated by a piezoelectric actuator and reflected by a damage. For this purpose, we studied a system made of two piezoelectric elements ideally mounted on a quasi-isotropic laminated composite plate including a damage. The simplifications of the real problem on which the model is based are stated and then the models of each of the subsystems involved are derived to obtain a comprehensive and complete physical model. Finally, the influential parameters of the model are analyzed and the results obtained are compared with those of the finite element method simulation.

In chapter five, the model established in the previous chapter is used to establish a method for quantifying the size and severity of a damage by parameters identification. The theory of the method is presented as well as a successful application on numerical data and on experimental data.

Finally, a general conclusion and perspectives for future developments are proposed.

The results presented in this manuscript have led to the following publications in international conferences and peer-reviewed scientific journals:

Articles in peer reviewed international journals

- **W. Briand, M. Rébillat, M. Guskov, and N. Mechbal**. "Upcoming damage size quantification in aeronautic composite structures based on imaging results post-processing." *Journal of Intelligent Material Systems and Structures*, 2021.
- (Submitted) **W. Briand, M. Rébillat, M. Guskov, and N. Mechbal**. "Damage size and severity quantification in quasi-isotropic composites by parameters identification approach." *Mechanical Systems and Signal Processing*, 2022.

International conferences

- **W. Briand, M. Rébillat, M. Guskov, and N. Mechbal**, "Damage Size Quanftification In Aeronautic Composite Structures Based On Imaging Results Post-Processing", in *IX ECCOMAS Thematic Conference on Smart Structures and Materials* (pp. 1-12). A. Benjeddou, N. Mechbal and JF Deu.
- **W. Briand, M. Rébillat, M. Guskov, and N. Mechbal**, "Damage imaging post processing for delamination size assessment of CFRP aeronautic structures." In *European Workshop on Structural Health Monitoring*, pp. 140-148. Springer, Cham, 2020.
- **W. Briand, M. Rébillat, M. Guskov, and N. Mechbal**, "Damage size quantification using Lamb waves by analytical model identification." In *European Workshop on Structural Health Monitoring*, 2022.
- **W. Briand, M. Rébillat, M. Guskov, and N. Mechbal**, "Lamb waves scattering model for identification of damage parameters." In *International Conference for CBM in Aerospace*, 2022.

Dataset

- **D. Zarouchas, A. Broer, G. Galanopoulos, W. Briand, R. Benedictus, T. Loutas**, "Compression Compression fatigue tests on single stiffener aerospace structures", DataverseNL,https://doi.org/10.34894/QNURER, 2021.

Chapter 3

Lamb waves based SHM in composite structures

Summary

In this chapter, we introduce the concept of Structural Health Monitoring and describe its benefits. Composite materials and the damage they can suffer are also briefly presented. We also provide the theoretical tools to understand piezoelectricity and Lamb waves propagation since we will use this technology throughout this thesis. Finally, we present the problem addressed in this thesis and give a literature review of this topic.

Contents

3.1 Structural Health Monitoring for aeronautic structures

3.1.1 Motivation and benefits of SHM

The airline industry is subjected to very high standards. Thus, commercial aircraft are visually inspected before each flight, and manufacturers along with international safety rules impose a maintenance schedule [7]. During these inspections, the aircraft is immobilized for several days and undergoes extensive non-destructive testing or NDT. The

NDT methods represent a set of techniques that allow to characterize the integrity of structures or materials without damaging them. Among the most used technologies we can mention are eddy current, ultrasonic inspection and penetrant testing.

These inspections are very costly for the airlines, both in terms of their own costs and the loss of revenue caused by the immobilization of the aircraft. During these inspections, it is sometimes necessary to proceed to dismantling operations in order to access certain parts of the structure, inaccessible directly to the maintenance teams, without being sure of the damage presence.

In addition to this, fixed interval inspections can lead to suboptimal costs as they can occur before the need for maintenance or too late, resulting in a prolonged shutdown of the aircraft.

Consequently, all this has led to the development of numerous works and studies on the automation of structural monitoring and control. All these studies have led to the development of what is called Structural Health Monitoring or SHM. An SHM system generally requires three important elements for the implementation of the damage monitoring strategy. First, the knowledge of the monitored structure and the different possible damage scenarios. The studied structure must also be equipped with appropriate sensors and actuators and specific instruments to obtain signals that can be used for damage detection and characterization. Finally, the relevant analysis of these data must allow the extraction of information on possible damage and on the integrity of the structure.

SHM systems are designed to monitor and test the condition and performance of structures such as: bridges and dams, buildings and stadiums, ships and platforms, aircraft, wind turbines, large-scale machinery and equipment. In addition, it allows the development of condition based maintenance, i.e. the triggering of maintenance at the optimal time to save costs. It also increases security by monitoring the aircraft's structural health in real time. In the future, we can even imagine rethinking the design of structures. More complex geometries could be considered because a SHM system would allow to establish a diagnosis on parts difficult to access with conventional NDT methods and thus save time and cost. A continuous control would also allow to avoid the oversizing of some parts which can represent a major advantage when one wishes to optimize the mass of the components used.

3.1.2 Principles of an SHM system

SHM involves many scientific fields such as signal processing, statistics, fracture mechanics, material engineering, etc. Therefore, it is hard to define it properly. To that end, Worden et al. stated the different axioms of SHM [8]:

(i) All materials have inherent flaws or defects.

(ii) The assessment of damage requires a comparison between two system states.

(iii) Identifying the existence and location of damage can be done in an unsupervised learning mode, but identifying the type of damage present and the damage severity can generally only be done in a supervised learning mode.

(iv) Sensors cannot measure damage. Feature extraction through signal processing and statistical classification is necessary to convert sensor data into damage information. Thus, without intelligent feature extraction, the more sensitive a measurement is to damage, the more sensitive it is to operational changes and environmental conditions.

(v) The length and time-scales associated with damage initiation and evolution dictate the required properties of the SHM sensing system.

(vi) There is a trade-off between the sensitivity to damage of an algorithm and its noise rejection capability.

(vii) The size of damage that can be detected from changes in system dynamics is inversely proportional to the frequency range of excitation.

These axioms introduce the interest of algorithms and the establishment of indicators or thresholds in the integration process of a SHM system. They provide a set of observations that are sufficiently objective to be generalized to any SHM system. Besides these axioms, Rytter proposed a classification of the different objectives an SHM system may have [3] as mentionned in the introduction. In this thesis, we will only focus on the damage size quantification level.

3.2 Damage in aerospace composite material

3.2.1 Laminate composite materials

The term composite material designates in a general way an assembly of at least two components whose properties complement each other to form a new heterogeneous material which has properties that the constituents alone do not have. In this thesis we are particularly interested in polymer matrix and carbon fiber reinforced composites, also called CFRP for Carbon Fiber Reinforced Polymer.

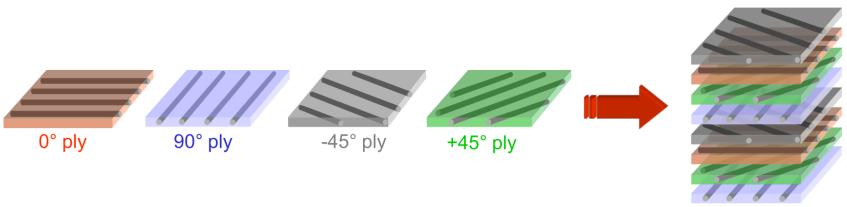

Fig. 3.1 Illustration of draping process. Adapted from [9].

These materials are frequently used in the industry in laminated form, that is to say that layers (called plies) of a fabric composed of carbon fibers pre-impregnated with resin

are stacked. This step is called draping Fig. 3.1. The material is then impregnated with resin before being cured in an autoclave. By playing on the orientation of the unidirectional folds, we can give the desired mechanical characteristics to the final material. For example, by balancing the stacking sequence, we can obtain a CFRP that has an identical stiffness in all directions of the plane: this is called a quasi-isotropic composite.

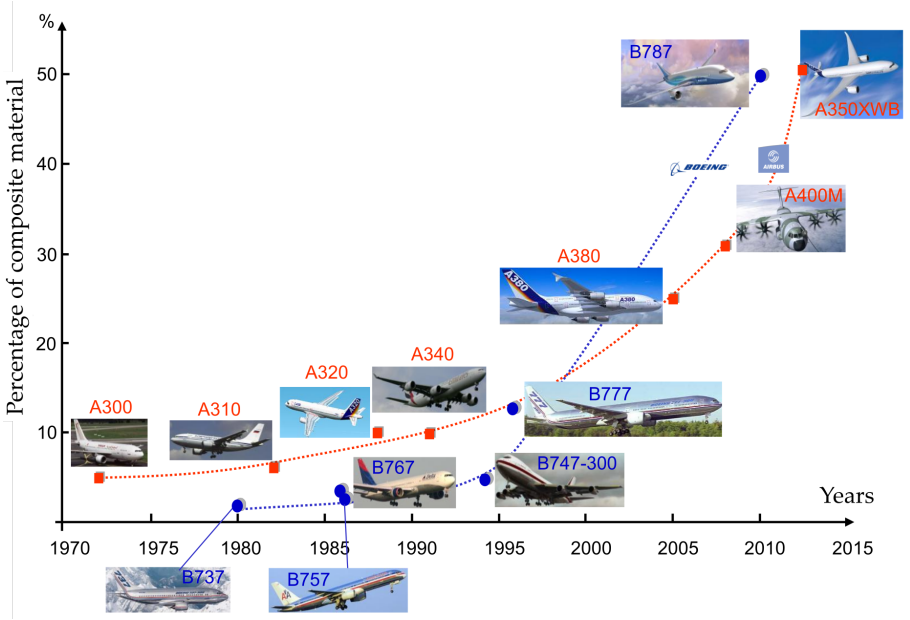

Fig. 3.2 Evolution of composite material percentage in commercial aircrafts composition. Adapted from [9].

These materials allow for flexibility in shaping and optimization, making it possible to create a product specifically adapted to the desired performance. They also provide good vibration damping and are less susceptible to corrosion than metallic materials. Finally, CFRPs offer very good mechanical properties in terms of stiffness and, above all, low weight, since a CFRP material is almost 40% lighter than an aluminum alloy for a given strength. For these reasons, their use in the civil and military aeronautics industry has become increasingly important over the decades, since it allows a reduction in fuel consumption. This share reaches up to more than 50% of the total weight of recent airliners like the A350 XWB of Airbus.

3.2.2 Damage in CFRP

Despite all their advantages, composite materials are not free of defects. Indeed, they are subject to many types of damage and unlike metallic materials, these damages are internal and therefore impossible to detect during a visual inspection before flight. In his book, Giurgiutiu describes in detail the damage mechanisms occurring during the life of a composite material [10]. We list here a non-exhaustive list of the most common damages.

- **Matrix cracking**: it is the most common damage that occurs in composite laminates. It is characterized by cracks that develop between two or more layers parallel to the ply fibers and extend through the ply thickness.
- **Fiber break**: it correspond to the local rupture of the fibers. This type of damage mainly affects the strength of the material and has little influence on its stiffness.
- **Fiber-matrix interface debonding**: it is characterized by a loss of adhesion of the matrix to the fiber. This usually occurs in areas of high interfacial stress concentration related to the presence of cracks. It can be triggered by thermal stress variations [11], cracking, structural aging, low velocity impact, or poor design.
- **Delamination**: it corresponds to the separation of two layers constituting the composite material. This type of damage results from the aggravation of one of the previously mentioned damages, or from an impact. The criticality of this damage makes it one of the main objects of the literature regarding damage inspection in composites [12, 10]. Delamination is one of the most important damages to consider because the strength of the composite material is strongly impacted by its development [13]. It is therefore necessary to detect the emergence of this type of damage before its size becomes critical.

The failure of the material is the result of the potential combination of all the elementary mechanisms of the unidirectional ply (fiber/matrix decohesion, intralaminar cracks, fiber breakage) and at the interface between the plies (delamination). These mechanisms can be initiated by the presence of intralaminar cracks present in the plies. These cracks can be generated by stress concentrations, stress field discontinuities between plies or can be initially present in the material (defects appearing during manufacturing or related to edge effects). Their propagation and coalescence is induced by mechanical stresses or thermal stresses.

3.3 Piezoelectric transducers

3.3.1 Origin of piezoelectricity

Piezoelectricy is derived from the ancient Greek *piezo* which means to squeeze or press. It describes the physical phenomenon that appears to a class of materials which generate an electrical field when subjected to a mechanical stress (also called direct piezoelectric effect). This phenomenon can also happen in the other way: when subjected to an external electrical field, the material will generate a mechanical stress (also called converse piezoelectric effect). This phenomenon was discovered by the brothers Pierre and Jacques Curie in 1880 [14].
The piezoelectric effect can be explained by looking at the crystal lattice of the material [15]. When the material undergoes a deformation, the barycenter of the positive and

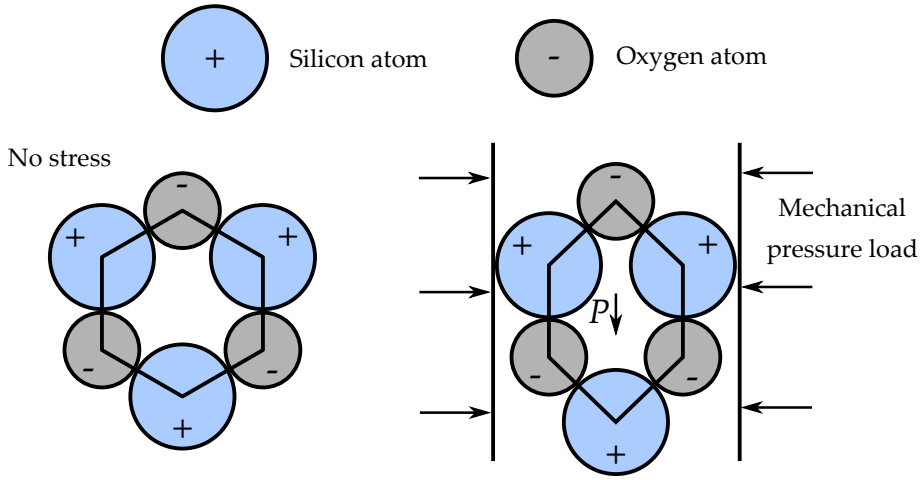

Fig. 3.3 Effect of mechanical compression load on a quartz unit cell.

negative charges that make up the mesh are slightly offset from each other. This creates an electrostatic dipole, hence the presence of an electric field. Fig. 3.3 illustrates this phenomenon for the case of a quartz. Piezoelectricity found many applications: speakers, microphone, energy harvesting, gas lighter, sensors, etc.

3.3.2 Constitutive laws

The constitutive laws of piezoelectricity are a set of two coupled equations. Here we consider only the case of linear piezoelectricity, that is to say that the deformations and the electric fields in play remain below a certain level. These equations can be written in several ways [16]. The formulation commonly use for stress analysis is [17]

$$\boldsymbol{\sigma} = \boldsymbol{C}^{E}\boldsymbol{\varepsilon} - \boldsymbol{e}^{\mathrm{T}}\boldsymbol{E} \tag{3.1}$$

$$\boldsymbol{D} = \boldsymbol{\chi}^{\sigma}\boldsymbol{E} + \boldsymbol{d}\boldsymbol{\sigma} \tag{3.2}$$

Given the symmetry of the different tensor involved in these equations, the Voigt notation is adopted. $\boldsymbol{\varepsilon}$ stands for the strain (6×1) matrix, $\boldsymbol{\sigma}$ stands for the stress (6×1) matrix, $\boldsymbol{C}$ is the (6×6) stiffness tensor. $\boldsymbol{D}$ stands for the electric displacement (3×1) vector, $\boldsymbol{E}$ is the electrical field (3×1) vector and $\boldsymbol{\varepsilon}$ stand for the dielectric permittivity (3×3) matrix. Electrical and mechanical quantities are coupled through $\boldsymbol{d}$ which is the (3×6) matrix of piezoelectric coefficients. They can be seen as the charge generated by unit stress and the strain generated by unit electrical field, respectively. $\boldsymbol{e}$ is the (3×6) matrix of piezoelectric stress coefficients and is related to $\boldsymbol{d}$ and $\boldsymbol{C}$ through the relation

$$\boldsymbol{e} = \boldsymbol{d}\boldsymbol{C}^{\mathrm{E}} \tag{3.3}$$

The superscripts σ, D and E mean that the quantities are measured at respectively zero stress $(\sigma = 0)$, zero electric displacement $(D = 0)$ or zero electrical field $(E = 0)$.

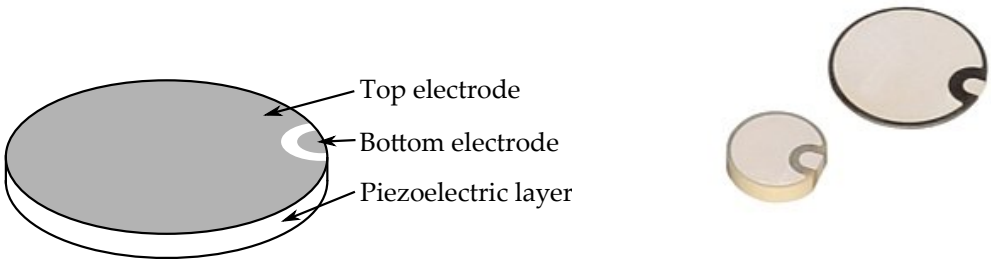

(a) (b)

Fig. 3.4 PZT transducer with wrapped electrodes diagram (b) and photo (a).

3.3.3 PZT patch

Piezoelectric material are used in a multitude of industrial fields. For guided waves based SHM, they are mainly used under the form of piezoelectric patches. These transducers can work both as actuator (generate stress when submitted to external electrical field) and sensor (generate voltage when squeezed). They are made of two planes electrodes facing each other and separated by a piezoelectric material. The most used is a ceramic called lead zirconate titanate (chemical formula $Pb[Zr_xTi_{1-x}]O$ with $0 \leq x \leq 1$) commonly known as PZT Fig. 3.4.

3.4 Lamb waves based SHM

3.4.1 Lamb waves propagation in isotropic material

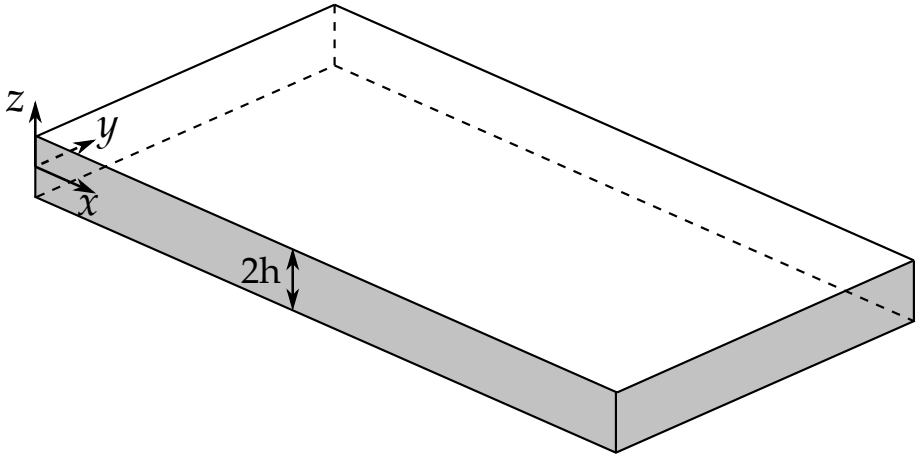

Fig. 3.5 Infinite isotropic plate considered for Lamb waves equations derivation.

In 1917, the mathematician Horace Lamb published a paper describing elastic waves propagation in plate medium which are now called Lamb waves in his honor. Whereas in infinite solid there are only two types of elastic waves (P waves and S waves), there is an infinity of modes of two types —called symmetric and anti-symmetric modes— in

thin walled structures. This comes from the multiples reflexions and interferences that occur due to top and bottom surface of the plate. Thus, Lamb waves modes existence and properties strongly depends on the frequency of interest and the thickness of the plate. In the following, we will derive the classical equations of Lamb waves theory in an isotropic infinite plate [6, 18] whose configuration is shown in Fig. 3.5.

Since we consider small strain, linear elastic, homogeneous and isotropic material we can write the Navier equation

$$(\lambda + \mu)\boldsymbol{\nabla}(\boldsymbol{\nabla}\cdot\boldsymbol{u}) + \mu\boldsymbol{\Delta}\boldsymbol{u} = \rho\ddot{\boldsymbol{u}} \tag{3.4}$$

where $\boldsymbol{u}$ denote the displacement vector, λ and μ are the Lamé's parameters, ρ is the material's density. $\ddot{\boldsymbol{u}}$ stands for the double time derivative of $\boldsymbol{u}$. By virtue of Helmholtz's theorem, $\boldsymbol{u}$ can be written as the sum of a curl-free vector field and a divergence-free vector field

$$\boldsymbol{u} = \boldsymbol{\nabla}\phi + \boldsymbol{\nabla}\times\boldsymbol{\Psi} \tag{3.5}$$

where $\phi \in \mathbb{R}$ and $\boldsymbol{\Psi} \in \mathbb{R}^3$. Eq. 3.4 can then be rearranged as two uncoupled equations

$$\boldsymbol{\Delta}\phi = \frac{1}{c_{\mathrm{P}}^2}\ddot{\phi}; \qquad \boldsymbol{\Delta}\boldsymbol{\Psi} = \frac{1}{c_{\mathrm{S}}^2}\ddot{\boldsymbol{\Psi}}. \tag{3.6}$$

c_{P} and c_{S} are respectively the pressure (longitudinal) and shear (transverse) wave speeds

$$c_{\mathrm{P}}^2 = \frac{\lambda + 2\mu}{\rho}; \qquad c_{\mathrm{S}}^2 = \frac{\mu}{\rho}. \tag{3.7}$$

Since the considered problem is y-invariant we can expand the Laplacian and Eq. 3.6 become

$$\frac{\partial^2\phi_x}{\partial x^2} + \frac{\partial^2\phi_z}{\partial z^2} = \frac{1}{c_{\mathrm{P}}^2}\ddot{\phi}; \qquad \boldsymbol{\Delta}\Psi_y = \frac{1}{c_{\mathrm{S}}^2}\ddot{\Psi}_y \tag{3.8}$$

where Ψ_y is the component of $\boldsymbol{\Psi}$ along y axis. In the following we consider a wave propagating toward positive x axis with a wavenumber k in harmonic regime at pulsation ω, meaning that ϕ and Ψ_y have the from

$$\phi(x,z,t) = f(z)e^{i(kx-\omega t)}; \qquad \Psi_y(x,z,t) = ig(z)e^{i(kx-\omega t)}. \tag{3.9}$$

By substitution and simplification by $e^{i(kx-\omega t)}$, we wave

$$f''(z) + \eta_{\mathrm{P}}^2 f(z) = 0 \tag{3.10}$$

$$g''(z) + \eta_{\mathrm{S}}^2 g(z) = 0 \tag{3.11}$$

where

$$\eta_{\mathrm{P}}^2 = \frac{\omega^2}{c_{\mathrm{P}}^2} - k^2; \qquad \eta_{\mathrm{S}}^2 = \frac{\omega^2}{c_{\mathrm{S}}^2} - k^2. \tag{3.12}$$

Solutions of Eq. 3.10 are

$$f(z) = A_1 \sin(\eta_P z) + A_2 \cos(\eta_P z) \tag{3.13}$$

$$g(z) = B_1 \sin(\eta_S z) + B_2 \cos(\eta_S z) \tag{3.14}$$

where A_1, A_2, B_1 and B_2 are constants and will be found from boundary conditions. In the present case, the last equations must be solved with respect to traction free boundary conditions on top and bottom surface of the plate

$$\sigma_{zz}\Big|_{z=\pm h} = 0; \qquad \sigma_{xz}\Big|_{z=\pm h} = 0. \tag{3.15}$$

The stress expressions in termes of potentials for motion invariant along y axis are

$$\sigma_{zz} = \lambda \frac{\partial^2 \phi}{\partial x^2} + (\lambda + 2\mu)\frac{\partial^2 \phi}{\partial z^2} - 2\mu \frac{\partial^2 \Psi_y}{\partial x \partial z} \tag{3.16}$$

$$\sigma_{xz} = \mu \left(2\frac{\partial^2 \phi}{\partial x \partial z} - \frac{\partial^2 \Psi_y}{\partial x^2} + \frac{\partial^2 \Psi_y}{\partial z^2} \right). \tag{3.17}$$

Substituting the potentials by their respective expression and after few manipulations, the boundary conditions can be written As

$$\sigma_{zz}(h) = 0 \iff (k^2 - \eta_S^2)(A_1 \sin(\eta_P h) + A_2 \cos(\eta_P h)) + 2k(B_1 \cos(\eta_S h) - B_2 \eta_S \sin(\eta_S h)) = 0 \tag{3.18}$$

$$\sigma_{zz}(-h) = 0 \iff (k^2 - \eta_S^2)(-A_1 \sin(\eta_P h) + A_2 \cos(\eta_P h)) + 2k(B_1 \cos(\eta_S h) + B_2 \eta_S \sin(\eta_S h)) = 0 \tag{3.19}$$

$$\sigma_{xz}(h) = 0 \iff 2k(A_1 \eta_P \cos(\eta_P h) - A_2 \eta_P \cos(\eta_P h)) + (k^2 - \eta_S^2)(B_1 \sin(\eta_S h) + B_2 \cos(\eta_S h)) = 0 \tag{3.20}$$

$$\sigma_{xz}(-h) = 0 \iff 2k(A_1 \eta_P \cos(\eta_P h) + A_2 \eta_P \cos(\eta_P h)) + (k^2 - \eta_S^2)(-B_1 \sin(\eta_S h) + B_2 \cos(\eta_S h)) = 0. \tag{3.21}$$

These last equations can be solved to find the constants A_1, A_2, B_1 and B_2 and therefore the expressions of f and g. Substitution in ϕ and Ψ_y respective expression, we can get the displacement and stress fields. The above system of equations can be reduced to a couple of 2-by-2 systems, one for symmetric motion and the other for antisymmetric motion. For symmetric motion we have

$$\begin{pmatrix} (k^2 - \eta_S^2)\cos(\eta_P h) & 2k\eta_S \cos(\eta_S h) \\ -2k\eta_P \sin(\eta_P h) & (k^2 - \eta_S^2)\sin(\eta_S h) \end{pmatrix} \begin{pmatrix} A_2 \\ B_1 \end{pmatrix} = \begin{pmatrix} 0 \\ 0 \end{pmatrix}. \tag{3.22}$$

Non trivial solutions of this homogeneous system exist only if the determinant of the matrix equals zero, that is to say

$$(k^2 - \eta_S^2)^2 \cos(\eta_P h)\sin(\eta_S h) + 4k^2 \eta_P \eta_S \sin(\eta_P h)\cos(\eta_S h) = 0 \tag{3.23}$$

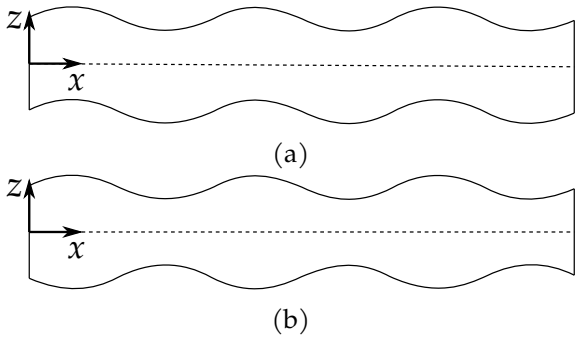

Fig. 3.6 Particle motion associated to antisymmetric (a) and symmetric (b) fundamentals Lamb waves modes.

which can be rearranged as

$$\frac{\tan(\eta_P h)}{\tan(\eta_S h)} = -\frac{(k^2 - \eta_S^2)^2}{4k^2\eta_S\eta_P}. \tag{3.24}$$

Eq. 3.24 is called the symmetric Rayleigh-Lamb equation. An analogous equation can be derived for antisymmetric motion

$$\frac{\tan(\eta_P h)}{\tan(\eta_S h)} = -\frac{4k^2\eta_S\eta_P}{(k^2 - \eta_S^2)^2}. \tag{3.25}$$

Since η_P and η_S depend on k, these transcendental equations do not have closed form solutions and must be solved numerically with the help of root-finding algorithms such as the bisection method.

Eq. 3.24 and Eq. 3.25 have an infinite number of complex solutions. If we only look at propagating wave —i.e. $k \in \mathbb{R}$—, the existence of Lamb waves modes essentially depends on the product of frequency and plate thickness. Below a certain cut-off frequency, there are only two modes called fundamental modes and denoted S_0 (fundamental symmetric mode) and A_0 (fundamental antisymmetric mode). Their respective particle motions are shown in Fig. 3.6.

3.4.2 Lamb wave propagation in laminate composite material

The knowledge of the propagation characteristics of Lamb waves in layered materials is of great importance to exploit these waves in SHM. However, the anisotropy of the plies causes a dependence of the wave speed on the propagation direction [19]. Moreover, the heterogeneous nature of the composite causes reflection and refraction phenomena at the interfaces between the layers. All this makes the solution of the problem much more difficult than the isotropic case. Many authors have been interested in this subject and proposed solution methods based on a semi-analytical or finite element approach [12]. The best known are the transfer matrix method or the global matrix method [20, 21].

3.5 Damage size quantification problem

3.5.1 Problem statement

In this thesis we address the problem of damage size quantification in composite materials. To perform this task, we use a sparse network of piezoelectric transducer able to emit and receive Lamb waves. As we mentioned it earlier, since the detection of delamination in the early stages of its existence is crucial for structure safety, we will focus on this type of damage. In the following, we define the damage size as the area of the delamination or as the radius of the damage, depending on the context. Since we focus on early life of a damage, we are only interested in small size of damage i.e. below a characteristics' length of 20 mm. The quantification problem we want to solve here can be written as an inverse problem

$$y = f(x) + \epsilon \tag{3.26}$$

where y is the damage size, x is the input data i.e. the raw signals recorded, f is the inversion model and ϵ is the independent noise. The approximation of f can be determined with different approaches, such as machine learning, signal processing, etc.

3.5.2 Literature review of damage size quantification methods

Various techniques are used to monitor possible damage apparition in composite aeronautical structures. One of the most common is the emission and reception of ultrasonic Lamb waves [18, 22]. Such waves can propagate over long distances in large structures thanks to their small attenuation ratio. Moreover, Lamb waves are easy to generate at high frequencies (and thus short wavelengths) using piezoelectric patches, making them able to interact even with small damages [8, 23]. A common SHM system to generate and sense Lamb waves is a network of piezoelectric elements acting both as actuators and sensors bonded on the surface of the structure to be monitored [24, 25].

Robust SHM algorithms based on Lamb waves have already shown great results for damage detection and localization purposes in composite structures [18]. However, there is still a huge need for reliable algorithms for damage size quantification in such structures. This task is very challenging since the interaction between the incident wave and the delamination is inducing non-linearities, as noticed by Dafydd et al. [26]. The experimental study focuses on three impacts with different energy level and it is demonstrated that the damage size has a high influence on the maximum of the envelope received signal.

Damage size assessment methods using piezoelectric generated Lamb waves are quite limited in literature. However, one method consists of finding a relevant damage indicator that varies in a monotonic manner with the damage size [27]. Another approach that has been proposed in the literature consists in training an Artificial Neural Network (ANN) on simulated data. The size of a damage is then estimated using experimental data processed by this ANN [28–30]. Statistical methods have also been investigated such as Bayesian updating techniques for crack size estimation [31] and delamination assessments [32].

Multi-class classification for damage quantification with a support vector machine have been also been successfully validated on a beam [33].

All these methods are either tested on few damage sizes with non-realistic damage type. Moreover, authors tend to conduct qualitative study on damage indicator relationship with damage size, and very few tried to build prediction model. A major contribution of this thesis is to provide two damage size estimation algorithms: one based on data-driven approach and a second one using an analytical model to identify damage characteristics. Quantification methods from literature also struggle with the lack of realistic data to be applied. That is why the second contribution of this thesis is to build and disseminate an open dataset of SHM dataset coming from fatigue test carried out on composite structures.

Chapter 4

ReMAP project experimental campaigns

Summary

One of the major goals of the European project ReMAP in which this thesis takes place is to validate the SHM approaches on data close to reality obtained during fatigue tests on representative samples of components used in aeronautics industry. In this chapter, we first present the motivations, the objectives and the actions of the ReMAP project. Then, we describe the measuring equipment used in the test campaigns as well as different samples. We summarize the different experimental campaigns carried out within the scope of the project: their objectives, their course as well as their results. Finally, we outline the pre-processing procedure applied to the Lamb waves signals. We also present an analysis of the measurement noise and we propose a first data processing based on damage indexes.

Contents

4.1 ReMAP project

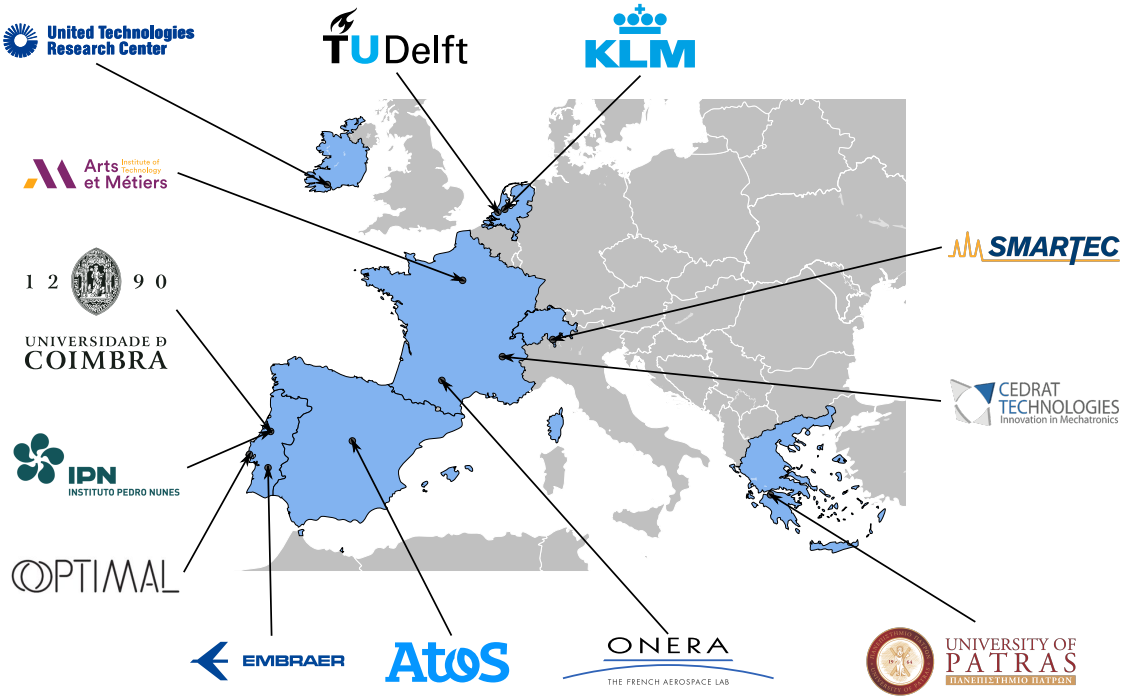

Fig. 4.1 Map of partners involved in ReMAP.

4.1.1 Motivation and objectives

Real-time Condition-based Maintenance for adaptive Aircraft Maintenance Planning (ReMAP) is a H2020 project funded by the European Union involving many universities, research centers and industry players as shown in Fig. 4.1. The goal of this four-year program is to develop an open source Integrated Fleet and Health Management solution for aircraft maintenance that will enable to reduce maintenance costs by shifting from fixed-interval inspections to condition based interventions (see Fig. 4.2). Modern aircraft already have hundreds of sensors at the subsystem level (cabin air conditioning and temperature control system, air cycle machine, variable frequency starter generator, wheels, brake shifting, etc.). There have been attempts to use this data to monitor these systems individually, but there is no work on incorporating diagnostic or prognostic results into an overall maintenance management system. The goal of ReMAP is to develop each element of the Condition Based Maintenance (CBM) chain, from a technological, methodological and regulatory point of view. This system must be able to rapidly acquire and process data from the device's sensors and establish a maintenance schedule in real time. The project aims to demonstrate and quantify the benefits of an SHM system: reduction of maintenance costs, potential gain in weight and reduction of technical failures. Finally, ReMAP plans to write a roadmap for the implementation and operation of the CBM approach in

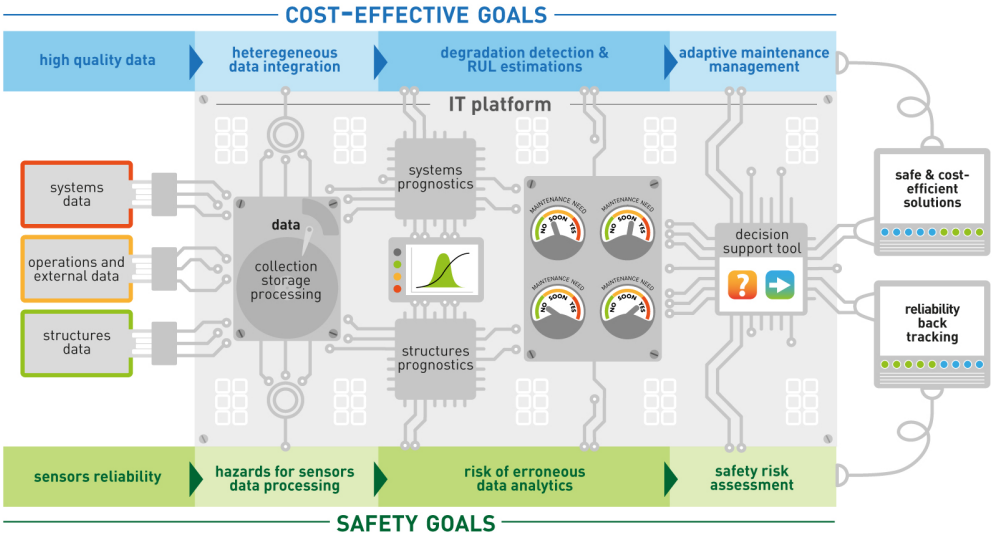

Fig. 4.2 ReMAP's cost-effective and safety goals (upper and lower bars) along with technology blocks.

Europe by proposing guidelines and standards for the certification and implementation of CBM.

4.1.2 Research focus

Structure level

Airliners are already equipped with hundreds of sensors. However, there is still no system deployed on an industrial scale to collect data regarding structural health of the aircraft. One of the objectives of ReMAP is to make the sensor technologies and SHM algorithms more mature by progressing from a Technology Readiness level (TRL)[1] of 3 at present to a TRL 5 by the end of the project. For this purpose, fatigue tests will be conducted in laboratory on samples representative of the primary structural elements of a modern aircraft. These elements are carbon fiber-epoxy composite panels with stiffeners. These samples will be instrumented with different SHM system technologies in order to collect data that will be post-processed using algorithms specially developed during the project. The goal of these algorithms is to assess the health of the structure in real time and to estimate its remaining useful life. These algorithms will be based on both experimental data and physical models. These samples will also be used to evaluate the potential mass gain of SHM systems by performing fatigue tests on lightweight samples. The raw data generated during these tests have been released[2] under public domain license and could be use by anyone for free [1].

[1] TRL are a type of measurement system developed by NASA and used to assess the maturity level of a particular technology. More information here.

[2] Link

Data collection storage and processing used

The project also includes work on the collection, storage and processing of data from the sensors. For example, edge-computing techniques will be explored to process the data on board and reduce the flow of data to be transmitted to the main system on the ground. Indeed, the volume of data to be processed is very large: a single flight generates 1 GB of data. In addition, it is planned to address the issue of security of these data.

Systems prognostics

(a) (b)

Fig. 4.3 Aircraft that will be monitored during 6 months: Embraer 175 (a) and Boeing 787 (b) from KLM airline.

It is planned to develop hybrid algorithms based on the data and physical models in order to establish a prognostic system at the scale of a complete aircraft. The goal is to estimate the time remaining before the next maintenance. These approaches will be applied in an operational environment. Indeed, during a six-months trial data from sensors of different subsystems (air cycle machine, wheels, brakes, etc.) of commercial aircraft will be accumulated. One of the objectives of the project is to develop a fleet-wide approach. For this, data will be collected on two different aircraft types from KLM airline: a Boeing 787 and an Embraer 175 Fig. 4.3.

Decision support tool

The project plans to exploit the results of the prognostic algorithms at the scale of a complete aircraft to establish an adaptive maintenance strategy for the fleet using optimization methods. This part of the project will provide a better understanding of the critical elements and sources of uncertainty in such a CBM system that can compromise the reliability of such a solution. The decision tool will have to produce proposals at lower cost and integrate a safety risk approach.

4.2 Material and technology involved

This chapter focuses on the SHM aspect of the ReMAP project and in particular the Lamb waves data. In this section we will describe the different measurement techniques at stake during the different test campaigns along with the material used that is to say, the acquisition hardware and the testing coupons.

4.2.1 Measurement systems

Acoustic Emission

When a defect occurs or grows within the part or if the material structure changes under fatigue, an elastic wave is generated and propagates through the structure. Acoustic emission is a passive SHM method that allows to capture these high frequency transient signals continuously. The signals are recorded if they exceed a threshold set by the user. Features can be computed from these signals like cumulative energy, number of hits, rising time, etc.

During the ReMAP project, two different acoustic emission systems were used. The one at University of Delft uses VS900-M receivers from Vallen Systeme GmbH which have a frequency range of 100 to 900 kHz. These receivers are combined with an external preamplifier with a gain of 34dB to amplify the received signals, and a Vallen System AMSY-6 digital 8-channel acquisition system along with the Vallen AE-Suite software. The threshold is set at 60 dBµV or 50 dBµV depending on the coupon. The acquisition system of University of Patras is composed of MICRO 200HF sensors from Physical Acoustics, which operate over a frequency range of 500 to 4500 kHz. The threshold is set at 62 dB or 65 dB depending on the coupon.

Fiber Bragg Gratings

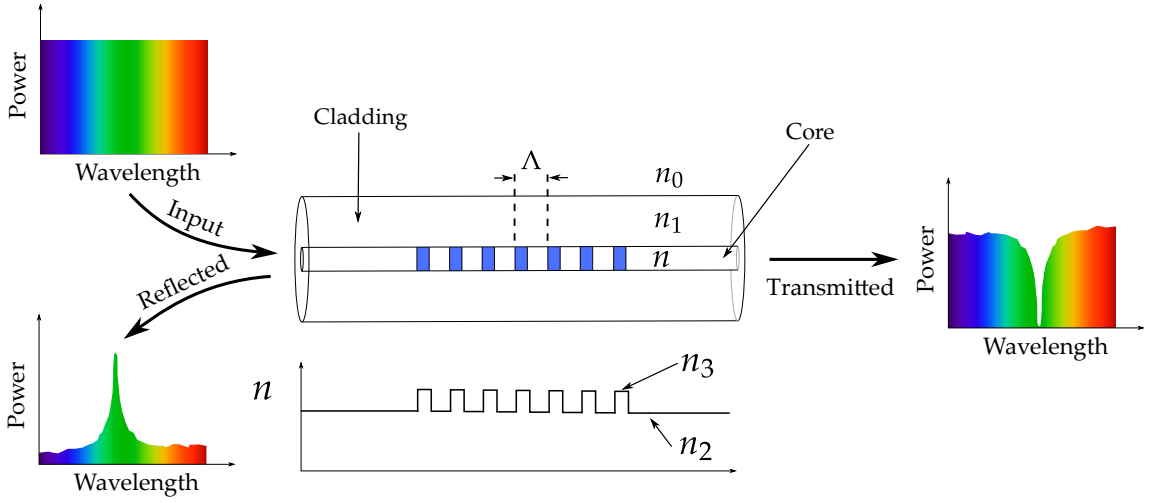

Fig. 4.4 Fiber Bragg Grating structure, with refractive index profile and spectral response.

Uniform Fiber Bragg Grating (FBG) are a particular type of axial strain sensor [34]. It is made of an optical fiber where the fiber core refractive index had been periodically changed on a short length. The new refractive index is selected to reflect a particular wavelength according to Bragg's law

$$\lambda_B = 2n\Lambda \tag{4.1}$$

where λ_B is the reflected wavelength (called Bragg wavelength), n is the effective refractive index of the grating (varying between n_2 and n_3) and Λ is the grating period. A broadband light source is placed at the fiber's extremity and the incoming light ray is partially reflected by the Bragg grating which acts as a band-stop filter with a cutoff wavelength λ_B. A fraction of light of wavelength λ_B is reflected back to the fiber's extremity where a light measurement system is set up to measure the wavelength of the reflected ray. When the fiber is deformed along the axis, the grating period Λ changes. According to Bragg's law Eq. 4.1 it means that the reflected wavelength is also modified. Then, by tracking the wavelength difference between the current state and the reference wavelength, it is possible to measure the local axial strain around the Bragg grating

$$\varepsilon = \frac{\mathrm{FBG} - \mathrm{FBG}_0}{\mathrm{FBG}_0} f_g \tag{4.2}$$

where FBG and FBG_0 correspond respectively to the wavelength in the current state and the reference wavelength at zero strain, whereas f_g is the gauge factor (1.2 pm/microstrain for the device used in the tests). In the current configuration several Bragg gratings are embedded into the same SMARTape sensor manufactured by Smartec, alongside optical fiber distributed sensing described in the following. The consecutive distance between two FBG sensors is 30 mm center to center and the sensor length is 10 mm. The position tolerance is of ±10 mm. The Bragg wavelength of the FBG used during the project is between 1520 and 1560 nm with 10 nm intervals. The FBG are connected to a two-channel sm130 dynamic interrogator from Micron Optics. The acquisition sampling frequency is 10 Hz and the gain level is set at 8 dB.

Distributed Strain Sensing

Distributed fiber-optic strain sensing (DFOS) is another family of optical fiber strain sensor [35]. The ones used in ReMAP are based on the Rayleigh backscattering technology. The setup is similar to the FBG one. A continuous laser source is placed at the extremity of the fiber and a fraction of the light will be scattered by the impurities in the fiber and reflected back to the source. The frequency spectrum of the reflected light in a deformed state is compared to the spectrum in the zero strain reference by calculating their cross-correlation. The maximum of the cross-correlation gives the frequency shift of the

reflected light which depends on the strain and the temperature [36]

$$\Delta\nu = C_T\Delta T + C_S\Delta\varepsilon \tag{4.3}$$

$$= C_S\Delta\varepsilon \qquad \text{at } \Delta T = 0 \tag{4.4}$$

where $\Delta\nu$, ΔT and $\Delta\varepsilon$ are respectively the shifts in frequency, temperature and strain. C_T and C_S stand for the Rayleigh temperature-frequency and strain-frequency coefficients, respectively. At constant temperature, the frequency shift is proportional to the strain variation.

The DFOS used in ReMAP are embedded alongside FBG into SMARTape sensors manufactured by Smartec. The DFOS are connected to a LUNA ODiSI-B Optial Distributed Sensor interrogator. The signals are processed with the manufacturer software. The acquisition rate is 23.8Hz.

Lamb waves

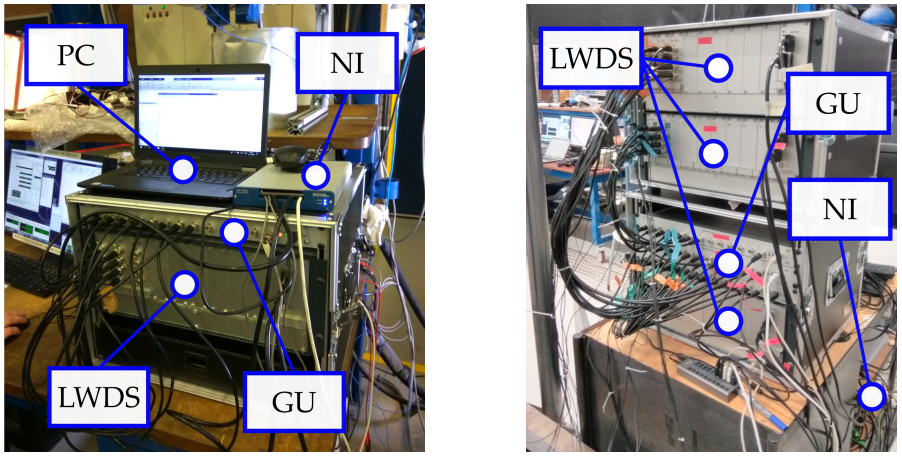

(a) (b)

Fig. 4.5 LW acquisition system used for L1 campaigns (a) and L2 campaign (b).

The samples are equipped with 20 cm diameter and 0.5 mm thickness NCE51 piezoelectric elements glued with an epoxy glue (Loctite EA9492) to capture and emit Lamb waves. The acquisition chain is composed of several devices. The Generation Unit (GU) generates the adequate input signal for Lamb waves excitation and send it to the Lamb Waves Detection System (LWDS). LWDS aims to amplify the input signal generated by the GU to adequately drive the piezoelectric elements and to trigger each channel in order to set them either in emitting or receiving mode. This device has been developed for the project by the company Cedrat Technologies [37]. A National Instrument USB-6366 acquisition board (NI) is used as an analog to digital converter with a sampling rate of 2 MHz and to interact with the other instruments through TTL signals. The acquisition process is performed automatically with an ad hoc MATLAB script.

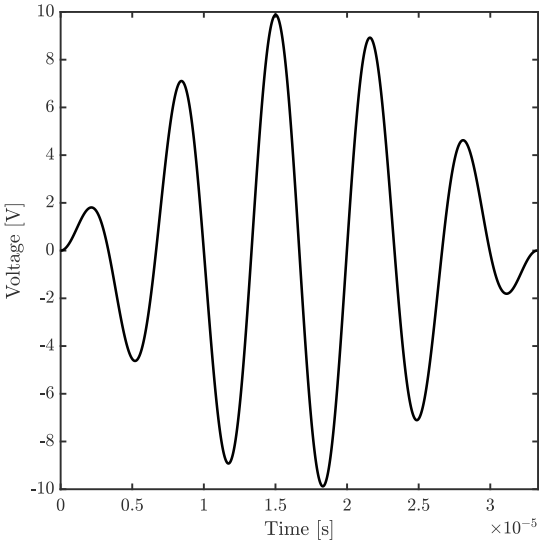

Fig. 4.6 5-cycles tone burst of central frequency 150 kHz.

Emission-reception tests are performed by emitting Lamb waves with a PZT and measuring the signals received by the rest of the piezoelectric elements. This process is repeated sequentially for each transducer in turn, leading to a total of $N_{\text{PZT}}(N_{\text{PZT}}-1)$ actuator-sensor paths where N_{PZT} is the total number of PZTs. The excitation signal is a N_c-cycles tone burst with a central frequency f_0, an amplitude A and defined as follows

$$x(t) = \begin{cases} A\sin(2\pi f_0 t)\sin\left(\frac{\pi f_0 t}{N_c}\right) & 0 < t < \frac{N_c}{f_0} \\ 0 & \text{otherwise.} \end{cases} \tag{4.5}$$

The LW acquisition has been used with 2 main configurations: one for the L1 campaigns and one for the L2 campaign. The overall diagram of the cabling can be found in App. B (see Fig. B.1 and Fig. B.2). The details of these test campaigns will be given in the following.

Digital Image Correlation

Besides SHM systems, the surface displacement field are calculated using a 2D optical method called Digital Image Correlation (DIC) [38]. This method relies on tracking a set of points on the surface of the specimen. The digital image correlation algorithm will determine the displacement of these points by finding the maximum correlation matrix between two images of the sample at different instants. The full displacement field over the whole structure is then inferred by interpolation. To improve the efficiency of the method, the samples are speckled randomly with a high contrast color (since ReMAP structures are black, a white paint had been used). The resulting displacement field can be post-processed with the software VIC-3D to obtain the strain field. With this technique, the full surface displacement field is captured unlike an extensometer —which capture only local displacement— or a strain gauge.

In ReMAP campaigns, the pictures are taken with a frequency of 0.5 Hz by using two 5 megapixels cameras manufactured by Point Grey equipped with 50 mm lens from Xenoplan.

4.2.2 Samples description

In this subsection, we will describe the different testing coupons that have been used during ReMAP test campaigns. All coupons have been manufactured by the company Optimal, partner of the project.

L0 coupon

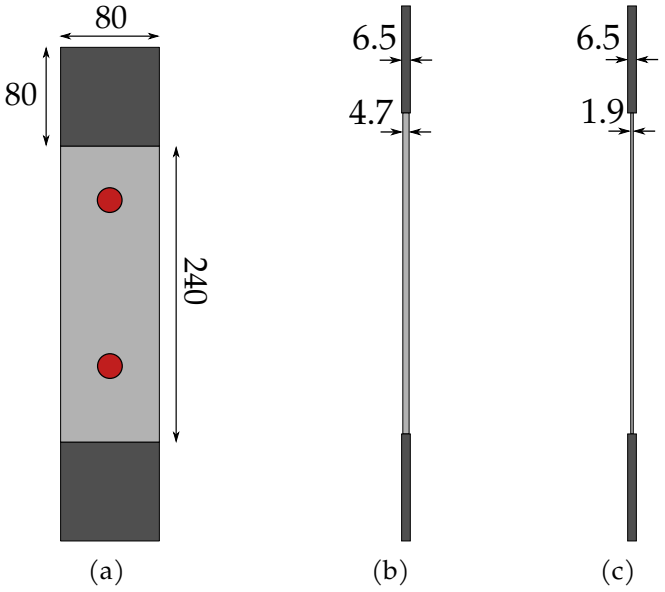

Fig. 4.7 Geometric properties of L0 coupons: front view with PZTs (a), EMB side view (b) and UPAT side view (c). All dimensions are in mm.

Table 4.1 Mechanical properties at 25°C of IM7/8552 unidirectional prepreg according to Hexcel [39].

Property	Unit	IM7/8552 UD
Density	$kg.m^{-3}$	1570
Tensile modulus (0°)	GPa	163
Tensile modulus (90°)	GPa	10
Tensile strength (0°)	MPa	2538
Tensile strength (90°)	MPa	92
Compression strength (0°)	MPa	1690
In-plane shear strength	MPa	106
Nominal Cured Ply Thickness	mm	0.131

The level 0 (L0) coupons are designed for qualifying PZT, FBG and DFOS sensors assembly on the substrate part. These sensorized coupons will be subjected to typical

Table 4.2 Geometric properties and mass of L0 coupons. The F superscript stands for the fabric layer.

Property	UPAT	EMB
Stacking sequence	$[45^F/0/45/90/-45/0]_s$	$[45^F/0/45/90/-45/0_2/45/90/-45/0_2/45/90/-45/0/45/-45]_s$
Total thickness [mm]	1.71	4.85
Mass [g]	180	300

Table 4.3 L0 population for each test.

Test	Type of sensors	UPAT specimens	EMB specimens	Total
Destructive test	-	1	0	1
Fatigue PZT	PZT	5	2	7
Ageing	PZT, FBG and DFOS	3	0	3

aeronautic environment (thermal and mechanical loads) to verify PZT and SMARTape sensing properties that should remain sensibly identical to the initial state. Thus, L0 specimens are shaped as rectangular tensile test specimens Fig. 4.7 and composed of three zones: a central part to glue sensors and two taps to hold the coupon in the tensile machine grips. The material selected is a IM7/8552 carbon fiber-reinforced epoxy unidirectional prepreg from Hexcell [39] with the properties specified in Tab. 4.1. The coupons are made of similar material than the specimens in the next test campaigns. L0 are made up with two different stacking cases: UPAT and EMB as described in Tab. 4.2.

L1 coupon

Table 4.4 Geometric properties of L1 coupons.

Property	Skin	Stiffener
Stacking sequence	$[45/-45/0/45/90/-45/0]_s$	$[45/-45/0/45/-45]_s$
Total thickness [mm]	1.83	2.62

The level 1 (L1) coupons are designed for compression-compression fatigue test purposes. The L1 panels consist of rectangular composite plate (called skin) with glued T-stiffener (called stiffener) made from the same material as L0 (IM7/8552 unidirectional prepreg). Skin and stiffener have different stacking sequences listed in Tab. 4.4. Resin tabs were added to the top and bottom of each coupon to better distribute the compression load during fatigue test. Dimensions of the specimens are shown Fig. 4.8. Each coupon weighs about 2.5 kg, tabs included. Some specimen contained an artificial disbond created during the manufacturing process by inserting a Teflon film between the stiffener foot and the skin. To monitor damage growth, several SHM systems were installed on each coupon as shown in Fig. 4.9: AE, FBG, DFOS and LW.

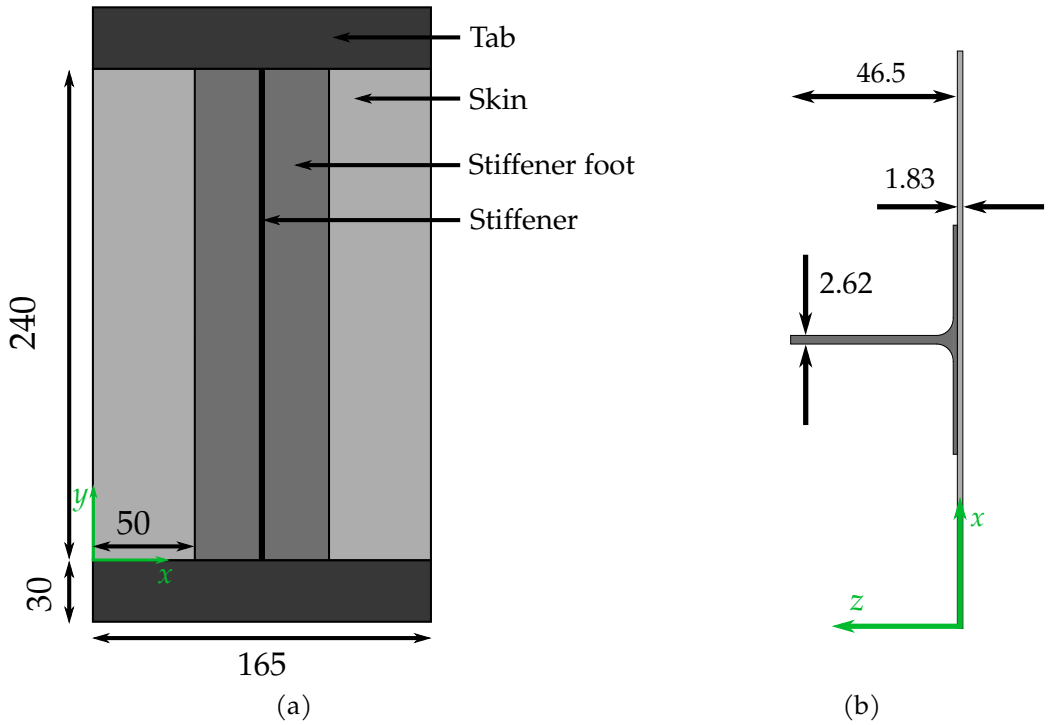

Fig. 4.8 Geometric properties of L1 coupons: front view (a) and cut view (b). All dimensions are in mm.

L2 coupon

L2 coupons are flat multi-stiffeners panels designed to be representative of subcomponents used in industry. These samples are made of the same material with the same stacking sequence as L1 coupons. Since they will be tested in compression-compression fatigue, resin tabs were added to the top and bottom of each coupon to better distribute the load. Dimensions of the specimens are shown Fig. 4.10. To monitor damage growth during fatigue, several SHM systems were installed on each coupon: AE, FBG, DFOS and LW. The locations of the PZTs can be found in Tab. A.2.

4.3 Validation of the test setup

In this section we describe the different test campaigns that took place as part of ReMAP.

4.3.1 L0 destructive test and strain measurements

Table 4.5 Macroscopic material properties obtained from experimental destructive test.

Coupon ID	Tensile modulus [GPa]	Tensile strength [GPa]
1	63.5	931
2	61.3	938

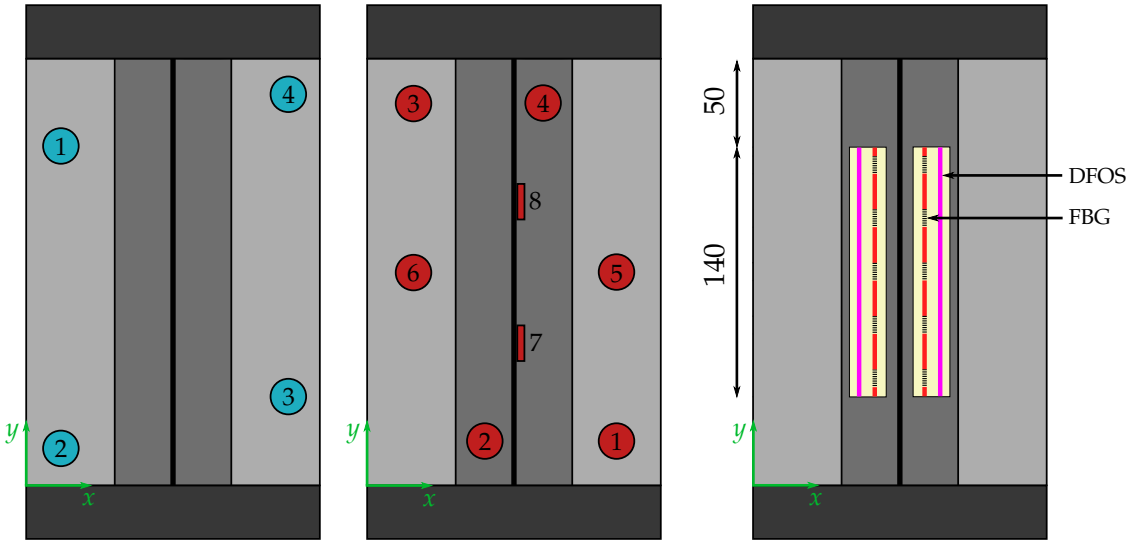

(a) (b) (c)

Fig. 4.9 Positions of SHM systems on L1 coupons: AEs (a), PZTs (b), FBGs and DFOSs (c). All dimensions are in mm.

To correctly perform the tests for piezoelectric elements and optical fibers, mechanical properties of the L0 coupons need to be assessed. That is why destructive tensile tests have be carried out to evaluate the elasticity modulus and the tensile strength of the samples.

A MTS tensile machine with a maximum load of 100 kN has been used to perform these experiments. It is equipped with sensors to track the moving crosshead displacement and stress. The strain is measured by a video correlation technique: four reference points are painted on the surface of the sample under testing and a camera records a video during the experiment. A Python script is then used to post-process the video to extract the position of reference points for each frame. The displacement between the points position is calculated at each time step to get the axial strain at the surface of the sample. The tested coupon is made of UPAT lay-up. Since L0 coupons are too large to be broken by the 100 kN tensile machine, the coupon used for tensile test is split in two parts to reduce the section and by so, the failure load Fig. 4.11.

For each part under test, the sample is placed at the center of the tensile machine's grips. The destructive test starts with a tensile speed of 1 mm/min. Finally, the stress versus strain graph is plotted to get the needed material properties Fig. 4.12. The mean material properties found are listed in Tab. 4.5.

4.3.2 L0 sensor reliability assessment

The objective of the sensor reliability assessment test is to demonstrate that piezoelectric elements can endure the L1 and L2 experimental test campaigns. We will check that the PZTs stay bonded to their host structure and are not damaged while experiencing thermal and mechanical solicitations representative of aeronautic operational conditions.

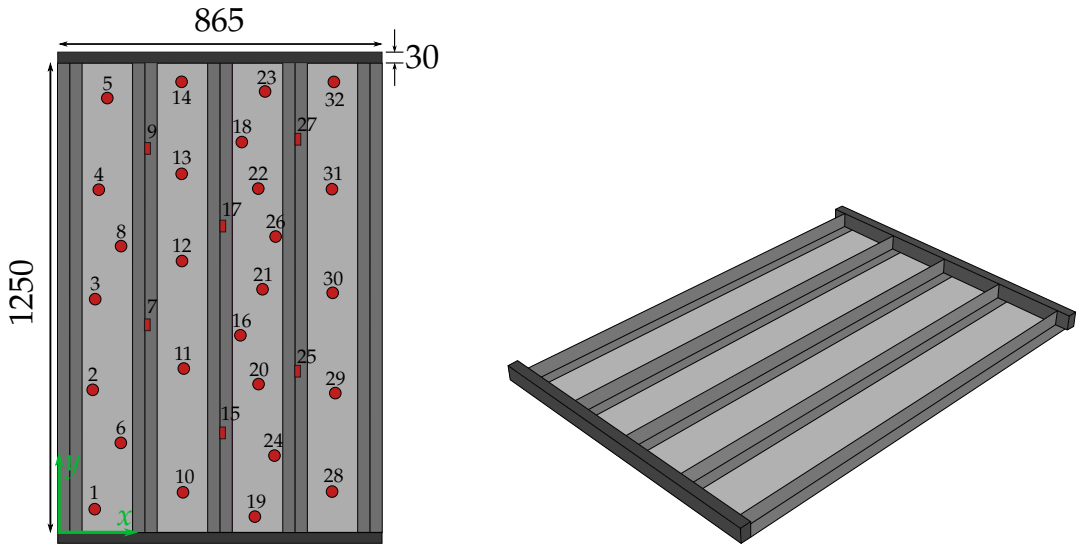

(a) (b)

Fig. 4.10 Geometric properties of L2 coupons: front view with sensors (a) and 3D view (b). All dimensions are in mm.

PZTs self-diagnostic procedure

The PZTs self-diagnostic procedure proposed here is based on piezoelectric elements static capacitance measurement, which can be estimated from its electromechanical impedance. The efficiency of this method has already been demonstrated experimentally and appears to be sensitive to both bonding issues and to partial or total PZTs element damaging [40]. Furthermore, this technique has already been used in an aeronautical context [41]. This explains why this approach has been retained for ReMAP and is briefly recalled here.

The electrical admittance of a piezoelectric element $Y(\omega)$ is defined as the inverse of its electrical impedance $Z(\omega)$, i.e. the ratio (in the frequency domain) between the current $I(\omega)$ and the voltage $V(\omega)$ across the considered element. When the PZTs undergoes free boundary conditions—that is to say when it is not bonded to any mechanical structure—its admittance is

$$Y_{\mathrm{f}}(\omega) = \frac{1}{Z(\omega)} = \frac{I(\omega)}{V(\omega)} = \frac{i\omega S \varepsilon_{33}}{t} = i\omega C_{\mathrm{f}}. \tag{4.6}$$

S and t are respectively the area and the thickness of the considered element, whereas ε_{33} stands for the dielectric constant of the PZT's constitutive material. The static capacitance of the free piezoelectric element is here denoted as C_{f}. If now a piezoelectric element bonded to a mechanical host structure is considered, in the low frequency range its admittance is [42]

$$Y_{\mathrm{b}}(\omega) = i\omega C_{\mathrm{f}} \left(1 - \kappa^2 \frac{Z_{\mathrm{s}}}{Z_{\mathrm{s}} + Z_{\mathrm{PZT}}}\right). \tag{4.7}$$

$Z_{\mathrm{s}}(\omega)$ and $Z_{\mathrm{PZT}}(\omega)$ are respectively the mechanical impedance of the host structure and of the piezoelectric element. κ stands for the electromechanical coupling coefficient between the piezoelectric element and its host structure and takes values between 0 and 1.

(a) (b)

Fig. 4.11 L0 coupons used for destructive test with width in mm (a) and experimental setup (b).

When the mechanical impedance of the host structure can be considered much greater than the one of the considered piezoelectric element—which is practically the case in the low frequency range—the previous equation can be rewritten

$$Y_b(\omega) = i\omega C_f(1 - \kappa^2) = i\omega C_b. \tag{4.8}$$

Here C_b stands for the static capacitance of the piezoelectric element once bonded to its host structure. The piezoelectric element self-diagnostic procedure used here is based on Eq. 4.6 and Eq. 4.8. From these equations, it appears that the admittance of a PZT bonded to a given host structure depends on the element geometric parameters S and t, as well as its electromechanical coupling coefficient κ. Thus, a healthy piezoelectric element correctly bonded to its host structure will have the static capacitance

$$C_b = \frac{S\varepsilon_{33}(1 - \kappa^2)}{t}. \tag{4.9}$$

In practice if the PZT itself is damaged, this will cause a reduction of its effective area S or of its dielectric coefficient ε_{33}. Therefore, the product $S\varepsilon_{33}$ will become $\alpha S\varepsilon_{33}$ with $0 < \alpha < 1$ and the damaged piezoelectric element will have the capacitance

$$C_b^E = \frac{\alpha S\varepsilon_{33}(1 - \kappa^2)}{t} = \alpha C_b < C_b. \tag{4.10}$$

Following this observation, any damage occurring on the piezoelectric element itself can be identified by monitoring its static capacitance and by checking if it is diminishing. Once the piezoelectric element is totally damaged, its static capacitance will be drastically reduced. On the other hand if a PZT is debonded from its host structure, its electrome-

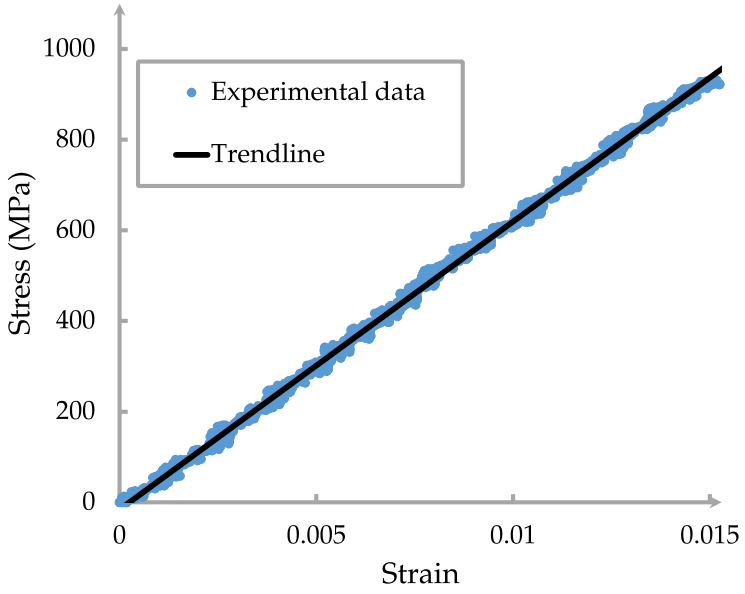

Fig. 4.12 Elastic part of stress-strain curve from destructive test of 42 mm width coupon.

chanical coupling coefficient κ will be reduced and become $\beta\kappa$ with $0 < \beta < 1$. The static capacitance of a piezoelectric element that is partially debonded is then

$$C_b^D = \frac{S\varepsilon_{33}(1-\beta^2\kappa^2)}{t} > C_b \tag{4.11}$$

As a consequence, any debonding occurring between the piezoelectric element and its host structure may be identified by monitoring again its static capacitance and especially if it increases. For a totally debonded piezoelectric element, its static capacitance will increase toward its static capacitance as a free element i.e. C_f in Eq. 4.6.

Given that damaging or debonding of the piezoelectric transducer will manifest as changes of its static capacitance value, any variation over a previously set threshold of the PZT static capacitance will be the consequence of damage or the PZT debonding. This threshold is chosen here as equal to 5%. Any deviation of a piezoelectric element static capacitance higher than this threshold will thus be interpreted as a sign of damage or piezoelectric element debonding. By denoting C_c the piezoelectric element static capacitance after its bonding and C its current static capacitance, we thus consider that a significant event (debonding or damage) has happened if the following condition is met

$$\frac{|\Delta C|}{C_c} = \frac{|C - C_c|}{C_c} > 5\%. \tag{4.12}$$

The impedance measurements will be performed with a LCR METER IM3533 manufactured by Hioki.

In addition to the piezoelectric element self-diagnostic procedure, emission-reception test will be carried out in order to validate the ability of a set of PZTs pair to be able to

send and receive signals consistently when enduring reliability test. Each of the two PZTs elements bonded on a given coupon will act sequentially as an actuator and a sensor. The signals measured during the first emission-reception test will be considered as reference signals and denoted as $R_n(t)$ where n stands for the actuator number. The signals collected during any upcoming emission-reception test will be denoted $T_n^i(t)$ where n stands again for the actuator number and i represents the emission-reception test number. On the basis of these signals, the cross-correlation coefficient $C_{i,n}$ for the emission-reception test number i and the PZT element number n will be computed as

$$C_{i,n} = 1 - |\max(R_n(t) * T_n^i(t))| \tag{4.13}$$

where $R_n(t) * T_n^i(t)$ stands for the cross-correlation between $R_n(t)$ and $T_n^i(t)$. We thus consider that a significant event (debonding or damage) has happened if $C_{i,n} > 5\%$.

Reliability assessment protocol and results

Table 4.6 Test protocol for piezoelectric elements reliability assessment.

Test ID	Nature of the test	Description
PZT_CTEC	Electromechanical on free PZT	Impedance measurement between 1 kHz and 200 kHz at 1V over 801 points repeated 4 times.
Healthy_CTEC	Electromechanical after bonding	
Healthy_ENSAM	Electromechanical	
ERT1	Emission-reception	Pitch-catch measurement with 10 successive repetitions of a 5-cycles tone burst with a central frequency of 150 kHz, an amplitude 10 V.
MT1	Electromechanical	Tensile fatigue test ran for 100 kcycles at 4 Hz frequency and at 0.07% strain level.
EMT_MT1_ENSAM	Electromechanical	
ERT_MT1_ENSAM	Electromechanical	
HWC	Hot and wet environment	10 cycles in climatic chamber going from room temperature to 70°C and 75% humidity during 30 min each.
EMT_HWC_ENSAM	Electromechanical	
ERT_HWC_ENSAM	Emission-reception	
MT2	Electromechanical	Tensile fatigue test ran for 100 kcycles at 4 Hz frequency and at 0.07% strain level.
EMT_MT2_ENSAM	Electromechanical	
ERT_MT2_ENSAM	Emission-reception	

Impedance measurements have been performed on free PZTs and after gluing on pristine coupons by CTEC, denoted respectively PZT_CTEC and Healthy_CTEC. Then additional impedance measurements have been performed at ENSAM before testing (denoted

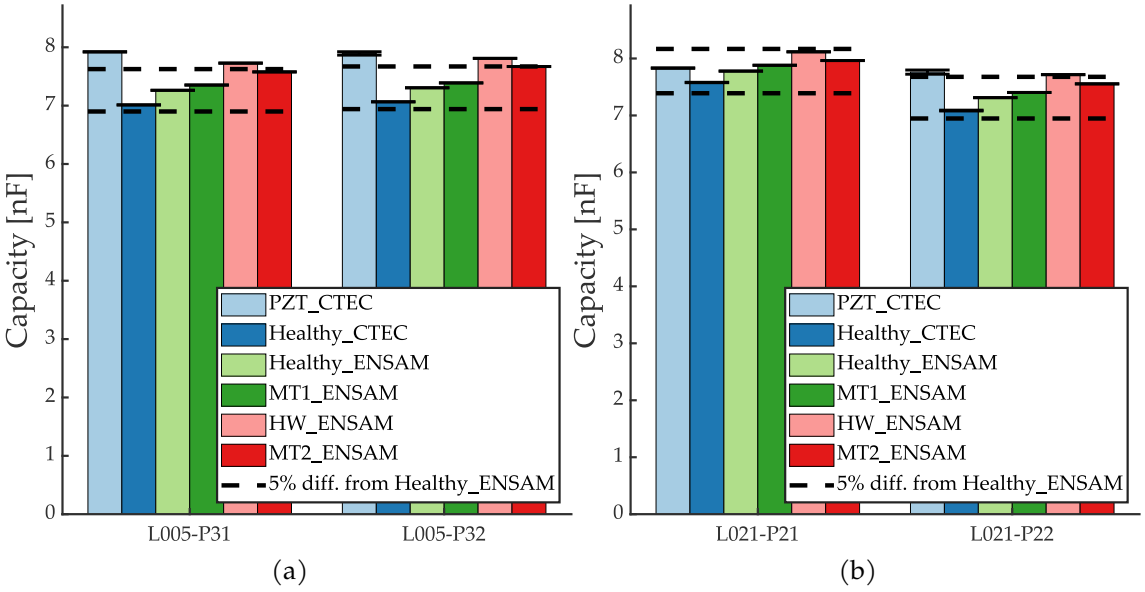

Fig. 4.13 Static capacitance of PZT P31 and P32 glued on L0 coupon number 05 made of EMB material (a) and static capacitance of PZT P21 and P22 glued on L0 coupon number 21 made of UPAT material (b).

as Healthy_ENSAM) and after each test (MT1_ENSAM, HW_ENSAM, MT2_ENSAM). Tab. 4.6 gives all the details about the experimental protocol. It should be noticed that temperature has an influence on static capacitance. Therefore, a temperature compensation approach has been used based on Lizé et al. work [43].

The first thing to notice is that the bonded PZTs static capacitance is lower than that of a free PZT as it can be seen in Fig. 4.13. This is an expected theoretical result from Eq. 4.11. Another point to consider is the difference of the static capacitance between the test Healthy_CTEC and Healthy_ENSAM. Since the coupon is the same between these two measurements and only travelled from CTEC to ENSAM, the results should be equal. This difference is probably due to the different experimental setup between the two sets or the difference of temperature. Indeed, the wires used in the experiments have their own admittance that can influence the result. Since the ENSAM experimental setup remained the same during the entire test campaign, the reference case used for the rest of the study will be Healthy_ENSAM.

Furthermore, we observe that the static capacitance increases only slightly after MT1 tests —about 1% on average according to Fig. 4.14a. This rise may be due to a very small debonding of the PZTs from the surface of the coupon. This is encouraging since it shows that the selected glue along with the gluing process is strong enough to withstand the fatigue test of L1 coupons. Unfortunately, the measures after the hot and wet test (HW_ENSAM) show a much larger increase that is above the 5% limit imposed. This may indicate that the glue and the gluing process are not appropriate for real flight conditions i.e. when facing realistic high temperature and humidity conditions. A possible alternative can come from structural bonding used on analogous hosting aircraft com-

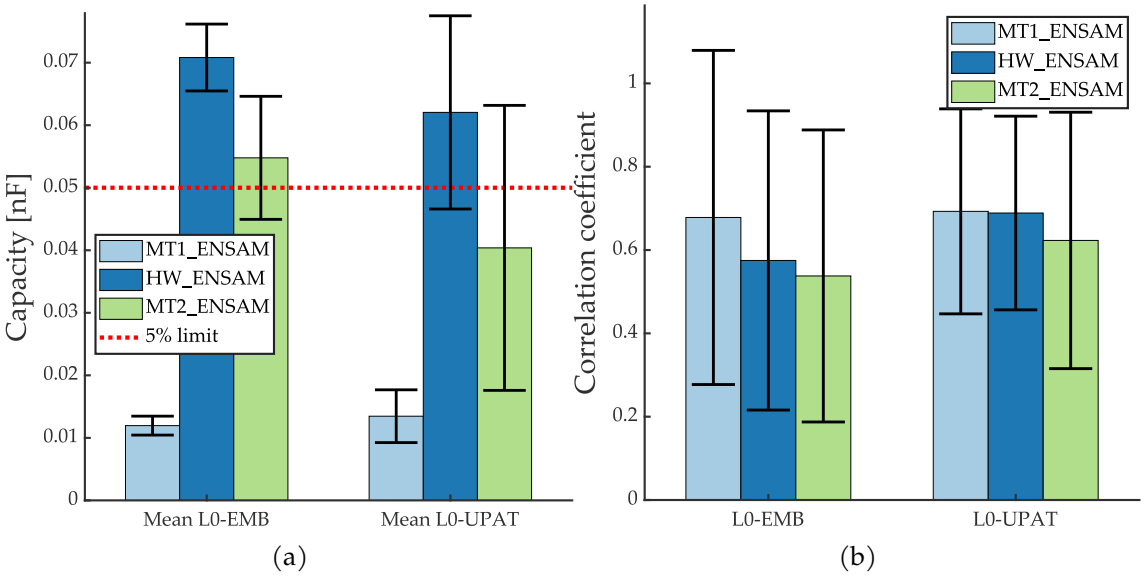

Fig. 4.14 Variation of static capacitance from the healthy state Healthy_ENSAM (a). Mean L0-EMB (respectively Mean L0-UPAT) is the mean variation for all PZTs glued on EMB coupons (respectively UPAT coupons). Correlation coefficients after the emission-reception tests (b).

ponents. Finally, after the MT2 test, a small static capacitance decrease can be observed. Although the magnitude of this latter transition appears near the variability of observations. This trend is observed for both specimen materials and might suggest that the hot and wet test have an influence that can evolve over longer time scales. This track, as well as alternative gluing solutions, might provide subjects of future investigations, beyond REMAP framework.

Besides, emission-reception tests were performed after PZTs gluing on pristine coupons by CTEC (respectively Healthy_CTEC). Then ENSAM performed the same test before testing (Healthy_ENSAM) and after each test (MT1_ENSAM, HW_ENSAM, MT2_ENSAM). To compare the results with the same devices, only the data coming from ENSAM tests are used here. To compute the correlation coefficient, for each PZT, each state (actuator or sensor) and each repetition, the studied signal is compared to each repetition of the same configuration in the Healthy_ENSAM pristine case. Fig. 4.14b shows the mean coefficient of every PZTs for each material with error bars corresponding to the standard deviation.

Regarding correlation coefficients, results on EMB coupons shows a slight decrease between MT1 and HW, but without any statistical significance. It decreases again with the same order of magnitude between HW and MT2, again without being statistically significant due to high variability. However, it is some kind of expected result since the bonding of the PZTs become weaker as the tests progress as seen from the static capacitance results. On the other hand, for UPAT coupons the mean coefficient does not vary throughout the test campaign. This is unexpected since the variation of capacitance indicates that the PZTs bonding is weaker after the MT2 test than in the healthy state. Since the variability observed in correlation coefficients is very high in comparison with the

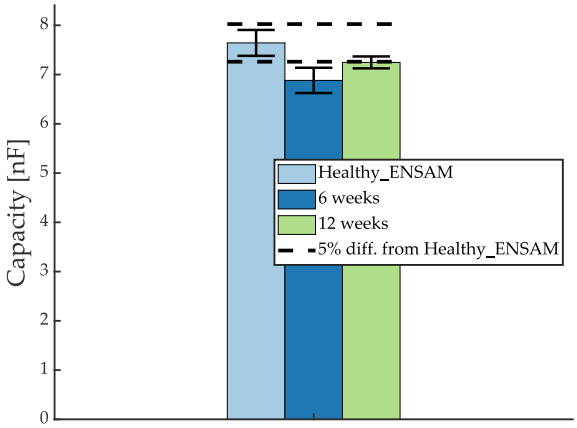

Fig. 4.15 Static capacitance of PZTs glued L0 coupon after 6 and 12 weeks of ageing in climatic chamber compared to healthy state.

one observed in static capacitance, it seems difficult to use the coefficient of correlation as a reliable indicator of PZT health. Thus, although the emission-reception test allows for validating the presence of readable transmission throughout the testing sequence, different indicators might be sought for possible combinations for higher sensitivity to PZT bonding and repeatability. Other studies might aim at determining optimally relevant indicator variation threshold values.

4.3.3 L0 sensor ageing assessment

The ageing test consists in placing L0 coupons in a climatic chamber in hot and wet conditions (35°C and 95% of humidity). After 6 and 12 weeks of testing a coupon is removed to perform PZTs self-diagnostic procedure and compare it to pristine state. The results are shown in Fig. 4.15. The healthy state is taken as the mean of static capacitance of PZTs bonded on UPAT material in Healthy_ENSAM state. It can be noticed that the static capacitance between the healthy state and after the ageing test differs. It means that the PZT bonding becomes weaker after this experiment. However, the amplitude of the static capacitance decrease does not seem related to the ageing process duration. Indeed, the decrease is more important with the coupon that stayed (6 weeks) than the coupon that was tested for 12 weeks. Nevertheless, as results for only one coupon are available, general conclusions cannot be drawn here.

4.4 Test campaigns

4.4.1 L1 fatigue test

Fatigue test campaigns on L1 coupons aim at collecting data on the whole life of a structural subcomponent, from the different sensors installed. Five test campaigns took place in all, however three of them included piezoelectric sensors to measure the propagation of Lamb waves. In the following, we will focus only on these three campaigns. The tests

Table 4.7 Summary of L1 fatigue test campaigns.

Campaign number	Test location	Sensors	Loading	Population	Other data
1	TUD	FBG,DFOS,AE,LW	CA CA - blocks	4 1	DIC
2	UPAT	FBG,AE,LW	CA - blocks	5	NDT
3	UPAT	FBG,AE,LW	Spectrum loading	10	NDT

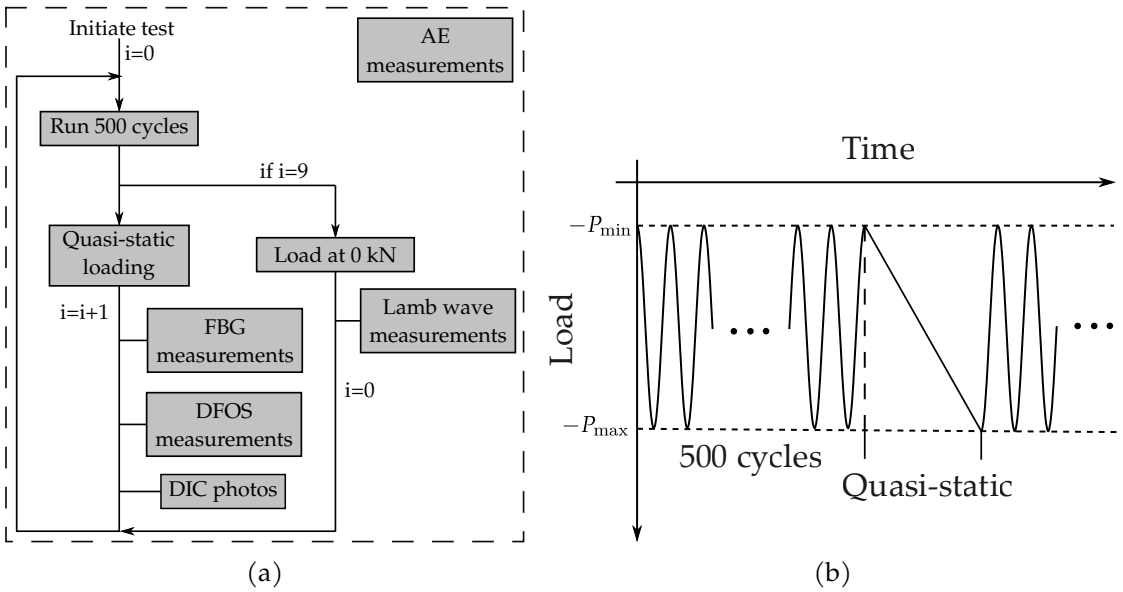

Fig. 4.16 First L1 test campaign protocol (a). Loading profile used for first L1 test campaign (b).

were carried out in the Delft Aerospace Structures and Materials Laboratory (DASML) in TUD and in Department of Mechanical Engineering and Aeronautics of University of Patras. Tab. 4.7 provides a list of the information related to these different campaigns.

For each of the test campaigns a different type of loading was used. For campaign 1 —except one coupon— a constant amplitude sinusoidal loading (CA) was used with a stress ratio of 10. During campaign 2 and for one sample from campaign 1, constant amplitude sinusoidal loading per block (CA block) was used, again with a stress ratio of 10. In this configuration the loading is at constant amplitude for a part of the test (one block) and then the amplitude is increased for the next block. For example, coupon L1-06 was loaded between -4 kN and -40 kN up to 10k cycles, then between -4.5 kN and -45 kN up to 80 k cycles and so on. Finally, for test campaign number 3, we used a spectrum loading following the TWIST algorithm [44] modified for a pure compression test. An example of spectrum loading sequence can be found in Tab. 4.8. For example, in this specific case 52 cycles were performed with an absolute minimum load of 4.7 kN and an absolute maximum load of 59.7 kN. Full details about each loading sequence and tested coupons are given in the ReMAP deliverable 4.5 [45]. For each of these loading, the frequency of the compression machine is set to 2 Hz.

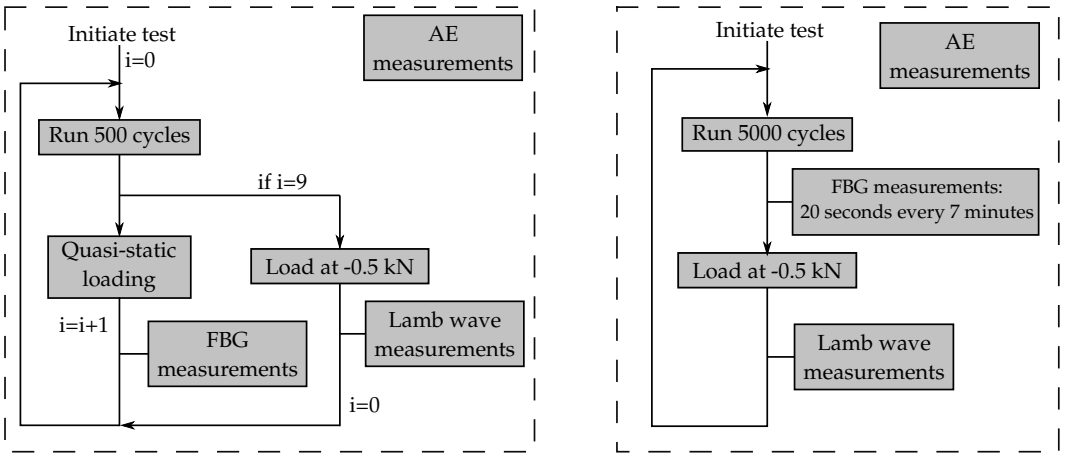

Fig. 4.17 Second L1 test campaign protocol (a) and third L1 test campaign protocol (b).

Table 4.8 Loading sequence used for spectrum loading in campaign 3.

Number of cycles	Absolute minimum load [kN]	Absolute maximum load [kN]
1	8	78
2	5	75
5	9	69
18	4.5	64.5
52	4.7	59.7
152	4.8	55.2
800	9.6	50.4
4170	14.1	45.9

In order to study the propagation of a defect during the fatigue test, damage is initiated in each specimen. Two types of defects are considered: either by means of an impact tower and a round tip steel impactor, or a piece of Teflon is inserted between two plies at the coupon manufacture.

Before the beginning of each campaign, LW measurements were done in pristine state right after PZT gluing by Cedrat Technologies. For each campaign a different protocol was adopted because of the differences in the equipment used. For campaign 1 the test is performed on an MTS machine with a maximum capacity of 500kN. The test is stopped every 500 cycles to perform a quasi-static loading from minimum to maximum load. During this loading measurements are made using FBG, DFOS and DIC. The test then continues for 500 cycles and so on until 5000 cycles are reached. The machine is then placed at zero loading and measurements are made using Lamb waves at multiple frequencies (50, 100, 125, 150, 200 and 250 kHz) with an amplitude of 10V and 10 repetitions for each measurement. These frequencies were selected to generate fundamentals Lamb waves modes only as shown in dispersion curves in Fig. 4.20. Dispersion curves relative to other quantities (wavelength, wavenumber and group celerity) can be found in App. G Once the measurements are completed, the fatigue test is resumed. In parallel, the AE sensors record

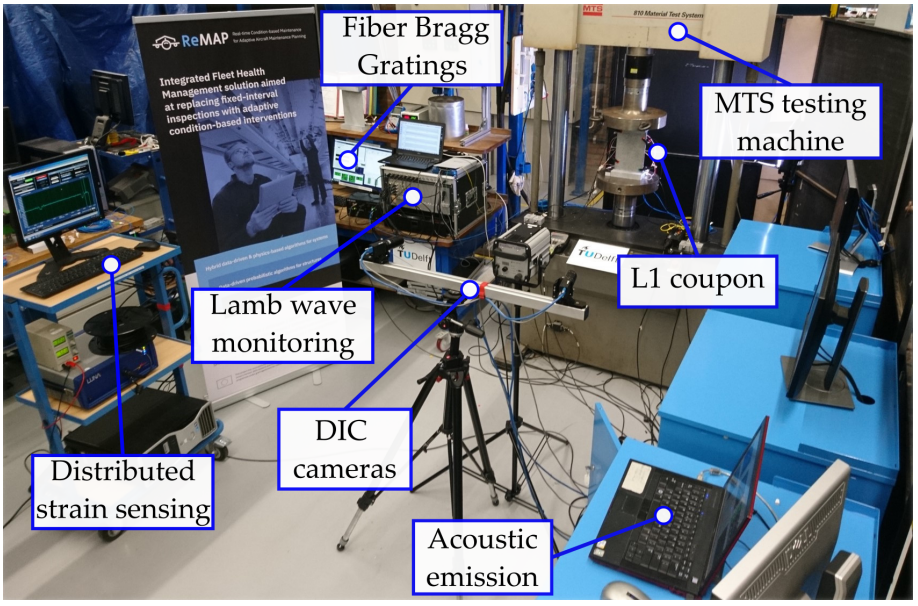

Fig. 4.18 Experimental setup of the L1 test campaign 1 at TUD.

continuously during the test. This process continues until the specimen is ruined. The protocol and the loading profile are shown in Fig. 4.16.

For campaign 2, the process is similar. It is carried out with an INSTRON 8802 machine, but there are no DFOS or DIC measurements. On the other hand, the test is interrupted from time to time to carry out NDT measurements using a Dolphicam. Moreover, during the LW measurements the machine exerts a constant load of -0.5 kN.

Campaign 3 is carried out on the same INSTRON 8802 machine as campaign 2. As for campaign 2, only the AE, FBG and LW systems are used. The FBG measurements are performed without interruption during the fatigue test. The test is interrupted every 5000 cycles to perform the LW measurements. The AE sensors record continuously during the test. The protocols for campaigns 2 and 3 are shown in Fig. 4.17.

During the test campaigns, some PZTs disbonded during the fatigue tests, or were weakened by the impacts used to initiate delamination. The signals from these damaged piezoelectric elements are therefore not usable. A procedure to identify the failed PZTs and discard them from post-processing results is described later in this chapter.

Despite the reliability test done beforehand, some PZTs failed during the fatigue test. We observe few debondings of PZTs placed on the stiffener during the campaign 1. However, campaigns 2 and 3 see more PZTs debondings and failures. This phenomenon could be explained by the fact that fatigue tests of campaigns 2 and 3 were run for a higher number of cycles. This would mechanically increase the probability to observe PZTs degradation. Besides, the loads considered during these campaigns were more important than the TUD fatigue tests. Finally, the impacts performed to initiate delamination may have weakened the adhesive bonding and the PZTs themselves, causing an anticipated ruin of the transducer.

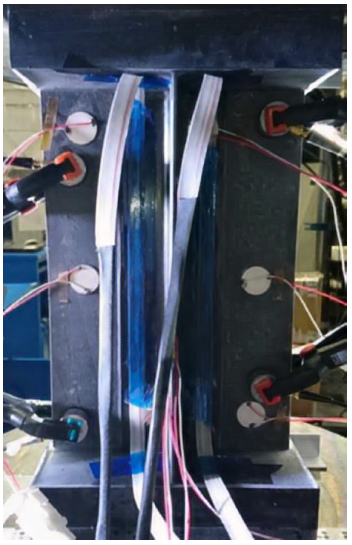

Fig. 4.19 Picture of L1 coupon.

For future work, it should be taken into account that impacts used to initiate damage may alter the PZTs bonded to the test structure. To avoid that issue, it would be worth investigating use of coating layers to protect the transducers of high stress levels. Another method could be to initiate fatigue damage with the help of laser shocks.

4.4.2 L1 laser shock test

With the goal of obtaining calibrated damage with ground truth measurements, a laser shocks testing was conducted. The objective is to produce delaminations of small size —of about a few millimeters in diameter— and similar to defects induced by the fatigue of an operating part. These tests took place on a single sample in the Processes and Engineering in Mechanics and Materials laboratory (PIMM) of ENSAM. This process —developed by the laser team of the laboratory [46]— is briefly detailed here.

The sample is placed in the test bench where the beam from a GAIA laser manufactured by Thales is split along two optical paths of equal distance so that the rays reach the impact zone on both sides of the structure at the same time as shown in Fig. 4.21a and 4.21c. The laser energy is focused on the target by the means of two convergent lens. An aluminum adhesive strip is placed on the impact point which will serve as a sacrificial layer. On top of this we add a layer of silicone adhesive which will confine the laser-induced explosion and increase the efficiency of the delamination process. When all this is in place, the laser delivers a pulse of 2.87 J on one face and 3.11 J on the other. On each side of the structure, the laser shock sublimates the sacrificial layer into a plasma that expands before relaxing. These expansion waves will propagate in the structure. At mid-thickness —i.e. at the intersection of the shock waves— the concentration of induced stress is high enough to disbond two plies and create a delamination. Nine shots were performed in total.

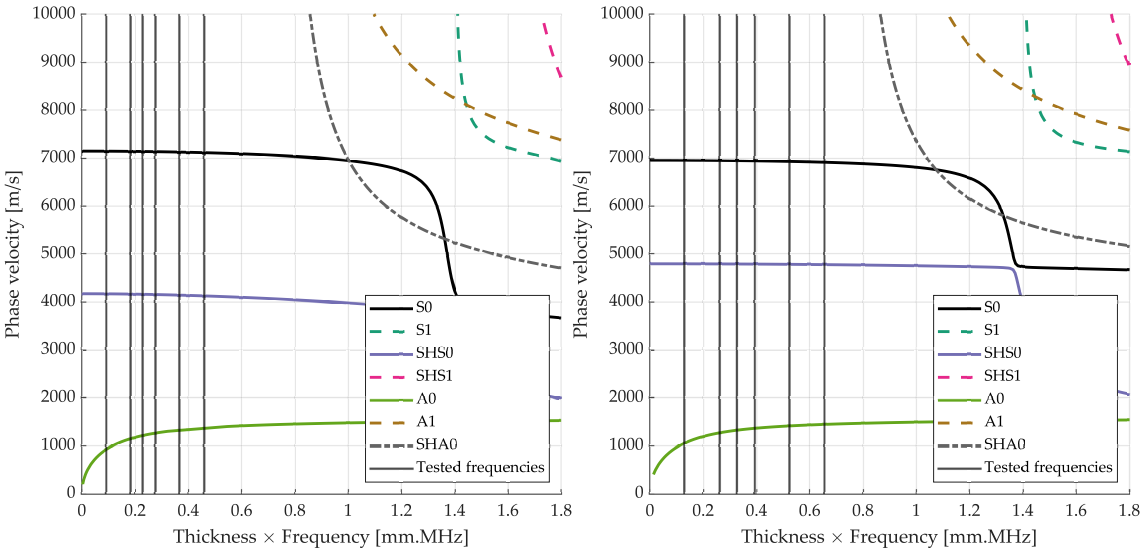

Fig. 4.20 Dispersion curve of phase celerity for two areas of L1 and L2 coupons: skin part (a) and stiffener part (b).

We proceed to a measurement of emission-reception of the reference Lamb waves in the healthy state, as well as after each laser shot. The excitation signal is a 5-cycle tone burst of 10 V amplitude whose center frequency is adjusted. The range of excitation frequencies lies between 50 kHz and 300 kHz with a step of 10 kHz with an additional frequency at 125 kHz, for a total of 27 frequencies. Each measurement is repeated 10 times.

After each shot, an ultrasonic A-scan measurement is performed with a Gekko unit manufactured by Eddyfi Technologies to check the presence of a delamination Fig. 4.22a. The linear probe is made of 64 elements with a frequency of 5 MHz and a cylindrical focus. Finally, an ultrasonic C-scan of the complete part was carried out after—the end of the experiment—in an immersion tank by the company Safran Fig. 4.22b with a frequency of 15 MHz. We can observe that the last two shots did not cause any delaminations.

4.4.3 L2 fatigue test

The purpose of the L2 test campaign is to test in fatigue multi-flat stiffener samples representative of full size aeronautical components. The campaign is similar to the campaign 1 of L1 coupons Tab. 4.7. The machine used is a MTS with a maximum load of 1000 kN. The samples are instrumented with AE, DFOS and LW sensors. In addition, the displacement of the backside of the tested specimen is measured by DIC, and the size of the defect present is measured by NDT using a Dolphicam while interrupting the test Fig. 4.23. A total of two panels are tested in quasi-static loading only and four panels are tested in fatigue including a specimen with a thin layup configuration. This thin layup is tested to illustrate the potential lightering allowed by SHM.

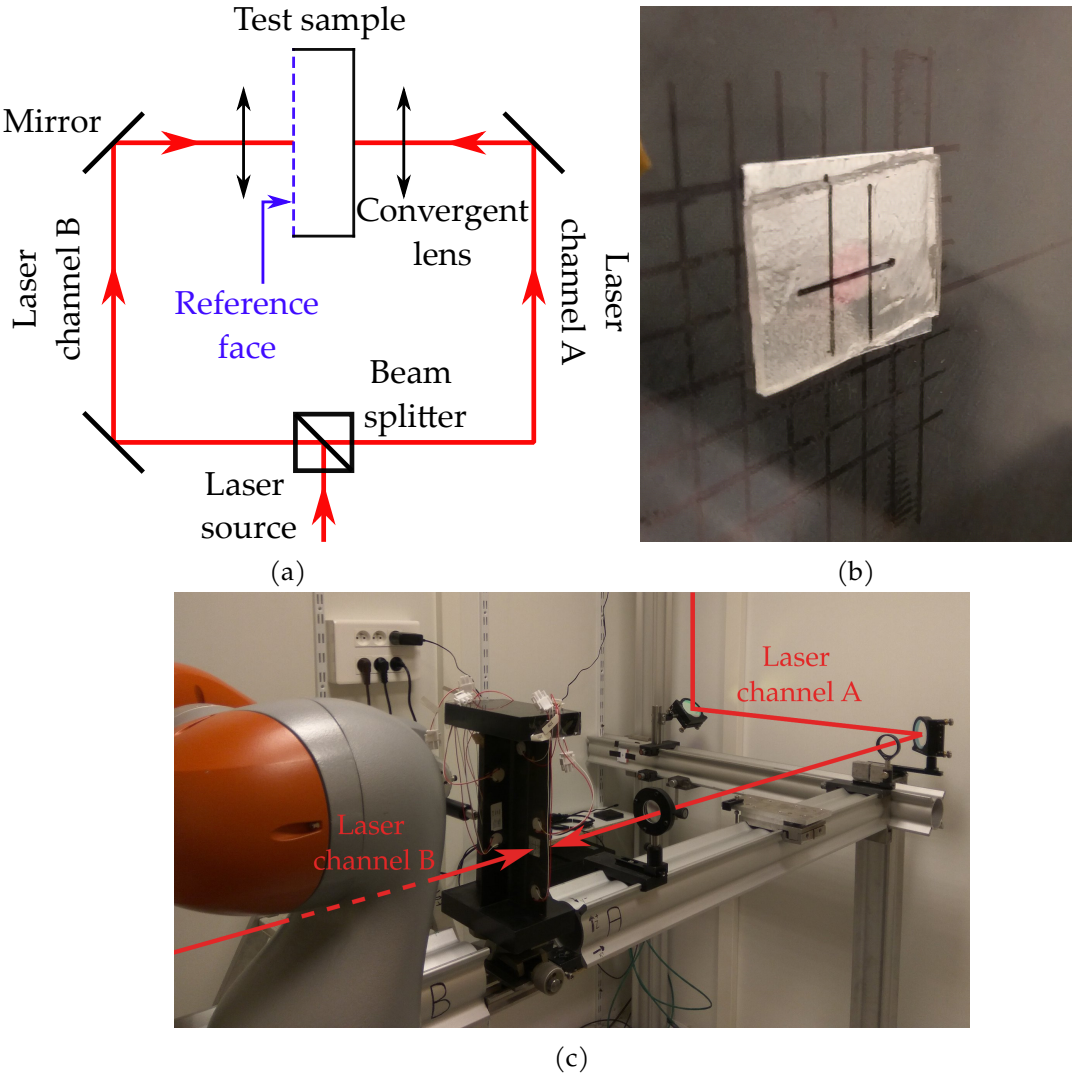

Fig. 4.21 Laser shocks experimental setup (a) and (c). Close-up view of the sample's tested zone (b). We can see the aluminum tape and the silicon layer.

The protocol used for fatigue is similar to the one of first L1 campaign performed at TUD Fig. 4.16a. The only difference is that for L2 coupons the quasi-static loading is done every 1 kcycles and LW measurements every 10 kcycles. Also, as for L1 campaigns, LW measurements were done in pristine state right after PZTs gluing by Cedrat Technologies.

To initiate the damage in the material two impacts of energy between 13 J and 15 J were carried out on two adjacent stiffeners in a zone close to the center of the coupons in order to observe a progression of the induced delamination.

As for L1 fatigue tests, we observed PZTs debonding and especially transducers failure. Indeed, since L2 coupons are much more robust than L1 it is necessary to perform several impacts to initiate a big enough delamination to see it growing during the fatigue test. These multiple impacts with a high energy led to disbonding and failure of many PZTs around the impacted area. To tackle this issue, new PZTs were glued at the same locations after the impact process.

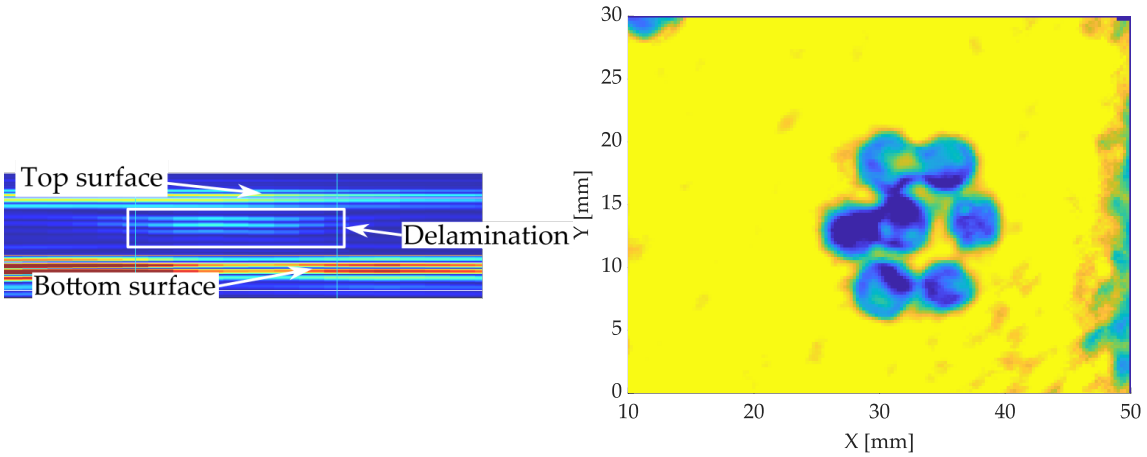

(a) (b)

Fig. 4.22 A-scan of the laser shocked area of the L1 coupon (a). C-scan of the laser shocked area of the L1 coupon (b).

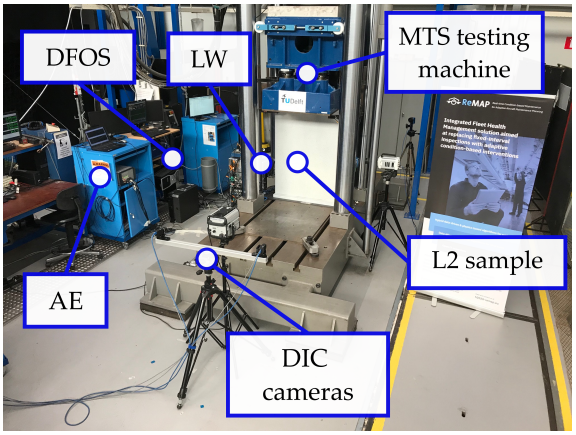

Fig. 4.23 Experimental setup of the L2 test campaign at TUD.

4.5 Data pre-processing and first analysis

4.5.1 Signal pre-processing

A pre-processing step is performed on raw signals to remove measurement noise and other experimental artifacts. This is a crucial step in order to improve the quality of results of the post-processing algorithms that will be used later. This denoising step is performed with a continuous wavelet transform. This method is selected because it gives good resolution in both time and frequency domain [47]. Moreover, it is well adapted to study non-stationary signals. This analysis consists in extracting the component of the signal the closest to the excitation frequency. The mother wavelet used here is the Morlet wavelet since it has a waveform close to the toneburst input signal. An example of a measured signal before and after denoising is shown Fig. 4.25. The pre-process effectively removed measurement noise and peaks caused by the switch between the emission and reception mode of the actuator channel of LWDS.

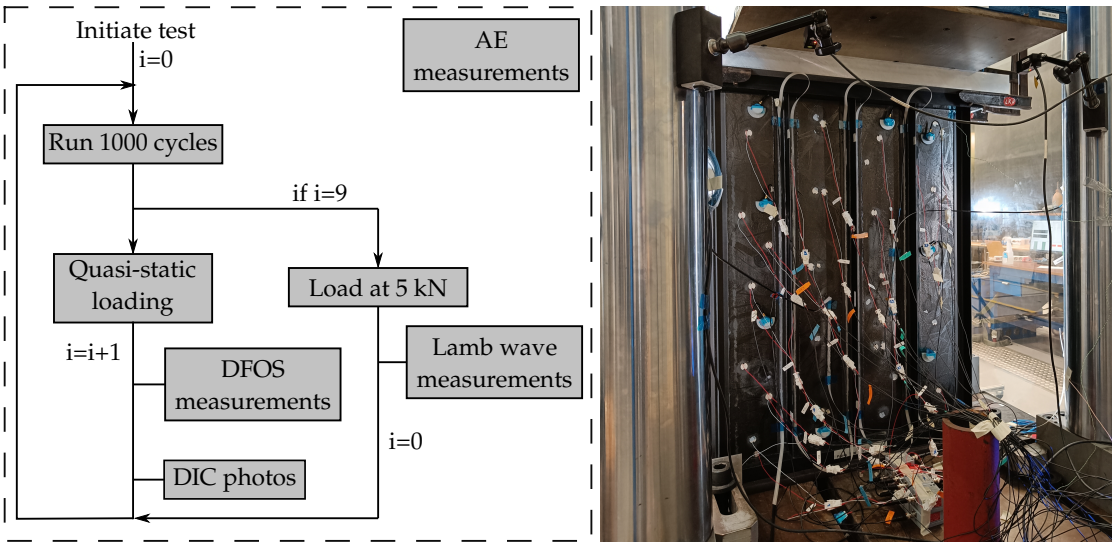

(a) (b)

Fig. 4.24 L2 fatigue test campaign protocol (a). L2 coupon being tested (b).

Table 4.9 Example of DI characteristics values for a good and a bad DI candidates. Computed from L1 coupons tested in campaign number 1.

DI name	Monoticity	Prognosability	Trendability	Global score
NRE6	0.7959	0.9949	0.7851	0.8586
NL_HARM2	0.4521	0.4624	0.0168	0.3104

4.5.2 Damage Index computation

For each tested coupon, a batch of 40 Damage Indexes (DIs) is computed for each actuator-sensor path, for each damage state at each excitation frequency. DIs are then summed over all paths of the structure to provide a global DI value. The list of all these DIs is provided in Appenddix (see Tab. C.1). The detailed mathematical definitions of these DIs can be found in reference [48].

As mentioned in the description of L1 and L2 fatigue campaigns, some coupons faced PZTs failure during the test. To identify the failure of PZTs, a procedure has been proposed in deliverable 4.5 of ReMAP [45]. It consists in computing the ratio of signal energy between the current damaged state and the reference state. This ratio is computed for each state and each actuator-sensor path. When a PZT suddenly fails, the energy ratios of all pairs where this PZT is involved drop abruptly. We used this procedure to identify which piezoelectric elements failed and at what time of the test. Once a PZT is considered as broken, it is discarded from DIs computation for later cycles. The DI is normalized by the number of active paths at each current state. Among all these DIs, some of them were retained for their possibility to be used as effective health indicators. To select the most relevant DI, a scoring process has been used based on features characteristics [49]. Monotonicity gives a measure M_i of the increasing or decreasing trend of the ith DI by

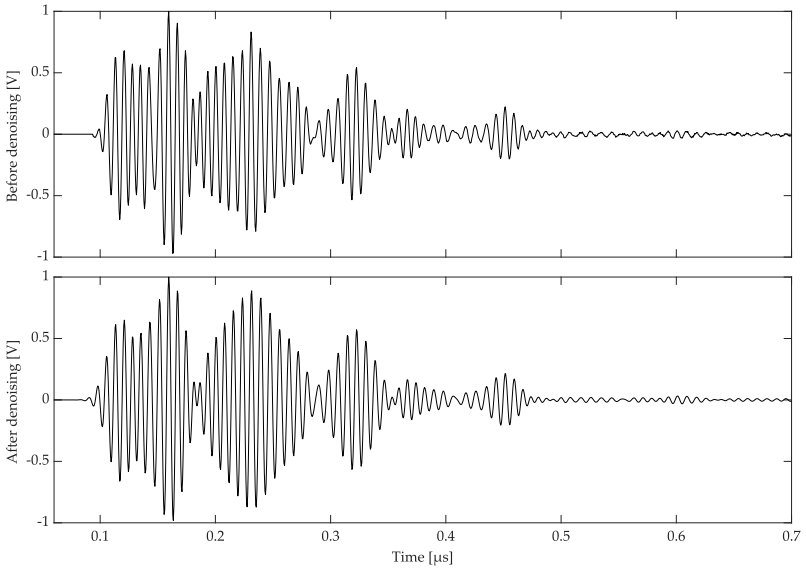

Fig. 4.25 Example of the signal received by a sensing PZT. The raw signal is at the top and the bottom one is the denoised signal. The excitation frequency is 125kHz. The signals are normalized between -1 and 1 for better clarity.

computing Spearman's rank-order correlation over all coupons

$$M_i = \frac{1}{N_S} \sum_{k=1}^{N_S} |\rho_S(x^i, t)| \tag{4.14}$$

where N_S is the number samples monitored and $\rho_S(x^i, t)$ is the Spearman's rank-order correlation between ith DI x^i and the number of cycles t, defined as

$$\rho_S(x^i, t) = 1 - \frac{6}{L(L^2-1)} \sum_{p=1}^{L} (x_p^i - t_p)^2. \tag{4.15}$$

L stands for the number of measurements whereas x_p^i and t_p are respectively the ith DI value and time value at time step p. An effective feature needs to vary in a monotonic manner with the damage condition of the structure. This would ensure that for a given value of the DI, there is an unique corresponding damage state.

Prognosability is calculated from the ratio of the deviation of the final values for each samples over the mean range of each sample. The prognosability P_i is computed as the exponential of the opposite of this ratio to get a number lying between 0 and 1.

$$P_i = \exp\left(-\frac{\text{std}(x^i(L))}{\text{mean}(|x^i(L) - x^i(1)|)}\right) \tag{4.16}$$

$$= \exp\left(-\frac{\sqrt{\frac{\sum_{k=1}^{N_S}(x_k^i(L)-\mu^i)^2}{N_S}}}{\sum_{k=1}^{N_S}\frac{|x_k^i(L)-x_k^i(1)|}{N_S}}\right) \tag{4.17}$$

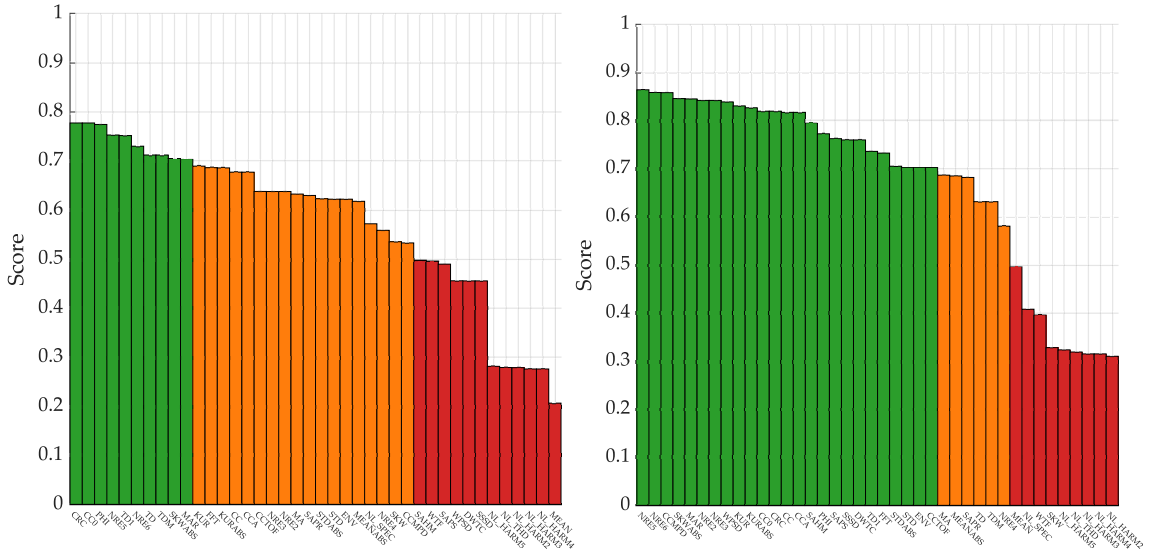

(a) (b)

Fig. 4.26 Score of all DIs for L1 campaign number 1 at an excitation frequency of 100 kHz (a) and 200 kHz (b). Bars in green correspond to score above 0.7, orange to a score above 0.5 and red to a score under 0.5.

where μ_i is the mean of final values of all coupons. DIs with high prognosability have well-clustered failure values and large range. This enables to model remaining useful life (RUL) of the structure for a wide range of cycles and then have enough data to estimate their self-parameters and predict an accurate value. On the contrary, features with poor prognosability will have a wide range of final value making the estimation of the RUL unreliable, and will have a small range to estimates RUL models parameters.

Trendability characterizes the degree to which the DIs have the same fundamental shape for all coupons and can be defined by the similar function form. This will simplify the progress of a specific degradation or prognostic model. It is computed as the absolute minimum Pearson correlation coefficient between all coupons.

$$T_i = \min_{j,k} \left(|\text{corr}(x_j^i, x_k^i)| \right) \qquad j,k \in [\![1; N_S]\!]. \tag{4.18}$$

Since the fatigue tests were not conducted during the same number of cycles, x_j and x_k can have different lengths. In that case, the shorter vector is resampled to match the length of the longer vector. To facilitate this process, their time vectors are first normalized to percent lifetime. Besides these three characteristics, high-performance DI must also show a low sensitivity to noise.

The global score S_i of each DI x_i is taken as the mean of M_i, P_i and T_i. It has to be noticed that these characteristics are computed from averaged DIs over each repetition to remove measurements noise influence. Also, since the experimental protocol (number of cycles, loading, etc.) were different between campaigns, the DIs are evaluated for each subset of coupons.

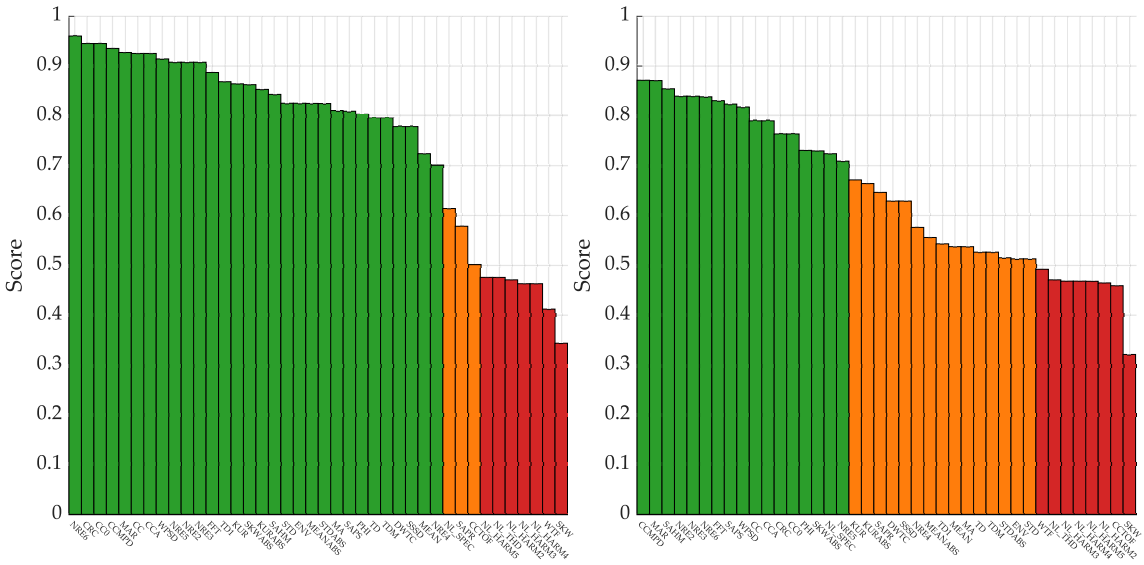

(a) (b)

Fig. 4.27 Score of all DI at an excitation frequency of 200 kHz for second L1 campaign for an excitation frequency of 100 kHz (a) and 200 kHz (b). Bars in green correspond to score above 0.7, orange to a score above 0.5 and red to a score under 0.5.

We plot the score of all DIs for the L1 campaign number 1 subset and for two different excitation frequencies Fig. 4.26. DIs with a mean global above 0.7 are in green, DIs with a mean global between 0.7 and 0.5 are in orange and DIs with a score under 0.5 are in red. It can be noticed that average scores at the lower frequency 100 kHz are lower than those for 200kHz. There are also many high DIs with good scores at high frequency. The same observation can be made for other available frequencies.

We also show the same graph for the others subsets of coupons from L1 campaigns number 2 and 3 at 200 kHz Figs. 4.27. It can be noticed that even if the ranking changes between the different frequencies and coupons subset, the order stays approximately the same. We can identify a group of high-performance DIs composed of features related to time delay, normalized residual energy and correlation.

Fig. 4.28 is an example of graphs for a DI (namely NRE6) that is a candidate to describe the current health state of the coupon, and another DI (namely NL_HARM2) that shows no clear evolution with damage state. Looking at DIs' evolution for all L1 coupons, it can be noticed that the trend is globally the same. It means that the selected DIs seems quite robust to the different fatigue scenario, to different environmental conditions and geometrical and material uncertainties such as the dimensions of the specimen and the exact position of the PZT. We also notice that NRE6 shows very little sensitivity to noise unlike NL_HARM2. The details of each characteristic are given in Tab. 4.9. We can remark that the prognosability of good features is very high: as stated previously, it means that RUL estimation with data-driven model like regression should work well.

For example, the residual energy based DIs (NRE_1, NRE_2 NRE_3, etc.) show good scores. We can assume that this is due to the damage growing during the fatigue test and

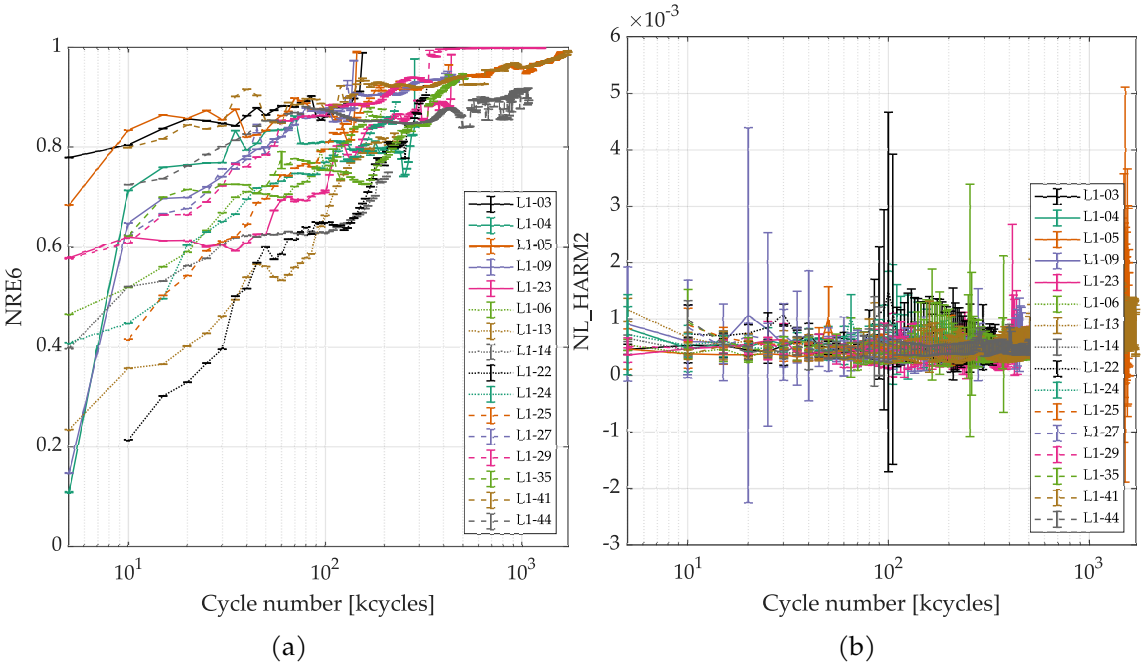

Fig. 4.28 Example of DI evolution for all tested coupons. NRE6 shows a monotonic trend with the number of cycles (a). NL_HARM2 seem not sensitive to structure health state (b). The signals considered here are measured with a 200 kHz excitation frequency.

thus more and more energy is reflected back to the receiving PZT. Similarly, correlation-based DIs (CC, CC0, etc.) also demonstrate positive results. One hypothesis is that as the damage increases in size, its edges change position. It is these changes that are detected by the correlation methods. On the contrary, if we look at the DIs based on the ratio between the fundamental frequency and the different harmonics (NL_HARM2, NL_HARM3, etc.), their performance for health monitoring is very poor. This can possibly be explained by the amplitude of the signals used. Indeed, to observe non-linear effects, one must use high amplitude excitation signals.

However, these results must be nuanced. These DIs do not allow to directly identify the causes of their evolution. Indeed, during a fatigue test, a composite structure sees several mechanisms occurring at the same time and at different scales due to the multi-interface nature of the material. When a composite structure is tested in compression-compression fatigue, it has been shown that the presence of voids stimulates fiber-matrix interface failure and delamination, leading to earlier unstable fiber fracture and shorter fatigue life [50]. These internal and global structural degradations alter the way Lamb waves propagate and may even introduce mode conversion [51]. All of these changes can have an impact on the calculated DIs. Moreover, it appeared that a mode conversion phenomenon (S0 to A0) occurs during the fatigue test, probably caused by the global degradation that we have just described. This phenomenon is described in detail in a publication wrote by ReMAP members [**?**]. Thus, we can point out that the DIs selected for health monitoring must be insensitive to this phenomenon.

In the case of L1 campaigns, a local damage is artificially generated to observe its evolution and accelerate the ruin of the specimen. The presence of this damage and the dynamics of its growth is also a factor that can influence the evolution of the DI. Understanding the mechanisms of composite degradation is an essential issue of SHM, however this subject is outside the scope of this thesis.

4.5.3 Noise characterization

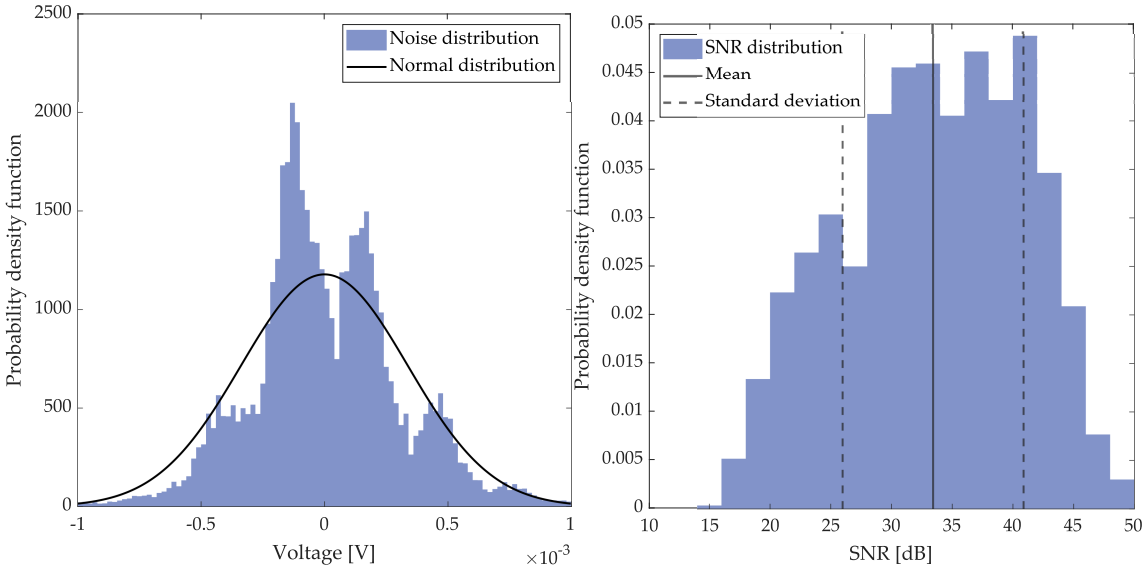

(a) (b)

Fig. 4.29 Probability density function of noise data in reference state for all L1 coupons and all frequencies except 50 kHz (a). SNR density function of noise data in reference state for all L1 coupons and all frequencies except 50 kHz (b).

Like all experimental measurements, the LW acquisitions performed during the ReMAP project are affected by a measurement noise. We are going to analyze this noise, on the one hand to evaluate if it can be limiting for the applications that we will carry out in the following chapters, and also to be able to add a noise close to reality to the numerical simulations that we will present. Since we are using a 16 bits acquisition board for LW acquisition as stated in subsection 4.2.1, the dynamic range (DR) in dB is

$$\mathrm{DR} = 20\log_{10}\left(2^{16}\right) \approx 96 \text{ dB}. \tag{4.19}$$

Moreover, the input range being between -10 V and 10 V the resolution is $\Delta V = 305\mu\text{V}$. Because of the latency during the emission of the signal by the generator, there is a time laps of about 75 µs where we measure the output of the acquisition chain with a constant and zero signal. In other words, this measurement corresponds to the measurement noise only. We use this portion of the signal for each of the captured signals to characterize the noise. For each measurement sequence, the first recorded signals contain an exponential decay due to the PZT discharge. As the first excitation frequency tested is 50 kHz, it is

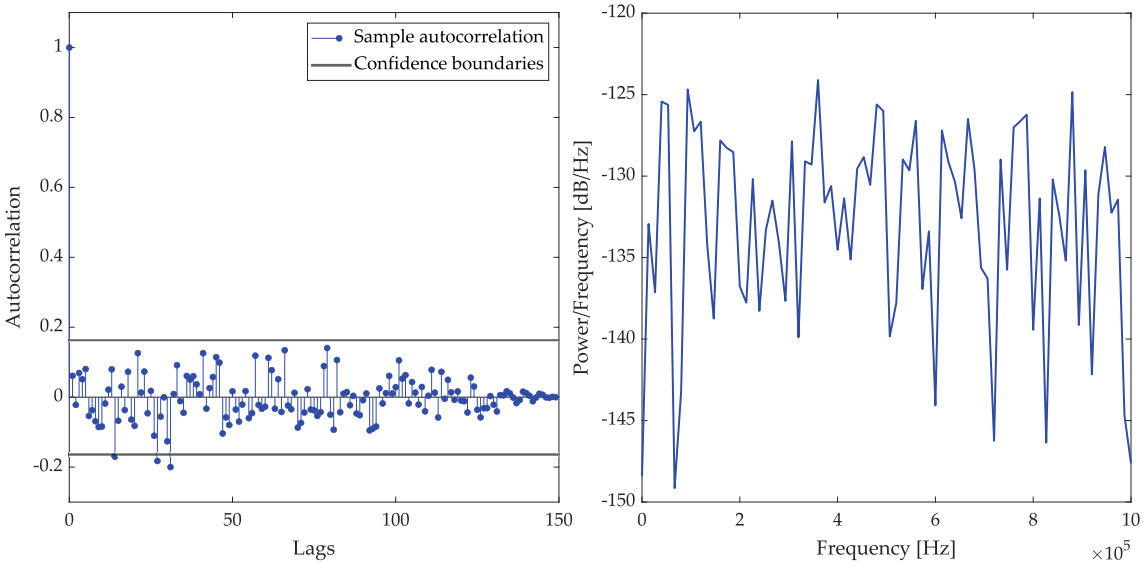

(a) (b)

Fig. 4.30 Autocorrelation function of a typical noise sample with confidence bounds (a). Power spectral density plot of the same noise sample (b).

these signals that are thus perturbed. This disturbance is effectively filtered by the pre-processing procedure but affects the characterization of the noise we want to achieve here. For simplicity in data processing, we will discard the signals with an excitation frequency of 50 kHz.

We collect the measurement noise on all measured samples, at all excitation frequencies except 50 kHz, for each reference measurement, for all channels and for each repetition. We plot the histogram of all these data in order to estimate the probability density function that best models the measurement noise Fig. 4.29a. We notice that the noise probability density distribution is multimodal with modes approximately spaced by the voltage resolution ΔV. On the same graph we plot the normal distribution with parameters that best fit the data (mean is 0 V, standard deviation is 338 µV). The noise data lies inside the normal distribution boundaries, that is why we will use a Gaussian noise to create artificial perturbation in the following chapters.

We also analyze the color of the measured noise by calculating the autocorrelation function of each noise sample. Fig. 4.30a shows a typical autocorrelation graph for a particular measurement. We notice that the obtained response contained a pulse at lag 0 whereas the autocorrelation sample at other lags lie inside the confidence bounds. This means that we can consider the process independent and therefore that we are dealing with white noise. Thus, if we calculate the spectral power density we notice that all the frequency components are present at approximately equal level Fig. 4.30b.

Finally, one of the figure of merit widely used in signal analysis is the Signal to Noise Ratio (SNR). It is expressed in dB and is calculated according to the formula

$$\text{SNR} = 10 \log_{10} \left(\frac{P_S}{P_N} \right) \tag{4.20}$$

where P_S and P_N are the power of the pure signal and the power of the noise, respectively. In this case, we consider the signals over their full duration. In order to isolate the signal S from the noise N we calculate the average over all the available repetitions for each measurement. Once this signal is obtained, we can separate the noise from the signal by computing the difference between the measured signal and the average

$$N_n = S_n - S_{\text{mean}} \tag{4.21}$$

where n denotes the considered repetition. We then get the SNR for this same repetition with formula Eq. 4.20. The SNR is calculated for all structures, at all frequencies except 50 kHz, for all transducers pairs and each repetition. We obtained the statistical distribution of the SNR that is shown Fig. 4.29b. The mean SNR is 33.4 dB and the standard deviation is 7.5 dB. It means that the signal as an amplitude 47 times higher than the noise on average. This ratio ensures a good signal quality and will help the post-processing performed later.

4.6 Conclusion

In this chapter, we presented the ReMAP project in which this thesis takes place. We introduced the project's motivations and actions. Then we listed the different SHM systems used during ReMAP test campaigns. We gave the experimental protocol of all test campaigns carried out during the project, focussing on LW acquisition process. Then we showed a first analysis on experimental data from L1 campaigns. In particular, we quantitatively assess the performance of each DI in a list of a few dozen. We established a group of some DIs that can be used for health monitoring and predictions purposes. We also studied the measurement noise from experiment to ensure the good quality of the experimental data.

Chapter 5

Data-driven damage size quantification based on imaging results post-processing

Summary

In this chapter, a damage quantification strategy relying on post-processing of Lamb waves based damage localization results is presented. This method is able to predict the upcoming sizes of a delamination after a training step. Inputs of the proposed method are localization index maps produced by damage localization algorithms and representing the presence likelihood of damage over the structure under study. The area covered by a high localization index around the estimated damage location are then extracted from these spatial probability index maps. A data-driven model representing the mathematical relationship between this quantification feature and the actual size of the damage is finally inferred and used to predict future damage size. The proposed method is successfully validated on experimental data coming from CFRP plate samples equipped with piezoelectric transducers. Delaminations induced by fatigue testing and laser shock are studied. The sensitivity of the method to input frequency and damage localization algorithms parameters is assessed and a method to automatically select its own parameters is proposed.

Contents

5.1 Introduction

5.1.1 Motivation

As mentioned in the previous chapters, the interaction of Lamb waves with damage is a complex phenomenon. The waveform reflected by the damage is strongly influenced by the size of the defect, its type (delamination, crack, impact or a combination of them), its shape, whether there are nonlinear dynamic interaction or mode conversion which are phenomena still poorly understood. All this makes measured signals harder to analyze. For such a difficult problem, data-driven methods seem to be good candidates for designing diagnostic methods in opposition with physically driven method, but however require learning. Indeed, by finding one or more damage indices that correctly capture the physical phenomena at stake, i.e. that evolves monotonically with the damage size, it is possible to use a learning algorithm on known data. The model thus obtained can be interpolated or extrapolated to estimate the size of unknown defects from raw signals. On one hand, interpolation means to look for a size lying in the learning range whereas on the other hand extrapolation seeks to predict damage size outside or the learning range. This type of method seems to be robust to complex damage shape encountered experimentally and is easier to implement than a complete physical modeling of the structure under study. The basic idea of this chapter is to present a quantification method based on this principle. We will first construct a damage index that evolves monotonically with the size of the damage by exploiting the results of localization methods. Damage localization algorithms take raw signals from sensor as input and return a map of index representing the likelihood of presence of damage over the surface of the structure under study. From this spatial probability index map, a region of high localization index is identified around the estimated damage location and the area of this region is computed. A data-driven model representing the mathematical relationship between this feature and the actual size of the damage is then inferred.

5.1.2 State of the art

In this thesis, we are interested in structures equipped with piezoelectric transducers that transmit and receive guided waves in a round-robin fashion. In this context, obtaining a map of the monitored structure reflecting its health state is a much more difficult task

than in the case of full field methods where the displacement field is measured completely on the structure with a laser vibrometer. However, such damage localization methods can be found in the literature, with the aim of obtaining the position of damage whose presence has been previously proven by a detection algorithm. The classical Time of Arrival (ToA) [52] method is a triangulation technique used for localization. Its underlying idea is to compute the travel time of the scattered wave on path actuator-damage-sensor by looking at the difference signal between damaged state and healthy state. The equations to be solved lead to a locus of possible damage positions. Time difference of arrival (TDoA) [52] is based on a similar principle. In this approach, difference of time of arrival of the wave scattered by the damage are computed at two sensors. This gives an equation of possible damage locations. In the Delay-And-Sum method (DAS) [53] for each actuator-sensor path, each point of the structure under interest is associated to the value of the signal at the theoretical time of arrival of the scattered wave. RAPID (Reconstruction Algorithm for the Probabilistic Inspection of Damage) [54, 55] algorithm is based on the computation of the probability index of a defect occurrence using the relative amplitude of the signal change on each actuator-sensor path. This probability index is computed using the signal difference coefficient and a ratio representing how far is the point from the direct path. The Excitelet method is the computation of an image of the structure where each location is associated with a value of an indicator that represents the probability index of the presence of a damage [56]. In this approach, this indicator is computed as the correlation between the signal measured between an actuator and a receiver with the theoretical signal obtained after the excitation wave has been scattered by a damage. The damage is considered here as a perfect dimensionless and omnidirectional reflector. The theoretical signal is computed as the convolution product of the excitation signal with the transfer function on the path actuator-point-sensor.

Some attempts have already been carried out to post-process Lamb waves based imaging results for damage size quantification purposes. In [57], the authors developed an algorithm based on ToA localization to assess the size of an impact. Each tip of the damage is localized and the damage size is computed as the area of the polygon formed by these tips. This method has been applied on a CFRP composite plate numerically and experimentally [57] and numerically on a plate with stiffeners [58]. A quantification strategy to assess the size of a crack and a hole has been proposed. This method is based on the localization of the tips of a crack and measuring the distance between them, or localizing the edge of the hole and measuring its diameter using two different imaging techniques. An application has been done on an aluminum plate [59]. Using a more sophisticated method, [29] proposed a data-driven approach relying on a Convolutional Neural Networks trained on a dataset composed of images generated by simulation with spectral finite element method and a localization algorithm called Excitelet [60]. In this dataset, the structure under interest is an aluminum plate containing a hole with various sizes and positions. Once the model performs well on this training set, it is applied on unknown datasets: one with numerical data generated the same way as the set used for training,

and an experimental dataset. In these articles, only one method of localization is applied, often with isotropic materials such as aluminum and on simple geometries like plates. In addition, applications are made with artificial damages as holes or slits, whereas there were very few on delaminations. Besides, there is no universal quantification method in the literature that can post-process images from different localization techniques and compare the results with each other.

5.1.3 Objectives

The objective of this chapter is to derive a data-based damage size quantification method and apply it to delaminations. It is proposed to construct a new damage index from the results of any localization method and then establish a quantification model that corresponds to a single value of the damage index with a damage size. It is also proposed to study the results obtained with different imaging methods. Finally, this approach will be evaluated on experimental data carried out with composite materials in order to place it in a case close to the industrial reality. The chapter is organized as follows. After reviewing the different damage localization methods used in this chapter, the proposed approach is explained in details. A method to automatically tuning hyperparameters is proposed. Preliminary tests are made on numerical simulation data to assess the sensitivity of the method to input frequency and damage localization algorithms. The approach is successfully validated on experimental data coming from CFRP plate samples equipped with a piezoelectric transducers network. These data come from two different fatigue datasets, the first one is the L1 compression-compression fatigue test carried out during ReMAP project while the other one is a tension-tension fatigue test. The method is also applied on a ReMAP L1 coupon with laser shock induced delaminations.

The work presented in this chapter was the subject of a published journal article [61].

5.2 Investigated damage localization methods

According to the different SHM levels described in Sec. 2, after detecting a damage in a structure the second step is to know its position. Damage localization methods are designed for this purpose. They are algorithms that take as input raw signals from piezoelectric transducers bonded on a structure. These raw signals are first denoised, filtered and time-aligned. The outputs of these algorithms are the estimated position of the damage and a map of the structure where each pixel is associated with a Damage Localization Index (DLI). The higher is this value, the higher the damage is likely to be localized at this position. The pixel with the maximum DLI is considered as the estimated position of the damage. The damage localization methods that will be used in the rest of this chapter are briefly described in this section. These methods have been selected for their relative simplicity and because they had been tried and tested in several papers. In the rest of the section, M_{PZT} denotes the number of piezoelectric elements.

5.2.1 Time of Arrival (ToA)

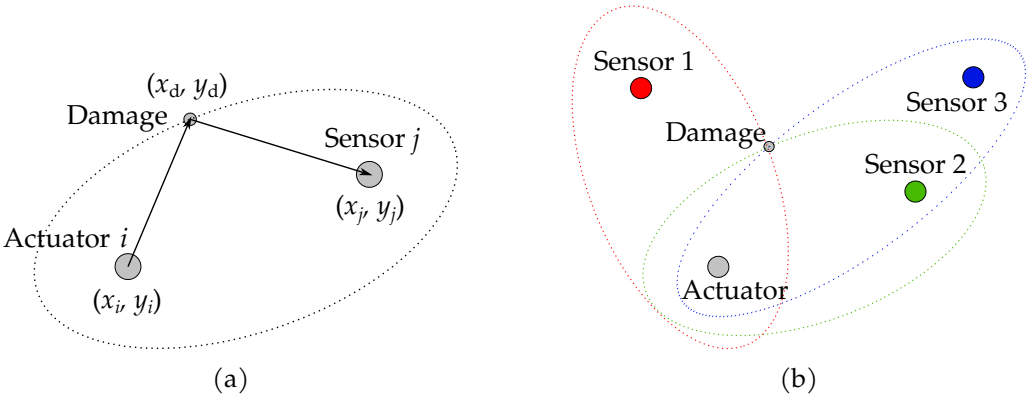

Fig. 5.1 Principle of ToA localization method for an isotropic material. Locus of possible damage location for a pair of transducers (a). Estimation of damage position from several paths (b).

Time of Arrival (ToA) method is a triangulation technique widely used for damage localization purposes. Considering each actuator i to sensor j path and a damage at the coordinates (x_d, y_d), it is intended to compute the time of flight of scattered wave on the path actuator-damage-sensor. To isolate the wave scattered by the damage, the signal considered here is the difference between the current damaged state and the healthy state. As such, the wave traveling on the direct path from actuator to sensor does not appear. The time of flight (or time of arrival) is then calculated as

$$\mathrm{ToA}_{ij}(x_d, y_d) = \frac{\sqrt{(x_i - x_d)^2 + (y_i - y_d)^2}}{c_g^{id}} + \frac{\sqrt{(x_j - x_d)^2 + (y_j - y_d)^2}}{c_g^{dj}} \tag{5.1}$$

where (x_i, y_i) and (x_j, y_j) are respectively the coordinates of the actuator i and the sensor j. c_g^{id} and c_g^{dj} are the group velocities on respectively the actuator-damage path and the damage-sensor path. The possible locations of the damage are lying on a locus drawing an ellipse for an isotropic material 5.1. The implementation of this algorithm described in [52] is used here. The structure under study is spatially sampled and the theoretical ToA $t_{ij}^{th}(x, y)$ is computed for each pixel of coordinates (x, y) and each pair of transducers ij. Then a damage localization index is obtained at each pixel of the structure by comparing the theoretical time of flight $\mathrm{ToA}_{ij}^{th}(x, y)$ to the one extracted from scattered signal ToA_{ij}^{xp}

$$\mathrm{DLI}_{\mathrm{ToA}}(x, y) = \sum_{i=1}^{M_{PZT}} \sum_{\substack{j=1 \\ j \neq i}}^{M_{PZT}} \exp\left(-\frac{1}{\tau}\left|\mathrm{ToA}_{ij}^{th}(x, y) - \mathrm{ToA}_{ij}^{xp}\right|\right). \tag{5.2}$$

τ is a focus parameter introduced in order to reduce the influence of secondary reflections of the scattered signal.

5.2.2 Time Difference of Arrival (TDoA)

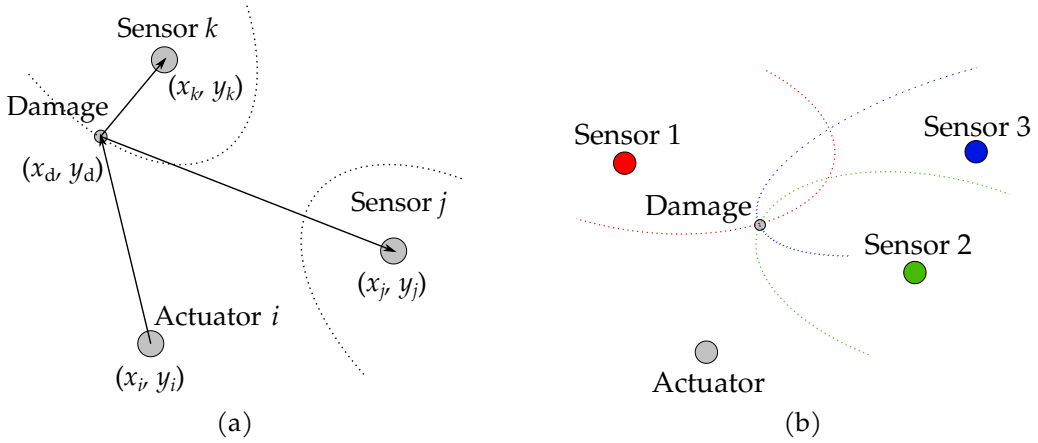

Fig. 5.2 Principle of TDoA localization method for an isotropic material. Locus of possible damage location for a triplet of transducers (a). Estimation of damage position from several paths (b).

Time Difference of Arrival (TDoA) is based on the same principle as ToA. The only difference is that in this method a group of three piezoelectric elements is considered: one actuator i and two sensors j and k. The damage is located at coordinates (x_d, y_d). Here we compute the difference of time of flight on the path actuator-damage-sensor of the diffracted wave for two different sensors j and k. In the same way as for the ToA method, the signal considered here is the difference between the current damaged state and the healthy state in order to isolate the wave scattered by the damage

$$\mathrm{TDoA}_{ijk}(x_d, y_d) = \mathrm{ToA}_{ij}(x_d, y_d) - \mathrm{ToA}_{ik}(x_d, y_d)$$

Since the time of flight is the same for the path actuator-damage, TDoA can be written

$$\mathrm{TDoA}_{ijk}(x_d, y_d) = \frac{\sqrt{(x_j - x_d)^2 + (y_j - y_d)^2}}{c_g^{dj}} - \frac{\sqrt{(x_k - x_d)^2 + (y_k - y_d)^2}}{c_g^{dk}} \tag{5.3}$$

where (x_j, y_j) and (x_k, y_k) are respectively the coordinates of the sensors j and k. c_g^{dj} and c_g^{dk} are the group velocities on respectively the damage-sensor j path and the damage-sensor k path. The possible locations of the damage are lying on a locus drawing a hyperbola for an isotropic material Fig. 5.2. As for ToA method, the structure under study is discretized spatially and the theoretical $\mathrm{TDoA}_{ijk}^{th}(x, y)$ is computed for each pixel of coordinates (x, y) and each triplet of transducers ijk. Then a damage localization index is obtained at each pixel of the structure by comparing the theoretical difference of time of flight $\mathrm{TDoA}_{ijk}^{th}(x, y)$

to the one extracted from scattered signal $\mathrm{TDoA}_{ijk}^{\mathrm{xp}}$ as stated in

$$\mathrm{DLI}_{\mathrm{TDoA}}(x,y) = \sum_{i=1}^{M_{\mathrm{PZT}}} \sum_{\substack{j=1 \\ j\neq i}}^{M_{\mathrm{PZT}}} \sum_{\substack{k=1 \\ k\neq j\neq i}}^{M_{\mathrm{PZT}}} \exp\left(-\frac{1}{\tau}\left|\mathrm{TDoA}_{ijk}^{\mathrm{th}}(x,y) - \mathrm{TDoA}_{ijk}^{\mathrm{xp}}\right|\right). \tag{5.4}$$

As in the ToA method, a focus parameter τ is introduced to limit the influence of secondary reflections.

5.2.3 Delay and Sum (DAS)

In the Delay-And-Sum method (DAS) [53], the structure under interest is spatially discretized. For each spatial location (x,y), the signals in the healthy state and in the current damaged state are processed to compensate attenuation

$$s_{ij}^{c}(t) = \frac{s_{ij}(t)}{\sqrt{d_{\mathrm{AS}}}} \tag{5.5}$$

where d_{AS} is the distance between the actuator i and the sensor j, and $s_{ij}(t)$ is the signal before compensation. Then the envelope of the difference signal between healthy state and current damaged state is computed using Hilbert transform. This residual signal is denoted $r_{ij}(t)$. Besides, for each image point of coordinates (x,y) the time of arrival $\mathrm{ToA}_{ij}(x,y)$ of the Lamb waves is estimated for the path actuator-point-sensor exactly as for ToA method 5.1. The DLI related to DAS is computed as an average over every actuator-sensor paths of each residual $r_{ij}(t)$ integrated over a time window centered around $\mathrm{ToA}_{ij}(x,y)$. The size of the time window is tuned by a parameter K

$$\mathrm{DLI}_{\mathrm{DAS}}(x,y) = \frac{1}{2K\Delta t} \sum_{i=1}^{M_{\mathrm{PZT}}} \sum_{\substack{j=1 \\ j\neq i}}^{M_{\mathrm{PZT}}} \int_{\mathrm{ToA}_{ij}(x,y)-K\Delta t}^{\mathrm{ToA}_{ij}(x,y)+K\Delta t} r_{ij}(t)\ \mathrm{d}t. \tag{5.6}$$

Δt denotes the time step of the signal and K is the number of time steps of half the time window.

5.2.4 Reconstruction Algorithm for the Probabilistic Inspection of Damage (RAPID)

The Reconstruction Algorithm for the Probabilistic Inspection of Damage (RAPID) [54] is aimed to compute the probability index of a defect occurrence using the relative amplitude of the signal change on each actuator-sensor path. This probability index P_{ij} is calculated from the signal difference coefficient $A_{ij} = 1-\rho_{ij}$ with ρ_{ij} the correlation coefficient between the healthy and the damaged state signals on the path from actuator i to sensor j. The feature also depends on a ratio representing how far is the point from the direct path. For each actuator-sensor path, a distribution function is drawn to represent this last property.

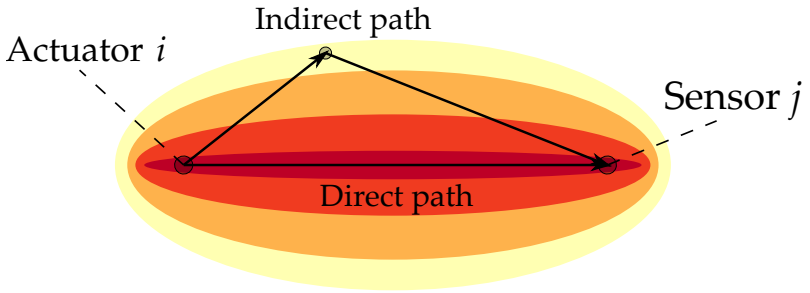

Fig. 5.3 Spatial distribution used in RAPID method.

Here an elliptical distribution is used and its spread is controlled by a real scalar parameter $\beta \in]1, +\infty[$. If β increases, the spatial distribution becomes more spread out and if β is close to 1 the distribution becomes very narrow. The structure under study is spatially sampled. At each pixel of coordinates (x, y) and each transducer pair ij the following probability index is defined

$$P_{ij}(x,y) = A_{ij}\left(\frac{\beta - R_{ij}(x,y)}{\beta - 1}\right) \tag{5.7}$$

with

$$R_{ij}(x,y) = \begin{cases} D_{ij}(x,y) & \text{when } D_{ij}(x,y) < \beta \\ \beta & \text{when } D_{ij}(x,y) \geqslant \beta \end{cases} \tag{5.8}$$

where

$$D_{ij}(x,y) = \frac{d_{\mathrm{AP}} + d_{\mathrm{PS}}}{d_{\mathrm{AS}}}. \tag{5.9}$$

d_{AP} is the distance actuator to point (x, y), d_{PS} the distance point (x, y) to sensor and d_{AS} the distance between the actuator and the sensor. The DLI associated with the point (x, y) is then expressed as a linear summation of the P_{ij} values for every pair of transducers

$$\mathrm{DLI}_{\mathrm{RAPID}}(x,y) = \sum_{i=1}^{M_{\mathrm{PZT}}} \sum_{\substack{j=1 \\ j \neq i}}^{M_{\mathrm{PZT}}} P_{ij}. \tag{5.10}$$

5.3 Image post-processing method

All the damage localization methods presented previously provide a map of DLI over the structure under study that will be processed to compute a quantification feature.

5.3.1 HDLI feature computation

For each damage localization method, these maps are normalized by the highest DLI value in the whole training set. The idea is then to compute a single feature that varies with the damage size in a monotonic manner. From Fig. 5.4a which constitutes a typical DLI map, it can be observed that there is a region where the DLI is higher than the rest of the image, without clear boundaries. The assumption made here is that the area of this region is a function of the actual damage size. Applying a threshold T to a DLI map gives a binary image where one or several regions with a DLI above the threshold can be identified. The next step is to isolate the region surrounding the estimated damage position that is to say the position with the maximum DLI.

The Moore-Neighbor image segmentation algorithm [62] is used to perform this task. It is intended to identify the boundaries of all the objects in a binary image. Beginning at a starting pixel called current pixel, the algorithm visits each pixel in the starting pixel's neighborhood (i.e. the 8 pixels that share a vertex or an edge with the current pixel) in clockwise direction. If a pixel belonging to the object is detected, it becomes the new current pixel. The procedure continues until matching the stopping criterion. The criterion used here (as it is the one implemented in MATLAB) is called Jacob's stopping criterion. It states that the algorithm stops after entering the starting pixel a second time in the same manner it has been entered initially.

The result of this threshold and segmentation steps is shown in Fig. 5.4b. The area of the isolated region is computed and denoted A. This area is divided by the total area A_{tot} of the structure under study in order to have a dimensionless damage index that will be called HDLI (High Damage Localization Index area) in the following.

$$\text{HDLI} = \frac{A}{A_{\text{tot}}} \tag{5.11}$$

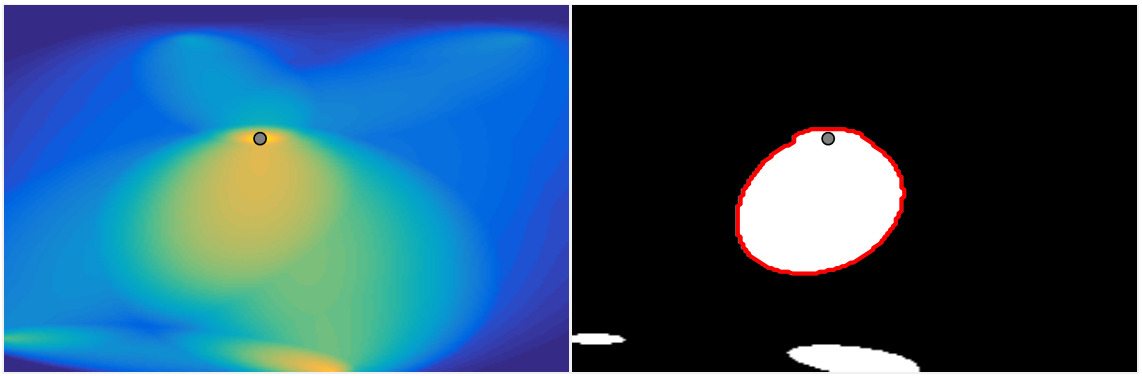

(a) (b)

Fig. 5.4 Damage localization results from RAPID method (a) and the binary image obtained after applying a threshold function (b). The gray circle is the estimated damage localization.

5.3.2 Damage quantification model training

To estimate the size of an unknown damage, a data-driven model is built. The workflow followed to infer and validate such a model is divided in two steps. The first one is the training step: it aims to train in a supervised manner a data-based model from a training set, i.e. a collection of signals corresponding to different damage states with the corresponding size of the damage. In the prediction step, the size of an unknown and potentially larger damage is predicted with the model previously inferred in order to validate its extrapolation performances.

Training step

Let us assume that a training set of N damage cases labeled with the associated damage size $\{(S_1, s_1), \dots, (S_N, s_N)\}$ is available. S_i is the set of signals from the transducers for the i^{th} damage case and s_i is the corresponding size of the damage. This dataset is processed through a given damage localization method. Then we get a new dataset $\{(I_1, s_1), \dots, (I_N, s_N)\}$ where I_i is the image returned by the damage localization algorithm. Once the HDLI of each training example is computed, the training set $\mathbf{X} = \{(h_1, s_1), \dots, (h_N, s_N)\}$ is available. h_i is the HDLI described previously computed from the i^{th} image. HDLI values close to 0 are discarded to improve the sensitivity of the method for large damage since the purpose is to extrapolate a model toward higher damage sizes. In the following, $\boldsymbol{H} \in \mathbb{R}^N$ and $\boldsymbol{S} \in \mathbb{R}^N$ will denote respectively the vector of HDLI features and the vector of damage sizes of all N training samples. To predict the future size of the damage under study, it is necessary to build a model that fits well the data on the training set and that can be extrapolated. Since the HDLI does not vary linearly with the damage size, a classical linear regression cannot be used. For the sake of simplicity, a polynomial regression is chosen. This method has the advantage to fit the data well and does not occult the physics of the model like other supervised machine learning approaches. Polynomial regression is then performed on $\mathbf{X}$, and the j^{th} coefficient of the regression model is denoted β_j

$$\hat{\boldsymbol{S}} = \sum_{j=0}^{d} \beta_j \boldsymbol{H}^j. \tag{5.12}$$

In Eq. 5.12, d is the degree of the polynomial, $\hat{\boldsymbol{S}} \in \mathbb{R}^N$ is the vector of estimated damage size and $\boldsymbol{H}^j \in \mathbb{R}^N$ is the vector of j^{th} power of the components of $\boldsymbol{H}$. In order to keep the model variance low, a variation of classic linear regression called ridge regression is used [63]. It is to adds a penalty term λ on the parameters β_i in the ordinary least square regression problem to control for their amplitude. The vector of regression coefficients $\hat{\boldsymbol{\beta}}$ must minimize the equation

$$\hat{\boldsymbol{\beta}} = \underset{\boldsymbol{\beta} \in \mathbb{R}^d}{\operatorname{argmin}} \left(\left\| \boldsymbol{S} - \boldsymbol{\beta} \boldsymbol{H} \right\|_2^2 + \lambda \left\| \boldsymbol{\beta} \right\|_2^2 \right). \tag{5.13}$$

The problem can be written under matrix form

$$\hat{\boldsymbol{\beta}} = \left(\boldsymbol{H}^T\boldsymbol{H} + \lambda\boldsymbol{I}\right)^{-1}\boldsymbol{H}^T\boldsymbol{S} \tag{5.14}$$

where $\boldsymbol{I}$ is the N-by-N identity matrix. The next step is to compute the optimal value for the penalty term λ_{opt} to minimize the error over the training set. In order to choose an optimal value for the penalty term, a gradient descent algorithm is used to minimize the cost function J with respect to λ. To avoid overlearning the model on the training data set, this cost function is calculated using a cross-validation technique. This step limits the risk that the model gives very good results only on the training set while the predictions on the test set are poor.

$$\lambda_{\text{opt}} = \underset{\lambda\in\mathbb{R}}{\operatorname{argmin}}\, J \tag{5.15}$$

Since the dataset considered here is small, we chose a cross-validation called *Leave-One-Out* which is suited for this type of case. The idea is to train the model on a new training set where one of the item has been left out. The error of the model is then computed for the removed item i

$$J_i = \frac{1}{2}|s_i - \hat{s}_i|^2 + \frac{\lambda}{2}\sum_{k=1}^{d}\|\beta_k\|_2^2, \quad \forall\, i \in [\![1; N]\!] \tag{5.16}$$

This process is repeated for every item of the training set i.e. N times. The cost function J used in the optimization problem Eq. 5.15 is computed as the mean of all J_i

$$J = \frac{1}{N}\sum_{i=1}^{N} J_i. \tag{5.17}$$

We finally must chose a value for the degree of the polynomial. Any degree high enough will yield to the same regression model because coefficients relative to high degree terms will be close to zero thanks to the regularization. Throughout this chapter, d is set to 8.

Prediction step

The data-driven model built earlier is then used to predict the size of an unknown and larger damage. The first step is to process the signal with the damage localization method to get a DLI image of the structure. Then the HDLI value h_{test} is computed from this image. The corresponding size s_{test} is finally estimated using the size quantification model previously built

$$\hat{s}_{\text{test}} = \sum_{k=0}^{d}\hat{\beta}_k h_{\text{test}}^k. \tag{5.18}$$

5.3.3 Methodology

The overview of the method is depicted in Fig. 5.5. M_{rep} stands for the number of measures for the same damage case and N is the size of the training set. The steps to follow are

Step 1 Get signals from each transducer on the plate.

Step 2 Process the signals corresponding to the i^{th} case with one of the damage localization algorithm described earlier. The result is a DLI image of the structure.

Step 3 Compute the HDLI associated with the image i.

Step 4 Repeat steps 2 and 3 for each $i \in [\![1; N]\!]$.

Step 5 Perform the polynomial regression model using the training set of HDLI previously computed and the known damage size of the corresponding damage case.

Step 6 Compute the HDLI value of an unknown damage case.

Step 7 Use the regression model to estimate the size of the damage.

In order to assess the performance of the inferred model, the following metric will be used in the rest of this chapter. It is defined as the relative error computed on training or test set

$$\varepsilon = \frac{1}{L} \sum_{l=1}^{L} \frac{|\hat{s}_l - s_l|}{s_l} \tag{5.19}$$

where L is the size of the dataset.

5.3.4 Parameters selection for damage quantification

As previously explained, the damage quantification method proposed here is tested with several damage localization methods: ToA, TDoA, RAPID and DAS. For each of these algorithms, a tuning parameter has to be chosen. In the ToA and TDoA algorithms, an exponential window function is introduced to reduce the effect of secondary reflections. This function depends on a decay rate τ Eq. 5.2. The DAS algorithm depends on the number of samples K over which time integration is performed Eq. 5.6. In the RAPID approach the user can set a parameter called β corresponding to the the spread of the spatial distribution around each path. Moreover, the post-processing method presented also depends on the threshold level T in the HDLI feature computation step.

In order to have an unique damage size for one HDLI, parameters need to be chosen to get a bijection between HDLI and damage size values. The tuning parameters for the localization algorithms used throughout this work are given in Tab. 5.1. These values have been set empirically.

The only parameter left to be selected is the threshold T. To illustrate the influence of this parameter on the obtained results, sensitivity of the RAPID algorithm to threshold is

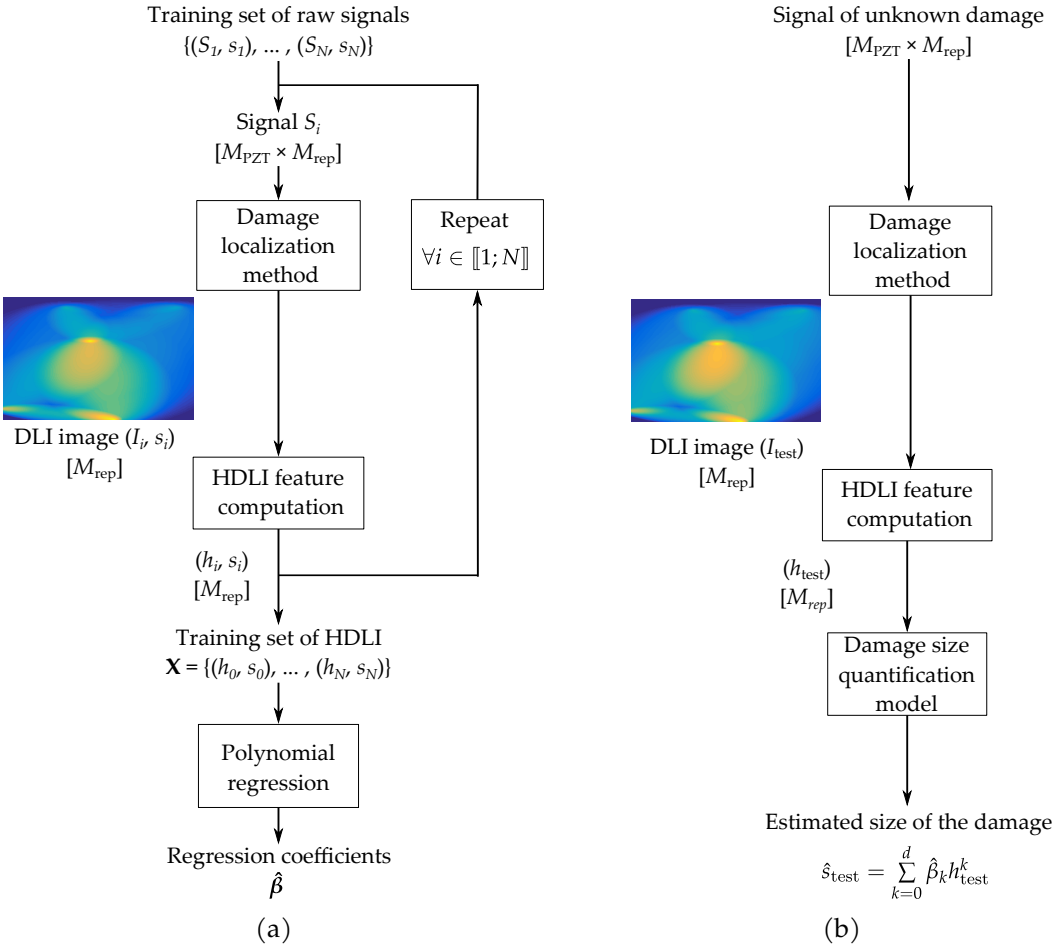

Fig. 5.5 Overview of the damage size quantification algorithm based on the post processing of localization algorithms. Description of the training step (a) and the prediction step (b).

depicted Fig. 5.6. The data comes from numerical simulation (more details can be found in the next subsection 5.4.1). We can observe that some threshold values lead to bijective function that can be used for damage size prediction whereas some others parameters values provide the same damage size for a wide range of HDLI and thus do not allow a priori for reliable damage size quantification. Thus, to get a threshold value that is compatible with the post-processing method described earlier, the optimal threshold T_{opt} minimizing the following cost function over the training set is selected:

$$T_{\text{opt}} = \underset{T \in \mathbb{R}}{\operatorname{argmin}} \left(\frac{1}{2N} \sum_{i=1}^{N} \|s_i - \hat{s}_i\|^2 \right) \tag{5.20}$$

Unfortunately, this cost function is not smooth and its derivative cannot be computed analytically. Moreover, many different local minima could exist. To find a threshold providing an acceptable error on the training set a minimization algorithm is used with different random starting points. The retained threshold T_{opt} is the one with the lowest associated

Table 5.1 Localization parameters selected.

Localization method	Parameter description	Symbol	Selected value
ToA & TDoA	Decay rate of an exponential windowed function applied to reduce secondary reflections.	τ	5×10^{-7} s
DAS	Number of samples over which time integration is performed.	K	1
RAPID	Parameter set to adjust the spread of the ellipses around each path.	β	1.05

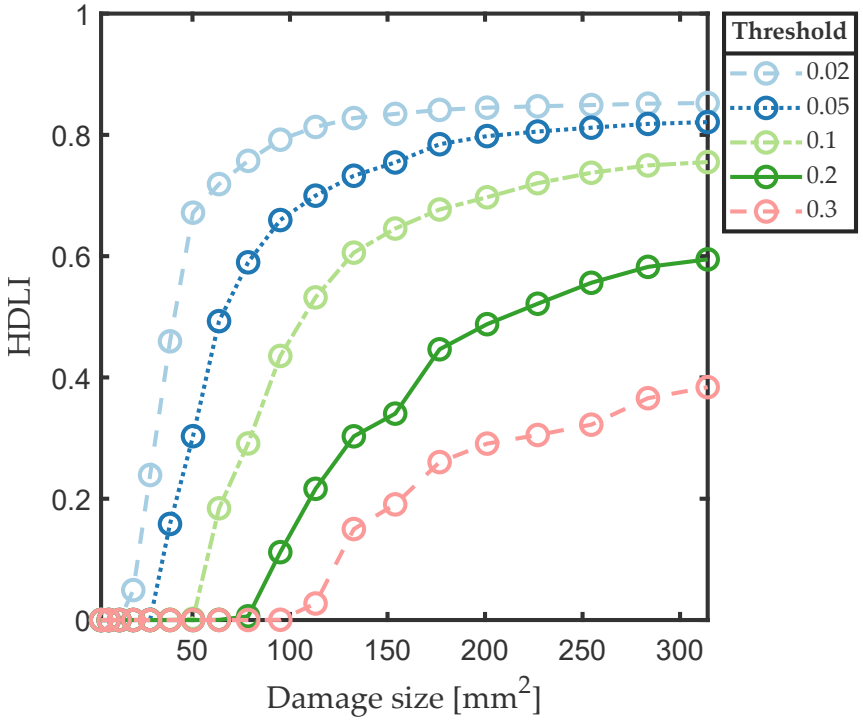

Fig. 5.6 HDLI sensitivity to threshold parameter using RAPID localization method.

value of the cost function. We use the simplex method [64] which is a derivative-free optimization technique.

5.4 Application of the proposed damage quantification method

The damage size quantification strategy is applied to different cases, both numerical and experimental.

5.4.1 Preliminary tests on simulation data

A preliminary test is done on data coming from numerical simulation to assess the performance of the method in the case of damage with well-defined boundaries. Another

objective is to study the influence of the excitation signal central frequency on quantification results.

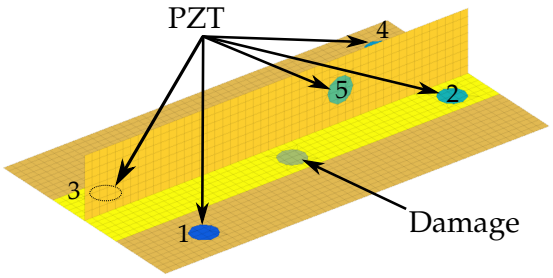

Fig. 5.7 FEM model of the stiffened panel used for simulation.

Table 5.2 Mechanical properties used for numerical simulation.

Density [g.cm^{-3}]	$E_{0°}$ [GPa]	$E_{90°}$ [GPa]	ν -
1.57	163	10	0.3

The structure under consideration is a stiffened composite panel made of carbon/epoxy IM7/8552 unidirectionnal laminates following the stacking sequence [45/0/45/90/-45/0]. The properties of one ply are given in Tab. 5.2. The FEM model of the structure equipped with piezoelectric elements and highlighting damage position is shown in Fig. 5.7. A set of 5 PZTs NCE51, each with a diameter of 20 mm and thickness of 0.1 mm, is surface-mounted on the composite plate. The coordinates of these transducers and of the simulated damage, along with the complete description of the FEM can be found in the paper from which this chapter is derived. The adopted formulation is based on piezoelectric Mindlin shells, taking into account the viscoelasticity of the composite core, the glue, and the piezoelectric coupling equations. Electrical degrees of freedom are included in addition to the nodal displacement [65, 66]. The model is meshed with 1 mm × 1 mm square shell elements. This mesh size was chosen to be compatible with the wavelength of the S0 mode at 160 kHz (40 mm), leading to 40 elements per wavelength which ensure mesh convergence. Since the other frequencies studied here have higher wavelength, the same mesh will be use for all frequencies. The time step for the transient simulation is 500 ns, leading to a sampling frequency of 2 MHz. The dynamic simulation is done with an implicit Newmark method using the MATLAB toolbox SDT [17].

The simulated damage has a circular shape with a radius varying from 1mm to 10mm by step of 0.5mm leading to 19 different damage cases. The delamination is modelled by a decrease of the Young modulus of 90% in the damaged area. This kind of model has been compared to experimental results [67]. It is shown that the delamination indeed induces a local stiffness reduction. Even if this model does not fully account for the nonlinear behavior of the delamination, it will be realistic enough to test our methodology. A healthy case i.e. without any damage is used as reference by the damage localization

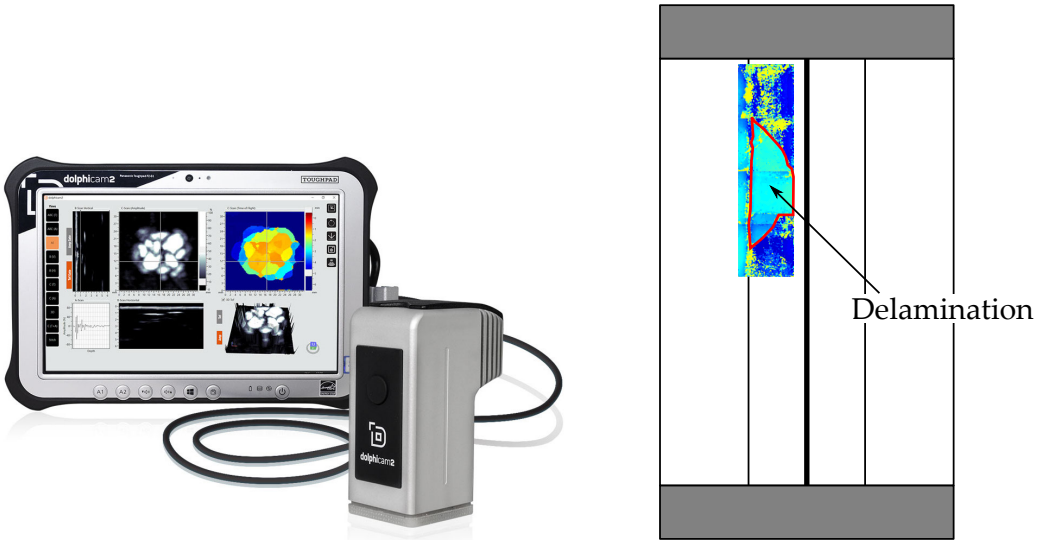

(a) (b)

Fig. 5.8 Dolphicam© NDT system used to control delamination growth (a). Illustration of the back side of a L1 coupon with artificial disbond. The area monitored by the probe has been added. The region highlighted in red is the delamination (b).

algorithms. The first 70% of this dataset is used as training set (from 1mm to 7mm) and the 30% left (from 7.5mm to 10mm) are used as testing set in order to assess the prediction performance of the damage quantification model. In an industrial context it corresponds to build a model with the smaller sizes of a damage when it is not yet an issue for the integrity of the structure. Then the prediction relies on the extrapolation of this model to upcoming larger size of the damage. Thus, it is possible to know when the delamination reaches a critical size that threaten the integrity of the structure.

The signal chosen is a 5-cycles tone burst with an amplitude of 10 V. We consider 3 central frequencies: 120, 140 and 160 kHz. Gaussian random noise is added to the received signal to introduce variability in the data. The signal to noise ratio is 70 dB. For each damage case 10 repetitions have been simulated. For any damage localization algorithm, each repetition in a damaged case is compared to each repetition in the healthy state leading to 100 different DLI maps.

5.4.2 Application to experimental data

ReMAP L1 fatigue data

We also apply the image post-processing method to the L1 coupon data of the ReMAP project described in the previous chapter. The main difficulty is to have enough ground truth data to perform the training of the model on the one hand, and to evaluate the prediction accuracy on the other hand. For this purpose we will use specimens that have been controlled by Dolphicam© ultrasonic probe regularly during the fatigue test. The results of these controls are presented in the form of an image of the inspected area where each

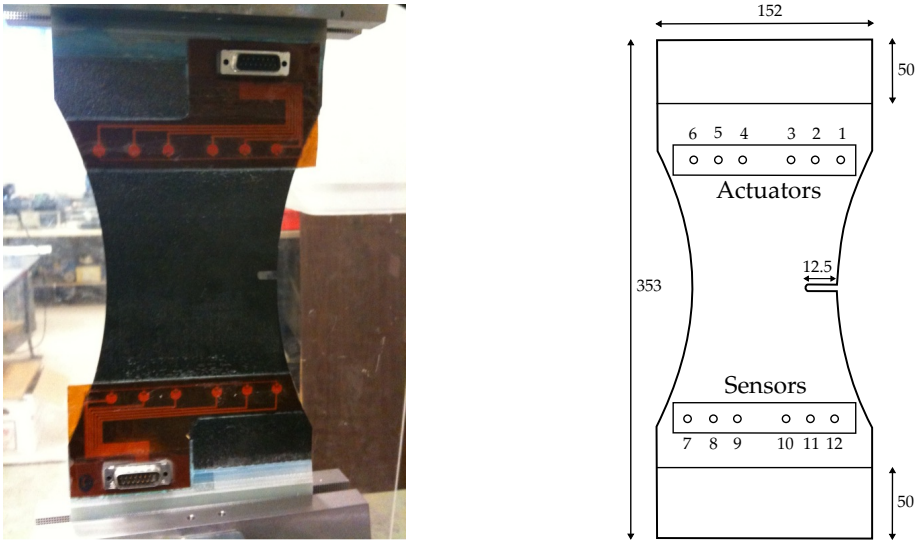

(a) (b)

Fig. 5.9 CFRP samples used in NASA dataset (a). Dimensions of the coupon in mm adapted from [69] (b).

color corresponds to a value of through-thickness time of flight. We extracted the delamination size from ultrasonic NDT images using the image-processing software Fiji [68] [1]. Each delamination size is associated with Lamb waves signals obtained at the same time of the test. This allows us to build a database of labeled data that we can use for quantification. The first 70% of the dataset will be used as a training set and the rest will be the test set. The excitation signal is a 5-cycles tone burst of 10 V amplitude and a 200 kHz central frequency.

ReMAP L1 laser shocks data

The method developed in this chapter is also applied to data obtained on the L1 sample with laser shock delamination as described in the previous chapter. In order to have a labelled database, we measured the size in both dimensions of the delaminations created. To proceed we used a GEKKO© A-scan NDT system along with a multi-element ultrasound probe. Each delamination size is associated with Lamb waves signals obtained at each new shock. This allows us to build a database of labeled data that we can use for quantification. The first 70% of the dataset will be used as a training set and the rest will be the test set. The excitation signal is a 5-cycles tone burst of 10 V amplitude and a 160 kHz central frequency.

NASA fatigue data

The post-processing strategy is also applied to experimental data coming from fatigue test carried out on CFRP specimens conducted jointly by NASA and Stanford University [70].

[1] https://fiji.sc/

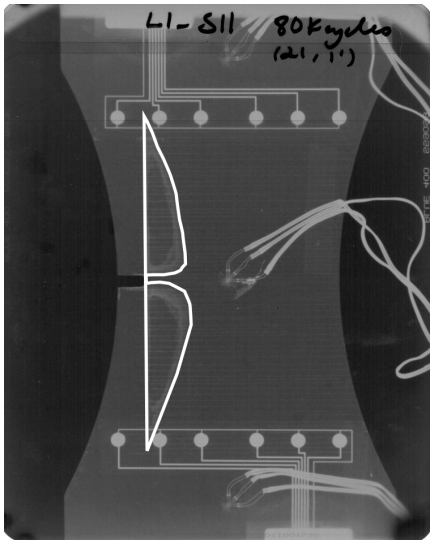

Fig. 5.10 X-ray image of specimen L1_S11 taken at 80 kcycles. The edges of the delamination are highlighted in white.

The specimens under study are CFRP composite plate with a dogbone shape and a notch at mid-length which geometrical dimensions can be found in Fig. 5.9. The specimen is equipped with a six-PZTs-sensor SMART Layer© from Acellent Technologies bonded at the top and at the bottom of the coupon. The transducers placed at the top of the coupon are used as actuators whereas the bottom piezoelectric elements are exclusively used as sensors. This leads to a total of 36 actuator-sensor paths. The experimental protocol is aimed to run a cycling tension-tension fatigue test. The presence of the notch induces a stress concentration that creates a delamination growing with the number of cycles. These fatigue tests were performed on a MTS machine with frequency of 5 Hz and a stress ratio of $R = 0.14$. The test was regularly interrupted to perform Lamb waves pitch-catch acquisition. The excitation signal used is a 5-cycles tone burst with a central frequency of 250 kHz and an amplitude of 50 V. The frequency is chosen to be the one where fundamental symmetric and antisymmetric are the most distinguishable as mentioned by [69]. An X-ray image is also taken at each interruption to visualize the size of the delamination Fig. 5.10. Several layups are available in this dataset. Here, the layups L1 and L2 had been retained with respectively the stacking sequences $[0_2/90_4]_s$ and $[0/90_2/45/-45/90]_s$. With these layups a delamination can be visualized growing progressively with the number of cycles, allowing a supervised machine learning approach. The dataset is split in one training set (first 70% of damage cases) and one test set (30% of others damage cases). Each damage case is composed of raw data from piezoelectric patches. Actual delaminations area were extracted from X-ray images with the image processing software Fiji [68] [2].

Table 5.3 Performance over the different datasets measured with training and test error in percentage.

Dataset	ToA		DToA		DAS		RAPID	
	$\varepsilon_{\text{train}}$	$\varepsilon_{\text{test}}$	$\varepsilon_{\text{train}}$	$\varepsilon_{\text{test}}$	$\varepsilon_{\text{train}}$	$\varepsilon_{\text{test}}$	$\varepsilon_{\text{train}}$	$\varepsilon_{\text{test}}$
Numerical	510	73	340	37	7.5	13	1.4	3.1
ReMAP L1 laser shocks	-	-	-	-	-	-	7.6	7.8
ReMAP L1 disbond	8.8	31	11	29	15	40	5	3.2
ReMAP L1 impact	20	52	14	39	-	-	11	11
L1_S11	200	32	140	36	36	31	12	7.8
L1_S12	220	50	300	70	62	38	13	6.2
L1_S18	390	49	410	36	31	20	19	7.8
L1_S19	750	85	400	78	29	47	38	27
L2_S11	410	52	420	55	6.9	15	3.6	5.6
L2_S17	24	31	55	37	8.4	9.8	19	25
L2_S18	110	3.9	110	20	160	33	150	5
L2_S20	12	29	77	11	5.2	4.2	10	3.5

5.4.3 Results

For each structure considered and each damage localization method, the performance of the proposed damage quantification algorithm are evaluated by two different ways. The first one is a plot where the x-axis is the true delamination area and the y-axis is the size predicted by the damage quantification algorithm. The $y = x$ line represents a prediction without error: the closer a value is to this line, the better the prediction. The 5% deviation from this line are also drawn in gray. As stated previously, for each structure considered, the dataset is split into a training set (the first 70% of the damage cases) and a testing set (the last 30% of the damage cases). The other way to assess the performance of the post-processing strategy proposed is to compute the error on the training set and the test set for each structure.

We first compare the results obtained with the four different localization methods studied here Fig. 5.11. ToA and TDoA exhibit poor results on both training and testing dataset. DAS performs well on the training set although the prediction on the testing set is far from the true size. The RAPID algorithm provides the best results on both training set and testing set as the predicted values are very close to the $y = x$ line. In the following, only the RAPID method will be used for applications to experimental data. Besides, it is worth noting that the performance of DAS and RAPID methods does not seem sensitive to noise.

Regarding the prediction made on ReMAP L1 specimens, the results are within the 5% deviation range from best prediction for the case with an artificial disbond Fig. 5.13a. However for the case of an impact damage the prediction error is larger. Besides, results on ReMAP laser shocks dataset shows a good trend for both training and test dataset even if some points are out of the 5% deviation range. The quantitication method gives satisfying results on both training set and testing set for each type of layup in NASA dataset Fig. 5.12.

[2] https://fiji.sc/

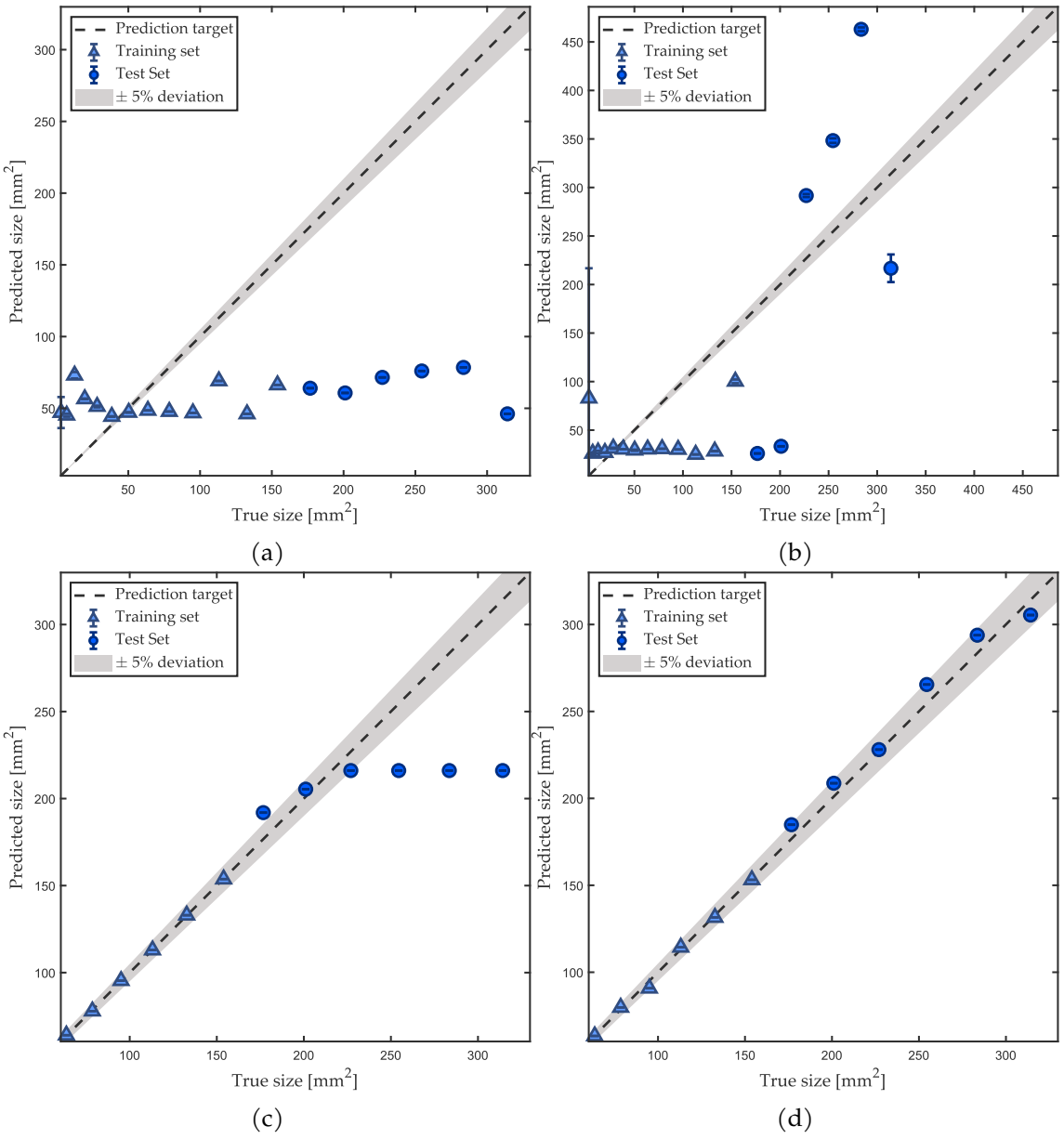

Fig. 5.11 Damage quantification performance using different damage localization methods on numerical data. ToA (a), DToA (b), DAS (c), RAPID (d). The diagonal $y = x$ line correspond to a prediction without error.

All these observations are confirmed by Tab. 5.3 which shows the error on the training set $\varepsilon_{\text{train}}$ and on the test set $\varepsilon_{\text{test}}$ to assess the performance for each localization method. We can observe that qualitative remarks made about the graphs are confirmed quantitatively here.

The influence of the excitation signal frequency on the prediction has been investigated. Fig. 5.15a relates the prediction error $\varepsilon_{\text{test}}$ on the NASA coupon L1_S11 for each frequency available in the dataset and for several learning rate i.e. several sizes of training set. Each rate corresponds to the percentage of the whole dataset used as training set. It can be seen that the prediction error is the lowest for an input signal at 250 kHz

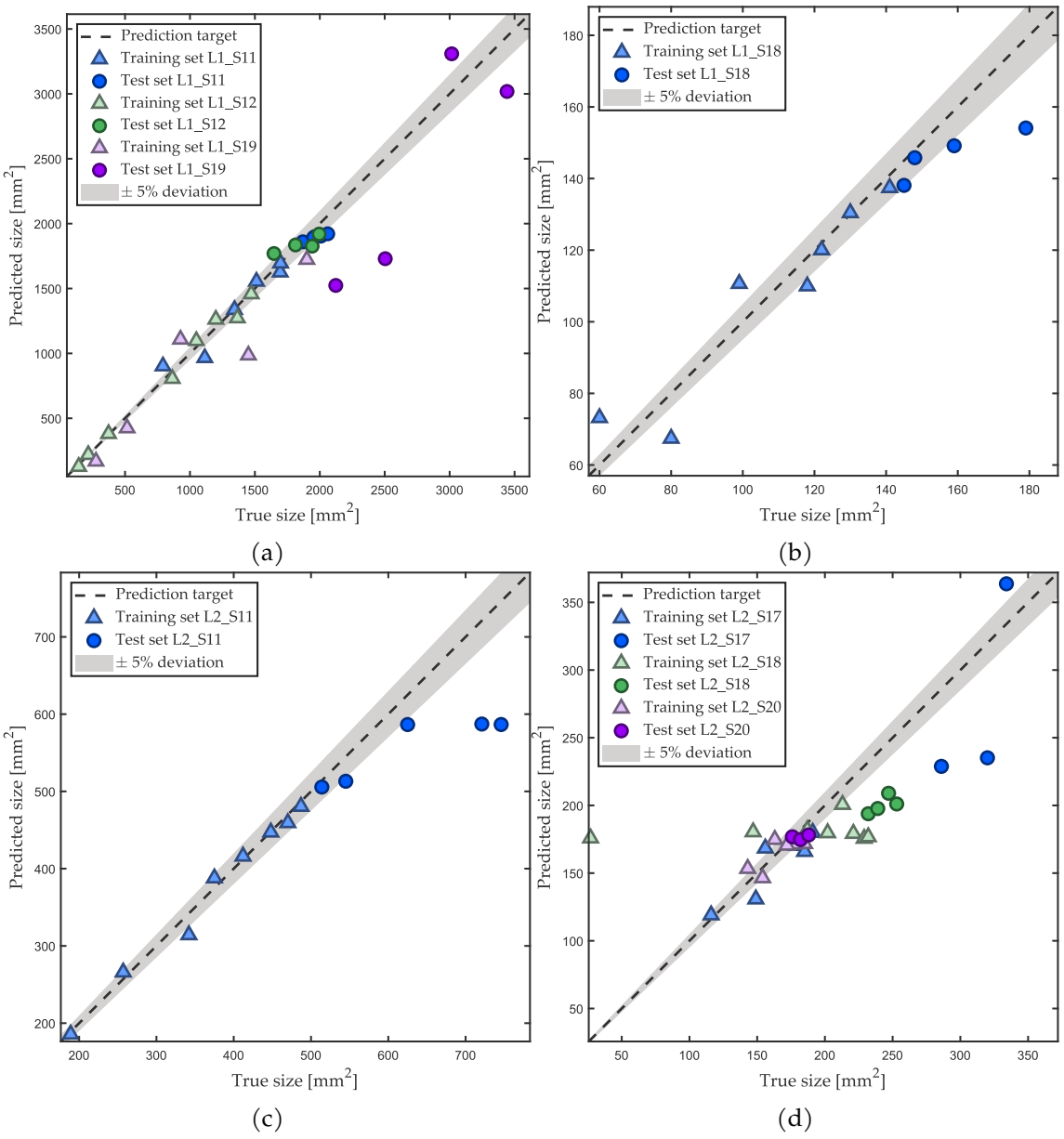

Fig. 5.12 Damage quantification performance using RAPID method on NASA data. L1 coupons (a) and (b), L2 coupons (c) and (d). The diagonal $y = x$ line correspond to a prediction without error.

and 300 kHz. Tab. 5.4 shows that this tendency can be observed for most of L1 samples. This confirms the choice made earlier of a 250 kHz excitation frequency. Moreover, one can see that the optimal frequency is not sensitive to the learning rate. The same kind of graph is drawn for ReMAP laser shocks data with a frequency step of 10 kHz Fig. 5.15b. Here, the best frequencies candidates do not depend on the learning rate as well. Unlike the NASA coupon, low prediction error is reached for different excitation frequency. Besides, Fig. 5.14 shows the sensitivity performance to the excitation frequency on the numerical dataset. In the same manner, at 140 kHz it is clear that the prediction is better than with other excitation frequencies.

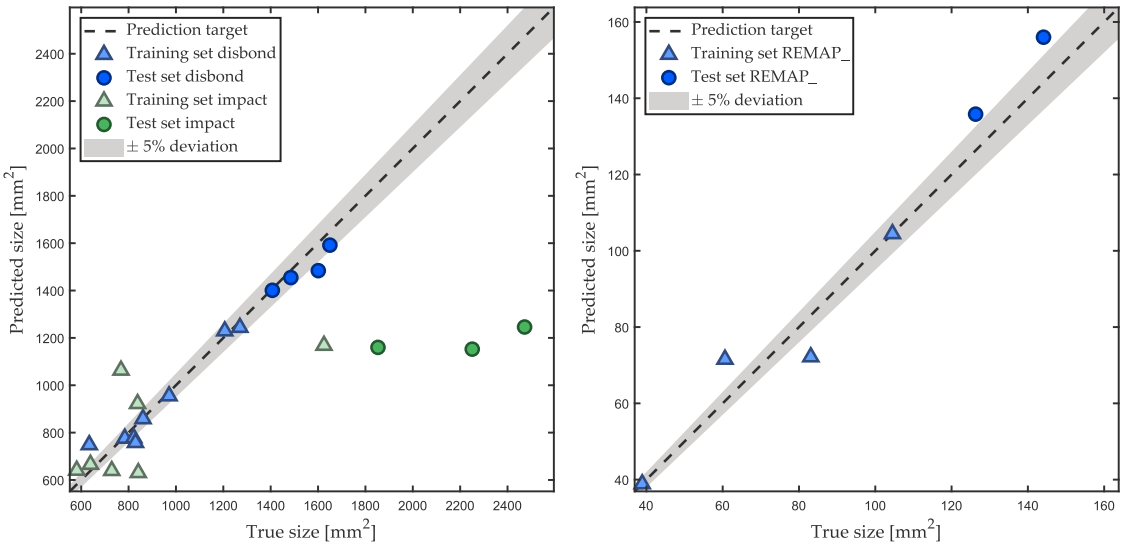

Fig. 5.13 Damage quantification performance using RAPID method on ReMAP L1 fatigue data (a) and ReMAP L1 laser shocks data (b).

Table 5.4 Influence of excitation signal frequency on the prediction error. For each frequency, the prediction error on each NASA L1 samples is computed.

Frequency [kHz]	L1_S11	L1_S12	L1_S18	L1_S19
150	8.29	1.50	9.39	26.83
200	6.80	7.52	25.09	28.82
250	7.80	4.63	6.48	19.04
300	2.90	20.39	14.96	18.29
350	31.13	20.40	27.49	16.52
400	14.66	22.17	20.08	16.16
450	19.92	28.37	24.15	13.13

5.5 Discussion

For both simulated and experimental data, the influence of the selected damage localization method is clear. HDLI computed with ToA or DToA shows no correlation with the true damage size leading to poor performance over training set and testing set. It could be explained by the fact that these methods only deal with time of arrival of the signal which is not influenced by the size of the damage. Another reason of this poor performance could also be the shape of the high DLI area which has a great influence on the quality of the regression. In the ToA and DToA, this region is made up of ellipses or hyperbolas which area does not clearly vary with the damage size as mentioned earlier in this chapter. Besides, DAS and RAPID both exhibit great results on the training set. This performance could be due to the fact that DAS and RAPID take amplitude of the signals into account, which make the HDLI more influenced by the size of the damage. Moreover, high DLI area in the DAS and RAPID methods is regular and HDLI varies in a monotonic

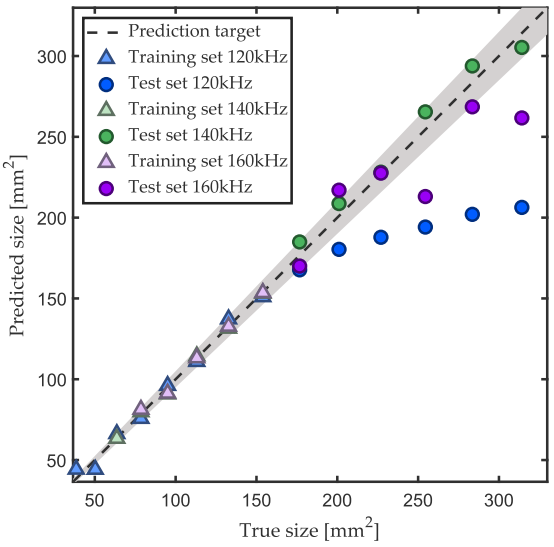

Fig. 5.14 Performance sensitivity to the excitation frequency using RAPID localization method on simulation data.

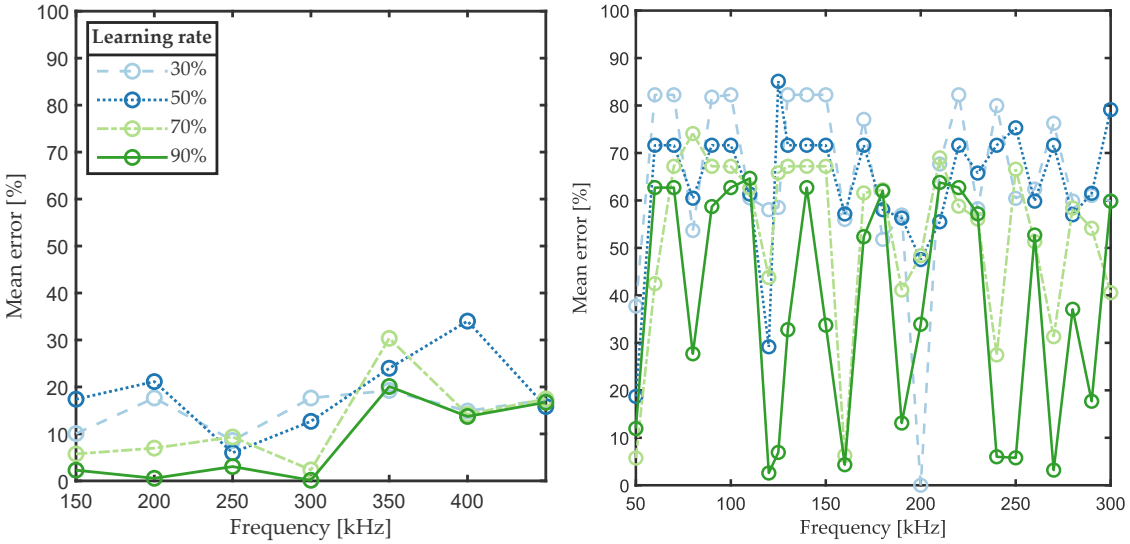

Fig. 5.15 Influence of the excitation signal frequency on the prediction error using RAPID method for the sample L1_S11 (a) and laser shocked ReMAP sample (b).

manner over the size of the damage which lead to a more accurate model. It can also be noticed that with DAS and RAPID methods, the HDLI is close to zero for small damage sizes (usually under 4mm). It would suggest an existence of a lower bound in damage size sensitivity for a given threshold T value. DAS method shows poor results on testing set. Indeed, above a certain level, the HDLI remains steady with the damage size. It means that above this level, each damage size leads to the same HDLI. It is also worth noting that post-processed localization images do not necessarily give good localization results. Indeed, these methods need to be fine tuned for each new study case. A solution to obtain both good localization and quantification outcomes would be to modify the algorithms

to highlight the damaged area and avoid the digital artifacts that RAPID is particularly prone to. It is possible for example to introduce a weight parameter in the computation of the DLI [71].

5.6 Illustration of transfer learning

Table 5.5 Prediction error of the transfer learning approach on NASA L1 coupons.

Frequency [kHz]	L1_S11	L1_S12	L1_S19
L1_S11	-	14.1	31.6
L1_S12	10.6	-	34.9
L1_S19	30.2	25.2	-

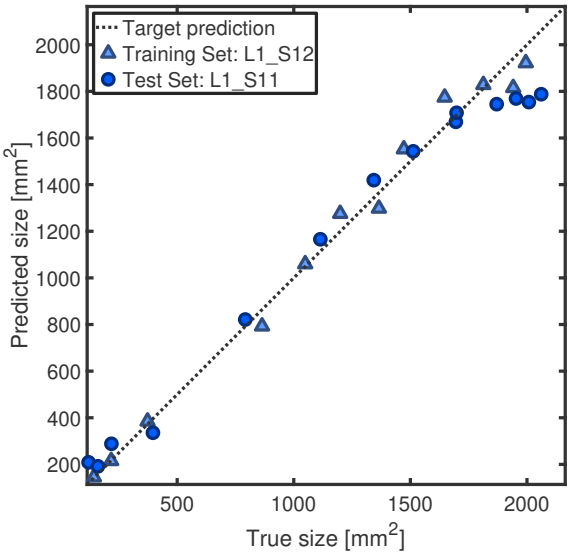

Fig. 5.16 Transfer learning applied to L1 NASA samples. Here the train set is the dataset L1_S12 and the test set is the dataset L1_S11.

So far in this chapter we have only considered the case where the training step was done on the same sample as the prediction. However, even if we have seen earlier that this approach allows to infer a model with good results on the test set, another way to predict the size of an unknown damage is to perform the training step on the full dataset of a coupon to infer a more accurate model. The established model is then applied to a damaged coupon with the same parameters (geometry, material, PZTs positions) to predict the size of the delamination. With this technique, the prediction is not made by extrapolating the model on unknown data but by evaluating the model on HDLI values similar to the training data, limiting the risk of error induced by extrapolating a polynomial model outside the training range. Moreover, this approach is closer to the industrial context since it does not require to have a training dataset for each coupon to be tested. This approach has been tested on the L1_S11, L1_S12 and L1_S19 coupons of the NASA dataset. For each

one of the three coupons, the training step was performed on the specimen in question and a prediction test was performed on each of the remaining coupons, leading to a total of 6 possible combinations where prediction error can be found in Tab. 5.5. An example of these results is shown in Fig. 5.16. For this set of coupons we obtain good results for some combinations, which shows that this method is encouraging. However, in this example this technique is not very robust since in some cases the method performs poorly. These results could be due to the lack of variety in the data. Indeed, for each damage case, only one measurement has been made, which does not allow to know the sensitivity of the acquired signals to noise. Another possible explanation is that the training is carried out on a single coupon. A training of the model on data from different coupons and multiple measurements for each damage case should limit the influence of the variation of the experimental, geometrical and material parameters and thus improve the reliability of this approach. Also, instead of applying the exact same quantification model, we could use transfer learning techniques such as Bayesian updating.

5.7 Conclusion

In this chapter, a damage quantification strategy based on a post-processing step of the results of damage localization method has been presented. Such a method allows for damage size assessment of a delaminated area by post-processing the images produced by damage localization algorithms such as ToA, TDoA, DAS and RAPID. From these images, a region of high localization index can be identified around the estimated damage location. The area of this region can be computed and used as a damage size sensitive feature. A data-driven model representing the mathematical relationship between this feature and the actual size of the damage is then inferred using a polynomial regression. The proposed method exhibits promising results with the RAPID method on numerical simulation data carried out on CFRP plate samples equipped with a stiffener. Moreover, the method is also successfully tested on experimental data of fatigue tests from NASA. We showed an illustration of transfer learning application.

Future work should focus on transfer learning techniques to improve the use of this data-driven method to a population of similar structures. An interesting approach could be to use Bayesian updating methods.

Chapter 6

Analytical model of Lamb waves emission, interaction with damage, and reception using piezoelectric elements

Summary

In this chapter, we analytically model the signal measured by a piezoelectric receiver being crossed by wave in a composite plate, resulting from the reflection of an incident wave by a damage. This incident wave is itself generated by another piezoelectric transducer. In the following, we present the different assumptions that allow us to simplify the problem, in particular the use of the Kane-Mindlin plate theory to model the symmetric fundamental mode of Lamb waves. We compare this approach with other plate theories and establish the equations governing the propagation of waves in the case of a transverse isotropic material. Then, we model analytically each of the subsystems: actuator, scattering by the damage and receiver. For this purpose, we rely on existing works in the literature and unify them to form a comprehensive model. We analyze the different parameters influencing this model and we validate the time signals obtained by comparing them to the results of the finite element method. This model will be used in the next chapter to carry out an identification algorithm to quantify the size and severity of the damage.

Contents

6.1 Introduction

6.1.1 Motivations and objectives

We have seen in the previous chapters that there exist data-based damage size quantification methods. The IPP strategy has shown its performances on numerical and experimental data. However, by using this type of approach, the physical part of the damage size quantification problem is overlooked. Yet the literature is rich in articles focusing on the different physical phenomena involved in the process of guided waves SHM. As mentioned in the first chapter, the propagation of Lamb waves is well known in isotropic materials, transverse isotropic materials and laminate composites which are of particular interest for aerospace applications. Similarly, analytical models of the effect of a piezoelectric actuator on its host structure exist. Crawley and de Luis proposed a model based on Euler-Bernoulli strain distribution and shear lag theory [72]. This approach is detailed for a 1D piezoelectric element glued to the structure through a bonding layer transmitting the shear produced by the actuator to the host structure. Shear lag theory is based on the assumptions that the adhesive only carries shear stress and adherends (transducer and plate) only deform axially [73]. Giurgiutiu extended this work for 2D circular and rectangular transducers [24]. In both cases the dynamics of the actuator is neglected, thus this model is only valid in the low frequency range. If the bonding layer is stiff and thin enough we can consider the piezoelectric wafer as ideally bonded to the structure. In this limit case, the actuator only produces shear stress on its perimeter. This simplified model is called pin-force model and is widely used in the literature. Huang et al. compiled several improvements of the shear lag model in their review [74] and developed a model taking the actuator dynamic into account [75]. This has also been done by Ostiguy et al. for laminate composite plate, who established a semi-analytical model by improving pin-force model with FEM simulation. Nevertheless, since we are interested in fundamental Lamb waves modes only, quasi-static theory –i.e. if we do not consider dynamics effects— will be sufficient in our study. That is why we will adapt the approach proposed by Raghavan and Cesnik [76] to model the displacement field produced by a piezoelectric disk

actuator bonded to a laminate composite plate. Besides, piezoelectric sensors are easier to model [77]. Indeed, the output voltage is proportional to the in-plane normal surface strain. However, it is essential to take into account the electrical boundary conditions applied to the transducer electrodes (closed or open circuit, which corresponds respectively to a connection to a charge or voltage amplifier). Finally, some analytical damage models exist. Grahn proposed an analytical model of scattering for blind hole in an isotropic plate [78]. He compared the results obtained with zeroth-order plate theory for extensional and flexural waves to the ones obtained with 3D elastic equations. The scattered wave is written as a Fourier-Bessel series and the unknown coefficients are determined from continuity conditions at damage interface. The comparison shown that both models have similar results in the low frequency range. Several articles investigated models based on plate theory by using different formulations and damage shapes. Cegla et al. studied the modes conversion for extensional and flexural waves induced by a blind hole in an isotropic plate [79]. Good agreement was found between the proposed model and experimental results. Vemula et al. did the same kind of analysis for a cylindrical inhomogeneity scattering flexural waves [80] and Sedaghati et al. for blind holes on each side of the plate that scatter extensional and flexural waves [81]. Mckeon et al. used a higher order plate theory for extensional waves called Kane-Mindlin theory and described a model for through hole scattering [82]. Wang et al. proceeded to the same analysis for a cylindrical inhomogeneity with a different thickness from the plate for transverse isotropic material [83]. Besides plate theory, several authors used the more accurate 3D elastic theory to describe higher frequency modes. Diligent et al. applied this method to model waves scattered by a through hole [84] and blind hole [85]. In both articles, the results are validated on FEM simulation results. Whereas [78, 84, 85] projected 3D elastic equations on cosine functions to solve the linear system of unknown coefficients, Moreau et al. used exponential functions to model irregular through hole [86] and irregular blind hole [87]. Poddar et al. proposed to use power functions to model step discontinuity in the plate [88], horizontal disbond [89] and crack in a stiffener [90].

However, even if these models are known and used to qualitatively design the PZTs network (size and position of the transducers, choice of excitation signal) [91, 92], there is no comprehensive analytical model of a signal received after the actuator-damage-sensor path in the literature. The advantages of such an analytical model would be multiple: computation of the signal induced by the wave scattered by the damage without reference state, computationally efficient and easy study of the influential parameters. Up to now, this kind of results can only be obtained by finite element simulation which is computationally expensive and requires a careful selection of the simulation parameters (time step, mesh size) to ensure convergence.

This complete analytical model can also be used to determine the size of the damage. For example, if we have the output signals of transducers mounted on a plate in an unknown state of damage. Then we can solve the inverse problem which consists in estimating the size and the severity of the damage by minimizing the difference between the

experimental received signal and the signal obtained with the model. To do this, we could use minimize a cost function with an optimization algorithm by tuning the parameters of interest. The speed of computation of the modeled signal is crucial for this approach because it requires numerous evaluations of the model: the use of a finite element model is therefore unfeasible. There is also an approach based on metamodels. It consists in using machine learning techniques to infer the transfer function between voltage excitation and output signal from FEM or experimental data. It allows for short computation time, but this approach does not enable physical interpretation of the hyperparameters [93, 94].

The objective of this chapter is to build an analytical model that takes as input the material and geometrical parameters of the problem as well as the input signal to return the signal received by the sensor after scattering by a damage. We will first present the assumptions made in the model and study the relevance of the selected plate theory in Sec. 6.1.2. Then in Sec. 6.3, Sec. 6.4 and Sec. 6.5 we will derive the model of each subsystem (wave scattering, actuator, sensor). Finally, we will study the relevant parameters of this model and compare it to finite element simulation data in Sec. 6.6.

6.1.2 Problem statement, assumptions and approximations

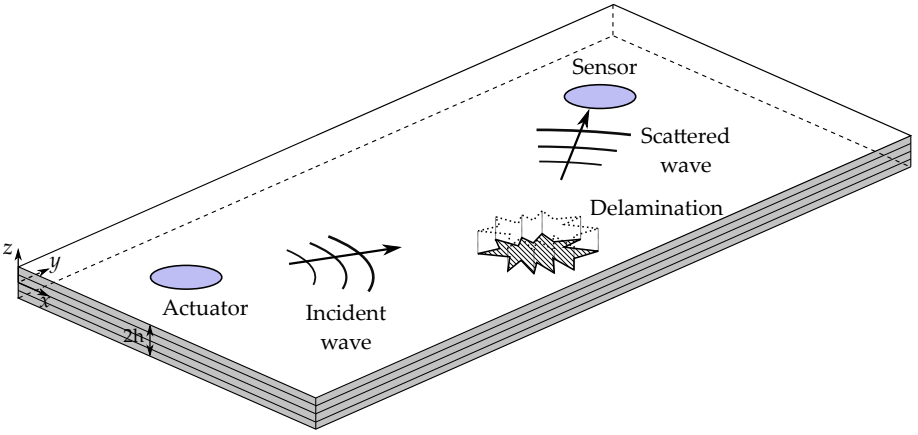

Fig. 6.1 Overall diagram of the scattering problem before simplification.

We consider a plate of laminate composite material on which two piezoelectric transducers are bonded. One of these transducers operates in emission mode while the other operates in reception mode. It is assumed that the presence of a damage in the plate has been detected beforehand. It is also assumed that its position is known thanks to the estimation given by a localization algorithm that has been previously run on the recorded signals. We seek to determine the time signal received by the sensor after scattering on the damage of the wave generated by the emitter. The figure Fig. 6.1 illustrates the global configuration of the problem. In order to model the physical phenomena involved, we make several assumptions and approximations that we will detail in this subsection.

As stated in the first chapter, piezoelectric transducers apply stress to the host structure when subjected to an electrical signal. This causes the propagation of Lamb waves in the

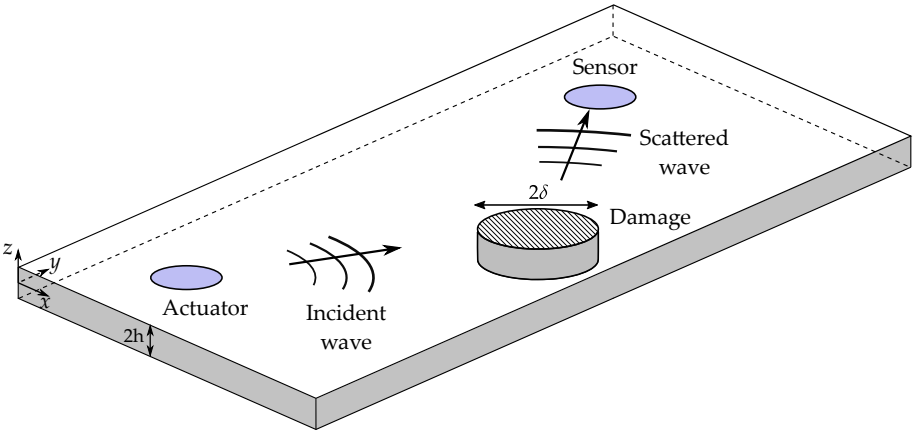

Fig. 6.2 Overall diagram of the scattering problem after simplification.

plate. At relatively low frequencies (i.e. for excitation signals of a few hundred kilohertz) and for thin plates, there are only two fundamental modes of propagation measurable by piezoelectric elements: the symmetric mode S_0 and the antisymmetric mode A_0. In the rest of the study, we will only be interested in the Lamb waves mode S_0. Indeed, it is the fastest propagating mode, with almost no dispersion which facilitates its identification. Besides, unlike A_0 mode it shows low attenuation caused by material damping in composite material [20]. On the contrary, the A_0 mode can be mixed with wave reflections on the edges of the plate and is much more attenuated, which makes its exploitation more complex.

In this chapter, we will only model the wave that interact with the damage. Experimentally, this signal is obtained by taking the difference between a reference measurement where the plate is in a healthy state and another measurement made in a state where the plate is damaged.

We make the assumption that the plate is infinite. Indeed, since we will work only with a wave packet reflected by the damage, it reaches the receiver before the eventual wave packets reflected by the damage and by the edges of the plate. We will also approximate the laminate composite material of the plate by a transverse isotropic material whose isotropy plane is the plane of the plate. Indeed, we will be interested in structures whose stacks are balanced (called quasi-isotropic material) to make the plate transverse isotropic as a whole.

We also assume that the piezoelectric elements are ideally bonded to the structure, i.e. with an infinitely thin and infinitely rigid adhesive layer. Moreover, it is assumed that these piezoelectric elements do not interfere with Lamb waves propagation.

Finally, we model the damage by a circular cylinder over the whole thickness of the plate and whose material properties are different from the rest of the structure. This inhomogeneity is therefore characterized by two parameters (in addition to its position): its

radius δ and its severity ξ defined as

$$\xi = 1 - \frac{E^*}{E} \tag{6.1}$$

where E^* and E are inhomogeneity's Young's modulus and plate's Young modulus, respectively. Therefore, a severity of 0 corresponds to the healthy case while a severity of 1 corresponds to a hole going through the plate.

This damage model is very common in the literature and corresponds to the loss of local stiffness in a composite plate subjected to an impact [67]. However, this kind of formulation does not take into account all physical interactions between Lamb waves and delamination. Indeed, delamination can induce modes conversion, meaning that a pure S_0 mode incident wave can be scattered into both S_0 and A_0, and sometimes higher orders modes [95–97]. Moreover, non-linear interactions can occur between the incident wave and the damage. It means that the scattered wave will contain harmonics components [98]. In this chapter, we do not consider these phenomena and only model a linear behavior with no mode conversion. Besides, the damage shape chosen is convenient since it allows for an equivalent severity even for delamination, which enable to wrap all kinds of severity into a single parameter.

Fig. 6.2 shows the studied system applying all these assumptions which are also summarized in Tab. 6.1.

Table 6.1 Summary of assumptions made to simplify the problem.

Subsystem	Assumptions
Plate	- Single layer - Transverse isotropic material
Waves propagation	- First extensional mode only - Plate theory approximation
Damage	Cylindrical through-tickness inhomogeneity with local reduction of stiffness
Piezoelectric transducers	- Ideal bonding - No influence on wave propagation

6.2 Plate theories for extensional and compressional motion

In the rest of this chapter, we will approximate Lamb waves according to the plate theory. A plate is a deformable solid whose one dimension is very small compared to the two others. Numerous theories exist depending on considered motion and kinematics assumptions. In this section, we seek to determine the most suitable plate theory to approximate S_0 Lamb wave mode. Therefore, we describe the most known of them involving extensional and compressional motion.

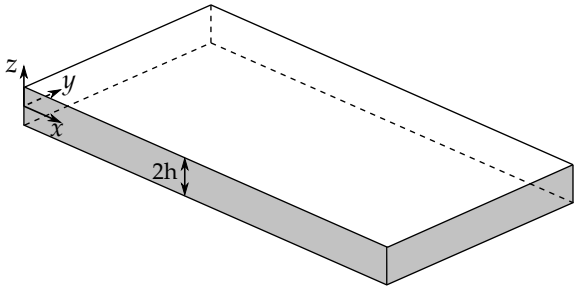

Fig. 6.3 Cross-sectional view of an infinite plate.

We consider the system described in Fig. 6.3. The plate under study is infinite and of thickness $2h$ with mid-surface located at the $z = 0$ coordinate. The structure is considered free and no load is applied. For the sake of simplicity, we assume that the plate is made of isotropic. We also assume a homogeneous material and that we stay in the linear elastic regime along with small strain. We want to model the extension-compression motion in a thin-walled structure with a propagation direction lying in the Oxy plate.

6.2.1 Plane stress

The lowest order theory for extensional and compressional wave is the plane stress assumption [99]. This hypothesis can be applied to thin plates, plates subject to high frequency excitation when the wavelength approaches the thickness, or both. The considered plate is acted upon only by load forces in the Oxy plane. The stresses σ_{zz}, σ_{zx} and σ_{zy} are zero on both sides of the plate and by continuity, they can only take very small values inside the plate compared to σ_{xx}, σ_{yy} and σ_{xy}. It is not a significant error to say that they are zero on any interior plane parallel to the faces. For the same reason, σ_{xx}, σ_{yy} and σ_{xy} do not depend on z, i.e. they remain constant over the entire thickness of the plate. Thus, the stress tensor has only three non-zero components

$$\boldsymbol{\sigma} = \begin{pmatrix} \sigma_{xx} & \sigma_{xy} & \sigma_{xz} \\ \sigma_{yx} & \sigma_{yy} & \sigma_{yz} \\ \sigma_{zx} & \sigma_{zy} & \sigma_{zz} \end{pmatrix} = \begin{pmatrix} \sigma_{xx} & \sigma_{xy} & 0 \\ \sigma_{yx} & \sigma_{yy} & 0 \\ 0 & 0 & 0 \end{pmatrix}. \tag{6.2}$$

From Hooke's law we deduce the strain tensor

$$\boldsymbol{\varepsilon} = \begin{pmatrix} \varepsilon_{xx} & \varepsilon_{xy} & 0 \\ \varepsilon_{yx} & \varepsilon_{yy} & 0 \\ 0 & 0 & \varepsilon_{zz} \end{pmatrix} \tag{6.3}$$

with

$$\varepsilon_{zz} = -\frac{\lambda}{\lambda + 2\mu}(\varepsilon_{xx} + \varepsilon_{yy}) \tag{6.4}$$

where λ and μ are the Lamé parameters. We also assume that the plate is thin enough such that there is no variation of displacement with respect to z. Thus, the displacement

components can be written

$$\begin{aligned} u_x(x,y,z,t) &= v_x(x,y,t) \\ u_y(x,y,z,t) &= v_y(x,y,t). \end{aligned} \tag{6.5}$$

We now want to write elastodynamic equations of the problem. We start with the equation for the x and y coordinates only. In the following, $\boldsymbol{v}$ denote the 2D displacement vector: $\boldsymbol{v} = v_x\boldsymbol{e_x} + v_y\boldsymbol{e_y}$ where $\boldsymbol{e_x}$ and $\boldsymbol{e_y}$ are unit vectors in direction x and y respectively. The Cauchy's equation of motion in case of zero body force

$$\boldsymbol{\nabla}\cdot\boldsymbol{\sigma} = \rho\frac{\partial^2\boldsymbol{v}}{\partial t^2} \tag{6.6}$$

and Hooke's law for an isotropic, elastic material and homogeneous material

$$\boldsymbol{\sigma} = \lambda\mathrm{tr}(\boldsymbol{\varepsilon})\boldsymbol{I}_2 + 2\mu\boldsymbol{\varepsilon}_2 \tag{6.7}$$

where $\boldsymbol{I}_2$ is the 2×2 identity matrix, $\mathrm{tr}(\boldsymbol{\varepsilon})$ is the trace of $\boldsymbol{\varepsilon}$ matrix and $\boldsymbol{\varepsilon}_2$ denotes the $\boldsymbol{\varepsilon}$ submatrix obtained by removing z row and column. Since we limit our study to small deformation, the strain tensor is given as

$$\boldsymbol{\varepsilon} = \frac{1}{2}\left(\boldsymbol{\nabla u} + (\boldsymbol{\nabla u})^{\mathrm{T}}\right) \tag{6.8}$$

where $\boldsymbol{\nabla u}$ denotes the gradient of the displacement field, see in App. D. Combining Eq. 6.6 and Eq. 6.7, we get

$$\lambda\boldsymbol{\nabla}\cdot(\mathrm{tr}(\boldsymbol{\varepsilon})\boldsymbol{I}_2) + 2\mu\boldsymbol{\nabla}\cdot\boldsymbol{\varepsilon}_2 = \rho\frac{\partial^2\boldsymbol{v}}{\partial t^2} \tag{6.9}$$

where $\boldsymbol{\nabla}\cdot$ is the divergence of a vector field, see in App. D. The right side of this equation can be written in terms of displacement. Using Eq. 6.8 and following the Einstein summation convention, the first member becomes

$$\mathrm{tr}(\boldsymbol{\varepsilon}) = \varepsilon_{xx} + \varepsilon_{yy} - \frac{\lambda}{\lambda+2\mu}(\varepsilon_{xx}+\varepsilon_{yy}) = \frac{2\mu}{\lambda+2\mu}(\varepsilon_{xx}+\varepsilon_{yy}) \tag{6.10}$$

$$\begin{aligned} (\boldsymbol{\nabla}\cdot(\mathrm{tr}(\boldsymbol{\varepsilon})\boldsymbol{I}_2)_i = \frac{2\mu}{\lambda+2\mu}\frac{\partial}{\partial x_j}\left(\varepsilon_{kk}\delta_{ij}\right) = \frac{2\mu}{\lambda+2\mu}\frac{\partial}{\partial x_j}\left(\frac{\partial v_k}{\partial x_k}\delta_{ij}\right) &= \frac{2\mu}{\lambda+2\mu}\frac{\partial}{\partial x_i}\left(\frac{\partial v_k}{\partial x_k}\right) \\ &= \frac{2\mu}{\lambda+2\mu}\frac{\partial}{\partial x_i}(\boldsymbol{\nabla}\cdot\boldsymbol{v}) \\ &= \frac{2\mu}{\lambda+2\mu}\boldsymbol{\nabla}(\boldsymbol{\nabla}\cdot\boldsymbol{v})_i \end{aligned} \tag{6.11}$$

for $i,j,k \in \{1,2\}$. x_i and x_j denote the Cartesian space coordinates x, y or z. The other term can also be rewritten using Eq. 6.8

$$\begin{aligned}
(\boldsymbol{\nabla}\cdot\boldsymbol{\varepsilon})_i &= \frac{\partial \varepsilon_{ij}}{\partial x_j} \\
&= \frac{1}{2}\frac{\partial}{\partial x_j}\left(\frac{\partial v_i}{\partial x_j} + \frac{\partial v_j}{\partial x_i}\right) \\
&= \frac{1}{2}\frac{\partial^2 v_i}{\partial x_j^2} + \frac{1}{2}\frac{\partial}{\partial x_i}\left(\frac{\partial v_j}{\partial x_j}\right) \\
&= \frac{1}{2}(\boldsymbol{\Delta v})_i + \frac{1}{2}\frac{\partial}{\partial x_i}(\boldsymbol{\nabla}\cdot\boldsymbol{v}) \\
&= \frac{1}{2}(\boldsymbol{\Delta v})_i + \frac{1}{2}\boldsymbol{\nabla}(\boldsymbol{\nabla}\cdot\boldsymbol{v})_i
\end{aligned} \tag{6.12}$$

for $i,j \in \{1,2\}$. $\boldsymbol{\Delta v}$ denotes the Laplacian of $\boldsymbol{v}$, see in App. D. Eq. 6.9 becomes

$$\rho\frac{\partial^2 \boldsymbol{v}}{\partial t^2} = \mu\frac{3\lambda+2\mu}{\lambda+2\mu}\boldsymbol{\nabla}(\boldsymbol{\nabla}\cdot\boldsymbol{v}) + \mu\boldsymbol{\Delta v} \tag{6.13}$$

or

$$\begin{aligned}
\rho\frac{\partial^2 u_x}{\partial t^2} &= 4\mu\frac{\lambda+\mu}{\lambda+2\mu}\frac{\partial^2 u_x}{\partial x^2} + \mu\frac{\partial^2 u_x}{\partial y^2} + \mu\frac{3\lambda+2\mu}{\lambda+2\mu}\frac{\partial^2 u_y}{\partial x\partial y} \\
\rho\frac{\partial^2 u_y}{\partial t^2} &= 4\mu\frac{\lambda+\mu}{\lambda+2\mu}\frac{\partial^2 u_y}{\partial y^2} + \mu\frac{\partial^2 u_y}{\partial x^2} + \mu\frac{3\lambda+2\mu}{\lambda+2\mu}\frac{\partial^2 u_x}{\partial x\partial y}.
\end{aligned} \tag{6.14}$$

We can also use replace the Lamé's parameters by their respective expression

$$\begin{aligned}
\rho\frac{\partial^2 u_x}{\partial t^2} &= \frac{E}{1-\nu^2}\frac{\partial^2 u_x}{\partial x^2} + \frac{E}{2(1+\nu)}\frac{\partial^2 u_x}{\partial y^2} + \frac{E}{2(1-\nu)}\frac{\partial^2 u_y}{\partial x\partial y} \\
\rho\frac{\partial^2 u_y}{\partial t^2} &= \frac{E}{1-\nu^2}\frac{\partial^2 u_y}{\partial y^2} + \frac{E}{2(1+\nu)}\frac{\partial^2 u_y}{\partial x^2} + \frac{E}{2(1-\nu)}\frac{\partial^2 u_x}{\partial x\partial y}
\end{aligned} \tag{6.15}$$

where E is the Young's modulus and ν the Poisson's ratio. We now want to obtain the dispersion relationship. We look at plane wave propagating in the wavenumber direction $\boldsymbol{k} = k_x\boldsymbol{e_x} + k_y\boldsymbol{e_y}$. The displacement field can then be written

$$\boldsymbol{u} = \begin{pmatrix} U_x e^{i(k_x x + k_y y - \omega t)} \\ U_y e^{i(k_x x + k_y y - \omega t)} \end{pmatrix} = \boldsymbol{U} e^{i(k_x x + k_y y - \omega t)} \tag{6.16}$$

where U_x and U_y are constants. The equations Eq. 6.15 lead to

$$\begin{aligned}
\rho\omega^2 U_x &= \frac{Ek_x^2}{1-\nu^2}U_x + \frac{Ek_y^2}{2(1+\nu)}U_x + \frac{Ek_xk_y}{2(1-\nu)}U_y \\
\rho\omega^2 U_y &= \frac{Ek_y^2}{1-\nu^2}U_y + \frac{Ek_x^2}{2(1+\nu)}U_y + \frac{Ek_xk_y}{2(1-\nu)}U_x.
\end{aligned} \tag{6.17}$$

These last equations can be written under matrix form

$$\begin{pmatrix} \frac{Ek_x^2}{1-\nu^2} + \frac{Ek_y^2}{2(1+\nu)} & \frac{Ek_xk_y}{2(1-\nu)} \\ \frac{Ek_xk_y}{2(1-\nu)} & \frac{Ek_y^2}{1-\nu^2} + \frac{Ek_x^2}{2(1+\nu)} \end{pmatrix} \begin{pmatrix} U_x \\ U_y \end{pmatrix} = \rho\omega^2 \begin{pmatrix} U_x \\ U_y \end{pmatrix}. \tag{6.18}$$

This is a classical eigenvalues' problem where the eigenvalues are $\rho\omega^2$. We find the two eigenvalues of the matrix with their associated eigenvectors

$$\begin{aligned} \omega_1^2 &= \frac{E}{\rho}\frac{(k_x^2+k_y^2)}{2(1+\nu)}; & \boldsymbol{U}_1 &= \begin{pmatrix} k_x \\ k_y \end{pmatrix} \\ \omega_2^2 &= \frac{E}{\rho}\frac{(k_x^2+k_y^2)}{1-\nu^2}; & \boldsymbol{U}_2 &= \begin{pmatrix} -k_x \\ k_y \end{pmatrix}. \end{aligned} \tag{6.19}$$

The first mode is the axial wave whereas the second mode is the shear wave. If we define $k^2 = k_x^2 + k_y^2$, the ratios ω_1/k and ω_2/k are the respective wave velocity of each mode. Since these velocities are constants, it means that both modes are not dispersive.

6.2.2 Kane-Mindlin theory

In 1956, Kane and Mindlin introduce a theory that takes into account the coupling between extensional and thickness modes of motion [100, 101]. That makes this theory valid for a wider frequency range and for thicker plates than plane stress theory. Kane and Mindlin made the assumption that the displacement field can be accurately approximated by

$$\begin{aligned} u_x(x,y,z,t) &= v_x(x,y,t) \\ u_y(x,y,z,t) &= v_y(x,y,t) \\ u_z(x,y,z,t) &= \frac{z}{h}v_z(x,y,t). \end{aligned} \tag{6.20}$$

We can notice that the main difference with plane-stress theory Eq. 6.5 is that the displacement component along z varies linearly along the thickness. To derive the equations of motion, we will use Euler-Lagrange equations. Since there is no load applied to the structure, we only need to express the internal energy T and the elastic potential energy V.

$$\begin{aligned} T &= \iiint \mathrm{d}T\,\mathrm{d}x\,\mathrm{d}y\,\mathrm{d}z \\ T &= \frac{1}{2}\iint_S \int_{-h}^{h} \left[\rho\left(\frac{\partial u_x}{\partial t}\right)^2 + \rho\left(\frac{\partial u_y}{\partial t}\right)^2 + \rho\left(\frac{\partial u_z}{\partial t}\right)^2\right] \mathrm{d}x\,\mathrm{d}y\,\mathrm{d}z \\ T &= \frac{1}{2}\iint_S \left[2h\rho\left(\frac{\partial v_x}{\partial t}\right)^2 + 2h\rho\left(\frac{\partial v_y}{\partial t}\right)^2 + \frac{2h\rho}{3}\left(\frac{\partial v_z}{\partial t}\right)^2\right] \mathrm{d}x\,\mathrm{d}y \end{aligned} \tag{6.21}$$

where S is the surface of the plate. From Eq. 6.20, we derive the terms of strain tensor

$$\varepsilon_{xx} = \frac{\partial v_x}{\partial x}; \qquad \varepsilon_{yy} = \frac{\partial v_y}{\partial y}; \qquad \varepsilon_{zz} = \frac{v_z}{h} \tag{6.22}$$

$$\varepsilon_{xy} = \frac{1}{2}\left(\frac{\partial v_x}{\partial y} + \frac{\partial v_y}{\partial x}\right); \quad \varepsilon_{xz} = \frac{z}{2h}\frac{\partial v_z}{\partial x}; \quad \varepsilon_{yz} = \frac{z}{2h}\frac{\partial v_z}{\partial y}. \tag{6.23}$$

The general expression of elastic potential energy is

$$V = \iiint \mathrm{d}V \,\mathrm{d}x\,\mathrm{d}y\,\mathrm{d}z = \frac{1}{2}\iint_S \int_{-h}^{h} (\varepsilon : C : \varepsilon)\,\mathrm{d}x\,\mathrm{d}y\,\mathrm{d}z. \tag{6.24}$$

Since we consider an isotropic material the expression becomes

$$\begin{aligned}
V =& \frac{1}{2}\iint_S \int_{-h}^{h} \left(\varepsilon_j C_{ij} \varepsilon_i\right) \mathrm{d}x\,\mathrm{d}y\,\mathrm{d}z \\
V =& \frac{1}{2}\iint_S \int_{-h}^{h} (\lambda + 2\mu)\left[\varepsilon_{xx}^2 + \varepsilon_{yy}^2 + \varepsilon_{zz}^2\right] \mathrm{d}x\,\mathrm{d}y\,\mathrm{d}z \\
&+ \frac{1}{2}\iint_S \int_{-h}^{h} \lambda\left[2\varepsilon_{xx}\varepsilon_{yy} + 2\varepsilon_{xx}\varepsilon_{zz} + 2\varepsilon_{yy}\varepsilon_{zz}\right] \mathrm{d}x\,\mathrm{d}y\,\mathrm{d}z \\
&+ \frac{1}{2}\iint_S \int_{-h}^{h} 4\mu\left[\varepsilon_{xy}^2 + \varepsilon_{xz}^2 + \varepsilon_{yz}^2\right] \mathrm{d}x\,\mathrm{d}y\,\mathrm{d}z \\
V =& \frac{1}{2}\iint_S (\lambda + 2\mu)\left[2h\left(\frac{\partial v_x}{\partial x}\right)^2 + 2h\left(\frac{\partial v_y}{\partial y}\right)^2 + \frac{2\kappa^2 v_z^2}{h}\right] \mathrm{d}x\,\mathrm{d}y \\
&+ \frac{1}{2}\iint_S \lambda\left[2h\frac{\partial v_x}{\partial x}\frac{\partial v_y}{\partial y} + 4\kappa v_z\frac{\partial v_x}{\partial x} + 4\kappa v_z\frac{\partial v_y}{\partial y}\right] \mathrm{d}x\,\mathrm{d}y \\
&+ \frac{1}{2}\iint_S \mu\left[2h\left(\frac{\partial v_x}{\partial y}\right)^2 + 2h\left(\frac{\partial v_y}{\partial x}\right)^2 + 4h\frac{\partial v_x}{\partial y}\frac{\partial v_y}{\partial x} + \frac{2h}{3}\left(\frac{\partial v_z}{\partial x}\right)^2 + \frac{2h}{3}\left(\frac{\partial v_z}{\partial y}\right)^2\right] \mathrm{d}x\,\mathrm{d}y.
\end{aligned} \tag{6.25}$$

κ is a constant whose introduction will be explained in the following. To derive the scalar equations of motion, we use the Euler-Lagrange equations [99] defined for each component $i = \{1, 2, 3\}$ as

$$\frac{\partial}{\partial t}\left(\frac{\partial \mathcal{L}}{\partial \dot{v}_i}\right) + \sum_{j=1}^{3}\frac{\partial}{\partial x_j}\left(\frac{\partial \mathcal{L}}{\partial v_{i,j}}\right) - \frac{\partial \mathcal{L}}{\partial v_i} = 0 \tag{6.26}$$

where the Lagrangian is defined as $\mathcal{L} = T - V$. v_i, $\dot{v}_i$ and $v_{i,j}$ are respectively the displacement along coordinate i, the derivative of this displacement with respect to time and the

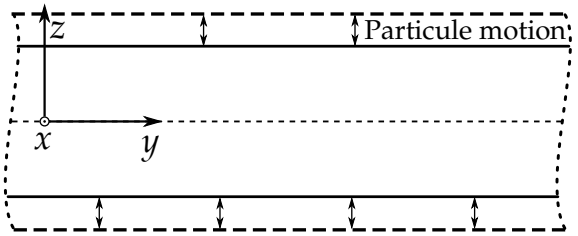

Fig. 6.4 Purely extensional thickness mode of the plate.

derivative of this displacement with respect to space variable x_j. Applying this equation to the kinetic energy density and the potential energy density we calculated earlier, and since integrals along thickness do not depend on integration limits, we get

$$\begin{aligned}
&(\lambda+2\mu)\frac{\partial^2 v_x}{\partial x^2}+\lambda\frac{\partial^2 v_y}{\partial x\partial y}+\frac{\lambda\kappa}{h}\frac{\partial v_z}{\partial x}+\mu\frac{\partial^2 v_y}{\partial x\partial y}+\mu\frac{\partial^2 v_x}{\partial y^2}=\rho\frac{\partial^2 v_x}{\partial t^2}\\
&(\lambda+2\mu)\frac{\partial^2 v_y}{\partial y^2}+\lambda\frac{\partial^2 v_x}{\partial x\partial y}+\frac{\lambda\kappa}{h}\frac{\partial v_z}{\partial y}+\mu\frac{\partial^2 v_x}{\partial x\partial y}+\mu\frac{\partial^2 v_y}{\partial x^2}=\rho\frac{\partial^2 v_y}{\partial t^2}\\
&\mu\frac{\partial^2 v_z}{\partial x^2}+\mu\frac{\partial^2 v_z}{\partial y^2}-\frac{3(\lambda+2\mu)\kappa^2}{h^2}v_z-\frac{3\lambda\kappa}{h}\frac{\partial v_x}{\partial x}-\frac{3\lambda\kappa}{h}\frac{\partial v_y}{\partial y}=\rho\frac{\partial^2 v_z}{\partial t^2}.
\end{aligned}\tag{6.27}$$

We can notice that unlike plane stress assumption, Kane-Mindlin theory introduces a coupling between v_z and in-plane displacements v_x and v_y. Kane and Mindlin introduced a coefficient κ in the expression of the elastic energy [100] in order to correct the error made by assuming that the component u_z varies linearly with z. Indeed, if this approximation is valid at low frequency, it is no longer the case when approaching the first pure thickness mode shown in Fig. 6.4. This correction coefficient is therefore chosen to make the angular frequency of the first pure thickness mode coincide between the Kane-Mindlin theory and the 3D theory. This angular frequency can be displayed by taking $v_x = v_y = 0$ and $v_z = e^{-i\omega_t t}$

$$\omega_{\mathrm{t}}^2=\frac{3\kappa^2}{h^2}\frac{(\lambda+2\mu)}{\rho}\tag{6.28}$$

whereas the same angular frequency obtained from the three-dimensional equations is [102]

$$\omega_{\mathrm{3D}}^2=\frac{\pi^2}{4h^2}\frac{(\lambda+2\mu)}{\rho}.\tag{6.29}$$

Equating ω_{t} and ω_{3D} we find

$$\kappa^2=\frac{\pi^2}{12}.\tag{6.30}$$

As in the previous subsection, we consider a plane wave propagating along the wavenumber $\boldsymbol{k}=k_x\boldsymbol{e_x}+k_y\boldsymbol{e_y}$

$$\boldsymbol{V}=\begin{pmatrix}V_x e^{i(k_x x+k_y y-\omega t)}\\ V_y e^{i(k_x x+k_y y-\omega t)}\\ V_z e^{i(k_x x+k_y y-\omega t)}\end{pmatrix}\tag{6.31}$$

where V_x, V_y and V_z are constants. The equations Eq. 6.27 become

$$\begin{pmatrix} (\lambda+2\mu)k_x^2+\mu k_y^2 & (\lambda+\mu)k_xk_y & -\frac{i\lambda\kappa}{h}k_x \\ (\lambda+\mu)k_xk_y & (\lambda+2\mu)k_y^2+\mu k_x^2 & -\frac{i\lambda\kappa}{h}k_y \\ \frac{3i\lambda\kappa}{h}k_x & \frac{3i\lambda\kappa}{h}k_y & \mu(k_x^2+k_y^2)+\frac{3(\lambda+2\mu)\kappa^2}{h^2} \end{pmatrix}\begin{pmatrix} V_x \\ V_y \\ V_z \end{pmatrix} = \rho\omega^2\begin{pmatrix} V_x \\ V_y \\ V_z \end{pmatrix} \tag{6.32}$$

which can be rearranged as

$$\begin{pmatrix} (\lambda+2\mu)k_x^2+\mu k_y^2-\rho\omega^2 & (\lambda+\mu)k_xk_y & -\frac{i\lambda\kappa}{h}k_x \\ (\lambda+\mu)k_xk_y & (\lambda+2\mu)k_y^2+\mu k_x^2-\rho\omega^2 & -\frac{i\lambda\kappa}{h}k_y \\ \frac{3i\lambda\kappa}{h}k_x & \frac{3i\lambda\kappa}{h}k_y & \mu(k_x^2+k_y^2)+\frac{3(\lambda+2\mu)\kappa^2}{h^2}-\rho\omega^2 \end{pmatrix}\begin{pmatrix} V_x \\ V_y \\ V_z \end{pmatrix} = 0. \tag{6.33}$$

In order to have non-trivial solutions, the determinant of this matrix must equal zero.

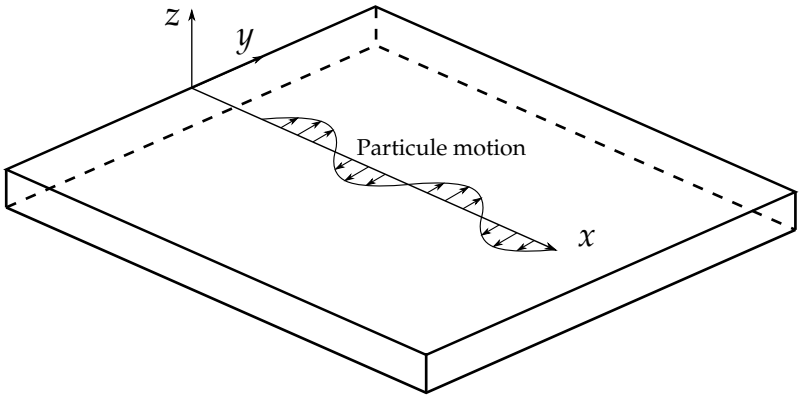

Fig. 6.5 Particle motion of SH wave propagating in x direction.

This gives us two dispersion relationships. The first one is

$$(k_x^2+k_y^2) = k_3^2 = \frac{\rho}{\mu}\omega^2 \tag{6.34}$$

and corresponds to shear wave polarized so that particle motion and direction of propagation are contained in the horizontal plane Oxy as illustrated in Fig. 6.5. Indeed the associated displacement vector is

$$\boldsymbol{V} = \begin{pmatrix} k_x \\ -k_y \\ 0 \end{pmatrix}. \tag{6.35}$$

The second relationship is

$$(k_x^2+k_y^2)^2 - 2B(k_x^2+k_y^2) + C = k^4 - 2Bk^2 + C = 0 \tag{6.36}$$

with

$$\begin{aligned} B &= \frac{\rho\omega^2}{2(\lambda+2\mu)} + \frac{\rho\left(\omega^2-\omega_t^2\right)}{2\mu} + \frac{3\kappa^2\lambda^2}{2h^2\mu(\lambda+2\mu)} \\ C &= \frac{\rho^2\omega^2\left(\omega^2-\omega_t^2\right)}{\mu(\lambda+2\mu)} \end{aligned} \tag{6.37}$$

where ω_t is the angular frequency of the first pure thickness mode, see Eq. 6.28. This equation is quadratic in k^2 and consequently has two solutions

$$\begin{aligned} k_1^2 &= B + \sqrt{B^2 - C} \\ k_2^2 &= B - \sqrt{B^2 - C}. \end{aligned} \tag{6.38}$$

These solutions correspond to axial wave modes: the first one approximates S_0 Lamb waves mode whereas the second one approximates S_1 Lamb waves mode. k_1 is real for all frequencies whereas k_2 is real only above the cut-off frequency ω_t. Under this cut-off frequency, k_2 is purely imaginary which means that the second axial mode is evanescent in this frequency range.

Higher order theories

It is possible to use theories that approximate the displacement field in an even finer way. For example, in 1958 Mindlin and Medick proposed to expand the displacement components in the form of Legendre polynomials in z/h [103]. In this formulation, there are five displacements functions to determine which greatly complicate the exploitation of this theory. Also, with Mindlin and Medick assumption, four adjustments factors —similar to κ in Kane-Mindlin theory— must be selected. Since this theory is far more complex than Kane-Mindlin and because Kane-Mindlin is accurate enough for our application, we will not use this theory here.

6.2.3 Dispersion curves

Table 6.2 Dispersion curves material and geometrical parameters.

Parameter	Unit	Value
Young's modulus	GPa	72
Poisson's ratio	-	0.3
Density	$kg.m^{-3}$	2700
Total thickness	mm	1

To compare the relevance of the described plate theories, we compare their associated dispersion curves with Lamb waves results. Lamb waves dispersion curves were obtained by solving the Rayleigh-Lamb equation for isotropic material using the bisection method.

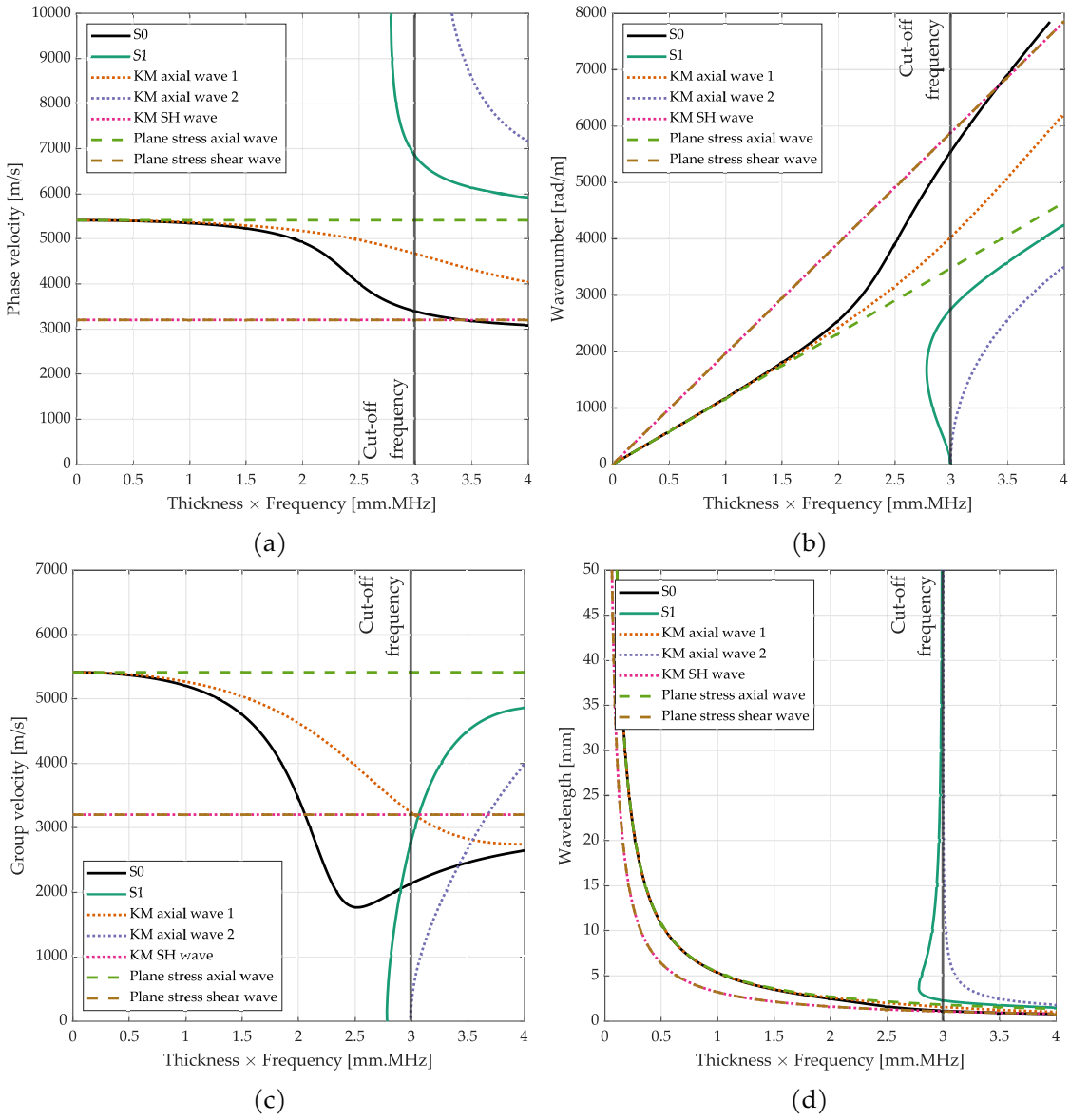

Fig. 6.6 Dispersion curves for phase velocity (a), wavenumber (b), group velocity (c) and wavelength (d). The solid lines S_0 and S_1 correspond to Lamb waves modes. KM stands for Kane-Mindlin theory.

The MATLAB toolbox that performed this task was created by the DYSCO team in Processes and Engineering in Mechanics and Materials laboratory (PIMM) [20, 21]. We plot the dispersion curves of several quantities: phase velocity, wavenumber, group velocity and wavelength Fig. 6.6. These curves are computed in terms of thickness by frequency product to make the results independent of the plate thickness. The considered plate is made of aluminum which parameters are given in Tab. 6.2. We notice that both studied plate theories give good approximation of Lamb waves behavior for the considered quantities at low frequency range. However, if plate thickness or excitation frequency increases (or both), plate stress formulation no longer follows the Lamb waves reference. Indeed, in this theory the wave dispersion is not taken into account unlike Kane-Mindlin theory.

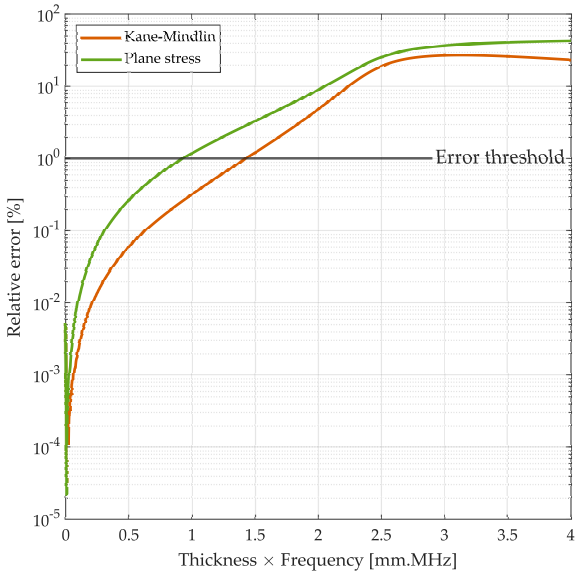

Fig. 6.7 Relative error between plate theory first axial mode wavenumbers and S_0 wavenumber.

This makes Kane-Mindlin valid for a wider range of frequency and thickness. This statement is quantitatively assessed by computing the error between the wavenumber of S_0 Lamb waves mode and the corresponding axial mode in plane stress and Kane-Mindlin theory Fig. 6.7. For example, if we take an acceptability threshold of 1% error, the plane stress theory is valid up to 0.93 MHz.mm whereas Kane-Mindlin theory is valid up to 1.42 MHz.mm. Therefore, since typical plate thickness and excitation frequency lies in this validity range, we will use Kane-Mindlin theory in the rest of this chapter.

6.3 Kane-Mindlin theory in transverse isotropic material

In the previous section, we showed that Kane-Mindlin plate theory provides a very good approximation of S_0 Lamb wave mode in frequencies range suitable for SHM applications. However, we considered the case of an isotropic plate. As mentioned in the introduction of this chapter, we are interested in Lamb waves propagation in composite plate that we will approximate as a transverse isotropic plate. We derive the equation of motion using Lagrange equations Eq. 6.26 in the same manner we did in the previous section. The kinetic energy T remains the same as the isotropic case Eq.6.21. The potential strain energy V is calculated in similar way except this time the compliance matrix $\boldsymbol{C}$ has four indepen-

dent parameters. The Hooke's law for transverse isotropic material is

$$\begin{pmatrix}\sigma_{11}\\ \sigma_{22}\\ \sigma_{33}\\ \sigma_{13}\\ \sigma_{23}\\ \sigma_{12}\end{pmatrix} = \begin{pmatrix} C_{11} & C_{12} & C_{13} & 0 & 0 & 0\\ C_{12} & C_{11} & C_{13} & 0 & 0 & 0\\ C_{13} & C_{13} & C_{33} & 0 & 0 & 0\\ 0 & 0 & 0 & C_{44} & 0 & 0\\ 0 & 0 & 0 & 0 & C_{44} & 0\\ 0 & 0 & 0 & 0 & 0 & \frac{C_{11}-C_{12}}{2}\end{pmatrix}\begin{pmatrix}\varepsilon_{11}\\ \varepsilon_{22}\\ \varepsilon_{33}\\ 2\varepsilon_{13}\\ 2\varepsilon_{23}\\ 2\varepsilon_{12}\end{pmatrix}. \tag{6.39}$$

We obtain the local equations of motion in the transverse isotropic case

$$\begin{aligned} C_{11}\frac{\partial^2 v_x}{\partial x^2} + \frac{C_{13}\kappa}{h}\frac{\partial v_z}{\partial x} + \frac{C_{11}+C_{12}}{2}\frac{\partial^2 v_y}{\partial x\partial y} + \frac{C_{11}-C_{12}}{2}\frac{\partial^2 v_x}{\partial y^2} &= \rho\frac{\partial^2 v_x}{\partial t^2}\\ C_{11}\frac{\partial^2 v_y}{\partial y^2} + \frac{C_{13}\kappa}{h}\frac{\partial v_z}{\partial y} + \frac{C_{11}+C_{12}}{2}\frac{\partial^2 v_x}{\partial x\partial y} + \frac{C_{11}-C_{12}}{2}\frac{\partial^2 v_y}{\partial x^2} &= \rho\frac{\partial^2 v_y}{\partial t^2}\\ C_{44}\frac{\partial^2 v_z}{\partial x^2} + C_{44}\frac{\partial^2 v_z}{\partial y^2} - \frac{3C_{33}\kappa^2}{h^2}v_z - \frac{3C_{13}\kappa}{h}\frac{\partial v_x}{\partial x} - \frac{3C_{13}\kappa}{h}\frac{\partial v_y}{\partial y} &= \rho\frac{\partial^2 v_z}{\partial t^2}\end{aligned} \tag{6.40}$$

By taking $C_{11} = C_{33} = \lambda+2\mu$, $C_{12} = C_{13} = \lambda$ and $C_{44} = \mu$, we can check that these equations recover the ones from isotropic case Eq. 6.27. These equations can also be written in a more compact manner as

$$\frac{C_{11}-C_{12}}{2}\boldsymbol{\Delta v} + \frac{C_{11}+C_{12}}{2}\boldsymbol{\nabla}(\boldsymbol{\nabla}\cdot\boldsymbol{v}) + \frac{C_{13}\kappa}{h}\boldsymbol{\nabla}v_z = \rho\frac{\partial^2\boldsymbol{v}}{\partial t^2} \tag{6.41}$$

$$C_{44}\boldsymbol{\Delta}v_z - \frac{3C_{33}\kappa^2}{h^2}v_z - \frac{3C_{13}\kappa}{h}\boldsymbol{\nabla}\cdot\boldsymbol{v} = \rho\frac{\partial^2 v_z}{\partial t^2} \tag{6.42}$$

where $\boldsymbol{v} = v_x(x,y)\boldsymbol{e_x}+v_y(x,y)\boldsymbol{e_y}$ and $v_z = v_z(x,y)$. Eq.(6.47) and (6.51) form a system of coupled partial derivatives equations. To uncouple it we use the Helmholtz's theorem which states that $\boldsymbol{v}$ can be decomposed as the sum of a curl-free vector field and a divergence-free vector field:

$$\boldsymbol{v}(x,y) = \boldsymbol{\nabla}\phi(x,y) + \boldsymbol{\nabla}\times\boldsymbol{\Psi}(x,y) \tag{6.43}$$

where ϕ is a scalar field and $\boldsymbol{\Psi}$ is a vector field. $\boldsymbol{\nabla}\times\boldsymbol{\Psi}$ denotes the curl of $\boldsymbol{\Psi}$, see in App. D. Since $\boldsymbol{v}$ lies on the Oxy, plane its coordinates can be written

$$\begin{aligned} v_x(x,y) &= \frac{\partial\phi}{\partial x}(x,y) + \frac{\partial\psi}{\partial y}(x,y)\\ v_y(x,y) &= \frac{\partial\phi}{\partial y}(x,y) - \frac{\partial\psi}{\partial x}(x,y)\end{aligned} \tag{6.44}$$

where ψ refers to the z coordinate of $\boldsymbol{\Psi}$. In the following, we consider that we are in time-harmonic conditions at ω angular frequency, which simplifies the time derivatives.

However, the factor $e^{-i\omega t}$ is omitted for readability reasons of the following developments and will be brought back for the final expression.

6.3.1 Shear wave

From Eq.6.41 it comes

$$\frac{C_{11}-C_{12}}{2}\Delta(\nabla\phi)+\frac{C_{11}+C_{12}}{2}\nabla(\Delta\phi)+\frac{C_{13}\kappa}{h}\nabla v_z+\frac{C_{11}-C_{12}}{2}\Delta(\nabla\times\psi) + \frac{C_{11}+C_{12}}{2}\nabla(\nabla\cdot(\nabla\times\psi))=-\omega^2\rho\nabla\phi-\omega^2\rho(\nabla\times\psi) \quad (6.45)$$

where $\nabla\cdot(\nabla\times\psi)=0$, leading to

$$\nabla\left(C_{11}\Delta\phi+\omega^2\rho\phi+\frac{C_{13}\kappa}{h}v_z\right)+\nabla\times\left(\frac{C_{11}-C_{12}}{2}\Delta\psi+\omega^2\rho\psi\right)=0. \quad (6.46)$$

Which gives two uncoupled equations

$$C_{11}\Delta\phi+\omega^2\rho\phi+\frac{C_{13}\kappa}{h}v_z=0 \quad (6.47)$$

$$\frac{C_{11}-C_{12}}{2}\Delta\psi+\omega^2\rho\psi=0 \quad (6.48)$$

Eq.6.48 is the well-known Helmoltz equation

$$\Delta\psi+k_3^2\psi=0 \quad \text{with} \quad k_3^2=\frac{2\rho}{C_{11}-C_{12}}\omega^2. \quad (6.49)$$

From what we saw in the previous section, this equation rules the propagation of the shear wave mode polarized in horizontal plane Eq. 6.34.

6.3.2 Axial waves

Eq.6.42 and Eq.6.44 give

$$C_{44}\Delta v_z-\frac{3C_{33}\kappa^2}{h^2}v_z-\frac{3C_{13}\kappa}{h}\nabla\cdot(\nabla\phi)-\frac{3C_{13}\kappa}{h}\nabla\cdot(\nabla\times\psi)+\rho\omega^2 v_z=0 \quad (6.50)$$

where $\nabla\cdot(\nabla\times\psi)=0$, leading to

$$C_{44}\Delta v_z+\left(\rho\omega^2-\frac{3C_{33}\kappa^2}{h^2}\right)v_z-\frac{3C_{13}\kappa}{h}\Delta\phi=0 \quad (6.51)$$

From Eq.6.47 it comes

$$v_z=-\frac{h}{C_{13}\kappa}(C_{11}\Delta\phi+\rho\omega^2\phi) \quad (6.52)$$

Applying $\boldsymbol{\Delta}$ to v_z expression we obtain

$$\boldsymbol{\Delta} v_z = -\frac{h}{C_{13}\kappa}(C_{11}\boldsymbol{\Delta}^2\phi + \rho\omega^2\boldsymbol{\Delta}\phi) \tag{6.53}$$

v_z and $\boldsymbol{\Delta} v_z$ are replaced by their respective expressions in Eq.6.51

$$\frac{C_{44}h}{C_{13}\kappa}(C_{11}\boldsymbol{\Delta}^2\phi + \rho\omega^2\boldsymbol{\Delta}\phi) + \frac{C_{44}h}{C_{13}\kappa}\left(\rho\omega^2 - \frac{3C_{33}\kappa^2}{h^2}\right)(C_{11}\boldsymbol{\Delta}^2\phi + \rho\omega^2\boldsymbol{\Delta}\phi) + \frac{3C_{13}\kappa}{h}\phi = 0 \tag{6.54}$$

It can be written under the form

$$\boldsymbol{\Delta}^2\phi + 2B\boldsymbol{\Delta}\phi + C\phi = 0 \tag{6.55}$$

with

$$\begin{aligned} B &= \frac{\rho\omega^2}{2C_{11}} + \frac{\rho(\omega^2 - \omega_t^2)}{2C_{44}} + \frac{3\kappa^2 C_{13}^2}{2h^2 C_{11}C_{44}} \\ C &= \frac{\rho^2\omega^2(\omega^2 - \omega_t^2)}{C_{11}C_{44}} \end{aligned} \tag{6.56}$$

We are interested in a plane wave propagating in a direction lying in the Oxy plane so we are looking for solutions of the form $(x, y) \mapsto e^{i(k_x x + k_y y - \omega t)}$ with $k_x, k_y \in \mathbb{C}$. Eq.6.55 becomes

$$k^4 - 2Bk^2 + C = 0 \tag{6.57}$$

with $k^2 = k_x^2 + k_y^2$. This is the same dispersion relationship we found for isotropic material Eq. 6.36. This equation admits two solutions corresponding to the two axial modes

$$\begin{aligned} k_1^2 &= B + \sqrt{B^2 - C} \\ k_2^2 &= B - \sqrt{B^2 - C} \end{aligned} \tag{6.58}$$

with $k_j^2 = k_{jx}^2 + k_{jy}^2$ for $j = \{1, 2\}$. From dispersion curves in the isotropic case Fig. 6.6, we know that $k_1 \neq k_2$. It means that we have two independent solutions of Eq. 6.55, so we can decompose ϕ as the sum of two other potentials

$$\begin{aligned} \phi &= C_1 e^{i(k_{1x}x + k_{2y}y - \omega t)} + C_2 e^{i(k_{2x}x + k_{2y}y - \omega t)} \\ &= \phi_1 + \phi_2 \end{aligned} \tag{6.59}$$

where C_1 and C_2 are constant. Each of these potentials satisfies Helmholtz equation

$$\boldsymbol{\Delta}\phi_j + k_j^2\phi_j = 0 \quad \text{with} \quad j = 1, 2 \tag{6.60}$$

6.3.3 Displacement field

From Eq.6.44 and Eq.6.52, displacement field can then be expressed as follows

$$\begin{aligned} v_x &= \left(\frac{\partial \phi_1}{\partial x} + \frac{\partial \phi_2}{\partial x} + \frac{\partial \psi}{\partial y}\right) e^{-i\omega t} \\ v_y &= \left(\frac{\partial \phi_1}{\partial y} + \frac{\partial \phi_2}{\partial y} - \frac{\partial \psi}{\partial x}\right) e^{-i\omega t} \\ v_z &= \left(\sigma_1 \phi_1 + \sigma_2 \phi_2\right) e^{-i\omega t} \end{aligned} \tag{6.61}$$

where

$$\sigma_j = \frac{hC_{11}}{2\kappa C_{13}} \left(k_j^2 - \frac{\rho\omega^2}{C_{11}}\right) \quad \text{with} \quad j = 1, 2. \tag{6.62}$$

Eq.6.61 can also be written in cylindrical coordinates r, θ and z

$$\begin{aligned} v_r &= \left(\frac{\partial \phi_1}{\partial r} + \frac{\partial \phi_2}{\partial r} + \frac{1}{r}\frac{\partial \psi}{\partial \theta}\right) e^{-i\omega t} \\ v_\theta &= \left(\frac{1}{r}\frac{\partial \phi_1}{\partial \theta} + \frac{1}{r}\frac{\partial \phi_2}{\partial \theta} - \frac{\partial \psi}{\partial r}\right) e^{-i\omega t} \\ v_z &= (\sigma_1 \phi_1 + \sigma_2 \phi_2) e^{-i\omega t}. \end{aligned} \tag{6.63}$$

The next section, we will study the Lamb waves scattering by a damage based on the Kane-Mindlin plate theory.

6.4 Extensional waves scattering by a cylindrical inhomogeneity

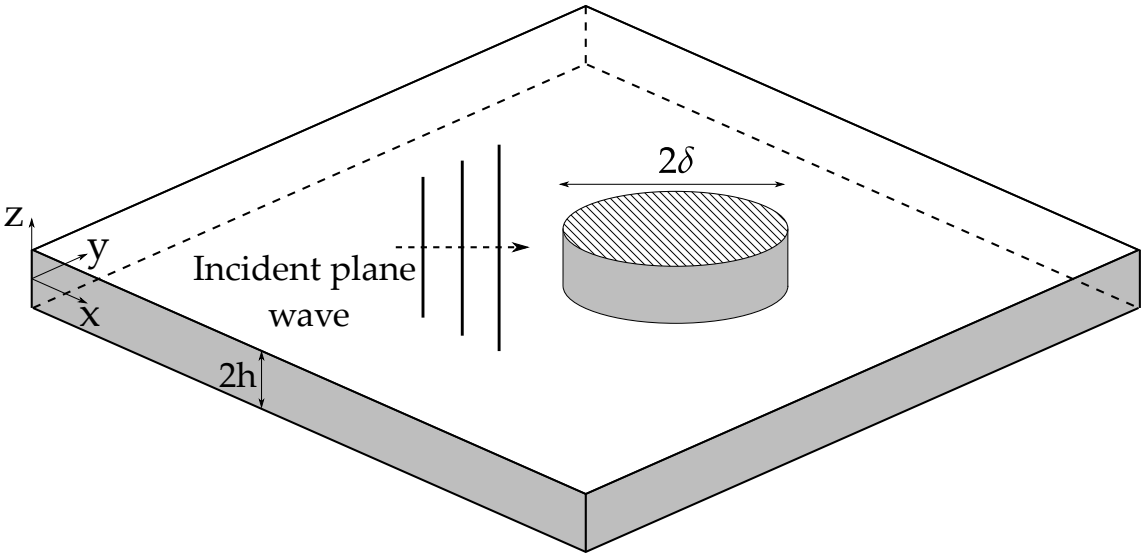

Fig. 6.8 Through-thickness cylindrical inhomogeneity in plate.

In this part we develop an analytical model of a plane monochromatic extensional wave propagating in a transverse isotropic plate after scattering by a cylindrical inho-

mogeneity. To do this we will first write the displacement field and stress components expressions for each wave: incident, scattered and transmitted. The respective potentials are then decomposed into Fourier series of Bessel and Hankel functions. Finally, the unknown coefficients of the series are identified by writing the continuity equations at the damage interface.

6.4.1 Plane waves scattering

Incident wave

We consider an incident plane axial wave of the first kind propagating along x axis to approximate S_0 Lamb waves mode. Then only the potential ϕ_1 is non-zero and from Eq. 6.63 it comes

$$\phi_1^{\mathrm{i}} = \frac{e^{ik_1 x}}{\sigma_1} = \frac{e^{ik_1 r\cos(\theta)}}{\sigma_1} \tag{6.64}$$

$$\phi_2^{\mathrm{i}} = \psi^{\mathrm{i}} = 0 \tag{6.65}$$

where the superscript "i" indicates that these potentials refer to incident wave. r and θ are the polar coordinates with $x = r\cos(\theta)$ and $y = r\sin(\theta)$. $\theta \longmapsto e^{ik_1 r\cos(\theta)}$ is a 2π-periodic function, meaning it can be written as a Fourier series

$$e^{ik_1 r\cos(\theta)} = \sum_{n=-\infty}^{\infty} c_n e^{in\theta} \tag{6.66}$$

where

$$c_n = \frac{1}{2\pi}\int_0^{2\pi} e^{ik_1 r\cos(t)} e^{-int}\,\mathrm{d}t \tag{6.67}$$

Bessel's first integral is defined as [104]

$$J_n(z) = \frac{i^{-n}}{2\pi}\int_0^{2\pi} e^{iz\cos(t)} e^{-int}\,\mathrm{d}t \tag{6.68}$$

So it comes

$$c_n = i^n J_n(k_1 r) \tag{6.69}$$

and the potential related to incident wave is

$$\phi_1^{\mathrm{i}} = \frac{1}{\sigma_1}\sum_{n=-\infty}^{\infty} i^n J_n(k_1 r) e^{in\theta}. \tag{6.70}$$

Scattered and transmitted wave

The wave potentials ϕ_1, ϕ_2 and ψ are all governed by Helmholtz equation. In the following we will denote f to designate any of these potentials and k the associated wave number. In cylindrical coordinates the Helmholtz equation is written

$$\Delta f + k^2 f = \frac{\partial^2 f}{\partial r^2} + \frac{1}{r}\frac{\partial f}{\partial r} + \frac{1}{r^2}\frac{\partial^2 f}{\partial \theta^2} + k^2 f = 0 \tag{6.71}$$

We seek a solution that can be written under the form

$$f(r,\theta) = R(r)\Theta(\theta). \tag{6.72}$$

Eq.6.71 becomes

$$\frac{\mathrm{d}^2 R}{\mathrm{d}r^2}(r)\Theta(\theta) + \frac{1}{r}\frac{\mathrm{d}R}{\mathrm{d}r}(r)\Theta(\theta) + \frac{1}{r^2}\frac{\mathrm{d}^2\Theta}{\mathrm{d}\theta^2}(\theta)R(r) + k^2 R(r)\Theta(\theta) = 0. \tag{6.73}$$

Eq.6.73 is then multiplied by $\frac{r^2}{R\Theta}$. On one side of the equation are the r dependent terms and on the other side are the θ dependent terms. To satisfy this equation, both sides must equal a constant m

$$r^2\left(\frac{1}{R}\frac{\mathrm{d}^2 R}{\mathrm{d}r^2} + k^2\right) + \frac{r}{R}\frac{\mathrm{d}R}{\mathrm{d}r} = -\frac{1}{\Theta}\frac{\mathrm{d}^2\Theta}{\mathrm{d}\theta^2} = m, \quad m \in \mathbb{R}. \tag{6.74}$$

Since f is a periodic function with respect to θ, m must be positive to Θ satisfies this condition. Then, let $m = n^2$ with $n \in \mathbb{R}$. The function Θ is governed by the well known harmonic oscillator equation whose general solution is

$$\Theta(\theta) = \Theta_0^+ e^{in\theta} + \Theta_0^- e^{-in\theta} \tag{6.75}$$

where Θ_0^+ and Θ_0^- are constants. We also know that Θ is 2π-periodic so we must have

$$\Theta(\theta + 2\pi p) = \Theta(\theta), \quad p \in \mathbb{Z}. \tag{6.76}$$

To satisfy this condition n needs to be an integer. Thus $n \in \mathbb{Z}$ and we can discard the $e^{-in\theta}$ part of the solution so we write

$$\Theta(\theta) = \Theta_0 e^{in\theta}. \tag{6.77}$$

On the other hand, the ordinary differential equation in $R(r)$ is the Bessel's equation

$$r^2\frac{\mathrm{d}^2 R}{\mathrm{d}r^2} + r\frac{\mathrm{d}R}{\mathrm{d}r} + (r^2k^2 - n^2)R = 0. \tag{6.78}$$

The solutions of Eq.6.78 are linear combination of Bessel's functions of the first and second kind J_n and Y_n, and Hankel's functions of the first kind and second kind defined

respectively as

$$\begin{aligned} H_n^{(1)}(z) &= J_n(z) + iY_n(z) \\ H_n^{(2)}(z) &= J_n(z) - iY_n(z) \end{aligned} \tag{6.79}$$

with $z \in \mathbb{C}$ [105]. In theory, any pair of these independent functions can be used to represent the solutions of Eq.6.78. Here we choose to write solutions of Bessel equation as linear combination of J_n and $H_n^{(1)}$. The general solutions of Eq. 6.78 are

$$R(r) = R_0 J_n(kr) + R_1 H_n^{(1)}(kr). \tag{6.80}$$

In the part of the plate outside the inhomogeneity, i.e. for $r > \delta$, the expected behavior of f is to be an outgoing wave. As mentioned earlier, $H_n^{(1)}(z) \sim \sqrt{\frac{2}{\pi z}} e^{i(z - n\frac{\pi}{2} - \frac{\pi}{4})}$ and $J_n(z) \sim \sqrt{\frac{2}{\pi z}} e^{-i(z - n\frac{\pi}{2} - \frac{\pi}{4})}$ when $|z| \to \infty$. To preserve physical meaning, we set the constant R_0 to 0 and only the $H_n^{(1)}$ part of the solution is kept. Then we write the solutions of Eq. 6.71 outside the inhomogeneity as

$$f^{\mathrm{s}}(r,\theta) = R^{\mathrm{s}}(r)\Theta(\theta) = \sum_{n=-\infty}^{\infty} f_n^{\mathrm{s}} H_n^{(1)}(kr) e^{in\theta} \tag{6.81}$$

where f_n^{s} are unknown coefficients. The exponent "s" refers to the wave scattered by the inhomogeneity.

For the waves inside the inhomogeneity, i.e. for $r < \delta$, the potential must be finite at $r = 0$. To preserve physical meaning we set $R_1 = 0$ and and only the J_n part of the solution is kept. Then we write the solutions of Eq. 6.71 inside the inhomogeneity as

$$f^{\mathrm{t}}(r,\theta) = R^{\mathrm{t}}(r)\Theta(\theta) = \sum_{n=-\infty}^{\infty} f_n^{\mathrm{t}} J_n(k^* r) e^{in\theta} \tag{6.82}$$

where f_n^{t} are unknown coefficients. The exponent "t" refers to the wave transmitted to the inhomogeneity. The exponent "*" indicates a quantities calculated with the inhomogeneity material parameters. We can now write the expression of each wave potential

$$\begin{aligned} \phi_1^{\mathrm{s}} &= \sum_{n=-\infty}^{\infty} A_n i^n H_n^{(1)}(k_1 r) e^{in\theta}; \quad \phi_1^{\mathrm{t}} = \sum_{n=-\infty}^{\infty} D_n i^n J_n(k_1^* r) e^{in\theta} \\ \phi_2^{\mathrm{s}} &= \sum_{n=-\infty}^{\infty} B_n i^n H_n^{(1)}(k_2 r) e^{in\theta}; \quad \phi_2^{\mathrm{t}} = \sum_{n=-\infty}^{\infty} E_n i^n J_n(k_2^* r) e^{in\theta} \\ \psi^{\mathrm{s}} &= \sum_{n=-\infty}^{\infty} C_n i^n H_n^{(1)}(k_3 r) e^{in\theta}; \quad \psi^{\mathrm{t}} = \sum_{n=-\infty}^{\infty} F_n i^n J_n(k_3^* r) e^{in\theta} \end{aligned} \tag{6.83}$$

where A_n, B_n, C_n, D_n, E_n, F_n are unknown coefficients. i^n is added in the summation term to match the form of ϕ_1^{i} Eq. 6.70. To evaluate these coefficients, the continuity equations for displacement and generalized stresses at the inhomogeneity interface are written.

6.4.2 Plate stresses

The generalized stresses or plate stresses are defined as

$$\begin{aligned}(N_{rr}, N_{\theta\theta}, N_{zz}, N_{r\theta}) &= \int_{-h}^{h} (\sigma_{rr}, \sigma_{\theta\theta}, \sigma_{zz}, \sigma_{r\theta})\, \mathrm{d}z \\ (R_{rz}, R_{\theta z}) &= \int_{-h}^{h} (\sigma_{rz}, \sigma_{\theta z}) z \, \mathrm{d}z.\end{aligned} \tag{6.84}$$

According to Hooke's law Eq. 6.39, the stresses in cylindrical coordinates in case of a homogeneous, transverse isotropic and linear elastic material under small deformation assumption are

$$\begin{aligned}\sigma_{rr} &= c_{11}\frac{\partial v_r}{\partial r} + c_{12}\left(\frac{1}{r}\frac{\partial v_\theta}{\partial \theta} + \frac{v_r}{r}\right) + c_{13}\frac{v_z}{h} \\ \sigma_{\theta\theta} &= c_{12}\frac{\partial v_r}{\partial r} + c_{11}\left(\frac{1}{r}\frac{\partial v_\theta}{\partial \theta} + \frac{v_r}{r}\right) + c_{13}\frac{v_z}{h} \\ \sigma_{zz} &= c_{13}\frac{\partial v_r}{\partial r} + c_{13}\left(\frac{1}{r}\frac{\partial v_\theta}{\partial \theta} + \frac{v_r}{r}\right) + c_{33}\frac{v_z}{h} \\ \sigma_{r\theta} &= c_{44}\left(\frac{1}{r}\frac{\partial v_r}{\partial \theta} + \frac{\partial v_\theta}{\partial r} - \frac{v_\theta}{r}\right) \\ \sigma_{rz} &= c_{44}\left(\frac{z}{h}\frac{\partial v_z}{\partial r}\right) \\ \sigma_{\theta z} &= \frac{c_{11} - c_{22}}{2}\left(\frac{z}{rh}\frac{\partial v_z}{\partial \theta}\right)\end{aligned} \tag{6.85}$$

It allows to derive the expression of the generalized stresses in terms of displacement

$$\begin{aligned}
N_{rr} &= 2h\left(c_{11}\frac{\partial v_r}{\partial r} + c_{12}\left(\frac{1}{r}\frac{\partial v_\theta}{\partial \theta} + \frac{v_r}{r}\right) + c_{13}\frac{v_z}{h}\right)\\
N_{\theta\theta} &= 2h\left(c_{12}\frac{\partial v_r}{\partial r} + c_{11}\left(\frac{1}{r}\frac{\partial v_\theta}{\partial \theta} + \frac{v_r}{r}\right) + c_{13}\frac{v_z}{h}\right)\\
N_{zz} &= 2h\left(c_{13}\frac{\partial v_r}{\partial r} + c_{13}\left(\frac{1}{r}\frac{\partial v_\theta}{\partial \theta} + \frac{v_r}{r}\right) + c_{33}\frac{v_z}{h}\right)\\
N_{r\theta} &= 2hc_{44}\left(\frac{1}{r}\frac{\partial v_r}{\partial \theta} + \frac{\partial v_\theta}{\partial r} - \frac{v_\theta}{r}\right)\\
R_{rz} &= \frac{2h^2c_{44}}{3}\frac{\partial v_z}{\partial r}\\
R_{\theta z} &= \frac{2h^2(c_{11}-c_{12})}{3r}\frac{\partial v_z}{\partial \theta}
\end{aligned} \tag{6.86}$$

6.4.3 Scattering coefficients' evaluation

We write the continuity equation of displacement field and generalized stresses at damage interface with the rest of the plate. For each component, the sum of incident and scattered waves equals to transmitted wave.

$$\begin{aligned}
v_r^{\mathrm{i}}(\delta,\theta) + v_r^{\mathrm{s}}(\delta,\theta) &= v_r^{\mathrm{t}}(\delta,\theta)\\
v_\theta^{\mathrm{i}}(\delta,\theta) + v_\theta^{\mathrm{s}}(\delta,\theta) &= v_\theta^{\mathrm{t}}(\delta,\theta)\\
v_z^{\mathrm{i}}(\delta,\theta) + v_z^{\mathrm{s}}(\delta,\theta) &= v_z^{\mathrm{t}}(\delta,\theta)\\
N_{rr}^{\mathrm{i}}(\delta,\theta) + N_{rr}^{\mathrm{s}}(\delta,\theta) &= N_{rr}^{\mathrm{t}}(\delta,\theta)\\
N_{r\theta}^{\mathrm{i}}(\delta,\theta) + N_{r\theta}^{\mathrm{s}}(\delta,\theta) &= N_{r\theta}^{\mathrm{t}}(\delta,\theta)\\
R_{rz}^{\mathrm{i}}(\delta,\theta) + R_{rz}^{\mathrm{s}}(\delta,\theta) &= N_{rz}^{\mathrm{t}}(\delta,\theta)
\end{aligned} \tag{6.87}$$

Since $\{e^{in\theta} : n \in \mathbb{Z}\}$ is a basis of $L^2([0,2\pi])$, each order of the sum can be solved separately. For each order n, the following linear system of equations must be solved

$$\begin{aligned}
\boldsymbol{\alpha_n}\boldsymbol{X_n} &= \boldsymbol{\beta_n}\\
\boldsymbol{X_n} &= \begin{pmatrix} A_n & B_n & C_n & D_n & E_n & F_n \end{pmatrix}^{\mathrm{T}}
\end{aligned} \tag{6.88}$$

where $\boldsymbol{\alpha_n} \in \mathbb{C}^{6\times 6}$ and $\boldsymbol{\beta_n} \in \mathbb{C}^{6\times 1}$. We approximate the infinite sum by a truncated one with N the last order of the series. Hence ϕ_1^{s} becomes

$$\phi_1^{\mathrm{s}} = \sum_{n=-N}^{N} A_n i^n H_n^{(1)}(k_1 r) e^{in\theta}. \tag{6.89}$$

Numerical considerations

In the linear system of equations Eq. 6.88, it appears that the columns of the matrix α_n are very unbalanced. Indeed, beyond cut-off frequency the wave number k_2 is purely imaginary, which leads to an exponential behavior of the functions J_n and $H_n^{(1)}$. Consequently, the terms of $\boldsymbol{\alpha_n}$ associated to ϕ_2^{s} and ϕ_2^{t} are larger by several orders of magnitude than the others. This produces an ill-conditioned linear system leading to unreliable solutions. To solve this problem we normalize these terms as follows [106]

$$\begin{aligned} H_n^{(1)}(kr) &\longrightarrow \frac{H_n^{(1)}(kr)}{H_n^{(1)}(k\delta)} \\ J_n(kr) &\longrightarrow J_n(kr)H_n^{(1)}(k\delta). \end{aligned} \tag{6.90}$$

For example, ϕ_1^{s} becomes

$$\phi_1^{\mathrm{s}} = \sum_{n=-N}^{N} A_n i^n \frac{H_n^{(1)}(k_1 r)}{H_n^{(1)}(k_1 \delta)} e^{in\theta} \tag{6.91}$$

Comparison with litterature

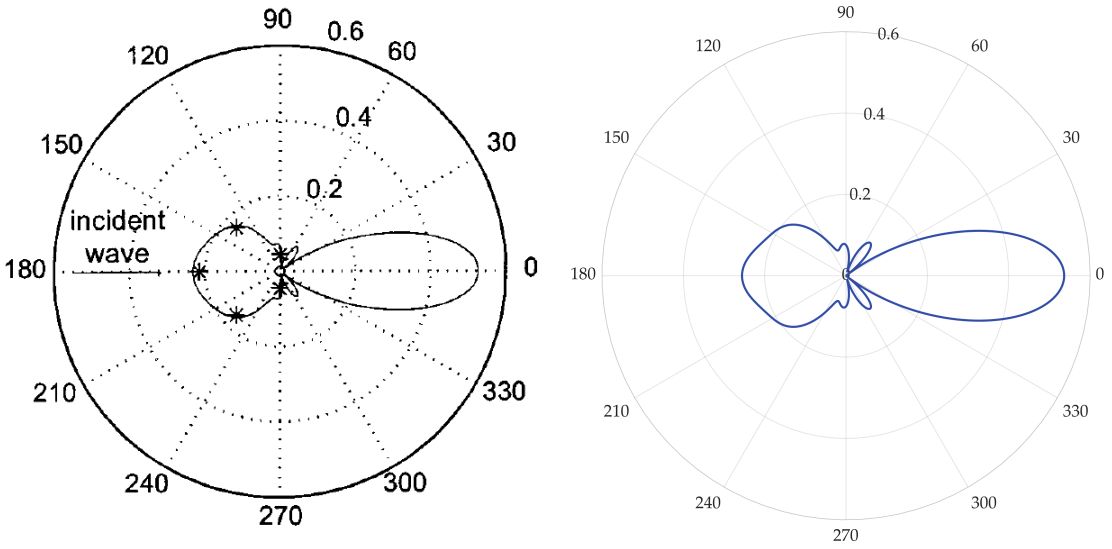

(a) (b)

Fig. 6.9 Scattering directivity pattern from Diligent et al. [84] (a) and the same pattern computed with the developed model (b).

In order to validate the implementation of the scattering model developed in this section, we use results from the literature obtained with isotropic material. As mentioned earlier, we consider a transverse isotropic plate and a damage as an inhomogeneity in the model developed here. Therefore, these comparisons are done to show that the current model recover the isotropic case and simpler forms of damage.

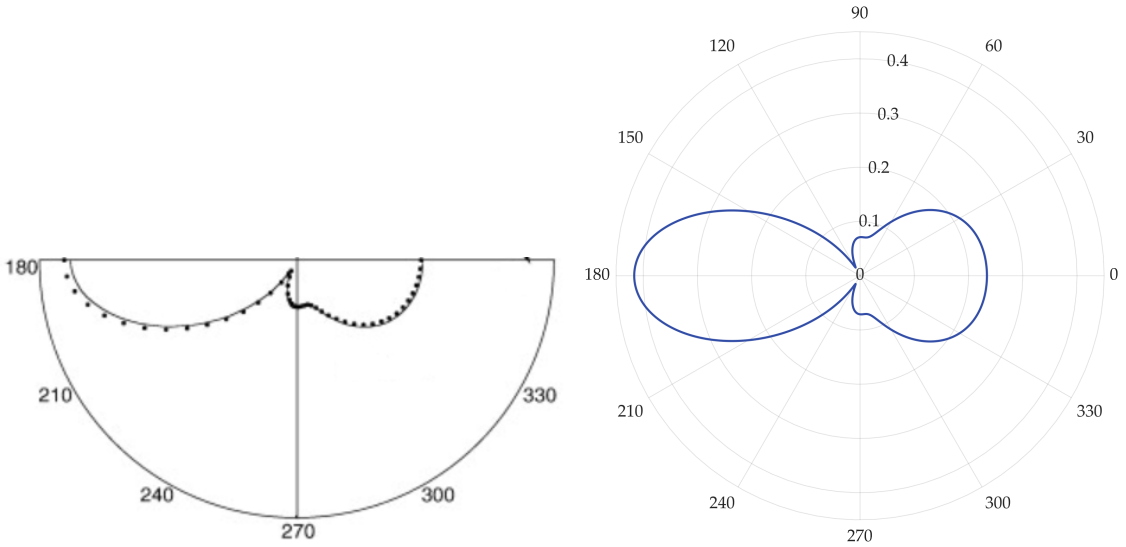

(a) (b)

Fig. 6.10 Scattering directivity pattern from Moreau et al. [86] (a) and the same pattern computed with the developped model (b).

To visualize the influence of the angle on the amplitude of the reflected S_0 mode, it is common to plot the scattering directivity pattern. This consists in plotting the quantity $|\sum_{n=-N}^{N} A_n i^n e^{in\theta}|$ versus θ. Taking $N = 5$ we find the results of Diligent et al. [84] Fig. 6.9 and those of Moreau et al. [86] in the case of circular damage Fig. 6.10 and isotropic material.

6.5 Signal modeling

So far, we have studied the scattering of a monochromatic plane wave of unit amplitude by a cylindrical inhomogeneity. In this section, we will use these results to compute the response of a PZT to the passage of a wave previously emitted by a piezoelectric actuator and scattered by a damage. To do this, we will first model the shape of the wave emitted by the actuator. We will also compute the response of the PZT sensor to the passage of the diffused wave. These two models will allow us to obtain the transfer function of the complete system. All that remains to be done is to compute the time response by signal synthesis. The general setup is shown Fig.6.11. An exciting PZT is located in (x_A, y_A) while a sensor PZT is located in (x_S, y_S). Both are on the surface $z = +h$ and have a radius c. A cylindrical inhomogeneity as considered in section 6.4.1 has its center at coordinates (x_D, y_D) and has a radius δ.

6.5.1 Actuator model

In the previous section 6.4.1, we considered that the incident wave was a harmonic and plane wave of unitary amplitude. In reality, the incident wave is generated by a piezoelectric patch. The wave amplitude depends on numerous parameters like the geometry of

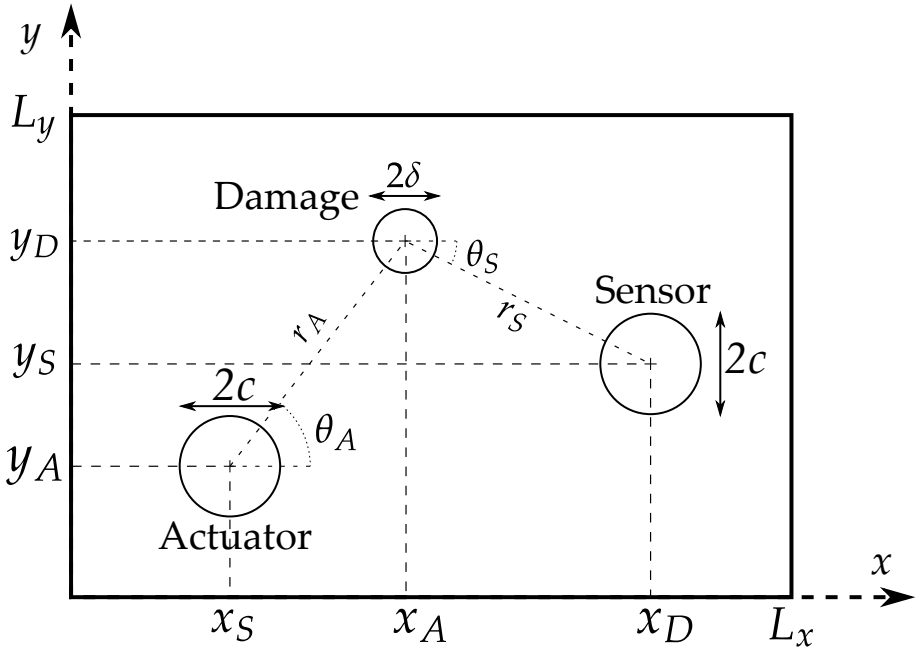

Fig. 6.11 2D diagram of the scattering problem by an inhomogeinity with emitter and receiver PZT.

the patch, its mechanical properties, the glue layer parameters, the frequency, etc. In this subsection an expression of the incident wave is derived. As mentioned in the introduction of this chapter Sec. 6.1.1, line-force model (also called pin-force model) is a classical way to model a PZT actuator [22]. It consists of assume that the actuator acts only along its perimeter producing a lineic force τ. This assumption can be made when the bonding layer is very thin, very stiff or both, and if the ratio $E_A h_A/(2Eh)$ is small. We define the two following parameters

$$\begin{aligned} \Gamma^2 &= \frac{G_b}{t_b}\left(\frac{1-\nu_A^2}{E_A h_A} + \alpha\frac{1-\nu_{21}^2}{2E_1 h}\right) \\ p &= \Gamma^2 \varepsilon_{ISA}\left[\Gamma I_0(\Gamma c)\left(\frac{1+\nu_A}{E_A h_A} + \alpha\frac{1-\nu_{21}}{2E_1 h}\right) - \left(\frac{(1-\nu_A)^2}{E_A h_A} + \alpha\frac{(1-\nu_{21})^2}{2E_1 h}\right)\frac{I_1(\Gamma c)}{c}\right]^{-1}. \end{aligned} \tag{6.92}$$

where G_b and t_b are respectively the shear modulus and the thickness of the glue layer; ν_A, E_A and h_A are respectively Poisson's ratio, Young's modulus and thickness of the PZT whereas ν_{21}, E_1 and $2h$ are the same parameters for the plane Oxy of the host structure. α is a coefficient that depends on dynamics conditions. In our case, $\alpha = 4$. ε_{ISA} is the strain induced by an electrical voltage V_{in}

$$\varepsilon_{ISA} = -d_{31}\frac{V_{in}}{h_A}. \tag{6.93}$$

I_0 and I_1 are modified Bessel functions of the first kind of order 0 and 1 respectively [105] whereas Γ is called the shear-lag parameter. In the ideal bonding case, the shear stress

can be expressed

$$\tau = \frac{1}{c^2} \lim_{\Gamma \to +\infty} \left(p \int_0^c I_1(\Gamma r) r \, \mathrm{d}r \right). \tag{6.94}$$

To compute τ numerically we take the value of the last expression for a large value of Γ. The total force applied on the PZT's perimeter to the structure is then $c\tau$.

Now we know the value of τ, we need to express the displacement field generated by the actuator. For that, we follow the procedure from Raghavan and Cesnik [76] which relies on Mal's work [107] and is an extension of their work on isotropic plate [108]. This approach is adapted here to a single layer plate made of transverse isotropy material whose plane of isotropy is Oxy. As we mentioned in Sec. 6.4, $H_0^{(1)}(k_1 r)$ represents waves that propagate forward and $H_0^{(2)}(k_1 r)$ waves that propagate backward. Since we consider forward propagating waves only, the final expression of the displacement is

$$u_i(x, y, h) = \frac{i}{4} \frac{N_i(k_1)}{D'_{\mathrm{G}}(k_1)} k_1 H_0^{(1)}(k_1 r). \tag{6.95}$$

We want to express the wave potential of the incident wave ϕ_1^{i} as Fourier series like we did in Eq. 6.70. Since we consider a pure S_0 wave, $\phi_2^{\mathrm{i}} = \psi^{\mathrm{i}} = 0$ and

$$\phi_1^{\mathrm{i}} = \frac{u_z}{\sigma_1}. \tag{6.96}$$

Considering that we have $kr \gg 1$, we can make the approximate Hankel function for large argument

$$H_0^{(1)}(k_1 r) \sim \frac{1 - i}{\sqrt{\pi k_1 r}} e^{i k_1 r}. \tag{6.97}$$

This assumption can be quantitatively evaluated by looking at the relative error between the Hankel function and its equivalent for large argument for a range of $k_1 r$. In Fig. 6.12 we can see that the error is of 1% for $k_1 r \approx 12$. For example for ReMAP skin material Fig. G.1 in App. G, it corresponds to a distance of two or three wavelengths for the range of frequency and plate thickness we consider in this study. We can conclude that this approximation is relevant since it is close to reality except in the immediate neighborhood of the actuator. In the same way as Eq. 6.70, we can write the expression Eq. 6.97 as a Fourier series

$$H_0^{(1)}(k_1 r) \sim \frac{1 - i}{\sqrt{\pi k_1 r}} \sum_{n=-\infty}^{\infty} i^n J_n(k_1 r) e^{i n \theta}. \tag{6.98}$$

We must pay attention to the polar coordinates used here. Indeed, so far in the actuator model derivation the origin of the polar coordinates system was the center of the actuator. However, in the scattering study we did earlier Sec. 6.4 the origin was the center of the damage. We keep the same notation for the radial coordinate r but since we assumed that the incident plane propagates with a zero angle, we need to subtract the angle between the x axis and the line going from actuator center to damage center θ_{A} Fig. 6.11. Hence,

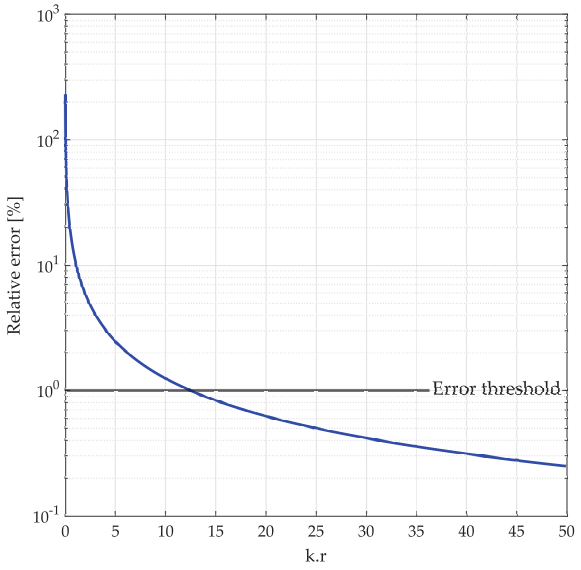

Fig. 6.12 Relative error between Hankel function of first kind and order 0 and its approximation for large argument Eq. 6.97. $k.r$ is the product of wavenumber and distance from the emitter.

the wave potential of the incident wave becomes

$$\phi_1^{\mathrm{i}} = \frac{ic\tau k_1}{4} \frac{N_3(k_1)}{D'_{\mathrm{G}}(k_1)} \frac{1-i}{\sqrt{\pi k_1 r}} \sum_{n=-\infty}^{\infty} i^n J_n(k_1 r) e^{in(\theta-\theta_{\mathrm{A}})}. \tag{6.99}$$

To compute the scattering coefficients A_n we follow the procedure described in section 6.4.1 by replacing ϕ_1^{i} by its new expression.

Because the matrix $\boldsymbol{G}$ is rank deficient when evaluated at one of the roots $\pm\zeta_i$, round off errors can occur when evaluating D'_G and $\boldsymbol{N}_i$ numerically. To make the result reliable and robust, we compute the analytical formula of these two terms with the software Mathematica and use it in the MATLAB implementation of the model.

6.5.2 Sensor response

Once we have computed the scattering coefficients, we need to calculate the transfer function between the excitation signal and the received signal. We will first derive the voltage measured at the terminals of a piezoelectric sensor in response to a deformation. This response depends on the electrical boundary conditions to which the PZT is subjected. We address the case where the electrical circuit is open, i.e. when the sensor is considered as a voltage source. It happens when the electrodes are connected to a voltage amplifier with high input impedance which is used when we have excitation frequency above few dozen kilohertz. The PZT is considered perfectly bonded to the plate and made of transversely isotropic along z axis. The derivation of electrical sensor response to a deformation in that

case can be found in Appendix Sec. E.2. In the end we obtain

$$H = K_S \iint_A \left(\varepsilon_1 + \varepsilon_2\right) \mathrm{d}A \tag{6.100}$$

where $K_S = \frac{d_{31} Y^E h_S}{\pi c^2 \left(\chi_3^\sigma (1-\nu) - 2 d_{31}^2 Y^E\right)}$. In cylindrical coordinates, $\varepsilon_1 = \varepsilon_{rr}$ and $\varepsilon_2 = \varepsilon_{\theta\theta}$ and from Eq.6.63 it comes

$$\begin{aligned}
\varepsilon_{rr} &= \frac{\partial u_r}{\partial r} = \frac{\partial^2 \phi_1}{\partial r^2} + \frac{\partial^2 \phi_2}{\partial r^2} - \frac{1}{r^2}\frac{\partial \psi}{\partial \theta} + \frac{1}{r}\frac{\partial^2 \psi}{\partial r \partial \theta} \\
\varepsilon_{\theta\theta} &= \frac{1}{r}\frac{\partial u_\theta}{\partial \theta} + \frac{u_r}{r} = \frac{1}{r^2}\frac{\partial^2 \phi_1}{\partial \theta^2} + \frac{1}{r^2}\frac{\partial^2 \phi_2}{\partial \theta^2} - \frac{1}{r}\frac{\partial^2 \psi}{\partial \theta \partial r} + \frac{1}{r}\frac{\partial \phi_1}{\partial r} + \frac{1}{r}\frac{\partial \phi_2}{\partial r} + \frac{1}{r^2}\frac{\partial \psi}{\partial \theta}.
\end{aligned} \tag{6.101}$$

All terms in ψ cancel out:

$$\varepsilon_{rr} + \varepsilon_{\theta\theta} = \frac{\partial^2 \phi_1}{\partial r^2} + \frac{\partial^2 \phi_2}{\partial r^2} + \frac{1}{r^2}\frac{\partial^2 \phi_1}{\partial \theta^2} + \frac{1}{r^2}\frac{\partial^2 \phi_2}{\partial \theta^2} + \frac{1}{r}\frac{\partial \phi_1}{\partial r} + \frac{1}{r}\frac{\partial \phi_2}{\partial r}. \tag{6.102}$$

We are working below the cut off frequency ω_t, it means that k_2 is purely imaginary and then that ϕ_2 fades out when $k_2 r \gg 1$. Finally ε_{ii} can be written

$$\varepsilon_{ii} = \frac{\partial^2 \phi_1}{\partial r^2} + \frac{1}{r^2}\frac{\partial^2 \phi_1}{\partial \theta^2} + \frac{1}{r}\frac{\partial \phi_1}{\partial r} \tag{6.103}$$

Replacing ϕ_1 by its expression from Eq. 6.84

$$\varepsilon_{ii} = \sum_{n=-N}^{N} \left(\frac{\mathrm{d}^2 H_n^{(1)}}{\mathrm{d}r^2}(k_1 r) - \frac{n^2}{r^2} H_n^{(1)}(k_1 r) + \frac{1}{r}\frac{\mathrm{d}H_n^{(1)}}{\mathrm{d}r}(k_1 r) \right) \frac{A_n i^n}{H_n^{(1)}(k_1 \delta)} e^{in\theta} \tag{6.104}$$

We rewrite the expression between parentheses in terms of Hankel's functions of different orders instead of derivatives

$$\begin{aligned}
\frac{\mathrm{d}H_n^{(1)}}{\mathrm{d}r}(k_1 r) &= \frac{n}{r} H_n^{(1)}(k_1 r) - k_1 H_{n+1}^{(1)}(k_1 r) \\
\frac{\mathrm{d}^2 H_n^{(1)}}{\mathrm{d}r^2}(k_1 r) &= \frac{n(n-1)}{r^2} H_n^{(1)}(k_1 r) - \frac{k_1 (2n+1)}{r} H_{n+1}^{(1)}(k_1 r) + k_1^2 H_{n+2}^{(1)}(k_1 r).
\end{aligned} \tag{6.105}$$

The expression between parentheses in Eq.6.104 becomes

$$\frac{\mathrm{d}^2 H_n^{(1)}}{\mathrm{d}r^2}(k_1 r) - \frac{n^2}{r^2} H_n^{(1)}(k_1 r) + \frac{1}{r}\frac{\mathrm{d}H_n^{(1)}}{\mathrm{d}r}(k_1 r) = k_1^2 H_{n+2}^{(1)}(k_1 r) - \frac{2k_1(n+1)}{r} H_{n+1}^{(1)}(k_1 r). \tag{6.106}$$

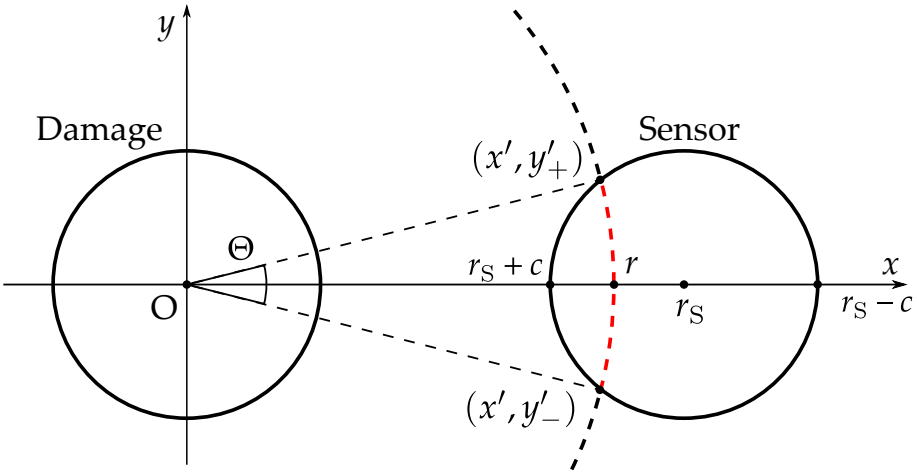

Fig. 6.13 Diagram of the double integral computation in sensor PZT response.

According to recurrence relations between Hankel's function derivative [105], Eq. [10.6.1], the expression of in-plane strains can be simplified to

$$\varepsilon_{rr} + \varepsilon_{\theta\theta} = \sum_{n=-N}^{N} \left(k_1^2 H_{n+2}^{(1)}(k_1 r) - \frac{2k_1(n+1)}{r} H_{n+1}^{(1)}(k_1 r) \right) \frac{A_n i^n}{H_n^{(1)}(k_1 \delta)} e^{in\theta} \tag{6.107}$$

The integral Eq. E.40 becomes

$$\begin{aligned} \int_A (\varepsilon_{rr} + \varepsilon_{\theta\theta})\, dA &= \int_r \int_\theta (\varepsilon_{rr} + \varepsilon_{\theta\theta})\, r \, \mathrm{d}\theta \, \mathrm{d}r \\ &= \sum_{n=-N}^{N} \int_r \int_\theta \left(k_1^2 H_{n+2}^{(1)}(k_1 r) - \frac{2k_1(n+1)}{r} H_{n+1}^{(1)}(k_1 r) \right) \frac{A_n i^n}{H_n^{(1)}(k_1 \delta)} e^{in\theta} r \, \mathrm{d}\theta \, \mathrm{d}r. \end{aligned} \tag{6.108}$$

In order to evaluate this integral, we follow the method proposed by Sohn and Lee [109]. We need to find the two crossing points between the circle of center $(0, 0)$ and radius r, and the circle of center $(r_S, 0)$ and radius c

$$\begin{aligned} x^2 + y^2 &= r^2 \\ (x - r_S)^2 + y^2 &= c^2 \end{aligned} \tag{6.109}$$

with $r_S - c \leqslant r \leqslant r_S + c$. The coordinates of the crossing points are then

$$x' = \frac{r^2 + r_S^2 - c^2}{2r_S}; \qquad y' = \pm \sqrt{r^2 - \left(\frac{r^2 + r_S^2 - c^2}{2r_S} \right)^2}. \tag{6.110}$$

From these two points, the central angle is obtained as

$$\Theta(r) = 2\tan^{-1}\left(\frac{\sqrt{r^2-\left(\frac{r^2+r_S^2-c^2}{2r_S}\right)^2}}{\frac{r^2+r_S^2-c^2}{2r_S}}\right) = 2\tan^{-1}\left(\sqrt{\left(\frac{2rr_S}{r^2+r_S^2-c^2}\right)^2-1}\right) \tag{6.111}$$

and the integral in Eq. 6.108 becomes

$$\int_r\int_\theta (\varepsilon_{rr}+\varepsilon_{\theta\theta})\, r\,\mathrm{d}\theta\,\mathrm{d}r = \int_{r_S-c}^{r_S+c}\int_{-\frac{\Theta}{2}}^{\frac{\Theta}{2}} (\varepsilon_{rr}+\varepsilon_{\theta\theta})\, r\,\mathrm{d}\theta\,\mathrm{d}r. \tag{6.112}$$

Since it may exist non zero angle between the damage center and the sensor center in the polar coordinates system centered on damage, we add this angle called θ_S to the integration angle $\Theta(r)$ Fig. 6.11. If $n \neq 0$ we have

$$\int_{\theta_S-\frac{\Theta(r)}{2}}^{\theta_S+\frac{\Theta(r)}{2}} e^{in\theta}\,\mathrm{d}\theta = \frac{1}{in}\left(e^{in\left(\theta_S+\frac{\Theta}{2}\right)}-e^{in\left(\theta_S-\frac{\Theta}{2}\right)}\right) = \frac{2e^{in\theta_S}}{n}\sin\left(\frac{n\Theta}{2}\right) \tag{6.113}$$

and if $n = 0$ we have

$$\int_{\theta_S-\frac{\Theta(r)}{2}}^{\theta_S+\frac{\Theta(r)}{2}} e^{in\theta}\,\mathrm{d}\theta = \Theta(r). \tag{6.114}$$

The integral of in-plane strain over the sensor surface finally becomes

$$\begin{aligned}\int_{r_S-c}^{r_S+c}\int_{\theta_S-\frac{\Theta(r)}{2}}^{\theta_S+\frac{\Theta(r)}{2}} (\varepsilon_{rr}+\varepsilon_{\theta\theta})\, r\,\mathrm{d}\theta\,\mathrm{d}r &= \frac{A_0}{H_0^{(1)}(k_1\delta)}\int_{r_S-c}^{r_S+c}\left(k_1^2H_2^{(1)}(k_1r)-\frac{2k_1}{r}H_1^{(1)}(k_1r)\right)\Theta(r)r\,\mathrm{d}r \\ &+ \sum_{\substack{n=-N\\ n\neq 0}}^{N}\frac{2i^nA_ne^{in\theta_S}}{nH_n^{(1)}(k_1\delta)}\int_{r_S-c}^{r_S+c}\left(k_1^2H_{n+2}^{(1)}(k_1r)-\frac{2k_1(n+1)}{r}H_{n+1}^{(1)}(k_1r)\right)\sin\left(\frac{n\Theta(r)}{2}\right)r\,\mathrm{d}r.\end{aligned} \tag{6.115}$$

By virtue of Eq. E.40, the transfer function between input and output voltages is

$$H(\omega) = K_S\left[\frac{A_0}{H_0^{(1)}(k_1\delta)}\int_{r_S-c}^{r_S+c}\left(k_1^2H_2^{(1)}(k_1r)-\frac{2k_1}{r}H_1^{(1)}(k_1r)\right)\Theta(r)r\,\mathrm{d}r\right.$$

$$+\sum_{\substack{n=-N\\n\neq 0}}^{N}\frac{2i^n A_n e^{in\theta_S}}{nH_n^{(1)}(k_1\delta)}\int_{r_S-c}^{r_S+c}\left(k_1^2H_{n+2}^{(1)}(k_1r)-\frac{2k_1(n+1)}{r}H_{n+1}^{(1)}(k_1r)\right)\sin\left(\frac{n\Theta(r)}{2}\right)r\,\mathrm{d}r\Bigg]. \quad (6.116)$$

6.5.3 Signal synthesis

We determined the response of the PZT to the passage of a wave in the harmonic regime. In reality the excitation signal may have a richer spectrum, for example a toneburst. To compute the response to such an input we first establish the Fourier transform of the input signal v_{in}.

$$V_{\text{in}}(\omega)=\int_{-\infty}^{\infty}v_{\text{in}}(t)e^{i\omega t}\,\mathrm{d}\omega. \quad (6.117)$$

From the transfer function expression we derived Eq. 6.116, the output voltage can be written in the frequency domain as

$$V_{\text{out}}(\omega)=H(\omega)V_{\text{in}}(\omega). \quad (6.118)$$

Then we took the inverse Fourier transform to get the time signal

$$v_{\text{out}}(t)=\int_{-\infty}^{+\infty}V_{\text{out}}(\omega)e^{-i\omega t}\,\mathrm{d}\omega. \quad (6.119)$$

6.5.4 From multilayered composite materials to transverse isotropic material

Table 6.3 Geometric and material properties of AS4/8552 plain weave ply used in Monarque project [110]. Material parameters are extracted from [111, 112, 39].

Property	Unit	Value
Stacking sequence	-	$[0,45,0,45]_s$
Ply thickness	mm	0.3
Total thickness	mm	2.4
$E_1 = E_2$	GPa	63.4
E_3	GPa	8.9
G_{12}	GPa	5.0
$G_{23} = G_{31}$	GPa	3.5
$\nu_{12} = \nu_{31}$	-	0.04
ν_{23}	-	0.30

As we stated in the presentation of the problem Sec. 6.1.2, we approximate laminate composite by a homogeneous transverse isotropic plate with a single layer. We make this assumption because we study quasi-isotropic laminate composite which means that the stacking sequence is balanced so that the anisotropy in the plane of the plate is reduced. To compute the equivalent elastic constants, we use the equations proposed by Sun and

Li in the general case of anisotropic solids [113]. In this approach, we assume that the thickness of each ply is small compared to the total laminate thickness and that stress and displacement are continuous at each layer interface. Since each ply is oriented, we need to express each ply stiffness matrix rotated of the orientation angle θ_{R}. We define the rotation matrix $\boldsymbol{R}$

$$\boldsymbol{R} = \begin{pmatrix} \cos(\theta_{\mathrm{R}}) & \sin(\theta_{\mathrm{R}}) & 0 \\ -\sin(\theta_{\mathrm{R}}) & \cos(\theta_{\mathrm{R}}) & 0 \\ 0 & 0 & 1 \end{pmatrix}. \tag{6.120}$$

Then the rotated stiffness matrix $\boldsymbol{C}'^{(n)}$ of ply n is

$$\boldsymbol{C}'^{(n)} = \boldsymbol{R}\boldsymbol{R}\boldsymbol{C}^{(n)}\boldsymbol{R}^{\mathrm{T}}\boldsymbol{R}^{\mathrm{T}} \tag{6.121}$$

or in Einstein notation

$$C'^{(n)}_{mnop} = R_{mi}R_{nj}R_{ok}R_{pl}C^{(n)}_{ijkl} \tag{6.122}$$

where $i, j, k, l, m, n, o, p \in 1, 2, 3$ and $\boldsymbol{C}^{(n)}$ is the stiffness matrix of the ply with a zero angle. Since we consider, transverse isotropic ply the equations from [113] can be simplified to

$$\begin{aligned}
\overline{C}_{11} &= \sum_{n=1}^{N} v_n C'^{(n)}_{11} + \sum_{n=2}^{N} \left(C'^{(n)}_{13} - \overline{C}_{13}\right)\left(C^{(1)}_{13} - C'^{(n)}_{13}\right)\frac{v_n}{C'^{(n)}_{33}} \\
\overline{C}_{12} &= \sum_{n=1}^{N} v_n C'^{(n)}_{12} + \sum_{n=2}^{N} \left(C'^{(n)}_{13} - \overline{C}_{13}\right)\left(C^{(1)}_{23} - C'^{(n)}_{23}\right)\frac{v_n}{C'^{(n)}_{33}} \\
\overline{C}_{13} &= \sum_{n=1}^{N} v_n C'^{(n)}_{13} + \sum_{n=2}^{N} \left(C'^{(n)}_{33} - \overline{C}_{33}\right)\left(C^{(1)}_{13} - C'^{(n)}_{13}\right)\frac{v_n}{C'^{(n)}_{33}} \\
\overline{C}_{23} &= \sum_{n=1}^{N} v_n C'^{(n)}_{23} + \sum_{n=2}^{N} \left(C'^{(n)}_{33} - \overline{C}_{33}\right)\left(C^{(1)}_{23} - C'^{(n)}_{23}\right)\frac{v_n}{C'^{(n)}_{33}} \\
\overline{C}_{22} &= \sum_{n=1}^{N} v_n C'^{(n)}_{22} + \sum_{n=2}^{N} \left(C'^{(n)}_{23} - \overline{C}_{23}\right)\left(C^{(1)}_{23} - C'^{(n)}_{23}\right)\frac{v_n}{C'^{(n)}_{33}}
\end{aligned} \tag{6.123}$$

$$\begin{aligned}
\overline{C}_{33} &= \left(\sum_{n=1}^{N} \frac{v_n}{C'^{(n)}_{33}}\right)^{-1} \qquad \overline{C}_{44} = \left(\sum_{n=1}^{N} \frac{v_n}{C'^{(n)}_{44}}\right)^{-1} \\
\overline{C}_{55} &= \left(\sum_{n=1}^{N} \frac{v_n}{C'^{(n)}_{55}}\right)^{-1} \qquad \overline{C}_{66} = \sum_{n=1}^{N} v_n C'^{(n)}_{66}
\end{aligned}$$

where $v_n = h_n/(2h)$ is the volume fraction of the lamina n. To assess the relevance of this procedure, we compare the dispersion curves of a laminate composite using the global matrix method [21] and the Kane-Mindlin theory using effective elastic coefficients. We consider the material used in the Monarque project [110] whose properties are stated in

Tab. 6.3. The plates used are made of woven AS4 fibers pre-impregnated with 8552 epoxy resin. We found the following equivalent stiffness matrix

$$\overline{C} = \begin{pmatrix} \overline{C}_{11} & \overline{C}_{12} & \overline{C}_{13} & 0 & 0 & 0 \\ \overline{C}_{12} & \overline{C}_{22} & \overline{C}_{23} & 0 & 0 & 0 \\ \overline{C}_{13} & \overline{C}_{23} & \overline{C}_{33} & 0 & 0 & 0 \\ 0 & 0 & 0 & \overline{C}_{44} & 0 & 0 \\ 0 & 0 & 0 & 0 & \overline{C}_{55} & 0 \\ 0 & 0 & 0 & 0 & 0 & \overline{C}_{66} \end{pmatrix} = \begin{pmatrix} 51.7 & 16.2 & 2.9 & 0 & 0 & 0 \\ 16.2 & 51.7 & 2.9 & 0 & 0 & 0 \\ 2.9 & 2.9 & 9.1 & 0 & 0 & 0 \\ 0 & 0 & 0 & 3.5 & 0 & 0 \\ 0 & 0 & 0 & 0 & 3.5 & 0 \\ 0 & 0 & 0 & 0 & 0 & 17.7 \end{pmatrix} \text{GPa}. \tag{6.124}$$

We can notice that

$$\begin{aligned} \overline{C}_{23} &= \overline{C}_{13} \\ \overline{C}_{11} &= \overline{C}_{22} \\ \overline{C}_{44} &= \overline{C}_{55} \\ \overline{C}_{66} &= \frac{\overline{C}_{11} - \overline{C}_{12}}{2} \end{aligned} \tag{6.125}$$

which indicates that the homogeneous model can be considered as transverse isotropic with the plane of isotropy being the plane of the plate. We plot the dispersion curves for several quantities: phase velocity, wavenumber, group velocity and wavelength in Fig. G.1 in App. G. We find that Kane-Mindlin theory combined with equivalent elastic constant procedure is close to the 3D theory.

6.5.5 Attenuation of guided wave

Since we want to quantitatively assess the scattered signal, we must take the wave attenuation into account. Attenuation is the loss of wave intensity when propagating through a medium. This phenomenon can be due to numerous factors, the most important of which are geometric spreading, material damping, wave dispersion, dissipation into adjacent media [114] . In our case, the adjacent media is air and its contribution to attenuation is assumed very small. Geometric spreading and wave dispersion are already taken into account in the model. However, we did not consider the material damping. To do so, several models have been studied to represent Lamb waves attenuation behavior. The most common are Kelvin-Voigt (KV) and hystereris (HT). In these models, the Young's modulus of the material is considered complex with an imaginary part proportional to a coefficient γ

$$E_{\text{KV}}(\omega) = E\left(1 - i\gamma_{\text{KV}}\frac{\omega}{\omega_0}\right) \tag{6.126}$$

$$E_{\text{HT}} = E(1 - i\gamma_{\text{HT}}). \tag{6.127}$$

Since the Young's modulus is complex, it implies that the wavenumbers becomes complex itself

$$\tilde{k} = k + i\eta. \tag{6.128}$$

Now if we replace $\tilde{k}$ by its expression in the scattered wave displacement field we get

$$u_j \propto e^{i(\tilde{k}x-\omega t)} = e^{-\eta} e^{i(kx-\omega t)} \tag{6.129}$$

In the case of the model we design in this chapter, we model the attenuation of the wave due to the material following this procedure by introducing η in the expression of k_1 after its calculation Eq. 6.128.

Besides, in finite element method simulations it is common to introduce material damping using Rayleigh damping. It consists in defining the damping matrix $\boldsymbol{C}$ as a linear combination of the mass $\boldsymbol{M}$ and the stiffness $\boldsymbol{K}$ matrices

$$\boldsymbol{C} = \alpha \boldsymbol{M} + \beta \boldsymbol{K} \tag{6.130}$$

where α and β are two positive real numbers. α is the mass proportional damping coefficient and introduces damping forces caused by the absolute velocities of the model and so simulates the idea of the model moving through a viscous medium. β is the stiffness proportional damping coefficient and introduces damping proportional to the strain rate, which can be thought of as damping associated with the material itself. These coefficients need to be adjusted to match experimental data for the frequency of interest.

Gresil and Giurgiutiu derived a relationship between this loss factor and Rayleigh damping coefficients [115]

$$\frac{1}{2}(\alpha + \beta\omega^2) = \eta c_0. \tag{6.131}$$

In the simulations that we will carry out in the following chapter to validate the theoretical model, we will consider a Rayleigh damping proportional to the stiffness matrix. Thus $\alpha = 0$ and so the coefficient η that we introduce in the expression of the wave number is written

$$\eta = \frac{2\pi^2 f^2}{c_0}\beta \tag{6.132}$$

where c_0 is the group velocity of the wave at angular frequency ω.

6.6 Study of the scattering model

6.6.1 Parametric study

Fourier series truncation

In the development of the scattering model, we have used a decomposition of the solution as a Bessel-Fourier series. In order to realize the numerical implementation of this model, we have to truncate this series up to an order N as we mentioned in the previous

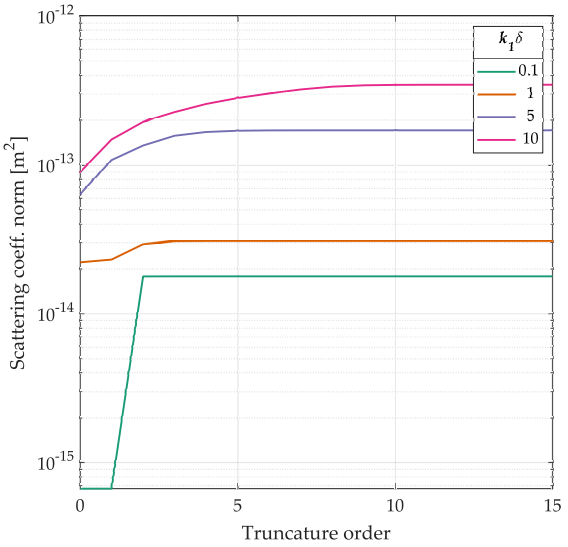

Fig. 6.14 Scattering coefficients vector's norm versus truncation index N for various values of parameter $k_1\delta$.

section Eq. 6.89. The question is to determine a value of N large enough to have a precise solution while being computationally fast. To do this, we study the convergence of the series by computing the norm of the vector $\begin{pmatrix} A_{-N} & A_{-N+1} & \cdots & A_{N-1} & A_N \end{pmatrix}^{\mathrm{T}}$ where A_n are the scattering coefficients from Eq. 6.89 for a range of N values. We plot the graph of the norm versus N for several values of the adimensional parameter $k_1\delta$ Fig. 6.14. We observe that for any $k_1\delta$ values, the norm converges when N increases. However, as $k_1\delta$ increases, the more terms of the series must be calculated. Since $k_1\delta$ is unlikely to be above 10 in our applications, we will take $N = 5$ for the rest of the chapter.

Scattering directivity

Here we seek to determine the influencing parameters of the scattering model. Wang and Chang [83] have shown that the scattering directivity pattern depends essentially on the adimensionnal parameter $k_1\delta$. In the same way, we therefore plot several directivity graphs of the S_0 mode —as we did earlier Sec. 6.4—, varying $k_1\delta$ Fig. 6.15 and keeping the other parameters constant. The material parameters are those of the Monarque project listed in Tab.6.3 and the severity ξ is set to 0.1. We notice that, indeed, the pattern is greatly modified when $k_1\delta$ evolves, either in amplitude or in shape. We can observe that for $k_1\delta$ small —that is to say below 1— we have a pattern with four lobes along angles 0°, 90°, 180° and 270°. This means that for this regime, a fraction of the wave is transmitted in straight line, another fraction is reflected back to the emitter and another fraction is reflected in the direction normal to the propagation direction. On the other hand, if $k_1\delta$ increases, the number of lobes also increases, which makes the shape of the displacement field associated with the reflected wave more complex. In other words, at such a regime, slightly changing the angle of the observation position of the reflected wave can cause a large difference in the measured amplitude. It is therefore essential to consider the influ-

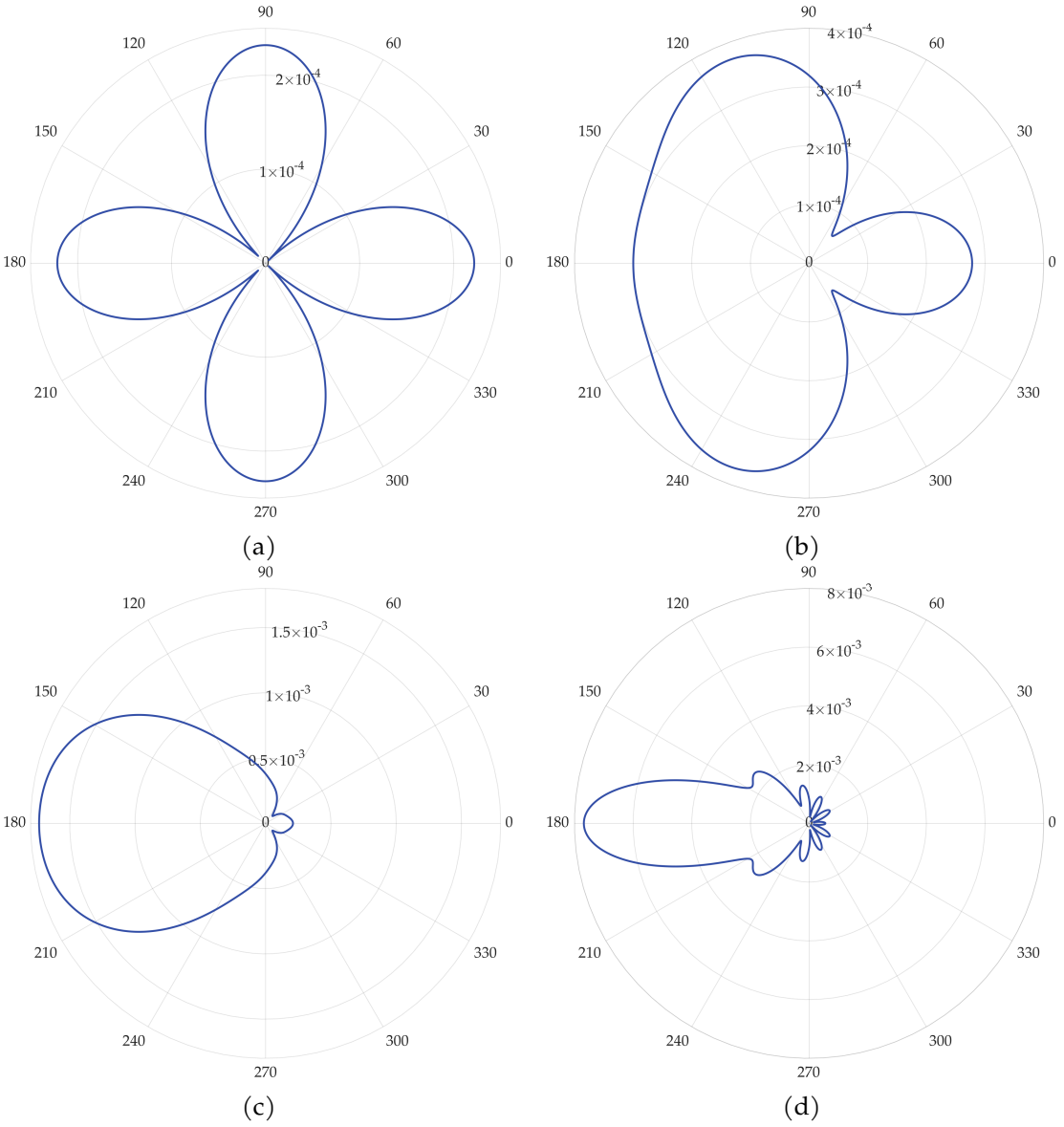

Fig. 6.15 Scattering directivity pattern for severity 0.1 and varying values of $k_1\delta$: $k_1\delta = 0.1$ (a), $k_1\delta = 1$ (b), $k_1\delta = 3$ (c) and $k_1\delta = 10$ (d).

ence of this parameter since it has a great importance on the accuracy of the results that we will obtain in the exploitation of this model.

Another parameter affecting the scattering pattern is the severity of the damage. By varying ξ, we notice that the shape of the directivity does not change but that it is scaled as a function of the severity value. We plot the directivity amplitude for several angles and for ξ going from 0 to 1 Fig. 6.16a. We observe that for strong damage severity ($\xi > 0.9$), the analytical model gives very chaotic results. This is due to the fact that for such values of ξ, the linear system of equations Eq.6.88 becomes ill-conditioned and gives unstable solutions. Since in our applications we consider damages that are not that severe, this will not be a problem for the following. We also observe that amplitude of the directivity

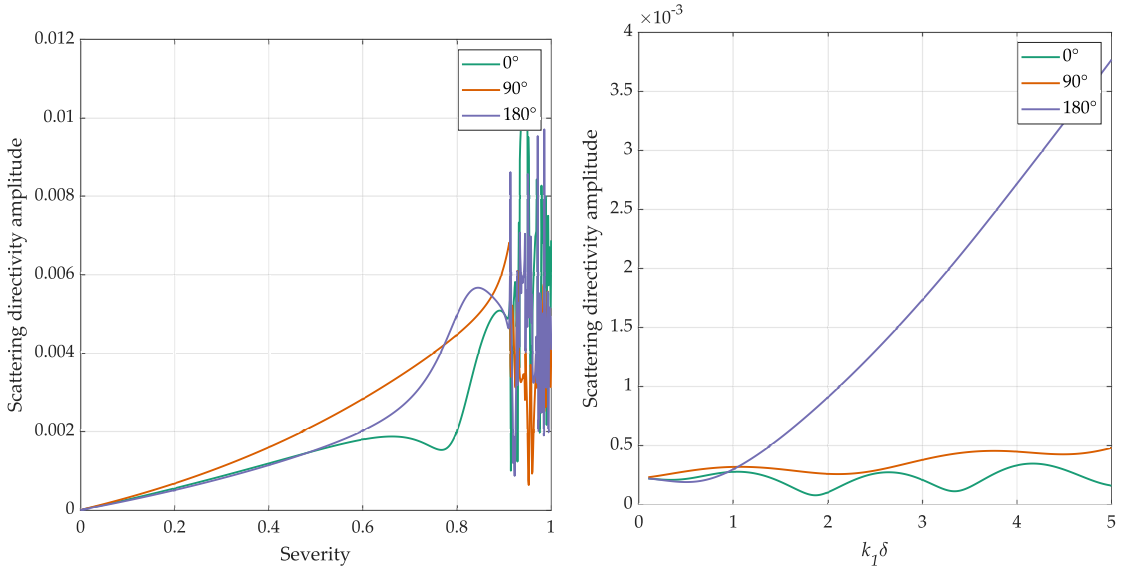

Fig. 6.16 Scattering directivity amplitude for different angles with varying damage severity (a) and varying $k_1\delta$ (b).

increases with severity. By plotting the same curve by varying $k_1\delta$, we observe that the directivity amplitude tends to increase with this parameter as shown in Fig. 6.16b.

In summary, it means that directivity pattern are sensitive to both damage size and severity which is very interesting for quantification purposes.

6.6.2 Validation on FEM data

FEM model

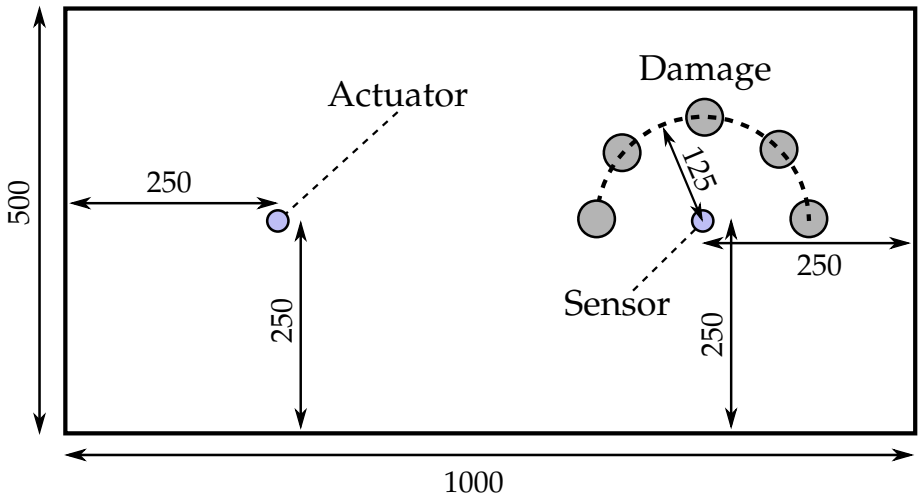

Fig. 6.17 Overall diagram of FEM model used for analytical model validation. All dimensions are in mm.

Table 6.4 Dimensions and material parameters of piezoelectric elements used for FEM simulation. The material is NCE51 and the values come from the manufacturer Noliac [116].

Property	Unit	Value
PZT radius	mm	12.5
PZT thickness	mm	1.0
E	GPa	62.5
ν	-	0.3
d_{31}	$N.C^{-1}$	-195×10^{-12}
e_{33}	$F.m^{-1}$	-1.638×10^{-8}

In order to validate the theoretical model that we have established, we compare the time signals obtained with the latter and those computed with the finite element method. Therefore, we consider a system composed of a laminate composite plate with two piezoelectric elements perfectly bonded to it Fig. 6.17. In the following, one of these elements will be used exclusively as an emitter while the other will be the receivers. In the chosen configuration, the actuator will generate two fundamental Lamb waves modes: A_0 and S_0. In order to clearly distinguish these two modes, the two PZTs are sufficiently distant so that the wave packets of each mode are split at the time they reach the sensor since their associated group velocity is different.

As earlier in this chapter, a damage is introduced as a cylindrical inhomogeneity of the material properties. The plate is made of the material used in the Monarque project [110] whose properties are listed in Tab. 6.3. The material and geometrical properties of the plate are given in Tab. 6.4.

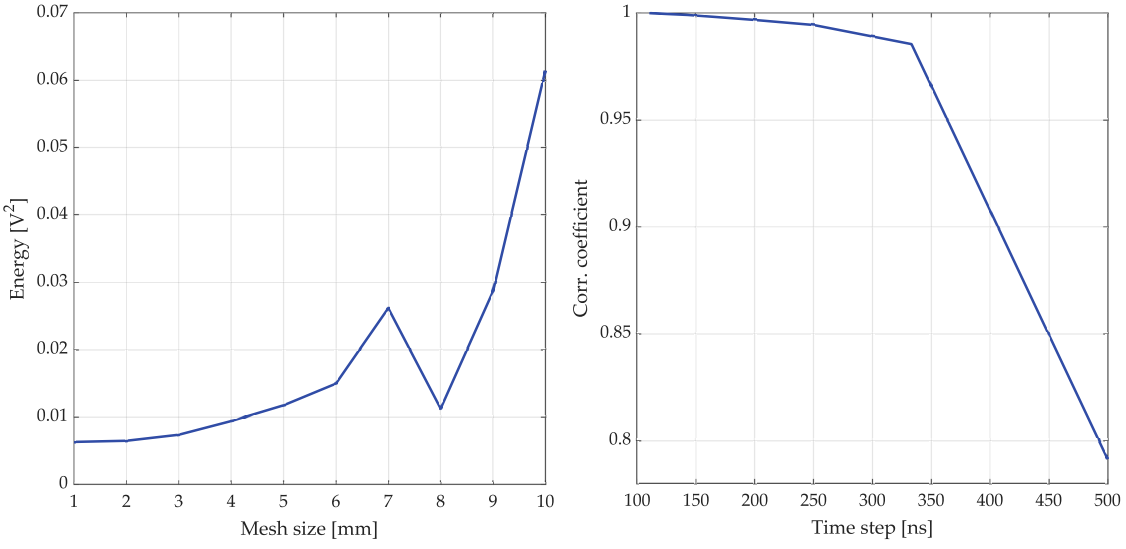

(a) (b)

Fig. 6.18 Energy convergence graph for varying mesh size (a) and correlation coefficient convergence graph for varying time step (b).

To carry out the finite element simulations, we use the MATLAB SDT toolbox developed by the company SDTools [17]. The plate is thus meshed with 4 nodes quadrilateral shell elements with a Mindlin shell formulation based on the (Mixed Interpolation of Tensorial Components) MITC element formulation. PZT are modeled by piezoelectric elements. We apply an implicit Newmark numerical integration scheme using the average constant acceleration method ($\beta_{\mathrm{Nw}} = 0.25$ and $\gamma_{\mathrm{Nw}} = 0.5$) [117]. We introduce material damping by using the Rayleigh method mentioned previously Eq. 6.130. We choose a damping proportional to the stiffness only: $\alpha = 0$ and $\beta = 6 \times 10^{-8}$. To obtain the optimal mesh size and time step, we study the convergence of the mesh. We start by looking at the mesh size convergence. To this end, a 5-cycles toneburst signal with a central frequency of 150 kHz is generated Sec. 4.2.1 with an amplitude of 10 V and we measure the response of the sensor over a period of 5 ms. We take a time step using the rule of thumb

$$\Delta t = \frac{1}{20 f_{\max}} \tag{6.133}$$

where $f_{\max}$ is the central frequency of the excitation signal. Several simulations are performed by varying the mesh size. We then plot the energy of the signal received by the sensor as a function of the mesh size Fig. 6.18a. We notice that the energy converges to a single value when we decrease the size of the mesh elements. In order to optimize the computation time, we will use elements of size 2 mm in the following. A similar study is performed to determine the optimal time step: the time step is progressively decreased and we compute the maximum of the cross-correlation between each pair of consecutive signals Fig. 6.18b. The shorter signal is interpolated in the frequency domain to match longer signal length. We observe that the correlation coefficient converges to 1 when time step becomes smaller as mentioned in [117]. For the rest of the chapter, we will choose a 200 ns time step to keep a good trade-off between performance and computation time.

Results

We first compare qualitatively the time signals obtained with the model developed in the present chapter and by the finite element method. We study a damage located on the actuator-sensor path with an angle $\theta_S = 180°$, a severity $\xi = 0.1$ and a radius $\delta = 5$ mm while the excitation signal has a central frequency of 150 kHz. If we study the case without material damping, we obtain the signal Fig. 6.19a. We notice that the amplitudes of the first wave packet match well. These signals are also temporally aligned, however we can notice when the FEM signal is more spread out in time. If we plot the same results but for thinner PZT of 0.1 mm thickness, this difference is greatly reduced Fig. 6.19b. It turns out that this difference comes essentially from the thickness of the PZT: if it increases, the wave packet spreads out in time and decreases in amplitude. This means that the actuator and sensor model we use are not suitable for PZT of large thickness. This may be due to several phenomena such as a change in the local stiffness of the plate caused by PZT presence or a non-uniform deformation along the z axis in sensor as mentioned by Duquenne

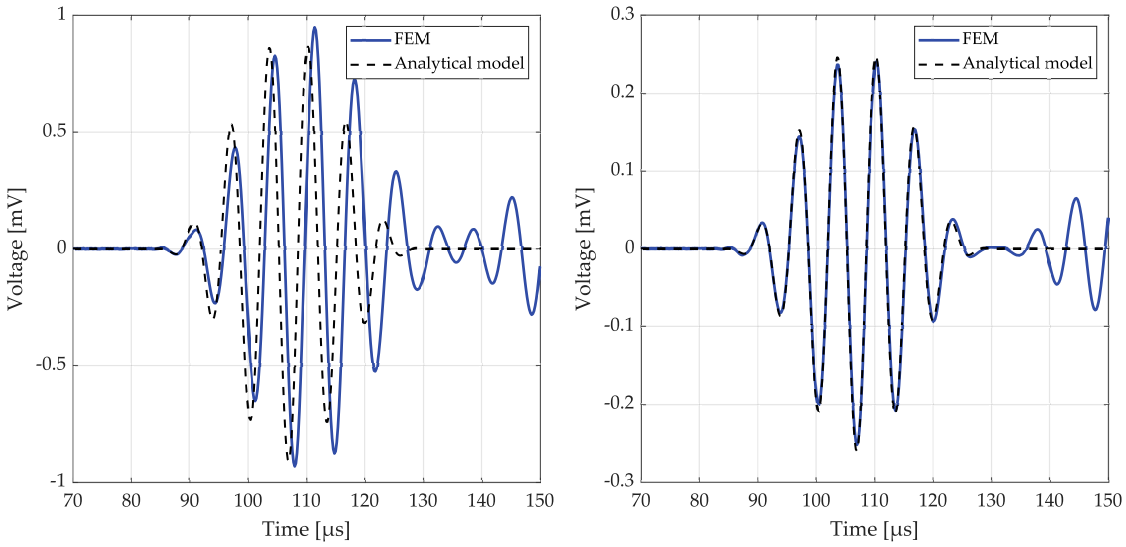

Fig. 6.19 Time signal comparison between analytical model and FEM simulation without damping for PZT of thickness 0.5 mm(a) and 0.1 mm (b).

et al. [118]. In their study, the authors also mentioned that the wavelength to PZT thickness ratio must be low to consider that the displacement imposed to the sensor interface is the surface displacement field associated to incident Lamb waves. This assumption is not met here which may partially explain the difference observed. Indeed, if the excitation frequency is lower, we observed that the discrepancy was smaller. However, for the PZT thickness we are dealing with here, this model is sufficiently accurate to estimate the scattered signal amplitude. If one wished to apply this model to thicker PZT, one would have to question the assumptions made, for example plane stress for the sensor PZT. It should also be noted that in Fig. 6.19, we observe other wave packets after the S_0 mode in the FEM signal. These are the A_0 mode and the reflections from the edges of the plate which are not taken into account in the analytical model.

Regarding computation time, the analytic model developed here showed great performance compared to the FEM simulation: few seconds versus 20 minutes on the same laptop.

If now we take material damping into account, we need to follow the approach described in Sec. 6.5.5. To select the value of η, we use Eq. 6.132. To compute the group celerity, we measure the time of flight between the excitation signal and the first wave packet using envelope of the signals. For excitation frequency of 150 kHz, we find $\eta = 4.8$ m^{-1}. The resulting time signal is shown in Fig. 6.20. We notice that the signal amplitude is lower than in Fig. 6.19a due to attenuation. We also observe that the signal amplitude is slightly lower than the FEM results, whereas in the non-damped case the amplitudes of analytical and FEM signal are very close. This can be due to the computation of η which relies on a very simple equation but which can capture all the physics phenomena that occur in material damping. However, the result obtained with the model are still of the same order

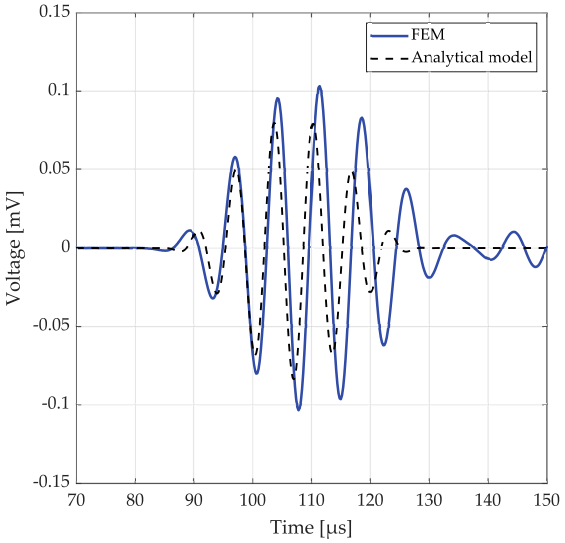

Fig. 6.20 Time signal comparison between analytical model and FEM simulation with damping for PZT of thickness 0.5 mm.

of magnitude than the FEM and this small difference should not disturb its exploitation. Regarding time alignment, there is no difference to notice with the case without damping.

We now quantitatively study the influence of the parameters on the model accuracy. To do this, several FEM simulations are carried out by varying a parameter at a time: the position of the damage and thus the angle θ_S, the excitation frequency, the size or the severity of the damage. Then, we compare the signals obtained with the analytical model developed in this chapter by computing two different metrics. The first one is the relative difference in amplitude, which is calculated from the envelopes of the signals between the maximum of the amplitude of the FEM signal and the analytical sensor signal. To compute these envelopes, we take the absolute value of the Hilbert transform of the temporal signals

$$\epsilon_{\text{ampl}} = \frac{|\max(|\mathcal{H}(S_{\text{FEM}}(t))|) - \max(\mathcal{H}(|S_{\text{model}}(t)|))|}{\max(|\mathcal{H}(S_{\text{FEM}}(t))|)} \tag{6.134}$$

where $\mathcal{H}$ stands for the Hilbert transform whereas S_{FEM} and S_{model} denote the signal obtained from FEM and the signal obtained with the analytical model, respectively. We define a second metric to evaluate the time correspondence between two signals. For this purpose we calculate the coefficient which maximizes the cross-correlation

$$\epsilon_{\text{cc}} = 1 - |\max(S_{\text{FEM}}(t) * S_{\text{model}}(t))| \tag{6.135}$$

where $S_{\text{FEM}}(t) * S_{\text{model}}(t)$ stands for the cross-correlation between S_{FEM} and S_{model}. ϵ_{cc} is defined such has to be 0 if the signals perfectly match and greater than 0 if the signals are out of sync. In order to study the S_0 mode only, we compare the signals on the time range going from the start of the wave packet of S_{model} to the end of the very same wave packet.

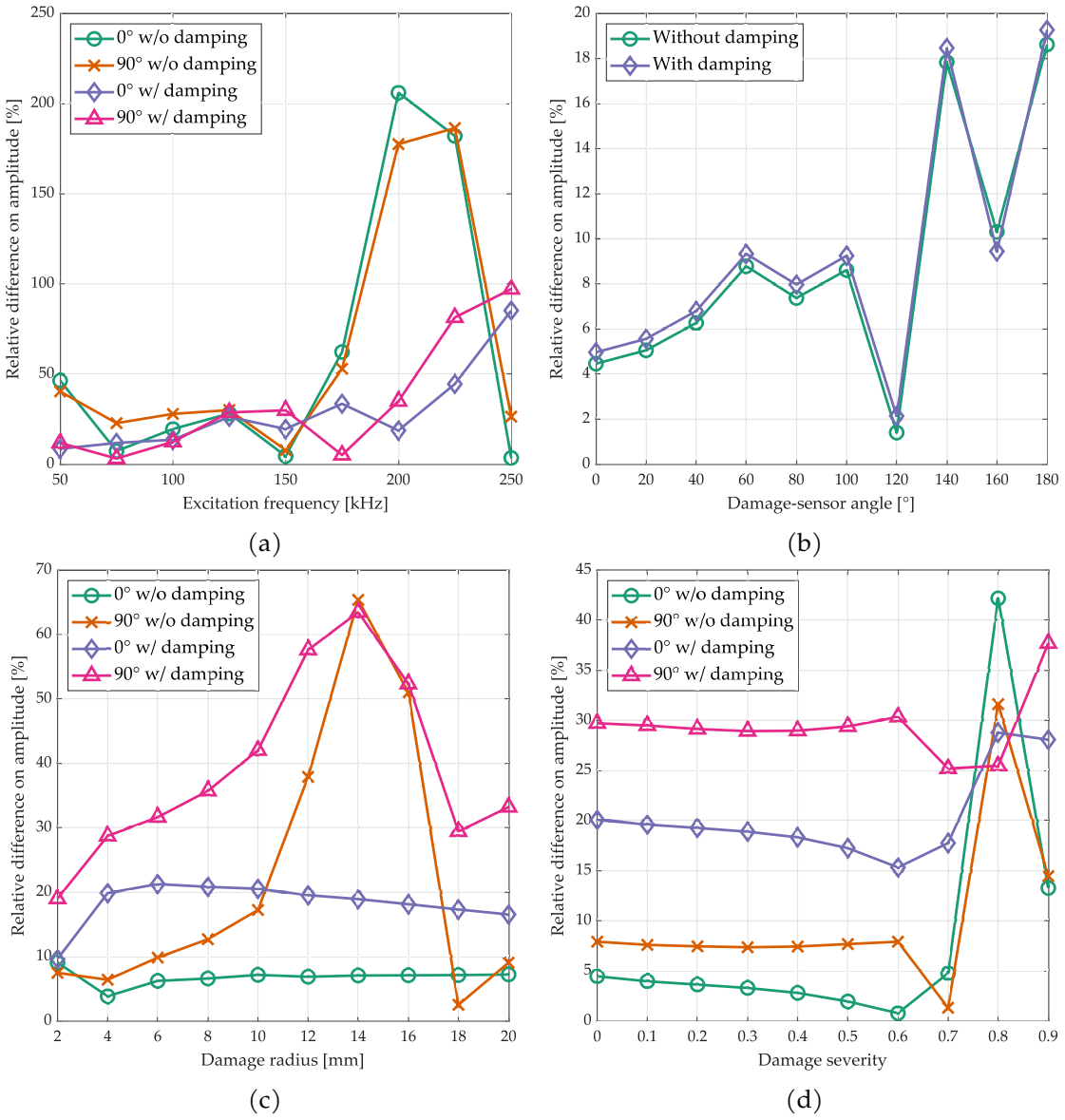

Fig. 6.21 Amplitude relative difference graphs for varying parameters, with and without material damping: excitation frequency (a), damage-sensor angle (b), damage radius (c) and damage severity (d).

If we look at the relative difference in amplitude and time as a function of frequency Fig. 6.21a and Fig. 6.22a, we notice a rise of the difference with frequency. To investigate the cause of this trend, we plot the transfer function of the model in Fig. 6.23. From Fig. 6.23a, we notice that the transfer function has a very small response around 275 kHZ . This means that the wavelength associated with the central excitation frequency is close to a multiple of the sensor diameter, here $\lambda \approx 2c$. By approaching this point, the amplitude of the response decreases and the spectrum of the excitation signal is distorted. This requires a finer mesh in the finite element model to correctly capture the physics of the problem. Indeed, if we choose finer elements, we obtain a constant difference for all frequencies.

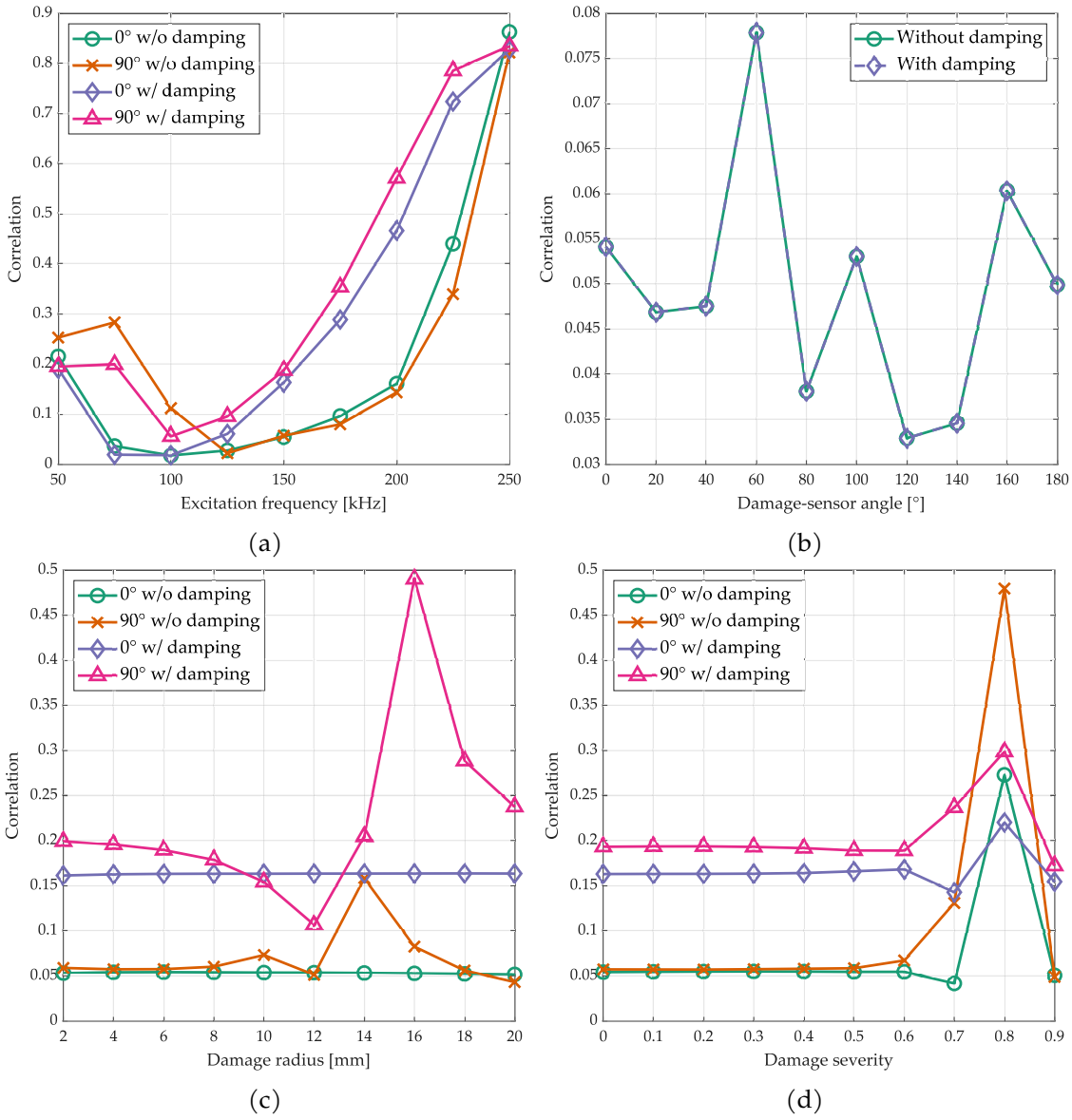

Fig. 6.22 Maximum cross-correlation error graphs for varying parameters, with and without material damping: excitation frequency (a), damage-sensor angle (b), damage radius (c) and damage severity (d).

A similar analysis can be conducted for the influence of the damage radius. Indeed, we observe a peak around 14 mm for the amplitude metric Fig. 6.21c for an angle of 90°. If we look at the transfer function of the complete system with this size of damage Fig. 6.23b, we notice that the response is close to a minimum for the excitation frequency 150 kHz. As for the influence of the frequency, by taking a finer mesh we obtain a constant relative difference in amplitude for all damage sizes.

Regarding the influence of the angle θ_S on the amplitude metric Fig. 6.21b, we notice that the damping has very little influence. The variation of difference for the range of angles is related to the discussion on the directivity profile we had earlier Sec. 6.6.1. A

small inaccuracy in the shape of the profile can lead to a relatively large difference in the result. The same analysis can be done for the time correlation metric Fig. 6.22b.

For severity, both metrics show large deviations for strong severities Fig. 6.21d and Fig. 6.22d. This is consistent with the point we made earlier in Sec. 6.6.1. For the other severities, the difference is constant. However, we observe that damping introduces an additional deviation from FEM.

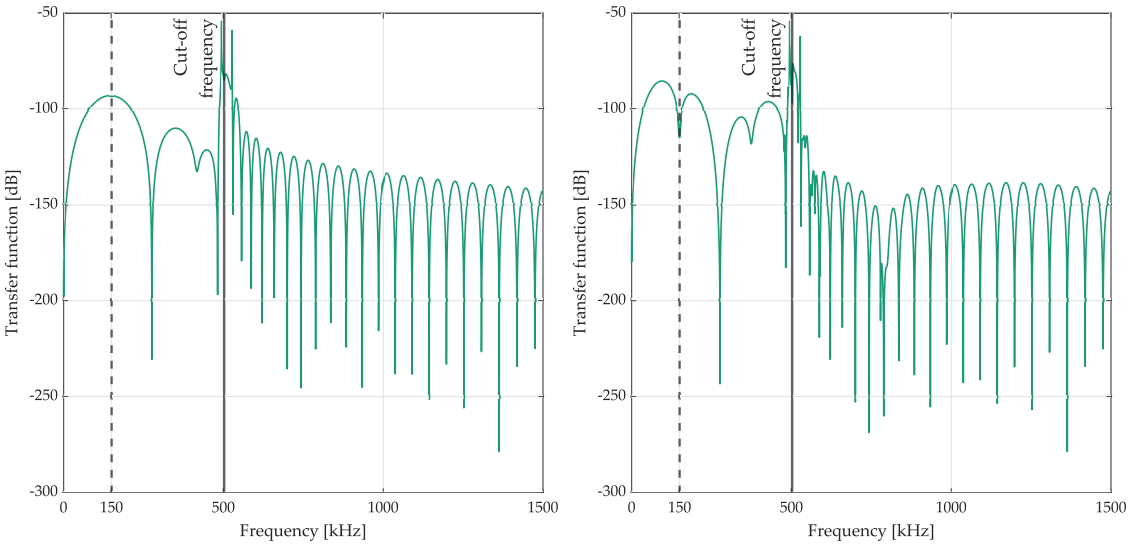

Fig. 6.23 Transfer functions of the system for a damage radius of 5 mm (a) and 14 mm (b).

6.7 Conclusion

In this chapter, we have developed an analytical model to predict the voltage measured by a piezoelectric sensor at the passage of a wave generated by a piezoelectric actuator and reflected by a damage. For this purpose, we studied a system made of two piezoelectric elements ideally mounted on a quasi-isotropic laminate composite plate including a damage. We have made several assumptions in order to model this system. In particular, we assimilated the plate to a single transverse-isotropic layer and the damage to a cylindrical inhomogeneity of the material properties. We also limited the study to the fundamental symmetric mode S_0. For this purpose we relied on the Kane-Mindlin plate theory and we showed that this was the most relevant in the isotropic case. Then we developed each of the subsystems of the problem (damage, actuator and sensor) by taking and adapting existing models of the literature. By unifying these different subsystems in a single model we managed to establish a comprehensive analytical model. We also performed a parametric study to establish the influential parameters of the model, namely the product $k\delta$ and the severity ξ. This model was then validated by comparing its results to those obtained by the finite element method. We have observed a very good matching in time

and amplitude for the PZT of small thickness and a slight time shift for the thickness of the PZT used in the experiments of ReMAP and Monarque projects. Finally, we quantitatively evaluated the model difference with respect to the FEM by varying the model parameters with and without damping.

The analytical model developed can have many applications, for example to improve imaging techniques by taking into account the directivity of the waves reflected by the damage, and create tuning curves that include damage size and severity. In the next chapter we will use this model to estimate the damage parameters from experimental signals.

This model can also be improved on several points. For example, it would be interesting to integrate the A_0 propagation mode. Indeed, there are in the literature models similar to those used here for the S_0 mode [83, 119, 80]. It would also be possible to model other kinds of damage such as blind holes [78, 79], which could have applications in the study of corrosion damage. It would also be possible to extend the range of validity of the existing model by choosing more realistic actuator and sensor models for thicker PZT. It would be wise to propose a more global formulation of the model applicable to any type of laminate composite, for example by writing the scattering equations for each ply and imposing continuity conditions at each interface between two layers. Finally, it would be interesting to study if the results obtained vary with the boundary conditions applied to the plate, for example a clamped structure.

Chapter 7

Damage size and severity quantification by parameters identification using analytical model

Summary

In this chapter we propose a damage size and severity assessment strategy using a parameters identification algorithm which does not require any learning step and thereby, no training data. To solve this inverse problem, we use the analytical model developed in the previous chapter. This approach consists in comparing the amplitude of the S_0 mode of the experimental or simulation signal to the signal obtained with the model. By tuning the damage size and severity we find the couples of values that provides the best match. The results are then combined for each actuator-sensor pair at each excitation frequency to give a single result. We also describe how the analytical model is updated to avoid amplitude mismatch. This method is applied to simulation data carried out on a quasi-isotropic plate including a damage of various size and severity. We also identify the damage characteristics from experimental data with the same configuration.

Contents

7.1 Motivation and objectives

In Chapter 4, we presented a data-driven method for damage size quantification. This family of methods is the most widespread in the literature since they allow to ignore the physics of the interaction between guided waves and damage. On the other hand, they require labeled data to be implemented, and these data are rarely available in large quantities. A different and original approach consists in using a theoretical model of the wave

propagation. For example, Masson et al. have developed a localization method which involves calculating the point in the structure which maximizes the correlation between the experimental signals and a model of wave propagation [60]. The damage is considered here as a point omnidirectional reflector. By developing an analogous method that takes into account the size and severity of the damage, one could expect to estimate these characteristics. This type of approach is advantageous because it does not require a learning step and therefore training data. It only implies to know the material characteristics of the structure and the piezoelectric patches, which are provided by the manufacturer.

The objective of this chapter is to solve the inverse problem of quantifying the size of the damage by also proposing to estimate its severity. For this we use the analytical model developed in the previous chapter which predicts the voltage measured by a piezoelectric sensor at the passage of a wave generated by a piezoelectric actuator and reflected by a damage. For this purpose, we studied a system made of two piezoelectric elements ideally mounted on a quasi-isotropic laminated composite plate including a damage.

We develop an algorithm to identify the characteristics of the damage after updating the analytical model. In the following, we first present the theory of the inversion method and then application results on FEM and experimental data.

7.2 Quantification by identification approach

7.2.1 General idea

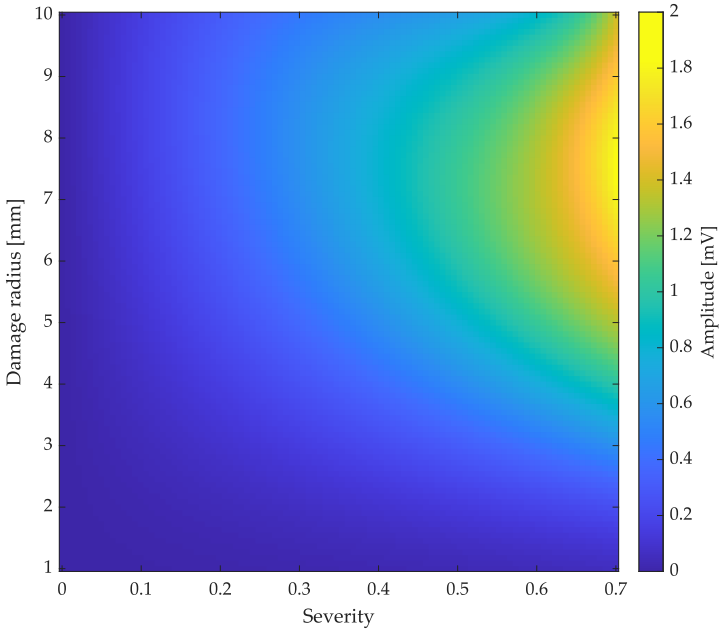

Fig. 7.1 Amplitude of the first wave packets of the signal obtained with the analytical model for various damage size and severity. The excitation frequency is 150 kHz.

In Chapter 5, an analytical model was developed to predict the voltage measured by a piezoelectric sensor at the passage of a wave generated by a piezoelectric actuator and diffracted by a damage. For this purpose, we studied a system made of two piezoelectric elements ideally mounted on a quasi-isotropic laminated composite plate including a damage. In this chapter we will develop an algorithm to quantify the size and severity of a damage from measured experimental or simulation signals. We defined the severity ξ in the same manner we did in previous chapter (see Eq. 6.1).

The general idea of the procedure we will present is to compare an unknown difference signal (i.e. the difference of the signals in the damaged state and in the healthy state for the same pair of PZTs) with the signal from the analytical model. By varying δ and ξ, respectively the radius and the severity of the damage, we can obtain a signal that best approximates the target signal. Indeed, as we have seen in Sec. 6.6.1, these two parameters have a great influence on the amplitude of the wave diffracted by the damage and thus on the signal measured by the sensor. The method developed here consists in solving an inverse problem by estimating the damage characteristics from the unknown signals available.

From the analysis of the analytical model in the previous chapter and the experimental data from the ReMAP project, we know that the size and severity of the damage have a large influence on the amplitude of the diffracted wave. To solve the inverse problem, we will therefore find the couple (δ, ξ) with which the analytical model gives an amplitude as close as possible to the experimental signal. However, in our analysis of the model, we noted that the severity and the size of the damage have analogous actions on the amplitude of the received signal. Indeed, while an increase in severity (i.e. if ξ decreases) tends to increase the amplitude, an increase in size induces a similar effect. Fig. 7.1 illustrates this phenomenon. In other words, there is no unique solution to the inverse problem.

However, since the damage leads to a directivity of the diffracted wave and because the frequency of the excitation signal also changes this directivity pattern, it is possible to reduce the admissible values by combining different results.For example, for a given path and frequency, we will have a group of (δ_1, ξ_1) values that match the model with the data. For another path and another frequency, there will be another group (δ_2, ξ_2). The true value of the couple is thus located in the intersection of group 1 and group 2 $(\delta, \xi) \in (\delta_1, \xi_1) \cap (\delta_2, \xi_2)$.

7.2.2 Model updating

Since we want to use the analytical model to match the amplitude of the theoretical signal with the unknown signal, we must ensure that this model has as little error as possible so as not to compromise the quality of the results. In the validation of the model in the previous chapter (see Sec. 6.6), we knew in advance the value of the Rayleigh damping used in the simulation. We could then get back to the value of the η attenuation parameter Eq. 6.132. Here we will have to estimate the damping from the data of the healthy state. Following the procedure of Gresil and Giurgiutiu [115], we assume that the amplitude of

the first wave packet is of the form

$$\phi = \frac{A}{\sqrt{r}} e^{-\eta r} e^{i(kr-\omega t)} \tag{7.1}$$

where ϕ is a general perturbation propagating along $\boldsymbol{e_r}$ with wavenumber k. We try to estimate the parameters A and η from the data.

First, we estimate η by plotting the first wave packet amplitude on the actuator-sensor direct path in the healthy state of the unknown signal, versus the distance between actuator and sensor. Then we perform regression using the trust region algorithm which is a nonlinear least squares estimation method. We also get the value of A.

In the previous chapter we noticed a shift in amplitude between the model and the finite element simulation. We stated that this difference comes from the actuator and sensor models that are less suitable for thick PZTs or high frequencies. To correct this mismatch, we propose to apply a multiplicative correction factor to the signal obtained from the model. For the same actuator-sensors pairs and from the estimated *eta*, we compute the theoretical signal amplitude on the direct path and in the healthy state with help of the transfer function H_{AS} (see App. F). We plot these amplitude values versus corresponding actuator-sensor distance. By fitting Eq. 7.1 to the data from the model, we find a multiplicative coefficient $\tilde{A}$. To reduce the error of the model, we will use apply the multiplicative correction factor $A/\tilde{A}$ to the analytical response in the rest of the chapter.

7.2.3 Image fusion process and algorithm architecture

Once the attenuation is identified and the model updated, amplitude maps are computed for a range of δ and ξ for each path and each excitation frequency considered. In the end, we have a dataset of the maximum amplitude of the first scattered wave packets for various damage characteristics. This computation step is quite computationally intensive but only needs to be done once for each structure. Then the comparison between precomputed maps and experimental signals are computationally inexpensive which is an asset for on-board implementation.

The next-step consists in retrieving the amplitude of the first scattered wave packet from the experimental or simulation signal. Then we look at the damage chart (i.e. the amplitude map for a range of damage size and severity) for the same actuator-sensor path and the same excitation frequency. To evaluate which (δ, ξ) have the best match with the analytical model result, each point is assigned a score between 0 and 1. This score is computed with the absolute value of a Gaussian function of mean equal to the amplitude of the unknown signal and of standard deviation σ

$$P_{ij} = \sqrt{2\pi}\sigma \exp\left(-\frac{1}{2}\left(\frac{X_{\text{xp}} - X_{\text{th}}}{\sigma}\right)^2\right) \tag{7.2}$$

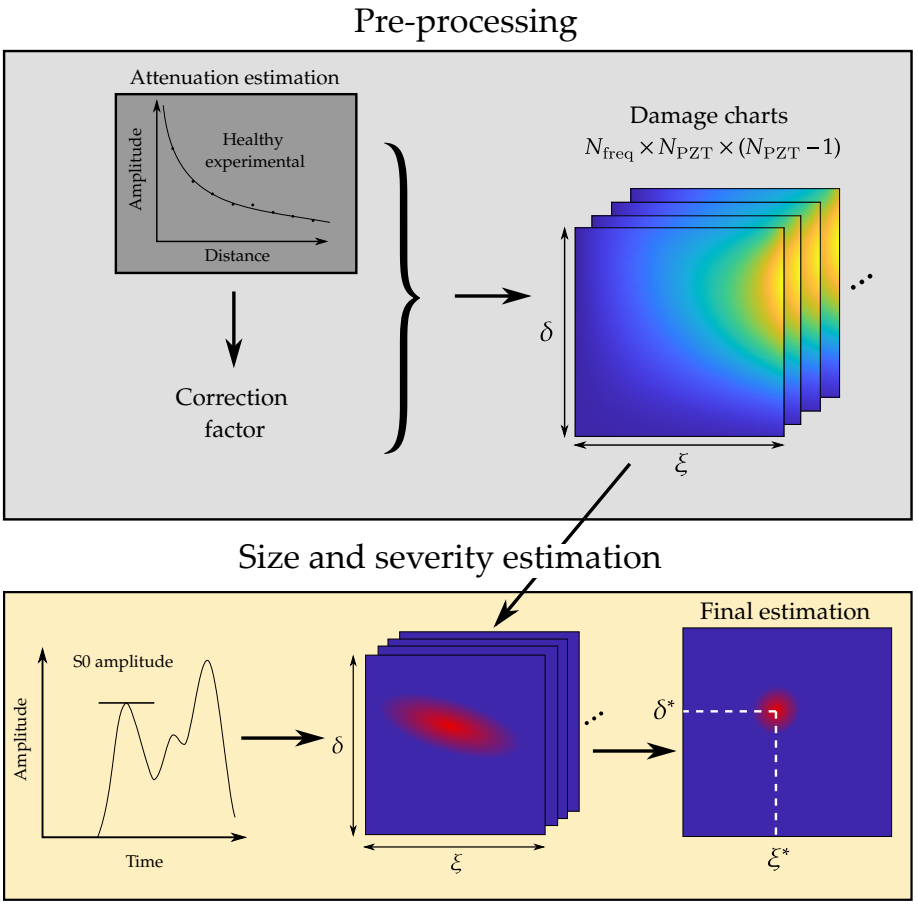

Fig. 7.2 Overview of the damage characteristics identification algorithm.

where X_{xp} and X_{th} are respectively the amplitude of the first wave packet of experimental signal and analytical signal. i, j are the index associated with the range of δ and ξ. The factor $\sqrt{2\pi}\sigma$ is introduced to have $P_{ij} \in [0,1]$. σ can be chosen by the user to have a more or less permissive comparison. In the following, based on the study of the model error seen in Sec. 6.6, we choose to have $3\sigma = 0.3X_{\text{th}}$. This way we ensure that 99.73% of the values lies within ±30% from X_{th}.

Once this process has been done for each patch and each frequency, we sum the results into a single image to reduce the admissible values of (δ, ξ). The estimated value is then computed as the one associated with the maximul score

$$(\delta^*, \xi^*) = \underset{(\delta,\xi)}{\text{argmax}}\, P_{ij}. \tag{7.3}$$

Fig. 7.2 shows the overview of the complete process.

7.3 Applications

To assess the performance of the proposed approach, it is applied to FEM data and experimental data. In both case, we study the same specimen configuration that has been used

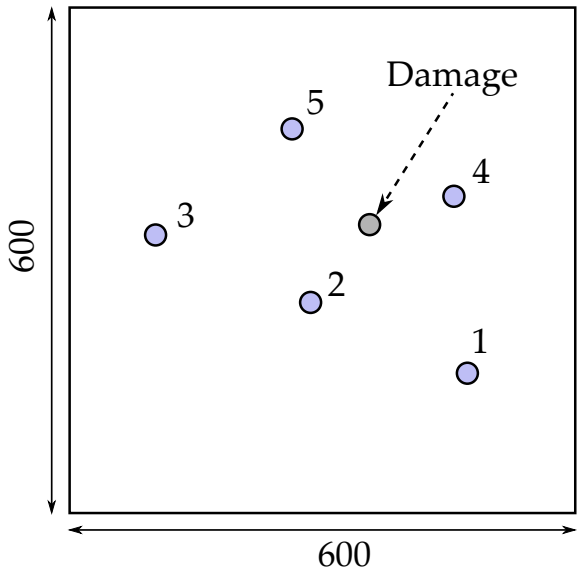

Fig. 7.3 Diagram of composite plate used in experiments. Dimensions are in mm.

in Monarque project [110]. The structure under study is a 600 mm by 600 mm composite plate of 2.4 mm thickness. Five piezoelectric transducers are bonded to its top surface which coordinates are specified in Tab. 6.4. An artificial damage is also introduced. The material properties of plate and piezoelectric material are the same as the ones in the Chapter 5 (see Sec. 6.6). Fig. 7.3 gives an overview of the setup.

7.3.1 Application to FEM data

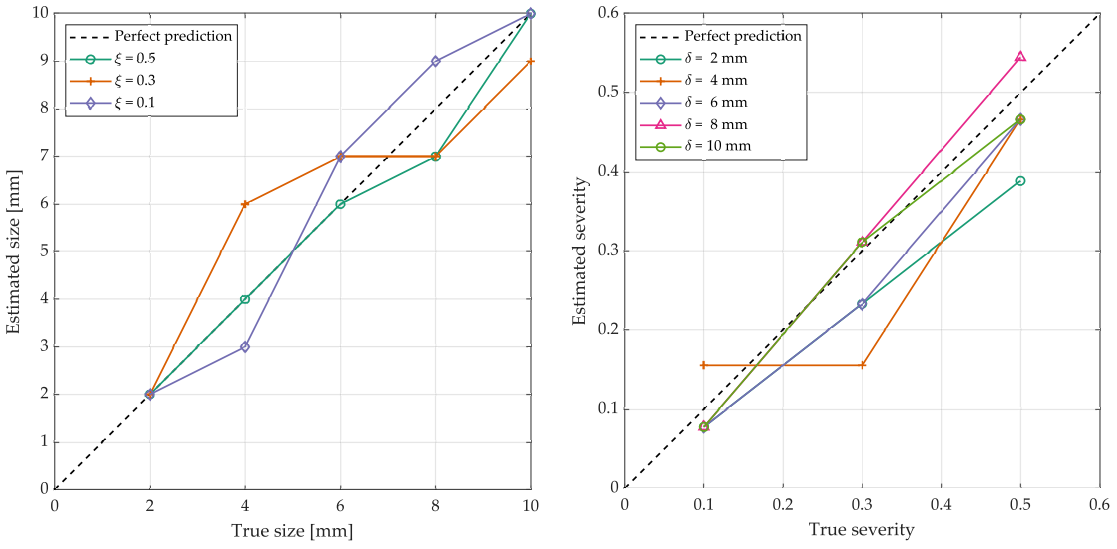

(a) (b)

Fig. 7.4 Results from identification algorithm for damage size (a) and damage severity (b) prediction.

We first apply the method to data coming from FEM where the damage is modeled as a decrease of stiffness in a cylindrical inhomogeneity. The FEM parameters are the same as in Chapter 5. Several damage sizes and severities are investigated. The considered excitation frequencies range from 50 to 200 kHz with a 25 kHz step. The prediction found are given Fig. 7.4 where we plot each estimated damage characteristic (size or severity) versus the true value.

We notice that for any considered severity the predicted sizes are very close to reference values. For severity prediction we also found relative good predictions. In that case, we can observe that the results seem more accurate when the damage size increases.

7.3.2 Application to experimental data

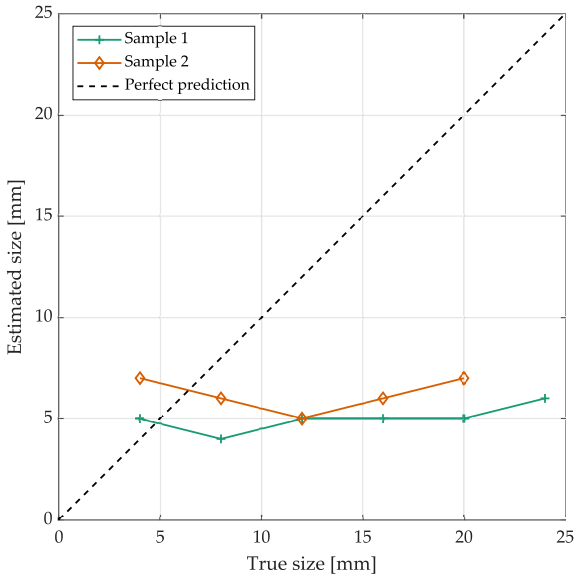

Fig. 7.5 Results from identification algorithm for damage size in experimental applications.

The method is now applied to experimental data. Here the damage is created through laser shocks in the same manner we detailed in Sec. 4.4.2. As we did for the L1 coupon, several adjacent delaminations were created and LW acquisitions were done between each shot with the same hardware as in ReMAP project. The considered excitation frequency range from 50 to 300 kHz with a 10 kHz step. As we did for the L1 coupon, ultrasonic NDT tests were performed to measure true damage size. Two coupons were tested in total. The estimated damage sizes are shown in Fig. 7.5. We obsverse that the first damage size is very close to the ground truth, however we see large discrepancy for further damage sizes. It can be explained by the shape of the created damage: since it is not a single delamination but an assembly of small damages, there is space between them (see Fig. 4.21). Besides damage size, we also estimated an equivalent severity for each coupon. We found $\xi = 0.6$ for the first coupon and $\xi = 0.4$ for the other.

7.4 Conclusion

In this chapter we introduced a damage size and severity quantification method. This approach relies on a parameters identification process which use the analytical model developed in the previous chapter. To perform this task, we find the numerical values of damage size and severity that minimize the difference between the amplitude of the scattered S_0 mode in the experimental signal and the analytical one. Since the solutions are not unique, we combine the results from all actuator-sensor pairs and all excitation frequencies to reduce the possibles values. We found very good results on FEM data and encouraging prediction on experimental data. However, to be fully validated this method needs to be tested on damage of increasing size. For example, it would be interesting to introduce a damage with the laser shocks technique and test the sample in fatigue. This would allow for a single delamination to grows in size. The sensitivity of the method to the frequency selected should also be assessed. Indeed, depending on piezoelectric elements geometries and excitation frequency, Lamb waves modes are not generated with the same magnitude. Then, if we carefully select the frequencies where A_0 has a low amplitude we can strongly improve the robustness of the method.

Future works should focus on testing this algorithm on more complex structures, e.g. a plate with a stiffener. It would also be interesting to make this method more robust in the evaluation of S_0 mode amplitude, for example by using mode identification methods to properly split the fundamentals Lamb waves modes.

Chapter 8

Conclusion and perspectives

8.1 Conclusion

The scope of this thesis was to propose methods for the quantification of damage size in composite materials. It is a multidisciplinary work bringing some answers to the problem of delamination size assessment in CFRP laminates equipped with piezoelectric elements representative of the aeronautical context.

To properly validate the developed quantification methods, it is necessary to have experimental data obtained in conditions close to the industrial context. For this purpose, we have carried out fatigue test campaigns on realistic samples of aeronautical structures to create a database that allows us to test the algorithms in question. The first step of these test campaigns was to verify the resistance of the piezoelectric elements to fatigue loading and we concluded that the transducers met the specifications. We then performed fatigue tests on samples with stiffeners by imposing different loading and initiating different types of damage. Following the same principle, we performed fatigue tests on large panels. The data obtained allow a rigorous validation of the proposed approaches. Moreover, as these data are publicly available, it is hoped that other researchers will use these results to validate their own methods, which will provide a point of comparison to judge the performance of the different approaches. We analyzed the L1 sample data to identify, among the classical damage indexes, the DI most likely to be used for quantification or prognostics. To make this selection in a quantitative way we used a score approach by classifying the DI according to their monotonicity, trendability and prognosability. We have identified several features that can be used as effective health indicators. Finally, we characterized the measurement noise to ensure the good quality of the measured signals on the one hand, and on the other hand to be able to reproduce a similar noise in the numerical simulations.

The problem addressed in this thesis being the damage size quantification methods by guided waves, we proposed two methods of different kinds. The first one is a data-driven method, based on the learning of a mathematical regression model from labeled input data and allowing to predict damage sizes from signals where the damage size is unknown. The regression is done by learning the different parameters of the model for several pairs of values (HDLI,δ) where HDLI is a feature defined from the images obtained by a localization algorithm. Once learned on the beginning of the life of a damage,

the quantification model allows to predict the size of the damage from signals obtained from the same structure. We applied this method on data from finite element simulations to identify the influential parameters. We also used several localization methods to calculate the HDLI and noticed that the RAPID approach gave the best results. We then obtained promising results on experimental data. We also illustrated a first approach to transfer learning by using the quantification model trained on a coupon to make prediction on another one with the same configuration and we found encouraging results. To consider an industrial deployment of data driven methods, it is imperative to develop this kind of approach.

The second method concerned the inversion of an analytical model for the estimation of the damage characteristics. For this we first developed an analytical model to predict the voltage measured by a piezoelectric sensor at the passage of a wave generated by a piezoelectric actuator and reflected by a damage. For this purpose, we studied a system made of two piezoelectric elements ideally mounted on a composite laminate plate including a damage. We established several simplifications, including using Kane-Mindlin plate theory to approximate Lamb waves and restricting ourselves to quasi-isotropic composite materials. By unifying different models from the literature, we managed to establish a comprehensive model. We have analyzed the different influential parameters of this model and compared it to the results obtained by the finite element method. We have highlighted the amplitude dependence of the received signal on the damage characteristics (size and severity) and on the excitation frequency. Then we developed an algorithm to identify the damage parameters, based on the fusion of results obtained on each path and each excitation frequency. We have applied this approach to finite element simulation data as well as to experimental data.

8.2 Perspectives and recommendation for future work

In this work we have brought some solutions to the different problems mentioned at the beginning of this thesis. However, additional studies deserve to be conducted in order to allow a better understanding of certain phenomena and to improve the quality of the results obtained. Regarding the test campaigns, it would be wise to have a reliable reference assessment of the damage characteristics —presence, position and size. This has been partly achieved since non-destructive testing measurements by ultrasonic waves have been carried out. However, these measurements require an interruption of the test in progress and are not automatic. Moreover, they depend strongly on the operator who performs them. A better solution would be to use a thermography measurement for each SHM acquisition. By applying a localized heat source such as a laser and recording with a thermal camera, it would be possible to post-process the resulting images to obtain information on the coupon's structural health reliably. To improve the quality of the tests, it would also be interesting to study the resistance of the piezoelectric elements to impacts. Indeed, during our tests we noticed that some piezoelectric patches broke at the time of

the impact around the collided zone. Yet, it is these PZTs that can give us the richest information on the damage. One way to overcome this problem would be to use laser shock delaminations to initiate the damage.

Regarding the data-driven method developed in this thesis, it would be wise to work on the transfer learning of the quantification model. The goal would be to train the model over the life of a sample and then use the learned model on a part of the same configuration —same geometry, same material and same configuration of PZT. Thus, we would avoid a component by component training which is difficult to consider in an industrial context. One way to achieve this task could be to use Bayesian inference methods by taking the values learned during the training phase as a priori probability of the model parameters. One could even consider training the model on a finite element model and then recalibrating the quantification model on experimental data to reduce the need for labelled experimental data.

The analytical model developed in this thesis can be improved on several points. For example, it would be interesting to integrate the A_0 propagation mode by following existing scattering model similar to those used here for the S_0 mode [83, 119, 80]. It would also be possible to model other kinds of damage such as blind holes [78, 79], which could have applications in the study of local corrosion damages. To improve the validity of the model, it is necessary to choose more realistic actuator and sensor models for thicker PZT. It would be wise to propose a more global formulation of the model applicable to any type of laminate composite, for example by writing the scattering equations for each ply and imposing continuity conditions at each interface between two layers.

For the analytical model inversion method, it would be interesting to study the influence of the variability of the material and geometric parameters of the system on the accuracy of the results. A better method of evaluating the attenuation would also make the results much more reliable. It would also be worthwhile to apply this method with a more elaborate model as we mentioned in the previous paragraph. In this way, we could use this algorithm to evaluate the damage size in the L1 and L2 data from ReMAP project. Finally, this method could be used as a basis for a hybrid data-driven and physics-based model to make the proposed method more flexible to damage whose nature deviates from a local inhomogeneity.

Appendix A

Sensors positions for L1 and L2 coupons of ReMAP project

Table A.1 AE and PZT sensors positions in mm. The asterisk indicates a PZT on the vertical part of the stiffener. In this case the center of the PZT is placed 25 mm from the top of the stiffener vertical part.

Sensor	x [mm]	y [mm]
PZT 1	140	25
PZT 2	65	25
PZT 3	25	215
PZT 4	100	215
PZT 5	140	120
PZT 6	25	120
PZT 7*	82.5	80
PZT 8*	82.5	160
AE 1	20	190
AE 2	20	20
AE 3	145	50
AE 4	145	220

Table A.2 PZT locations on L2 coupons. The asterisk indicates a PZT on the vertical part of the stiffener. In this case the center of the PZT is placed 25 mm from the top of the stiffener vertical part.

PZT	x [mm]	y [mm]	PZT	x [mm]	y [mm]	PZT	x [mm]	y [mm]	PZT	x [mm]	y [mm]
1	143	100	9*	238	871	17*	428	677	25*	638	441
2	123	307	10	343	140	18	473	879	26	588	643
3	143	530	11	333	355	19	543	100	27*	638	871
4	123	737	12	343	570	20	523	307	28	743	140
5	143	960	13	333	785	21	543	530	29	733	355
6	188	213	14	343	1000	22	523	737	30	743	570
7*	238	441	15*	428	247	23	543	960	31	733	785
8	188	643	16	473	449	24	588	213	32	743	1000

Appendix B

Lamb waves acquisition system cabling diagrams

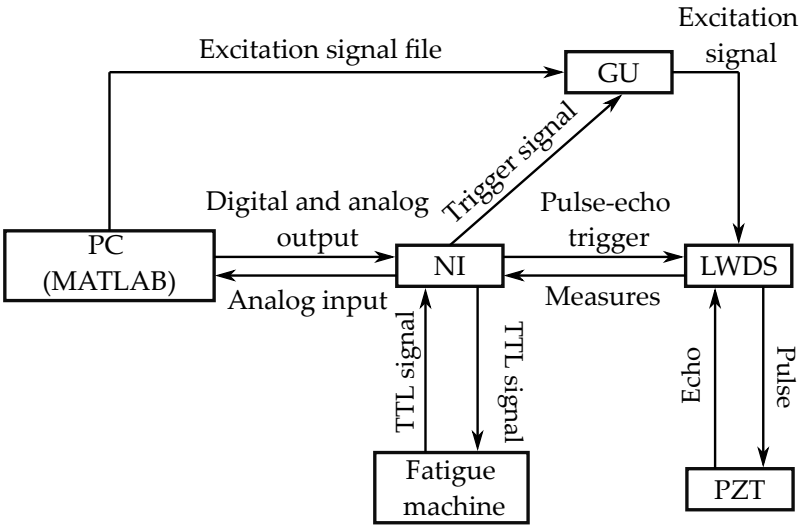

Fig. B.1 Cabling of LW acquisition system for L1 campaigns.

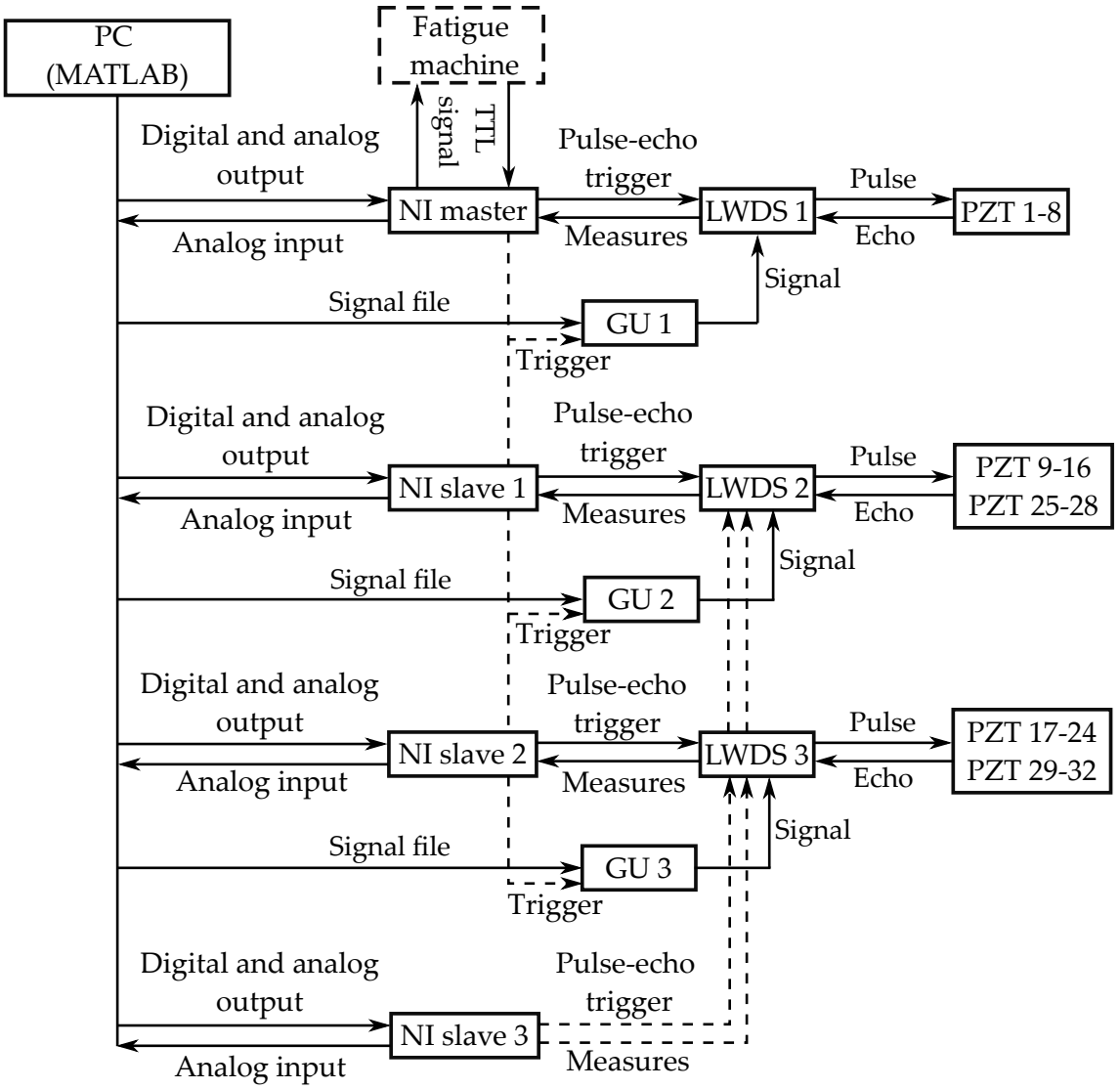

Fig. B.2 Cabling of LW acquisition system for L2 campaign.

Appendix C

Damage Indexes definition

Table C.1 List and descriptions of damage indexes.

DI name	Description	DI name	Definition
CC	FFT-based implementation of the maximum of the correlation	SSSD	Signal Sum of squared Differences
CCA	MATLAB-based implementation of the maximum of the correlation	WPSD	Welch-based Power Spectral Density
CC0	MATLAB-based implementation of the zero-lag correlation	WTF	Welch-based transfer function Cross-correlation maximum
CRC	MATLAB-based implementation of the correlation coefficient	CCTOF	Cross-correlation based TOF percentage difference
NRE2	Normalized residual energy 2	CCMPD	Cross-correlation maximum percentage difference
NRE3	Normalized residual energy 3	DWTC	Discrete Wavelet Transform approximation coefficients
NRE4	Normalized residual energy 4	NL_HARM2	FFT ratio of the difference signal at 2f0 over f0
NRE5	Normalized residual energy 5	NL_HARM3	FFT ratio of the difference signal at 3f0 over f0
NRE6	Normalized residual energy 6	NL_HARM4	FFT ratio of the difference signal at 4f0 over f0
MA	Maximum amplitude of the difference	NL_HARM5	FFT ratio of the difference signal at 5f0 over f0
FFT	FFT ratio of the difference signal over the sum of signals at f0	NL_THD	Total harmonic distortion of the difference signal
ENV	Energy of the envelope of the difference	NL_SPEC	Spectral energy in the “nonlinear” part versus the “linear” one
PHI	Energy of the phase of the difference	MEAN	Mean of the difference signal
TD	Time Delay	MEANABS	Mean of the absolute value of the difference
TDM	Time Delay of Max	STD	Standard deviation of the difference signal
TD1	Time Delay of the first wave packet	STDABS	Standard deviation of the absolute value of the difference signal
MAR	Maximum Amplitude Relative	SKW	Skewness of the difference signal
SAPR	Signal Amplitude Peak Ratio	SKWABS	Skewness of the absolute value of the difference signal
SAPS	Signal Amplitude Peak Squared percentage differences	KUR	Kurtosis of the difference signal
SAHM	Signal Amplitude Hilbert transform Maximum	KURABS	Kurtosis of the absolute value of the difference

Appendix D

Theoretical tools for infinitesimal strain theory

D.1 Vector calculus

In the following we denote ϕ a scalar field and $\boldsymbol{\Psi}$ a vector field.

D.1.1 Gradient

Cartesian coordinates	Cylindrical coordinates
$\boldsymbol{\nabla}\phi = \begin{pmatrix} \frac{\partial \phi}{\partial x} \\ \frac{\partial \phi}{\partial y} \\ \frac{\partial \phi}{\partial z} \end{pmatrix}$	$\boldsymbol{\nabla}\phi = \begin{pmatrix} \frac{\partial \phi}{\partial r} \\ \frac{1}{r}\frac{\partial \phi}{\partial \theta} \\ \frac{\partial \phi}{\partial z} \end{pmatrix}$

D.1.2 Divergence

Cartesian coordinates	Cylindrical coordinates
$\boldsymbol{\nabla}\cdot\boldsymbol{\Psi} = \frac{\partial \Psi_x}{\partial x} + \frac{\partial \Psi_y}{\partial y} + \frac{\partial \Psi_z}{\partial z}$	$\boldsymbol{\nabla}\cdot\boldsymbol{\Psi} = \frac{1}{r}\frac{\partial}{\partial r}(r\Psi_r) + \frac{1}{r}\frac{\partial \Psi_\theta}{\partial \theta} + \frac{\partial \Psi_z}{\partial z}$

D.1.3 Curl

Cartesian coordinates	Cylindrical coordinates
$\boldsymbol{\nabla}\times\boldsymbol{\Psi} = \begin{pmatrix} \frac{\partial \Psi_z}{\partial y} - \frac{\partial \Psi_y}{\partial z} \\ \frac{\partial \Psi_z}{\partial x} - \frac{\partial \Psi_x}{\partial z} \\ \frac{\partial \Psi_y}{\partial x} - \frac{\partial \Psi_x}{\partial y} \end{pmatrix}$	$\boldsymbol{\nabla}\times\boldsymbol{\Psi} = \begin{pmatrix} \frac{1}{r}\frac{\partial \Psi_z}{\partial \theta} - \frac{\partial \Psi_\theta}{\partial z} \\ \frac{\partial \Psi_r}{\partial z} - \frac{\partial \Psi_z}{\partial r} \\ \frac{1}{r}\left(\frac{\partial}{\partial r}(r\Psi\theta) - \frac{\partial \Psi_r}{\partial \theta}\right) \end{pmatrix}$

D.1.4 Laplacian

Cartesian coordinates	Cylindrical coordinates
$\Delta\phi = \frac{\partial^2\phi}{\partial x^2} + \frac{\partial^2\phi}{\partial y^2} + \frac{\partial^2\phi}{\partial z^2}$	$\Delta\phi = \frac{1}{r}\frac{\partial}{\partial r}\left(r\frac{\partial\phi}{\partial r}\right) + \frac{1}{r^2}\frac{\partial^2\phi}{\partial\theta^2} + \frac{\partial^2\phi}{\partial z^2}$

D.1.5 Vector calculus identities

$$\nabla\cdot(\nabla\times\boldsymbol{\Psi}) = 0$$
$$\nabla\times\left(\nabla\phi\right) = 0$$
$$\nabla\times(\nabla\times\boldsymbol{\Psi}) = \nabla(\nabla\cdot\boldsymbol{\Psi}) - \Delta\boldsymbol{\Psi}$$
$$\Delta\phi = \nabla^2\phi = \nabla\cdot\left(\nabla\phi\right)$$

D.2 Infinitesimal strain tensor in cylindrical coordinates system

In cylindrical coordinates (r,θ,z), the displacement vector can be written as

$$u = u_r\boldsymbol{e_r} + u_\theta\boldsymbol{e_\theta} + u_z\boldsymbol{e_z}. \tag{D.1}$$

The components of the infinitesimal strain tensor are given by

$$\begin{aligned}
\varepsilon_{rr} &= \frac{\partial u_r}{\partial r} & \varepsilon_{r\theta} &= \frac{1}{2}\left(\frac{1}{r}\frac{\partial u_r}{\partial\theta} + \frac{\partial u_\theta}{\partial r} - \frac{u_\theta}{r}\right)\\
\varepsilon_{\theta\theta} &= \frac{u_r}{r} + \frac{1}{r}\frac{\partial u_\theta}{\partial\theta} & \varepsilon_{\theta z} &= \frac{1}{2}\left(\frac{\partial u_\theta}{\partial z} + \frac{1}{r}\frac{\partial u_z}{\partial\theta}\right)\\
\varepsilon_{zz} &= \frac{\partial u_z}{\partial z} & \varepsilon_{rz} &= \frac{1}{2}\left(\frac{\partial u_r}{\partial z} + \frac{\partial u_z}{\partial r}\right)
\end{aligned} \tag{D.2}$$

D.3 Hooke's law for transverse isotropic materials

$$\begin{pmatrix}\sigma_{11}\\ \sigma_{22}\\ \sigma_{33}\\ \sigma_{13}\\ \sigma_{23}\\ \sigma_{12}\end{pmatrix} = \begin{bmatrix} C_{11} & C_{12} & C_{13} & 0 & 0 & 0\\ C_{12} & C_{11} & C_{13} & 0 & 0 & 0\\ C_{13} & C_{13} & C_{33} & 0 & 0 & 0\\ 0 & 0 & 0 & 2C_{44} & 0 & 0\\ 0 & 0 & 0 & 0 & 2C_{44} & 0\\ 0 & 0 & 0 & 0 & 0 & C_{11}-C_{12}\end{bmatrix}\begin{pmatrix}\varepsilon_{11}\\ \varepsilon_{22}\\ \varepsilon_{33}\\ \varepsilon_{13}\\ \varepsilon_{23}\\ \varepsilon_{12}\end{pmatrix} \tag{D.3}$$

$$E_1 = E_2 = E; \qquad \nu_1 = \nu_2 = \nu; \qquad \eta = \nu\sqrt{\frac{E}{E_3}} \tag{D.4}$$

$$
\begin{aligned}
C_{11} &= E\frac{1-\eta^2}{(1+\nu)(1-\nu-2\eta^2)} \\
C_{12} &= E\frac{\nu+\eta^2}{(1+\nu)(1-\nu-2\eta^2)} \\
C_{13} &= E\frac{\nu_3}{1-\nu-2\eta^2} \\
C_{33} &= E_3\frac{1-\nu}{1-\nu-2\eta^2} \\
C_{44} &= G_3
\end{aligned}
\tag{D.5}
$$

Appendix E

Actuator and sensor modeling

E.1 Actuator model

In this section we derive the expression of displacement field generated by a piezoelectric patch actuator bonded to a plate. For that, we follow the procedure from Raghavan and Cesnik [76] which relies on Mal's work [107] and is an extension of their work on isotropic plate [108]. This approach is adapted here to a single layer plate made of transverse isotropy material whose plane of isotropy is Oxy. In the following, we assume we are in the linear elastic regime along with small strain and that the material is homogeneous. The 3D equation of motion in case of an infinite solid can be written in terms of displacement as

$$\tilde{\boldsymbol{\nabla}}\boldsymbol{C}\tilde{\boldsymbol{\nabla}}^{\mathrm{T}}\boldsymbol{u} = \rho\ddot{\boldsymbol{u}} \tag{E.1}$$

where ρ is the material density and $\boldsymbol{C}$ is the stiffness matrix defined earlier Eq. 6.39. The operator $\tilde{\boldsymbol{\nabla}}$ is defined as

$$\tilde{\boldsymbol{\nabla}} = \begin{pmatrix} \frac{\partial}{\partial x} & 0 & 0 & 0 & \frac{\partial}{\partial z} & \frac{\partial}{\partial y} \\ 0 & \frac{\partial}{\partial y} & 0 & \frac{\partial}{\partial z} & 0 & \frac{\partial}{\partial x} \\ 0 & 0 & \frac{\partial}{\partial z} & \frac{\partial}{\partial y} & \frac{\partial}{\partial x} & 0 \end{pmatrix}. \tag{E.2}$$

We introduce the following constants that correpond to the squares of bulk wave (i.e. wave that exist in infinite solids) speeds along different directions [120]

$$\begin{aligned}
a_1 &= \frac{C_{11}}{\rho} && \text{compressionnal wave in plane of isotropy} \\
a_2 &= \frac{C_{33}}{\rho} && \text{compressionnal wave along } z \text{ axis} \\
a_3 &= \frac{C_{44}+C_{13}}{\rho} && \text{vertical shear wave in the plane of isotropy} \\
a_4 &= \frac{C_{66}}{\rho} && \text{shear wave along } z \text{ axis} \\
a_5 &= \frac{C_{44}}{\rho} && \text{horizontal shear wave in the plane of isotropy.}
\end{aligned} \tag{E.3}$$

We now consider the case of a harmonic plane wave propagating along the wavenumber of coordinates $\boldsymbol{k} = k_x\boldsymbol{e_x} + k_y\boldsymbol{e_y} + \zeta\boldsymbol{e_z}$ with an angular frequency ω

$$\boldsymbol{u} = \boldsymbol{K}e^{i(k_x x + k_y y + \zeta z - \omega t)} \tag{E.4}$$

where $\boldsymbol{K}$ is a vector of constants. Replacing $\boldsymbol{u}$ by its expression in Eq. E.1 we get the Christoffel equation

$$\begin{pmatrix} a_1k_x^2 + a_4k_y^2 + a_5\zeta^2 & (a_1 - a_4)k_xk_y & a_3k_x\zeta \\ (a_1 - a_4)k_xk_y & a_4k_x^2 + a_1k_y^2 + a_5\zeta^2 & a_3k_y\zeta \\ a_3k_x\zeta & a_3k_y\zeta & a_5(k_x^2 + k_y^2) + a_2\zeta^2 \end{pmatrix} \begin{pmatrix} K_1 \\ K_2 \\ K_3 \end{pmatrix} = \omega^2 \begin{pmatrix} K_1 \\ K_2 \\ K_3 \end{pmatrix} \tag{E.5}$$

or

$$\begin{pmatrix} a_1k_x^2 + a_4k_y^2 + a_5\zeta^2 - \omega^2 & (a_1 - a_4)k_xk_y & a_3k_x\zeta \\ (a_1 - a_4)k_xk_y & a_4k_x^2 + a_1k_y^2 + a_5\zeta^2 - \omega^2 & a_3k_y\zeta \\ a_3k_x\zeta & a_3k_y\zeta & a_5(k_x^2 + k_y^2) + a_2\zeta^2 - \omega^2 \end{pmatrix} \begin{pmatrix} K_1 \\ K_2 \\ K_3 \end{pmatrix} = 0 \tag{E.6}$$

For this last equation to have non trivial solutions, the determinant of the matrix must equal zero. For fixed values of k_x, k_y and ω there are three pairs of roots $\pm\zeta_i$ with $i = \{1, 2, 3\}$

$$\begin{aligned} \zeta_1^2 &= -\left(\frac{\beta}{2\alpha}\right) + \sqrt{\left(\frac{\beta}{2\alpha}\right)^2 - \frac{\gamma}{\alpha}} \\ \zeta_2^2 &= -\left(\frac{\beta}{2\alpha}\right) - \sqrt{\left(\frac{\beta}{2\alpha}\right)^2 - \frac{\gamma}{\alpha}} \\ \zeta_3^2 &= \frac{\omega^2 - a_4\left(k_x^2 + k_y^2\right)}{a_5} \end{aligned} \tag{E.7}$$

where

$$\begin{aligned} \alpha &= a_2a_5 \\ \beta &= \left(a_1a_2 + a_5^2 - a_3^2\right)\left(k_x^2 + k_y^2\right) - \omega^2\left(a_2 + a_5\right) \\ \gamma &= \left(a_1(k_x^2 + k_y^2) - \omega^2\right)\left(a_5(k_x^2 + k_y^2) - \omega^2\right). \end{aligned} \tag{E.8}$$

The eigenvectors associated to these roots are

$$\boldsymbol{e}_1 = \begin{pmatrix} q_{11}k_x\zeta_1 \\ q_{11}k_y\zeta_1 \\ -q_{31} \end{pmatrix}; \qquad \boldsymbol{e}_2 = \begin{pmatrix} q_{11}k_x\zeta_2 \\ q_{11}k_y\zeta_2 \\ -q_{32} \end{pmatrix}; \qquad \boldsymbol{e}_3 = \begin{pmatrix} -k_y \\ k_x \\ 0 \end{pmatrix} \tag{E.9}$$

where

$$\begin{aligned} q_{11} &= a_2 a_3 \\ q_{31} &= (a_3^2 - a_5^2)(k_x^2 + k_y^2) + a_5\omega^2 + \beta + \alpha\zeta_1^2 \\ q_{32} &= (a_3^2 - a_5^2)(k_x^2 + k_y^2) + a_5\omega^2 + \beta + \alpha\zeta_2^2. \end{aligned} \tag{E.10}$$

The other eigenvectors $\boldsymbol{e}_4$, $\boldsymbol{e}_5$ and $\boldsymbol{e}_6$ are obtained by replacing ζ_i by $-\zeta_i$. The general solution can now be written as

$$\boldsymbol{u} = \left(K_{1+}\boldsymbol{e}_1 e^{i\zeta_1 z} + K_{2+}\boldsymbol{e}_2 e^{i\zeta_2 z} + K_{3+}\boldsymbol{e}_3 e^{i\zeta_3 z} + K_{1-}\boldsymbol{e}_4 e^{-i\zeta_1 x_4} + K_{2-}\boldsymbol{e}_5 e^{-i\zeta_2 x_5} + K_{3-}\boldsymbol{e}_6 e^{-i\zeta_3 x_6}\right) e^{i(k_x x + k_y y - \omega t)}. \tag{E.11}$$

With this general solution for infinite solid, we seek the particular solution for the current plate problem by introducing boundary conditions. These boundary conditions are applied through tensile stress on top and bottom surfaces of the plate as

$$\begin{aligned} \sigma_{i3}(x, y, h) &= f_i(x, y, h) \\ \sigma_{i3}(x, y, -h) &= 0 \end{aligned} \tag{E.12}$$

where the functions f_i depend on the shape of the actuator. We define the 2D spatial Fourier transform of the displacement field as

$$\boldsymbol{U}(k_x, k_y) = \int_{-\infty}^{\infty}\int_{-\infty}^{\infty} \boldsymbol{u}(x, y) e^{-i(k_x x + k_y y)}\, \mathrm{d}x\, \mathrm{d}y \tag{E.13}$$

and the inverse Fourier transform as

$$\boldsymbol{u}(x, y) = \frac{1}{4\pi^2}\int_{-\infty}^{\infty}\int_{-\infty}^{\infty} \boldsymbol{U}(k_x, k_y) e^{i(k_x x + k_y y)}\, \mathrm{d}k_x\, \mathrm{d}k_y. \tag{E.14}$$

Then we denote $\boldsymbol{\Sigma}$ and $\boldsymbol{F}$ the Fourier transform of variables $\boldsymbol{\sigma}$ and $\boldsymbol{f}$ respectively. In the following we define the displacement-stress vector as

$$\begin{pmatrix} \boldsymbol{U} \\ \boldsymbol{\Sigma} \end{pmatrix} = \begin{pmatrix} \boldsymbol{Q}_{11} & \boldsymbol{Q}_{12} \\ \boldsymbol{Q}_{21} & \boldsymbol{Q}_{22} \end{pmatrix} \begin{pmatrix} \boldsymbol{E}_{\mathrm{t}}(z) & 0 \\ 0 & \boldsymbol{E}_{\mathrm{b}}(z) \end{pmatrix} \begin{pmatrix} \boldsymbol{C}_+ \\ \boldsymbol{C}_- \end{pmatrix} \tag{E.15}$$

where

$$\begin{aligned}
\boldsymbol{Q}_{11} &= \begin{pmatrix} \boldsymbol{e}_1 & \boldsymbol{e}_2 & \boldsymbol{e}_3 \end{pmatrix} \\
\boldsymbol{Q}_{12} &= \begin{pmatrix} \boldsymbol{e}_4 & \boldsymbol{e}_5 & \boldsymbol{e}_6 \end{pmatrix} \\
\boldsymbol{Q}_{21} &= i\rho \begin{pmatrix} a_5 k_x \left(q_{11}\zeta_1^2 - q_{31}\right) & a_5 k_x \left(q_{11}\zeta_2^2 - q_{32}\right) & -a_5 k_y \zeta_3 \\ a_5 k_y \left(q_{11}\zeta_1^2 - q_{31}\right) & a_5 k_y \left(q_{11}\zeta_2^2 - q_{32}\right) & a_5 k_x \zeta_3 \\ \zeta_1 \left(\mu - a_2 q_{31}\right) & \zeta_2 \left(\mu - a_2 q_{32}\right) & k_x k_y \left(a_3 + 2a_4 - a_1 - a_5\right) \end{pmatrix} \\
\boldsymbol{Q}_{22} &= i\rho \begin{pmatrix} a_5 k_x \left(q_{11}\zeta_4^2 - q_{31}\right) & a_5 k_x \left(q_{11}\zeta_5^2 - q_{32}\right) & -a_5 k_y \zeta_6 \\ a_5 k_y \left(q_{11}\zeta_4^2 - q_{31}\right) & a_5 k_y \left(q_{11}\zeta_5^2 - q_{32}\right) & a_5 k_x \zeta_6 \\ \zeta_4 \left(\mu - a_2 q_{31}\right) & \zeta_5 \left(\mu - a_2 q_{32}\right) & k_x k_y \left(a_3 + 2a_4 - a_1 - a_5\right) \end{pmatrix}
\end{aligned} \tag{E.16}$$

$$\mu = (a_1 - 2a_4) q_{11} k_x^2 + (a_3 - a_5) q_{11} k_y^2 \tag{E.17}$$

$$\begin{aligned}
\boldsymbol{E}_\mathrm{t}(z) &= \mathrm{Diag}\left[\begin{pmatrix} e^{i\zeta_1 z} & e^{i\zeta_2 z} & e^{i\zeta_3 z} \end{pmatrix}\right] \\
\boldsymbol{E}_\mathrm{b}(z) &= \mathrm{Diag}\left[\begin{pmatrix} e^{i\zeta_4 z} & e^{i\zeta_5 z} & e^{i\zeta_6 z} \end{pmatrix}\right].
\end{aligned} \tag{E.18}$$

We can then express the boundary conditions on top and bottom surfaces of the plate as a 6×6 linear system of equations

$$\begin{pmatrix} \boldsymbol{Q}_{21}\boldsymbol{E}_\mathrm{t}(h) & \boldsymbol{Q}_{22}\boldsymbol{E}_\mathrm{b}(h) \\ \boldsymbol{Q}_{21}\boldsymbol{E}_\mathrm{t}(-h) & \boldsymbol{Q}_{22}\boldsymbol{E}_\mathrm{b}(-h) \end{pmatrix} \begin{pmatrix} \boldsymbol{C}_+ \\ \boldsymbol{C}_- \end{pmatrix} = \begin{pmatrix} \boldsymbol{F} \\ 0 \end{pmatrix} \tag{E.19}$$

where we denote the matrix of the system as $\boldsymbol{G}$ and its determinant D_G. Since we consider a circular actuator the functions f_i are defined as

$$f_1 = \delta(r - c)\cos(\theta); \qquad f_2 = \delta(r - c)\sin(\theta); \qquad f_3 = 0 \tag{E.20}$$

where δ is the Dirac delta function (which should not be confused with the size of the damage), c is the radius of the actuator whereas r and θ are the polar spatial coordinates. Their respective 2D Fourier transforms are

$$F_1 = 2i\pi \frac{k_x}{k} c J_1(kc); \qquad F_2 = 2i\pi \frac{k_y}{k} c J_1(kc); \qquad F_3 = 0 \tag{E.21}$$

where J_1 is the Bessel function of the first kind and order one, whereas k and θ are the polar wavenumber coordinates defined as $k^2 = k_x^2 + k_y^2$ and $\theta = \tan^{-1}(k_x/k_y)$. The constants C_i in Eq. E.19 can be analytically solved using Cramer's rule

$$\boldsymbol{C} = \frac{1}{D_G} \begin{pmatrix} \det(\boldsymbol{G}_1) \\ \vdots \\ \det(\boldsymbol{G}_6) \end{pmatrix} \tag{E.22}$$

where $\boldsymbol{G}_i$ is the matrix formed by replacing the column i of $\boldsymbol{G}$ by the column vector $\begin{pmatrix}\boldsymbol{F} & 0\end{pmatrix}^{\mathrm{T}}$. The displacement field can then be expressed as

$$\boldsymbol{U}(k_x,k_y,z)=\frac{1}{D_G(k_x,k_y)}\begin{pmatrix}\boldsymbol{Q}_{11} & \boldsymbol{Q}_{12}\end{pmatrix}\begin{pmatrix}\boldsymbol{E}_{\mathrm{t}}(z) & 0\\ 0 & \boldsymbol{E}_{\mathrm{b}}(z)\end{pmatrix}\begin{pmatrix}\det(\boldsymbol{G}_1)\\ \vdots\\ \det(\boldsymbol{G}_6)\end{pmatrix}=\frac{\boldsymbol{N}(k_x,k_y,z)}{D_G(k_x,k_y,z)}. \tag{E.23}$$

Let us calculate the radial displacement component on the top surface generated by the actuator. For that we compute the inverse Fourier transform of the component $i=\{1,2,3\}$ of U

$$\begin{aligned}u_i(x,y,h)&=\frac{1}{4\pi^2}\int_{-\infty}^{\infty}\int_{-\infty}^{\infty}U_i(k_x,k_y)e^{i(k_xx+k_yy)}\,\mathrm{d}k_x\,\mathrm{d}k_y\\&=\frac{1}{4\pi^2}\int_{-\infty}^{\infty}\int_{-\infty}^{\infty}\frac{N_i(k_x,k_y)}{D_G(k_x,k_y)}e^{i(k_xx+k_yy)}\,\mathrm{d}k_x\,\mathrm{d}k_y\\&=\frac{1}{4\pi^2}\int_{0}^{\infty}\int_{0}^{2\pi}\frac{N_i(k,\theta)}{D_G(k,\theta)}e^{ik(x\cos\theta+y\sin\theta)}k\,\mathrm{d}k\,\mathrm{d}\theta\\&=\frac{1}{4\pi^2}\int_{-\infty}^{\infty}\int_{0}^{\pi}\frac{N_i(k,\theta)}{D_G(k,\theta)}e^{ik(x\cos\theta+y\sin\theta)}k\,\mathrm{d}k\,\mathrm{d}\theta.\end{aligned} \tag{E.24}$$

Since Oxy is a plane of isotropy, we can take $x=r$ and $y=0$ without loss of generality

$$u_i(x,y,h)=\frac{1}{4\pi^2}\int_{-\infty}^{\infty}\int_{0}^{\pi}\frac{N_i(k,\theta)}{D_G(k,\theta)}e^{ikr\cos(\theta)}k\,\mathrm{d}k\,\mathrm{d}\theta \tag{E.25}$$

Since we study a transverse isotropic material, it can be shown that the ratio $N_i(k,\theta)/D_G(k,\theta)$ is in fact independent of θ

$$u_i(x,y,h)=\frac{1}{4\pi^2}\int_{-\infty}^{\infty}\frac{N_i(k)}{D_G(k)}k\,\mathrm{d}k\int_{0}^{\pi}e^{ikr\cos(\theta)}\,\mathrm{d}\theta. \tag{E.26}$$

From Eq. 6.68, we can write the integral over θ in terms of Bessel function of first kind and order zero

$$u_i(x,y,h)=\frac{1}{4\pi}\int_{-\infty}^{\infty}\frac{N_i(k)}{D_G(k)}kJ_0(|kr|)\,\mathrm{d}k. \tag{E.27}$$

To evaluate the remaining integral for real wavenumbers k, we consider the contour integral in the complex k plane represented in Fig. E.1. The integrand is singular at the roots of $D_G(k)=0$ which corresponds to the dispersion relationship of the considered prob-

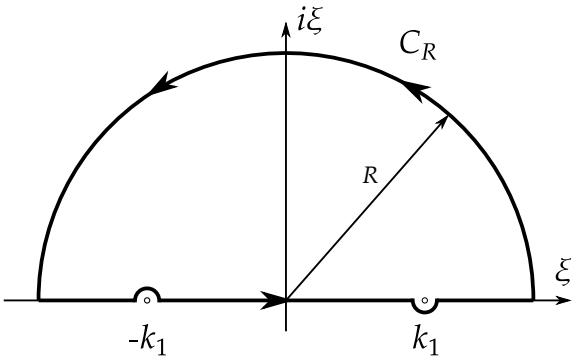

Fig. E.1 Diagram for wavenumber complex integral calculation.

lem. As mentioned in the presentation of the problem Sec. 6.1.2, we are only interested in symmetric mode waves below the cut-off frequency. This means that there are two singularities on the real k axis: k_1 and $-k_1$. Besides, below ω_t, k_2 is purely imaginary so its contribution is not taken into account in the displacement response. In order to apply the residue theorem, the integration contour is indented such as to exclude $-k_1$ and include k_1. By virtue of residue theorem we then have [121]

$$\int_{-\infty}^{\infty} \frac{N_i(k)}{D_G(k)} k J_0(|kr|)\,\mathrm{d}k + \int_{C_R} \frac{N_i(k)}{D_G(k)} k J_0(|kr|)\,\mathrm{d}k = 2i\pi \left(\frac{N_i(k_1)}{D'_G(k_1)} k_1 J_0(k_1 r) \right) \tag{E.28}$$

where $D'_G(k_1)$ is the derivative of D_G evaluated at k_1. From Jordan's lemma, the integral along C_R vanishes when $R \to \infty$. We can finally write the expression of the radial displacement

$$u_i(x, y, h) = \frac{i}{2} \frac{N_i(k_1)}{D'_G(k_1)} k_1 J_0(k_1 r) \tag{E.29}$$

and we decompose J_0 as $\frac{1}{2}\left(H_0^{(1)}(k_1 r) + H_0^{(2)}(k_1 r)\right)$. We get the final expression of the displacement field component

$$u_i(x, y, h) = \frac{i}{4} \frac{N_i(k_1)}{D'_G(k_1)} k_1 \left(H_0^{(1)}(k_1 r) + H_0^{(2)}(k_1 r)\right). \tag{E.30}$$

E.2 Sensor response

We start from the constitutive equations Eq. 3.1 and Eq. 3.2. $\boldsymbol{e}$ is replaced by its expression from Eq. 3.3

$$\boldsymbol{\sigma} = \boldsymbol{C}^E \boldsymbol{\varepsilon} - (\boldsymbol{d}\boldsymbol{C}^E)^{\mathrm{T}} \boldsymbol{E} \tag{E.31}$$

$$\boldsymbol{D} = \boldsymbol{\chi}^{\sigma} \boldsymbol{E} + \boldsymbol{d}\boldsymbol{\sigma}. \tag{E.32}$$

Substituting σ by its expression in Eq. E.32 leads to

$$\boldsymbol{D} = \left(\boldsymbol{\chi}^{\sigma} - \boldsymbol{d}\boldsymbol{C}^{E}\boldsymbol{d}^{\mathrm{T}}\right)\boldsymbol{E} + \boldsymbol{d}\boldsymbol{C}^{E}\boldsymbol{\sigma}. \tag{E.33}$$

We study a PZT made of transverse isotropic material with isotropy along the plane of the PZT. Eq. E.33 becomes

$$\begin{aligned}
\begin{pmatrix} D_1 \\ D_2 \\ D_3 \end{pmatrix} = \Bigg[& \begin{pmatrix} \chi_1^{\sigma} & 0 & 0 \\ 0 & \chi_1^{\sigma} & 0 \\ 0 & 0 & \chi_3^{\sigma} \end{pmatrix} \\
& - \begin{pmatrix} 0 & 0 & 0 & 0 & d_{15} & 0 \\ 0 & 0 & 0 & d_{15} & 0 & 0 \\ d_{31} & d_{31} & d_{33} & 0 & 0 & 0 \end{pmatrix} \begin{pmatrix} C_{11}^E & C_{12}^E & C_{13}^E & 0 & 0 & 0 \\ C_{21}^E & C_{11}^E & C_{13}^E & 0 & 0 & 0 \\ C_{31}^E & C_{31}^E & C_{33}^E & 0 & 0 & 0 \\ 0 & 0 & 0 & C_{44}^E & 0 & 0 \\ 0 & 0 & 0 & 0 & C_{55}^E & 0 \\ 0 & 0 & 0 & 0 & 0 & C_{66}^E \end{pmatrix} \begin{pmatrix} 0 & 0 & d_{31} \\ 0 & 0 & d_{31} \\ 0 & 0 & d_{33} \\ 0 & d_{15} & 0 \\ d_{15} & 0 & 0 \\ 0 & 0 & 0 \end{pmatrix} \Bigg] \begin{pmatrix} E_1 \\ E_2 \\ E_3 \end{pmatrix} \\
& + \begin{pmatrix} 0 & 0 & 0 & 0 & d_{15} & 0 \\ 0 & 0 & 0 & d_{15} & 0 & 0 \\ d_{31} & d_{31} & d_{33} & 0 & 0 & 0 \end{pmatrix} \begin{pmatrix} C_{11}^E & C_{12}^E & C_{13}^E & 0 & 0 & 0 \\ C_{21}^E & C_{11}^E & C_{13}^E & 0 & 0 & 0 \\ C_{31}^E & C_{31}^E & C_{33}^E & 0 & 0 & 0 \\ 0 & 0 & 0 & C_{44}^E & 0 & 0 \\ 0 & 0 & 0 & 0 & C_{55}^E & 0 \\ 0 & 0 & 0 & 0 & 0 & C_{66}^E \end{pmatrix} \begin{pmatrix} \varepsilon_1 \\ \varepsilon_2 \\ \varepsilon_3 \\ \varepsilon_4 \\ \varepsilon_5 \\ \varepsilon_6 \end{pmatrix}.
\end{aligned} \tag{E.34}$$

Given that the thickness of the piezoelectric patch is small compared to its diameter, and given that the stress on the free surface are $\sigma_3 = \sigma_4 = \sigma_5 = 0$ the plane stress assumption can be made. Hence, Eq. E.34 can be reduced to

$$\begin{aligned}
D_3 = & \left(\chi_3^{\sigma} - \begin{pmatrix} d_{31} & d_{31} & 0 \end{pmatrix} \begin{pmatrix} Q_{11}^E & Q_{12}^E & 0 \\ Q_{21}^E & Q_{11}^E & 0 \\ 0 & 0 & Q_{66}^E \end{pmatrix} \begin{pmatrix} d_{31} \\ d_{31} \\ 0 \end{pmatrix} \right) E_3 \\
& + \begin{pmatrix} d_{31} & d_{31} & 0 \end{pmatrix} \begin{pmatrix} Q_{11}^E & Q_{12}^E & 0 \\ Q_{21}^E & Q_{11}^E & 0 \\ 0 & 0 & Q_{66}^E \end{pmatrix} \begin{pmatrix} \varepsilon_1 \\ \varepsilon_2 \\ \varepsilon_6 \end{pmatrix}
\end{aligned} \tag{E.35}$$

where Q_{ij}^E are the terms of the reduced stiffness matrix which is for a transverse isotropic material

$$\begin{pmatrix} Q_{11}^E & Q_{12}^E & 0 \\ Q_{21}^E & Q_{11}^E & 0 \\ 0 & 0 & Q_{66}^E \end{pmatrix} = \frac{1}{1-\nu^2} \begin{pmatrix} Y^E & \nu Y^E & 0 \\ \nu Y^E & Y^E & 0 \\ 0 & 0 & G(1-\nu^2) \end{pmatrix}$$

where Y^E and ν are respectively the piezoelectric Young's modulus and Poisson's ratio. It comes

$$D_3 = d_{31}\frac{Y^E}{1-\nu}\Big(\varepsilon_1 + \varepsilon_2\Big) - \Big(2d_{31}^2\frac{Y^E}{1-\nu} - \chi_3^\sigma\Big)E_3. \tag{E.36}$$

As mentioned earlier the PZT sensor is placed in an open electric circuit. Hence, no current circulate in the circuit meaning that no charge accumulate on piezoelectric patch electrodes. This imposes the following condition:

$$\iint_A D_3 \,\mathrm{d}A = 0 \tag{E.37}$$

where $A = \pi c^2$ is the surface of the electrode.

In Sec. 6.4, we derived the scattering displacement field for a unitary incident wave. Since all the operations we have performed to obtain the system of equations Eq. 6.88 are linear, we can multiply the response of the piezoelectric sensor by the amplitude of the signal at the frequency studied. It also means that the voltage response we derive here for a unitary incident wave is the transfer function between the input and output voltage. In the following, we will denote this transfer function H which is defined

$$\boldsymbol{E} = -\boldsymbol{\nabla} H \implies H = -\int_0^{h_S} E_3 \,\mathrm{d}z \tag{E.38}$$

where h_S is the thickness of the PZT sensor. Then integration of Eq. E.36 over all directions gives

$$0 = d_{31}\frac{Y^E}{1-\nu}h_S \iint_A \Big(\varepsilon_1 + \varepsilon_2\Big)\,\mathrm{d}A + \Big(2d_{31}^2\frac{Y^E}{1-\nu} - \chi_3^\sigma\Big)AH. \tag{E.39}$$

Then the output voltage can be written

$$\begin{aligned} H &= \frac{d_{31}Y^E h_S}{\pi c^2\Big(\chi_3^\sigma(1-\nu) - 2d_{31}^2 Y^E\Big)} \iint_A \Big(\varepsilon_1 + \varepsilon_2\Big)\,\mathrm{d}A \\ &= K_S \iint_A \Big(\varepsilon_1 + \varepsilon_2\Big)\,\mathrm{d}A \end{aligned} \tag{E.40}$$

Appendix F

Actuator-sensor transfer function

In this study, we study a system similar to Fig. 6.2 except this time we are only interested in the wave travelling on the direct path actuator to sensor. In the following we will derive the transfer function H_{AS} between the input voltage send to the actutor and the output voltage measured by the sensor. We start from the sensor response expression Eq. E.40

$$H_{\text{AS}} = K_{\text{S}} \iint_A \left(\varepsilon_{rr} + \varepsilon_{\theta\theta}\right) \mathrm{d}A \tag{F.1}$$

with $K_{\text{S}} = \frac{d_{31} Y^E h_{\text{S}}}{\pi c^2 \left(\chi_3^g (1-\nu) - 2 d_{31}^2 Y^E\right)}$. ε_{rr} and $\varepsilon_{\theta\theta}$ respective expression in terms of displacement components are

$$\varepsilon_{rr} = \frac{\partial u_r}{\partial r} \tag{F.2}$$

$$\varepsilon_{\theta\theta} = \frac{1}{r}\frac{\partial u_\theta}{\partial \theta} + \frac{u_r}{r}. \tag{F.3}$$

Since the displacement field generated by the actuator is circular in our problem, $u_\theta = 0$ and from Eq. 6.95 it comes

$$\varepsilon_{rr} + \varepsilon_{\theta\theta} = \frac{i\tau c}{4} \frac{N_1(k_1)}{D'_{\text{G}}(k_1)} k_1 \left(\frac{H_0^{(1)}(k_1 r)}{r} - k_1 H_1^{(1)}(k_1 r) \right) \tag{F.4}$$

where τ is the shear stress generated by the actuator. To evaluate the integral of the last expression over the sensor's surface we follow the same procedure as we did in Sec. 6.5.2

$$H_{\text{AS}} = K_{\text{S}} \frac{i\tau c}{4} \frac{N_1(k_1)}{D'_{\text{G}}(k_1)} k_1 \int_{d_{\text{AS}}-c}^{d_{\text{AS}}+c} \left(\frac{H_0^{(1)}(k_1 r)}{r} - k_1 H_1^{(1)}(k_1 r) \right) r \Theta(r) \, \mathrm{d}r \tag{F.5}$$

where d_{AS} is the distance between the actuator center and the sensor center.

Appendix G

Dispersion curves

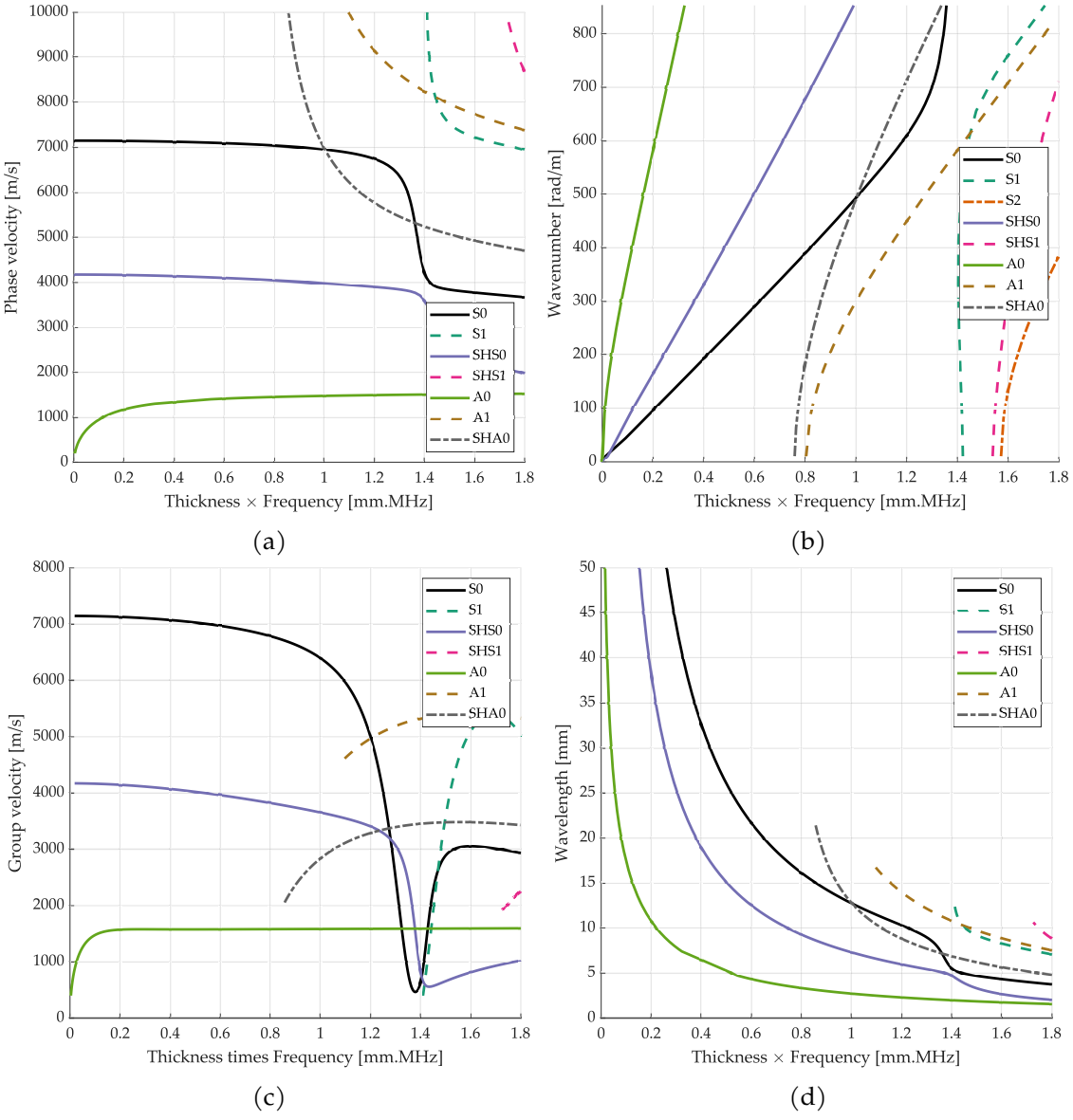

Fig. G.1 Dispersion curves for skin part of L1 and L2 coupons from ReMAP project. Phase velocity (a), Wavenumber (b), group velocity (c) and wavelength (d).

References

[1] D. Zarouchas, A. Broer, G. Galanopoulos, W. Briand, R. Benedictus, and T. Loutas, "Compression Compression fatigue tests on single stiffener aerospace structures," 2021.

[2] L. Chehami, E. Moulin, J. de Rosny, and C. Prada, "Accuracy of Green's function estimation from correlation of diffuse elastic waves on thin plates," *The Journal of the Acoustical Society of America*, vol. 146, pp. 3505–3511, Nov. 2019.

[3] A. Rytter, *Vibrational Based Inspection of Civil Engineering Structures*. PhD thesis, Aalborg University, 1993.

[4] ACARE, "Strategic Research and Innovation Agenda – 2017 update," tech. rep., ACARE, 2017.

[5] M. Zámková, M. Prokop, and R. Stolín, "Factors Influencing Flight Delays of a European Airline," *Acta Universitatis Agriculturae et Silviculturae Mendelianae Brunensis*, vol. 65, pp. 1799–1807, Oct. 2017.

[6] V. Giurgiutiu, *Structural Health Monitoring with Piezoelectric Wafer Active Sensors*. Elsevier, 2007.

[7] S. P. Ackert, "Basics of Aircraft Maintenance Programs for Financiers," Oct. 2010.

[8] K. Worden, C. R. Farrar, G. Manson, and G. Park, "The fundamental axioms of structural health monitoring," *Proceedings of the Royal Society A: Mathematical, Physical and Engineering Sciences*, vol. 463, pp. 1639–1664, June 2007.

[9] F. Laurin, "Introduction générale sur les matériaux composites," 2011.

[10] V. Giurgiutiu, *Structural Health Monitoring of Aerospace Composites*. Boston, MA: Elsevier, 2015.

[11] H. Dhieb, J. G. Buijnsters, K. Elleuch, and J. P. Celis, "Effect of relative humidity and full immersion in water on friction, wear and debonding of unidirectional carbon fiber reinforced epoxy under reciprocating sliding," *Composites Part B: Engineering*, vol. 88, pp. 240–252, Mar. 2016.

[12] R. Lammering, U. Gabbert, M. Sinapius, T. Schuster, and P. Wierach, *Lamb-Wave Based Structural Health Monitoring in Polymer Composites*. Springer, 2017.

[13] G. C. Pardoen, "Effect of Delamination on the Natural Frequencies of Composite Laminates," *Journal of Composite Materials*, vol. 23, pp. 1200–1215, Dec. 1989.

[14] J. Curie and P. Curie, "Développement par compression de l'électricité polaire dans les cristaux hémièdres à faces inclinées," *Bulletin de Minéralogie*, pp. 90–93, 1880.

[15] R. G. Ballas, "The Piezoelectric Effect – an Indispensable Solid State Effect for Contemporary Actuator and Sensor Technologies," *Journal of Physics: Conference Series*, vol. 1775, p. 012012, Jan. 2021.

[16] "IEEE Standard on Piezoelectricity," *ANSI/IEEE Std 176-1987*, pp. 0_1–, 1988.

[17] E. Balmes and A. Deraemaeker, "SDT Piezoelectric module." SDTools, 2001.

[18] Z. Su and L. Ye, *Identification of Damage Using Lamb Waves: From Fundamentals to Applications*. Springer, 2009.

[19] L. Wang and F. G. Yuan, "Group velocity and characteristic wave curves of Lamb waves in composites: Modeling and experiments," *Composites Science and Technology*, vol. 67, pp. 1370–1384, June 2007.

[20] S. Guo, *Contribution to the Study of Guided Waves Propagation and Attenuation in Anisotropic Composite Laminates Made up of Viscoelastic Composite Materials: Application to A380 Mounted Nacelle Parts*. These en préparation, Paris, HESAM, 2017.

[21] S. Guo, M. Rebillat, and N. Mechbal, "Dichotomy property of dispersion equation of guided waves propagating in anisotropic composite plates," *Mechanical Systems and Signal Processing*, vol. 164, p. 108212, Feb. 2022.

[22] V. Giurgiutiu, "Coupling of PWAS Transducers to the Monitored Structure," in *Structural Health Monitoring with Piezoelectric Wafer Active Sensors*, pp. 395–443, Elsevier, 2007.

[23] U. Ashwin, S. Raja, and C. N. Sathyanarayana, "Formulation of 36-noded piezoelectric spectral finite element scheme with active/passive layers coupled by Lagrange multipliers," *Smart Materials and Structures*, vol. 23, p. 085017, July 2014.

[24] V. Giurgiutiu, "Tuned Lamb Wave Excitation and Detection with Piezoelectric Wafer Active Sensors for Structural Health Monitoring," *Journal of Intelligent Material Systems and Structures*, vol. 16, pp. 291–305, Apr. 2005.

[25] J. Wang and Y. Shen, "An enhanced Lamb wave virtual time reversal technique for damage detection with transducer transfer function compensation," *Smart Materials and Structures*, vol. 28, p. 085017, July 2019.

[26] I. Dafydd and Z. Sharif Khodaei, "Analysis of barely visible impact damage severity with ultrasonic guided Lamb waves," *Structural Health Monitoring*, vol. 19, pp. 1104–1122, July 2020.

[27] Y. Liu, M. Y. Fard, A. Chattopadhyay, and D. Doyle, "Damage assessment of CFRP composites using a time-frequency approach," *Journal of Intelligent Material Systems and Structures*, vol. 23, pp. 397–413, Mar. 2012.

[28] Z. Su and L. Ye, "Lamb Wave Propagation-based Damage Identification for Quasi-isotropic CF/EP Composite Laminates Using Artificial Neural Algorithm: Part II - Implementation and Validation," *Journal of Intelligent Material Systems and Structures*, vol. 16, pp. 113–125, Feb. 2005.

[29] R. Miorelli, C. Fisher, A. Kulakovskyi, B. Chapuis, O. Mesnil, and O. D'Almeida, "Defect sizing in guided wave imaging structural health monitoring using convolutional neural networks," *NDT & E International*, vol. 122, p. 102480, Sept. 2021.

[30] A. Kulakovskyi, *Development of a SHM System by Elastic Guided Waves Applied to Aeronautic Structures*. PhD thesis, Université Paris-Saclay, France, May 2019.

[31] J. Yang, J. He, X. Guan, D. Wang, H. Chen, W. Zhang, and Y. Liu, "A probabilistic crack size quantification method using in-situ Lamb wave test and Bayesian updating," *Mechanical Systems and Signal Processing*, vol. 78, pp. 118–133, Oct. 2016.

[32] T. Peng, A. Saxena, K. Goebel, Y. Xiang, S. Sankararaman, and Y. Liu, "A novel Bayesian imaging method for probabilistic delamination detection of composite materials," *Smart Materials and Structures*, vol. 22, no. 12, p. 125019, 2013.

[33] M. Ghrib, M. Rébillat, G. Vermot des Roches, and N. Mechbal, "Automatic damage type classification and severity quantification using signal based and nonlinear model based damage sensitive features," *Journal of Process Control*, vol. 83, pp. 136–146, Oct. 2018.

[34] P. Ferdinand, S. Magne, V. Dewynter-Marty, S. Rougeault, and L. Maurin, "Applications of Fiber Bragg Grating Sensors in the Composite Industry," *MRS Bulletin*, vol. 27, pp. 400–407, May 2002.

[35] P. Martinez Bueno, M. Martinez, C. Rans, and R. Benedictus, "Strain Monitoring Using a Rayleigh Backscattering System for a Composite UAV Wing Instrumented with an Embedded Optical Fiber," *Advanced Materials Research*, vol. 1135, pp. 1–19, 2016.

[36] K. Kishida, Y. Yamauchi, and A. Guzik, "Study of optical fibers strain-temperature sensitivities using hybrid Brillouin-Rayleigh system," *Photonic Sensors*, vol. 4, pp. 1–11, Mar. 2014.

[37] G. JAUSSAUD, J. Rebufa, M. Fournier, M. LOGEAIS, N. Bencheikh, M. REBILLAT, and M. Guskov, "Improving Lamb Wave detection for SHM using a dedicated LWDS electronics," in *11th Symposium on NDT in Aerospace*, (Saclay, France), pp. 1–7, NTD, Nov. 2019.

[38] F. Laurin, J. S. Charrier, D. Lévêque, J. F. Maire, A. Mavel, and P. Nuñez, "Determination of the Properties of Composite Materials Thanks to Digital Image Correlation Measurements," *Procedia IUTAM*, vol. 4, pp. 106–115, Jan. 2012.

[39] Hexcel, "HexPly 8552 Product Data Sheet," 2020.

[40] G. Park, C. R. Farrar, A. C. Rutherford, and A. N. Robertson, "Piezoelectric Active Sensor Self-Diagnostics Using Electrical Admittance Measurements," *Journal of Vibration and Acoustics*, vol. 128, pp. 469–476, Jan. 2006.

[41] S. G. Taylor, G. Park, K. M. Farinholt, and M. D. Todd, "Diagnostics for piezoelectric transducers under cyclic loads deployed for structural health monitoring applications," vol. 22, p. 025024, Jan. 2013.

[42] C. Liang, F. Sun, and C. Rogers, "Coupled Electro-Mechanical Analysis of Adaptive Material Systems — Determination of the Actuator Power Consumption and System Energy Transfer," *Journal of Intelligent Material Systems and Structures*, vol. 5, pp. 12–20, Jan. 1994.

[43] E. Lizé, M. Rébillat, N. Mechbal, and C. Bolzmacher, "Estimation of the temperature field on a composite fan cowl using the static capacity of surface-mounted piezoceramic transducers.," *IFAC-PapersOnLine*, vol. 50, pp. 11689–11694, July 2017.

[44] J. Schijve, A. M. Vlutters, Ichsan, and J. C. ProvóKluit, "Crack growth in aluminium alloy sheet material under flight-simulation loading," *International Journal of Fatigue*, vol. 7, pp. 127–136, July 1985.

[45] R. Project, "ReMAP Deliverable D4.5 - Diagnostic Methodologies for Damage Detection in Composite Airframe Structures," 2021.

[46] M. Ghrib, L. Berthe, N. Mechbal, M. Rébillat, M. Guskov, R. Ecault, and N. Bedreddine, "Generation of controlled delaminations in composites using symmetrical laser shock configuration," *Composite Structures*, vol. 171, pp. 286–297, July 2017.

[47] E. D. Niri and S. Salamone, "A probabilistic framework for acoustic emission source localization in plate-like structures," *Smart Materials and Structures*, vol. 21, p. 035009, Feb. 2012.

[48] A. Rahbari, M. Rébillat, N. Mechbal, and S. Canu, "Unsupervised damage clustering in complex aeronautical composite structures monitored by Lamb waves: An inductive approach," *Engineering Applications of Artificial Intelligence*, vol. 97, p. 104099, Jan. 2021.

[49] J. B. Coble, *Merging Data Sources to Predict Remaining Useful Life – An Automated Method to Identify Prognostic Parameters*. PhD thesis, The University of Tennessee, Knoxville, May 2010.

[50] H. Liu, H. Cui, W. Wen, and H. Kang, "Fatigue characterization of T300/924 polymer composites with voids under tension-tension and compression-compression cyclic loading," *Fatigue & Fracture of Engineering Materials & Structures*, vol. 41, no. 3, pp. 597–610, 2018.

[51] C. Zhang, Z. Zhang, H. Ji, J. Qiu, and C. Tao, "Mode conversion behavior of guided wave in glass fiber reinforced polymer with fatigue damage accumulation," *Composites Science and Technology*, vol. 192, p. 108073, May 2020.

[52] C. Fendzi, N. Mechbal, M. Rébillat, M. Guskov, and G. Coffignal, "A general Bayesian framework for ellipse-based and hyperbola-based damage localization in anisotropic composite plates," *Journal of Intelligent Material Systems and Structures*, vol. 27, pp. 350–374, Feb. 2016.

[53] J. E. Michaels, "Detection, localization and characterization of damage in plates with an in situ array of spatially distributed ultrasonic sensors," *Smart Materials and Structures*, vol. 17, p. 035035, May 2008.

[54] X. Zhao, H. Gao, G. Zhang, B. Ayhan, F. Yan, C. Kwan, and J. L. Rose, "Active health monitoring of an aircraft wing with embedded piezoelectric sensor/actuator network: I. Defect detection, localization and growth monitoring," *Smart Materials and Structures*, vol. 16, pp. 1208–1217, June 2007.

[55] Z. Sharif-Khodaei and M. H. Aliabadi, "Assessment of delay-and-sum algorithms for damage detection in aluminium and composite plates," *Smart Materials and Structures*, vol. 23, p. 075007, May 2014.

[56] N. Quaegebeur, P. C. Ostiguy, and P. Masson, "Correlation-based imaging technique for fatigue monitoring of riveted lap-joint structure," *Smart Materials and Structures*, vol. 23, p. 055007, May 2014.

[57] A. Sorrentino and A. De Fenza, "Damage Detection in Complex Composite Material Structures by using Elliptical Triangulation Method," in *The 11th International Workshop on Structural Health Monitoring*, (Standford, USA), DEStech Publications, Inc., Sept. 2017.

[58] A. Sorrentino and A. De Fenza, "Improved elliptical triangulation method for damage detection in composite material structures," *Proceedings of the Institution of Mechanical Engineers, Part C: Journal of Mechanical Engineering Science*, vol. 231, pp. 3011–3023, Aug. 2017.

[59] A. Migot, Y. Bhuiyan, and V. Giurgiutiu, "Numerical and experimental investigation of damage severity estimation using Lamb wave–based imaging methods," *Journal of Intelligent Material Systems and Structures*, vol. 30, pp. 618–635, Mar. 2019.

[60] N. Quaegebeur, P. Masson, D. Langlois-Demers, and P. Micheau, "Dispersion-based imaging for structural health monitoring using sparse and compact arrays," *Smart Materials and Structures*, vol. 20, p. 025005, Feb. 2011.

[61] W. Briand, M. RÉBILLAT, M. GUSKOV, and N. MECHBAL, "Upcoming damage size quantification in aeronautic composite structures based on imaging results post-processing," *Journal of Intelligent Material Systems and Structures*, 2021.

[62] S. L. E. Rafael C. Gonzalez, Richard E. Woods, *Digital Image Processing Using MATLAB*. Prentice Hall, 2002.

[63] J. Friedman, T. Hastie, and R. Tibshirani, *The Elements of Statistical Learning: Data Mining, Inference, and Prediction*. New York: Springer series in statistics, 2001.

[64] J. C. Lagarias, J. A. Reeds, M. H. Wright, and P. E. Wright, "Convergence Properties of the Nelder–Mead Simplex Method in Low Dimensions," *SIAM Journal on Optimization*, vol. 9, pp. 112–147, Jan. 1998.

[65] E. Balmes, M. Guskov, M. Rebillat, and N. Mechbal, "Effects of temperature on the impedance of piezoelectric actuators used for SHM," in *14th Symposium on Vibration, Shock and Noise (VISHNO)*, (France), pp. 1–6, June 2014.

[66] E. Balmes and A. Deraemaeker, "Modeling structures with piezoelectric materials, SDT tutorial," 2013.

[67] J.-H. Kim, F. Pierron, M. Wisnom, and K. Syed-Muhamad, "Identification of the local stiffness reduction of a damaged composite plate using the virtual fields method," *Composites Part A: Applied Science and Manufacturing*, vol. 38, pp. 2065–2075, Sept. 2007.

[68] J. Schindelin, I. Arganda-Carreras, E. Frise, V. Kaynig, M. Longair, T. Pietzsch, S. Preibisch, C. Rueden, S. Saalfeld, B. Schmid, J.-Y. Tinevez, D. J. White, V. Hartenstein, K. Eliceiri, P. Tomancak, and A. Cardona, "Fiji: An open-source platform for biological-image analysis," *Nature Methods*, vol. 9, pp. 676–682, July 2012.

[69] C. Larrosa, K. Lonkar, and F.-K. Chang, "In situ damage classification for composite laminates using Gaussian discriminant analysis," *Structural Health Monitoring*, vol. 13, pp. 190–204, Mar. 2014.

[70] A. Saxena, K. Goebel, C. C. Larrosa, and F.-K. Chang, "CFRP Composites Data Set," 2011.

[71] K. Liu, S. Ma, Z. Wu, Y. Zheng, X. Qu, Y. Wang, and W. Wu, "A novel probability-based diagnostic imaging with weight compensation for damage localization using guided waves," *Structural Health Monitoring*, vol. 15, pp. 162–173, Mar. 2016.

[72] E. F. Crawley and J. de Luis, "Use of piezoelectric actuators as elements of intelligent structures," *AIAA Journal*, vol. 25, no. 10, pp. 1373–1385, 1987.

[73] D. A. Dillard, "Chapter 1 - Fundamentals of stress transfer in bonded systems," in *Adhesion Science and Engineering* (D. A. Dillard, A. V. Pocius, and M. Chaudhury, eds.), pp. 1–44, Amsterdam: Elsevier Science B.V., Jan. 2002.

[74] G. Huang, F. Song, and X. Wang, "Quantitative Modeling of Coupled Piezoelectric-Elastodynamic Behavior of Piezoelectric Actuators Bonded to an Elastic Medium for Structural Health Monitoring: A Review," *Sensors*, vol. 10, pp. 3681–3702, Apr. 2010.

[75] X. D. Wang and G. L. Huang, "Wave Propagation in Electromechanical Structures: Induced by Surface-Bonded Piezoelectric Actuators," *Journal of Intelligent Material Systems and Structures*, vol. 12, pp. 105–115, Feb. 2001.

[76] A. Raghavan and C. Cesnik, "Modeling of Guided-wave Excitation by Finite-dimensional Piezoelectric Transducers in Composite Plates," in *48th AIAA/ASME/ASCE/AHS/ASC Structures, Structural Dynamics, and Materials Conference*, Structures, Structural Dynamics, and Materials and Co-located Conferences, American Institute of Aeronautics and Astronautics, Apr. 2007.

[77] F. Lanza di Scalea, H. Matt, and I. Bartoli, "The response of rectangular piezoelectric sensors to Rayleigh and Lamb ultrasonic waves," *The Journal of the Acoustical Society of America*, vol. 121, pp. 175–187, Jan. 2007.

[78] T. Grahn, "Lamb wave scattering from a circular partly through-thickness hole in a plate," *Wave Motion*, vol. 37, pp. 63–80, Jan. 2003.

[79] F. B. Cegla, A. Rohde, and M. Veidt, "Analytical prediction and experimental measurement for mode conversion and scattering of plate waves at non-symmetric circular blind holes in isotropic plates," *Wave Motion*, vol. 45, pp. 162–177, Jan. 2008.

[80] C. Vemula and A. N. Norris, "Flexural wave propagation and scattering on thin plates using Mindlin theory," *Wave Motion*, vol. 26, pp. 1–12, Aug. 1997.

[81] A. Sedaghati, F. Honarvar, M. Tabatabaeipour, and A. N. Sinclair, "Investigation of the scattering of Lamb waves from a generalized circular cavity by using Poisson/Mindlin plate theories and numerical simulation," *Proceedings of the Institution of Mechanical Engineers, Part C: Journal of Mechanical Engineering Science*, vol. 234, pp. 152–170, Jan. 2020.

[82] J. C. P. Mckeon and M. K. Hinders, "Lamb wave scattering from a through hole," *Journal of Sound and Vibration*, vol. 224, pp. 843–862, July 1999.

[83] C. H. Wang and F.-K. Chang, "Scattering of plate waves by a cylindrical inhomogeneity," *Journal of Sound and Vibration*, vol. 282, pp. 429–451, Apr. 2005.

[84] O. Diligent, T. Grahn, A. Boström, P. Cawley, and M. J. S. Lowe, "The low-frequency reflection and scattering of the S0 Lamb mode from a circular through-thickness hole in a plate: Finite Element, analytical and experimental studies," *The Journal of the Acoustical Society of America*, vol. 112, pp. 2589–2601, Dec. 2002.

[85] O. Diligent and M. J. S. Lowe, "Reflection of the s0 Lamb mode from a flat bottom circular hole," *The Journal of the Acoustical Society of America*, vol. 118, pp. 2869–2879, Oct. 2005.

[86] L. Moreau, M. Caleap, A. Velichko, and P. D. Wilcox, "Scattering of guided waves by through-thickness cavities with irregular shapes," *Wave Motion*, vol. 48, pp. 586–602, Nov. 2011.

[87] L. Moreau, M. Caleap, A. Velichko, and P. D. Wilcox, "Scattering of guided waves by flat-bottomed cavities with irregular shapes," *Wave Motion*, vol. 49, pp. 375–387, Mar. 2012.

[88] B. Poddar and V. Giurgiutiu, "Scattering of Lamb waves from a discontinuity: An improved analytical approach," *Wave Motion*, vol. 65, pp. 79–91, Sept. 2016.

[89] B. Poddar and V. Giurgiutiu, "Complex modes expansion with vector projection using power flow to simulate Lamb waves scattering from horizontal cracks and disbonds," *The Journal of the Acoustical Society of America*, vol. 140, p. 2123, Sept. 2016.

[90] M. F. Haider, R. Joseph, V. Giurgiutiu, and B. Poddar, "An efficient analytical global–local (AGL) analysis of the Lamb wave scattering problem for detecting a horizontal crack in a stiffened plate," *Acta Mechanica*, Nov. 2019.

[91] C. Fendzi, J. Morel, M. Rebillat, M. Guskov, N. Mechbal, and G. Coffignal, "Optimal sensors placement to enhance damage detection in composite plates," in *European Workshop on Structural Health Monitoring*, (Nantes, France), 2014.

[92] W. Ostachowicz, R. Soman, and P. Malinowski, "Optimization of sensor placement for structural health monitoring: A review," *Structural Health Monitoring*, p. 1475921719825601, Jan. 2019.

[93] H. Yun, R. Rayhana, S. Pant, M. Genest, and Z. Liu, "Nonlinear ultrasonic testing and data analytics for damage characterization: A review," *Measurement*, vol. 186, p. 110155, Dec. 2021.

[94] H. Postorino, M. Rebillat, E. Monteiro, and N. Mechbal, "Towards an industrial deployment of PZT based SHM processes: A dedicated metamodel for Lamb wave propagation," in *European Workshop on Structural Health Monitoring 2020*, pp. 1–12, July 2020.

[95] R. Chennamsetti, K. Balasubramaniam, M. Joshi, and K. Chitti Venkata, "Interaction of guided Lamb waves with an asymmetrically located delamination in a laminated composite plate," *Smart Materials and Structures*, vol. 19, p. 065009, Apr. 2010.

[96] C. Ramadas, K. Balasubramaniam, M. Joshi, and C. V. Krishnamurthy, "Interaction of the primary anti-symmetric Lamb mode (Ao) with symmetric delaminations: Numerical and experimental studies," *Smart Materials and Structures*, vol. 18, p. 085011, June 2009.

[97] L. Schubert, M. Barth, T. Klesse, B. Köhler, and B. Frankenstein, "Guided elastic waves and their impact interaction in CFRP structures characterized by 3D laser scanning vibrometry," in *The 15th International Symposium on: Smart Structures and Materials & Nondestructive Evaluation and Health Monitoring* (T. Kundu, ed.), (San Diego, California), p. 69350G, Mar. 2008.

[98] Y. Shen and V. Giurgiutiu, "WaveFormRevealer: An analytical framework and predictive tool for the simulation of multi-modal guided wave propagation and interaction with damage," *Structural Health Monitoring: An International Journal*, vol. 13, pp. 491–511, Sept. 2014.

[99] J. Achenbach, *Wave Propagation in Elastic Solids*. North Holland, 1973.

[100] T. R. Kane and R. D. Mindlin, "High-Frequency Extensional Vibrations of Plates," *Journal of Applied Mechanics*, vol. 23, pp. 277–283, June 1956.

[101] M. Rucka, *Guided Wave Propagation in Structures. Modelling, Experimental Studies and Application to Damage Detection*. PhD thesis, Politechnika Gdańska, 2011.

[102] J. Yang, *Introduction to the Mathematical Theory of Vibrations of Elastic Plates, an-by RD Mindlin*. World Scientific, 2006.

[103] R. D. Mindlin and M. A. Medick, "Extensional Vibrations of Elastic Plates," tech. rep., Office of Naval Research, Apr. 1958.

[104] E. W. Weisstein, "Bessel Function of the First Kind." https://mathworld.wolfram.com/BesselFunctionoftheFirstKind.html, Feb. 2022.

[105] F. W. J. Olver, A. O. Daalhuis, D. W. Lozier, B. I. Schneider, R. F. Boisvert, C. W. Clark, B. R. Miller, B. V. Saunders, H. S. Cohl, and M. A. McClain, "NIST Digital Library of Mathematical Functions." http://dlmf.nist.gov/, 2020.

[106] D. C. Ricks and H. Schmidt, "A numerically stable global matrix method for cylindrically layered shells excited by ring forces," *The Journal of the Acoustical Society of America*, vol. 95, pp. 3339–3349, June 1994.

[107] A. K. Mal, "Wave propagation in layered composite laminates under periodic surface loads," *Wave Motion*, vol. 10, pp. 257–266, June 1988.

[108] A. Raghavan and C. E. S. Cesnik, "Finite-dimensional piezoelectric transducer modeling for guided wave based structural health monitoring," *Smart Materials and Structures*, vol. 14, pp. 1448–1461, Nov. 2005.

[109] H. Sohn and S. J. Lee, "Lamb wave tuning curve calibration for surface-bonded piezoelectric transducers," *Smart Materials and Structures*, vol. 19, p. 015007, Nov. 2009.

[110] H. Postorino, *Structural Health Monitoring En Relation Aux Endommagements Produits Par Choc Laser Dans Des Structures Aéronautique En Composite*. PhD thesis, HESAM, Paris, To be published.

[111] M. Rouse, D. R. Ambur, J. Bodine, and B. Dopker, *Evaluation of a Composite Sandwich Fuselage Side Panel with Damage and Subjected to Internal Pressure*, vol. 110309. Langley Research Center, 1997.

[112] T. T. Ata and D. Coker, "3D Simulation of Dynamic Delamination in Curved Composite Laminates," *Procedia Structural Integrity*, vol. 21, pp. 130–137, Jan. 2019.

[113] C. Sun and S. Li, "Three-Dimensional Effective Elastic Constants for Thick Laminates," *Journal of Composite Materials*, vol. 22, pp. 629–639, July 1988.

[114] K. J. Schubert and A. S. Herrmann, "On attenuation and measurement of Lamb waves in viscoelastic composites," *Composite Structures*, vol. 94, pp. 177–185, Dec. 2011.

[115] M. Gresil and V. Giurgiutiu, "Prediction of attenuated guided waves propagation in carbon fiber composites using Rayleigh damping model," *Journal of Intelligent Material Systems and Structures*, vol. 26, pp. 2151–2169, Nov. 2015.

[116] Noliac, "NCE51 Product Data Sheet," 2020.

[117] M. Géradin and D. J. Rixen, *Mechanical Vibrations: Theory and Application to Structural Dynamics*. John Wiley & Sons, 2014.

[118] E. Moulin, S. Grondel, J. Assaad, and L. Duquenne, "Modeling a surface-mounted Lamb wave emission-reception system: Applications to structural health monitoring," *The Journal of the Acoustical Society of America*, vol. 124, pp. 3521–3527, Dec. 2008.

[119] C. T. Ng, M. Veidt, L. R. F. Rose, and C. H. Wang, "Analytical and finite element prediction of Lamb wave scattering at delaminations in quasi-isotropic composite laminates," *Journal of Sound and Vibration*, vol. 331, pp. 4870–4883, Oct. 2012.

[120] V. T. BUCHWALD, "RAYLEIGH WAVES IN TRANSVERSELY ISOTROPIC MEDIA," *The Quarterly Journal of Mechanics and Applied Mathematics*, vol. 14, pp. 293–318, Aug. 1961.

[121] F. B. Hildebrand, *Advanced Calculus for Applications*. Pearson College Division, 1976.

William BRIAND

Lamb waves based active sparse tomography for damage size quantification in composite structures: data-driven and analytical inversion methods

Résumé : Cette thèse concerne le contrôle de santé des structures composites aéronautiques (en anglais « Structural Health Monitoring » ou SHM) par ondes guidées générées par des transducteurs piézoélectriques. L'objectif général est de proposer et de valider expérimentalement des méthodes permettant de quantifier la taille d'un dommage de type délaminage présent dans la structure à surveiller. La première contribution de cette thèse est la création et la publication d'une base de données libre d'accès et de réutilisation de mesures SHM issues d'essais de fatigue de structures en composite représentatives de composants aéronautiques. La seconde contribution est le développement et la validation sur des dommage de taille inconnue d'une approche de quantification basée purement sur les données qui consiste à entrainer un modèle mathématique à partir de données labélisées et d'un descripteur original calculé à partir d'images de localisation. La troisième contribution est le développement et la validation d'une méthode de quantification qui repose sur l'estimation de paramètres liés au dommage à partir d'un modèle physique et qui ne nécessite pas de données de référence. Pour résoudre ce problème inverse, un modèle analytique est développé pour prédire le signal mesuré par un capteur piézoélectrique au passage d'une onde générée par un actionneur piézoélectrique et diffractée par un dommage. Ce modèle théorique est ensuite utilisé pour remonter à la taille et à la sévérité du défaut. Ces deux méthodes de quantification, basées l'une sur les donnée et l'autre sur un modèle physique, ont été validées sur des signaux issus de simulations numériques et sur des signaux expérimentaux.

Mots clés : Contrôle de santé des structures, SHM, matériau composite, transducteur piézoélectrique, apprentissage supervisé, quantification, ondes de Lamb, identification de paramètre, délaminage, fatigue, aéronautique

Abstract : This thesis concerns the structural health monitoring of aeronautical composite structures (SHM) using guided waves generated by piezoelectric transducers. The general objective is to propose and validate experimentally several methods to quantify the size of a delamination type damage present in the structure to be monitored. The first contribution of this thesis is the creation and publication of an open access and reusable database of SHM measurements from fatigue tests of composite structures representative of aeronautics components. The second contribution is the development and validation on damage of unknown size of a purely data-based quantification approach that consists in training a mathematical model from labeled data and an original mathematical descriptor computed from localization images. The third contribution is the development and validation of a quantification method that relies on the estimation of damage-related parameters from a physical model and does not require reference data. To solve this inverse problem, an analytical model is developed to predict the signal measured by a piezoelectric sensor at the passage of a wave generated by a piezoelectric actuator and diffracted by a damage. This theoretical model is then used to estimate the size and severity of the damage. These two quantification methods, one based on data and the other on a physical model, have been validated on signals from numerical simulations and on experimental signals.

Keywords : Structural Health Monitoring, composite material, piezoelectric transducer, supervised machine learning, size quantification, Lamb wave, parameter identification, delamination, fatigue, aerospace